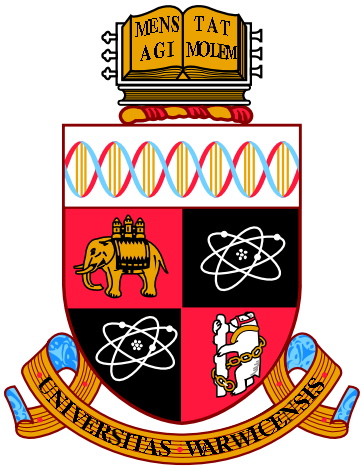

Investigating the Structure of Amyloid Aggregates using Solid-State Nuclear Magnetic Resonance

by

Robert Thomas Kelly

Thesis

Submitted to the University of Warwick

for the degree of

Doctor of Philosophy

School of Life Sciences

January 2015

THE UNIVERSITY OF WARWICK

Contents

List of Tables

List of Figures

Acknowledgements

The people that have earnt first place in the acknowledgements for this thesis are my NMR *triumviri*: Steven P. Brown, Oleg N. Antzutkin and Józef R. Lewandowski. There is no doubt that without these three, this thesis would not exist. I thank Steven for introducing me to, and guiding me through, the world of NMR. I thank Oleg for introducing me to the fascinating world of amyloid proteins and their associated pathologies, and for the Northern Lights. I thank Józef for teaching me everything I know about the experimental side of NMR, and for his continual assistance this area.

My Scandinavian collaborators, who have provided samples or taught me while I was spending time in their institutions, primarily Andrei Filipov at Luleå Tekniska Universitet, but also the Härd and Nielsen groups in Uppsala and Aarhus, deserve significant recognition. Dinu Iuga has also been extremely helpful regarding experiments performed using the UK 850 MHz Solid-State NMR Facility.

My lab partner for many years, and good friend, Jonny Lamley has been a consistent font of knowledge and advice.

I thank all those in the Millburn House office for creating an enjoyable atmosphere in which to perform my research, and the characters that I have met on my travels over the last 3 years who have always made me feel welcome.

Financial support from the BBSRC in funding this research and the UK 850 MHz Solid-State NMR Facility in funding a conference trip to Chamonix is gratefully acknowledged.

To my parents and brothers, who have always supported me in my efforts, I hope this work is a fitting testament to their love and generosity. And finally, for sharing this period of my life with me, and for being my light in the dark, I will be forever indebted to Claire.

Robert T. Kelly

Made in LaTeX

Declarations

The work contained within this thesis is a result of my original research, carried out between October 2011 - September 2014, under the supervision of Prof. Steven P. Brown, Prof. Oleg N. Antzutkin and Dr. Józef R. Lewandowski at the University of Warwick. Where contributions of others are included, these are indicated within the text. This work has not been submitted for another degree.

Results contained within Chapter 8 have been accepted for publication and contains work based on collaborative research, the individual contribution of the author regarding this work has been made clear. The publication's details are:

Lendel C, Bjerring B, Dubnovitsky A, Kelly RT, Filippov A, Antzutkin ON, Nielsen N Chr, Härd T (2014) A Hexameric Peptide Barrel as a Building Block of Amyloid-β Protofibrils *Angew. Chem. Int. Ed.* 53:12756-12760 [1]

The author has also contributed to the following publication, though the work for this is not shown in this thesis:

Antzutkin ON, Iuga D, Filipov A, Kelly RT, Becker-Baldus J, Brown SP, Dupree R (2012) Hydrogen Bonding in Alzheimer's Amyloid-β Fibrils Probed by ^{15}N $\{^{17}$O$\}$ REAPDOR Solid-State NMR Spectroscopy. *Angew. Chem. Int. Ed.* 124:10435-10438. [2]

Abstract

Crucial biological processes are often dictated by the action of proteins, including cell growth, intercellular communication and apoptosis. The behaviour and function of proteins, and other important bio-macromolecules, is inherently linked to the 3D conformation of the polypeptide and the range of dynamics within the structure. The rapidly developing tool, solid-state NMR, is uniquely placed to structurally probe large, non-crystalline macromolecules, such as proteins, and provide data at atomic-level resolution. Amyloid diseases, such as Alzheimer's disease and Parkinson's disease, are linked to neuronal damage caused by toxic species which occur through misfolding and aggregation of naturally expressed proteins. Aggregation of the 36-43 residue protein amyloid-beta (Aβ) is thought to be involved in the pathology of Alzheimer's disease.

In this thesis, solid-state NMR is used to obtain ^{1}H, ^{15}N and ^{13}C chemical shifts for U-[^{13}C, ^{15}N] A$\beta_{1\text{-}40}$ aggregates formed in the presence of copper, a metal found in abnormally high concentrations in amyloidogenic plaques in Alzheimer's-disease-afflicted patients' brains via post-mortem examination. A suite of 2D ^{13}C-^{13}C DARR and ^{15}N-^{13}C DCP experiments alongside 2D and 3D X-^{1}H, ^{15}N-^{1}H-^{1}H and ^{13}C-^{15}N-^{1}H. Inverse Detection experiments employed at $\sim$100 kHz MAS frequency is employed to obtain chemical shift values. TALOS-N provides torsion angle restraints and sec-

ondary chemical shift analysis is performed to identify turn and β-sheet regions. The results are compared to previously published models, and indicate the sample is similar to a brain-derived fibrillar structure.

2D ^{13}C-^{13}C DARR experiments are also performed on selectively labelled samples of $A\beta_{1\text{-}42}$ with cysteine replacements at locations A21 and A30. This cross-linking mechanism between C21 and C30 has been shown to stabilise an oligomeric form, thought to be the most toxic, on the aggregatory pathway to fibrils. The labels allow detailed characterisation of the turn region between residues 22 and 29. The incorporation of the oligomers into lipid membranes was studied by 1D ^{31}P NMR, specifically to investigate the effect of the oligomers on the stability of the membranes and the effect of cholesterol and curcumin, a potentially therapeutic compound currently of high interest, on this de-stabilisation. Work with collaborators has enabled the oligomeric form to be modelled and the results indicate these toxic oligomers form a hexamer barrel structure, with the hydrophobic sidechains contained within the barrel. The secondary structure of the oligomer is shown to contain 3 or 4 β-sheets; with an extended β-sheet region between K16-V24, 1 or 2 β-sheets between N27 and V36, and then a short β-sheet between V39 and A42. A method for inter-molecular β-sheet interaction in the hexamer is postulated. A method for further aggregation from this oligomeric form to a protofibrillar form has also been suggested, thus enabling a claim to be made for an on-pathway nature for this oligomeric form.

Abbreviations

2QF	Double Quantum Filtering
Aβ	Amyloid-Beta
AD	Alzheimer's Disease
APP	Amyloid Precursor Protein
BMRB	Biological Magnetic Resonance data Bank
CSA	Chemical Shift Anisotropy
COSY	COrrelation SpectroscopY
CP	Cross Polarisation
cw	Continuous Wave
CWLG	Continuous Wave Lee-Goldburg
DARR	Dipolar-Assisted Rotational Resonance
DCP	Double Cross Polarisation
DMPC	Dimyristoylphosphatidylcholine
DOPC	Dioleylphosphatidylcholine
DRAMA	Dipolar Recovery At the Magic Angle
DRAWS	Dipolar Recoupling with A Windowless Sequence
EM	Electron Microscopy
EPR	Electron Paramagnetic Resonance
FID	Free Induction Decay
FT	Fourier Transform
GB1	B1 Immunoglobulin Binding Domain of Protein G
HORROR	HOmonucleaR ROtary Resonance
LvN	Liouville-von Neumann
MAS	Magic-Angle Spinning

MD	Molecular Dynamics
NMR	Nuclear Magnetic Resonance
NOE	Nuclear Overhauser Effect
NOESY	Nuclear Overhauser Effect SpectroscopY
PAS	Principal Axis System
PD	Parkinson's Disease
PDB	Protein Data Bank
PDSD	Proton-Driven Spin Diffusion
PFGs	Pulsed Field Gradients
ppm	Parts Per Million
QM	Quantum Mechanics
R^2	Rotational Resonance
R^3	Rotary Resonance Recoupling
REDOR	Rotational-Echo DOuble Resonance
rf	Radio Frequency
RFDR	Radio Frequency-driven Dipolar Recoupling
S/N	Signal-to-Noise
SEDOR	Spin-Echo DOuble Resonance
SPINAL	Small Phase Incremental ALternation decoupling
SPPS	Solid Phase Peptide Synthesis
TALOS	Torsion Angle Likelihood Obtained from Shifts and sequence similarity
TDSE	Time-Dependent Schrodinger Equation
TMS	Tetramethylsilane
TPPM	Two Pulse Phase Modulation
TSAR	Third Spin-Assisted Recoupling
WALTZ	Wideband, Alternating-phase, Low-power Technique for Zero-residual splitting
WT	Wild Type
ZQ	Zero Quantum

1 Introduction

1.1 The History and Development of NMR

1.1.1 The History of NMR

Nuclear magnetic resonance (NMR) is a widely used tool for structural and dynamical investigations of samples. The very first spectra were taken ∼70 years ago, although plenty of groundwork was required before those seminal spectra of paraffin and water were produced in 1946. [3,4] To truly put NMR in its historical context we must begin in the 1920s. Quantum theory was undergoing major development as experimental results were being explained by theoreticians. In 1922 a pair of German physicists, Otto Stern and Walther Gerlach, discovered the quantised intrinsic property of spin angular momentum in the famous 'Stern-Gerlach' experiment. [5] However, though this pair performed the correct experiment for investigating the phenomenon, they found the beam contained only two components as opposed to three or one (which was expected at the time); they had the incorrect theory for explaining such results. This was provided later, in 1925, by George Uhlenbeck and Samuel Goudsmit who proposed that the electron had an intrinsic angular momentum, or spin, equal to $\pm\hbar/2$. [6] In the following two years Schrödinger and Heisenberg formulated a new branch of quantum mechanics replacing the previous quantum theory (1926), [7, 8] before Wolfgang Pauli derived the mathematical theory behind electron spin and quantum mechanics (1927). [9] In 1927 Stern and Gerlach's experiment was altered by Phipps and Taylor so that they were able to detect nuclear magnetic moments; they observed and measured the deflection of a beam of hydrogen molecules. [10] Paul Dirac's derivation of relativistic quantum mechanics then used electron spin as

a central pillar of the theory (1928). [11]

Several years later in 1936, the first attempt to find NMR in condensed matter was made by C.J. Gorter, as he searched unsuccessfully for a ^{7}Li resonance in crystalline lithium fluoride and for the protons in crystalline potassium alum. [12] The following year Isidor Rabi, working at Columbia University, designed an experiment that would identify nuclear resonance; by passing a beam of molecules through a strong and constant magnetic field, and irradiating this with a small oscillating magnetic field set at right angles to the beam, as the frequency of the oscillating field approached the Larmor frequency of the nucleus under investigation he observed magnetic resonance absorption. The use of varying magnetic field strength for the small beam was, in fact, suggested to Rabi by Gorter. In 1942 Gorter and Broer tried to find the NMR signal for ^{7}Li in solid lithium chloride and for ^{19}F in solid potassium fluoride, but again it evaded them. [13] The problem has since been realised as being located in the purity of the crystals used such that the longitudinal relaxation times, T_1, the time taken for the return of magnetisation to equilibrium, were very long, resulting in the fact that saturation may have caused the lack of observation of the resonance. So the eventual pioneers of the NMR in bulk materials were Purcell at Harvard and Bloch at Stanford at the end of 1945, recording the NMR signals for protons in solid paraffin wax and protons in water, respectively. Both groups were aware of the dangers of saturation, and were able to avoid it; the Stanford group even introduced paramagnetic salts into some of their samples so as to enhance relaxation. [3, 4] The Harvard group followed up their discovery of NMR with an extensive investigation of NMR in solids, liquids and gases. [14]

1.1.2 Development of NMR

The groundwork was now laid for significant developments to push NMR from an interesting nuclear phenomenon to the powerful investigative tool that it is today.

That NMR can be used to investigate structure, when exacted on solid-state samples, originates from the mathematical form of the spatial dependence of the magnetic dipolar interaction,[1] $(3\cos^2\theta - 1)\, r^{-3}$, where $\vec{r}$ is the vector connecting the two nuclei between which this interaction occurs, and θ is the angle between $\vec{r}$ and the static external magnetic field, B_0. In 1948, G. Pake published a finding which was crucial in the develoment of NMR; he had obtained the distance between water molecules in a single crystal of gypsum with an accuracy of 2%. [15]

[1] which will be expanded upon in detail later

The earliest NMR experiments were performed using iron electromagnets which could generate fields of 2 T, or large permanent magnets of up to 1 T. NMR signals were initially detected by continuous wave (cw) methods. Throughout the 1960s and 70s a process of refinement of NMR equipment occurred which has led to the modern spectrometers of today, current magnets reach 1 GHz proton Larmor frequency ($\sim$23.5 T) with a uniformity in field of 1 in 10^9. Concordantly cw-based techniques were replaced with pulsed methods. Pulse methods were significantly boosted by Hahn's 1950 discovery of spin echoes and from a proof by Lowe and Norberg in 1957 that a free induction decay (FID) is the Fourier transform (FT) of the NMR cw spectrum. [16,17] This boost was twinned with the availability of fast Fourier transform algorithms which were utilised in solution state NMR but which followed later in the solid state. NMR could now be used to find distances in single crystals, however NMR needed to be shown as a valid tool to use when working with powder samples.

Magic-angle spinning (MAS) provided an ingenious solution to the line broadening in powder sample spectra due to anisotropic interactions, present in the solid state. Andrew et al, in 1958, and Lowe, in 1959, were the first to investigate the effect of rotation on a solid sample, and when spun at an angle of $\sim$54.74° to the static magnetic field, previously broad lines were shown to narrow significantly. [18, 19] ssNMR no longer required single crystal samples.

The use of Cross Polarisation (CP), specific double-resonance irradiation, to transfer magnetisation from an abundant spin to a dilute spin so as to greatly enhance the NMR signal on the secondary nuclear species was shown by Hartmann and Hahn in 1962, initially exacted without any sample rotation. [20] Spin decoupling was then shown to reveal all three ^{19}F resonances in a sample containing CaF_2, C_6F_6 and NaF when a train of 180° pulses were applied on ^{23}Na during acquisition, where previously, without the decoupling, the NaF resonance was lost. [21] CP and decoupling were combined in a landmark publication in 1972 by Pines, Gibby and Waugh providing well resolved ^{13}C NMR spectra. [22]

Schaefer and Stejskal made the step to then combine a decoupled CP experiment while rotating the sample at the 'magic' angle and showed the improvement available to spectroscopists by employing this technique on many solid materials. [23] NMR had now evolved to a level of sophistication such that the modern day experiment would be recognised. The CP MAS technique developed above, is still used widely today as a workhorse of many labs and is crucial in investigating biological macromolecules, due to the importance of low-γ nuclei such as ^{13}C and ^{15}N.

The technique above removed heteronuclear dipolar couplings, through the use of decoupling, and chemical shift anisotropies, through the use of MAS, providing well resolved spectra from which chemical shift values could be obtained. The information that was removed, however, would be of use if it could be selectively re-introduced and so dipolar recoupling methods began to emerge to achieve this. In 1989 Guillion and Schaefer, reported a sequence which enabled ^{13}C-^{15}N dipolar couplings to be recovered through use of two 180° pulses on the ^{15}N channel per rotor period. By comparing the spectra obtained with and without these pulses the ^{13}C-^{15}N coupling could be measured. [24] The sequence was called rotational-echo double-resonance (REDOR), and drew from Slichter's spin-echo double-resonance (SEDOR) experiments. [25] In 1990 Tycko and Dabbagh introduced dipolar recovery at the magic-angle (DRAMA) a pulse sequence which enabled ^{13}C dipole-dipole couplings of $(CH_3)_2C(OH)SO_3Na$, whereby 5% of the molecules were ^{13}C labelled at both methyl carbons, to be measured. [26]

With the ability to now selectively reintroduce various interactions, NMR was evolving to a suitable level of sophistication for investigating small biological molecules, and so, as the new millennium dawned, solid-state NMR began to take its place as a well situated probe of structure and dynamics for biological macromolecules.

1.1.3 NMR of Proteins

Introduction to Biological NMR

Solution-state NMR developed more rapidly than solid-state NMR and, therefore, many large steps in the field came from this, the major branch of the technique. In the 1970s the technique was being used to investigate the interplay between biomolecular structure, dynamics and function, and a crucial finding was made by Wüthrich and Wagner in 1978; the 1D ^{1}H NMR resonance of aromatic residues in a small globular protein was recorded as a function of temperature and the results suggested the aromatic side chains within the hydrophobic core could rotate. [27] That X-ray diffraction could offer a snap shot image of a protein and solution-state NMR could provide information on the dynamics was very exciting, and suggested that the complementary techniques could be used to fully characterise important biomolecules. In 1976 Ernst and co-workers published a report showing that 2D correlation spectroscopy, or COSY, NMR experiments were possible and would be vital for the technique to continue solving increasingly complex tasks; this great step forward was then followed

in 1979 with the first use of 2D nuclear Overhauser enhancement spectroscopy, or NOESY, NMR. [28, 29] The following year, Wüthrich and Ernst revealed the use of the NOESY experiment for elucidating proton-proton relaxation networks in biological macromolecules. [30] Ernst would be awarded the Nobel Prize for 'his contributions to the development of the methodology of high resolution nuclear magnetic resonance spectroscopy' in 1991. In 1985, Kurt Wüthrich's group in Zurich reported the use of solution NMR to solve the first de novo structure of a protein, through obtaining 202 ^{1}H-^{1}H distance constraints from NOE spectroscopy (NOESY) experiments - a leading achievement for Wüthrich, who would be jointly awarded the Nobel Prize in 2002 for 'his development of nuclear magnetic resonance spectroscopy for determining the three-dimensional structure of biological macromolecules in solution'. [31]

In 1999 Opella and co-workers determined structures of the M2 channel-lining segments from nicotinic acetylcholine and NMDA receptors by NMR spectroscopy, using solution NMR experiments on micelle samples and solid-state NMR experiments on bilayer samples. [32] The work utilised a technique called PISEMA[2] (Polarisation Inversion Spin-Exchange at the Magic Angle) which is a valuable technique in the investigation of oriented samples, such as membranes, in the presence and absence of magic-angle spinning. [33] For more on the PISEMA technique see [34].

By 2002 ssNMR had evolved to such a level of sophistication, through developments in magnetic field strength, decoupling and recoupling pulse sequences and sample preparation, that the Oschkinat group in Berlin published the first 3D structure of a protein, the SH3 domain of α-spectrin, by solid-state NMR. [35] Through use of a micro-crystalline sample, selective labelling and the use of 2D homonuclear proton-driven spin diffusion (PDSD) experiments, [36] many ^{13}C and ^{15}N assignments could be made such that an overall fold of the protein could be produced. ssNMR had been shown as a viable tool for structurally investigating proteins, and interest would rapidly increase in the technique.

With the increase in robust experimental sequences, see Table 1 in [37], and the availability of high quality experimental equipment, it is unsurprising that recently biological solid-state NMR has rapidly increased in usage for investigating crucial biomacromolecules. MAS frequencies have been increasing due to intelligent probe design, such that proton detected solid-state NMR methods have been unlocked and used to solve the 3D structure of a protein, [38] with MAS frequencies now exceeding 100 kHz using state of the art probes. NMR probes have also been designed

[2]Developed in 1994 by Wu, Ramamoorthy and Opella

to combat the heating which results from the use of radio frequency (rf) pulses of samples, which is crucial for the maintenance of samples at biologically stable temperatures over long experimental time periods. In 2011 another step forward for biological NMR occurred in the use of proton detected 4D experiments to generate distance restraints sufficient for the unambiguous structure solving of ubiquitin. [39] Alongside the relentless experimental and hardware advances, computational abilities have grown considerably and many structure solving programs now exist which can be used to solve structures when provided solely with chemical shift data. [40] Modern day biological solid-state NMR has solved the 3D structure of several proteins in the 10s of kDa region with the largest currently being the Type-III secretion system needle, weighing in at 257 kDa, solved by Lange and co-workers. [41] Other notable ssNMR studies into proteins are the structural solving of the B1 immunoglobulin binding domain of protein G (GB1), a 6 kDa, 56 residue protein, [38, 42] and the analysis of the membrane protein bacteriorhodopsin by the Griffin group. [43] Further examples of protein structures determined using solid-state NMR include the Baldus group's determination of the structure and dynamics of the 52-residue membrane polypeptide phospholamban, [44] alongside the secondary structure and dynamics of a seven-helix receptor, sensory rhodopsin II from *Natronomonas pharaonis* from the same group. [45] The Opella group further determined the structure of a membrane protein with two trans-membrane helices in aligned phospholipid bicelles using solid-state spectroscopy using PISEMA and other techniques. [46]

With the developments and wide-spread use as shown above, clearly solid-state NMR is a tool which is very well suited for this study on amyloid aggregates.

1.2 Introduction to Amyloid Proteins, Fibrils and Aβ

Amyloid diseases such as Alzheimer's (AD), Parkinson's (PD) and transmissible spongiform encephalopathy are an area of high scientific interest, see § 1.2.1 below. Different techniques can be employed to investigate the structure, dynamics and typical behaviours of the amyloid proteins, which are believed to play leading roles in the pathology of these diseases. ssNMR has recently become a technique of intense interest; this stems from the limitations involved with classical structure solving techniques such as solution-state NMR and X-ray crystallography. Solution-state NMR has an inherent size limit on the structures it can solve; it is also reliant on the solubility of any molecules for investigation. X-ray crystallography relies upon the crystallisation of a potential structure; a structure with significant dynamics would

prove difficult to crystallise. Furthermore, that crystals are not needed in ssNMR unlocks the option of many different conditions in which the sample can be, such that, for example, functionality at high or low temperature can be investigated. ssNMR is now accepted as a suitable technique for solving protein structures and, also, protein structures when incorporated in lipid membranes.

Membrane proteins (6792 entries) and amyloid fibril (147 entries) structures comprise around only 7% of the structures in the Protein Data Bank (PDB) (total number of entries: 103015; http://www.rcsb.org, Sept 2014), which is surprising considering their importance: membrane proteins control the interchange of information and substances across the cell membrane; defend against invading pathogens; and control the delivery of complex instructions needed for the cells cycle. [47, 48]

With recent improvements in ssNMR it has become an achievable goal to structurally solve these proteins; MAS, intelligent rf pulse sequences and improvements in low temperature NMR have brought this topic to a really exciting stage of development. [49] The significance of this project stems from the growing prevalence of neurodegenerative diseases; AD is estimated at affecting one in eight people over the age of 65 and more than 26 million people worldwide, [50] PD is the most common neurodegenerative movement disorder affecting more than 4 million people worldwide. [51] With an aging population, never before have these diseases been more important, and a pharmacological remedy is likely to be based on structural information of the interaction of toxic species in an *in situ* or *in vivo* environment. This is a target of several ssNMR groups around the world. [52–54]

Amyloid-beta (Aβ) is a 36 to 43 amino acid residue peptide, which exists naturally in the brain as a relatively unstructured monomer [55] derived from the amyloid precursor protein (APP); [56] a transmembrane protein that is localized on the cell membrane or in intracellular vesicles, [57] which undergoes alternative splicing to generate several isoforms that are defined by the number of amino acids in each. Resulting APP isoforms can have 770, 751, 714, 695, 563, and 365 amino acids, with the smallest two unable to generate Aβ. [58] APP, spliced by either β or γ secretase, produces isoforms of Aβ, which vary in their toxicities, with $A\beta_{1-42}$ currently seen as the most neurotoxic, see Fig. 1.1. [59] Aβ's progression from monomer to a hairpin-structured fibrillar aggregate (fibrils are fibres with nanoscopic dimensions) is associated with the onset of events that lead to AD. [60] Fibrillar forms, see Fig. 1.1, of Aβ have been well documented; [61–64] interest developed when AD affected patients' brains were found to contain fibrillar plaques, and the reasonable postulate was made that this material was the causative agent of the disorder. This

view was later reinforced by a number of observations; for example, amyloid fibrils formed from the Aβ peptide were found to be toxic to cultured neuronal cells and to cause both membrane depolarization and alterations in the frequency of their action potentials. Moreover Aβ fibrils were shown to cause neuronal loss and microglial activation when injected into the cerebral cortex of aged rhesus-monkeys. [48] However, though elderly people inevitably develop amyloid plaques (admittedly the quantity of which can vary) only ∼30% of octogenarians develop AD, suggesting that amyloid fibrils alone might not destroy neurons. [49] Recently focus has moved from fibrils to a soluble oligomeric species, which may or may not be on pathway to fibrils, as the primary cause for neuronal death; evidence is beginning to mount that this could well be the case. [60,65,66] Current research is focussing on finding the structures of these oligomers and discovering whether they are on or off pathway; if they are off pathway, it will be interesting to discover whether they are the final stage of aggregation or to what structure they themselves finally aggregate.

1.2.1 NMR of Aβ

One of the earliest ssNMR papers on Aβ, published in 1991, reports the use of rotational resonance to measure the distances between carbons in a peptide fragment, [67] - this work and the initial structural data taken on Aβ, published in 1995, was performed by Lansbury, Griffin and co-workers; they investigated the 34-42 section of Aβ by finding ^{13}C-^{13}C distances and chemical shifts. [68] Following this, from the same collaboration, a further publication on the 34-42 Aβ fragment was published investigating the backbone conformation. [69] In the following year in 1998, Meredith and co-workers reported a parallel β-sheet structure of fibrillar $A\beta_{10\text{-}35}$ as found from carrying out distance measurements from selectively labelled samples using dipolar recoupling ssNMR methods. [70] This method (DRAWS) [71] was then used by the same group in the same year for a secondary publication revealing inter- and intrastrand distances on the same sample fragment. [72] Fig. 1.2 displays two types of β-sheet arrangement, antiparallel and parallel; work at this time often investigated which of these forms fibrils adopted.

In 2000, the Meredith group produced two publications, one revealing the use of DRAWS to find interstrand distances of 5.3 ± 0.3 Å with in-register parallel β-strand fibrils, with the secondary structure found from intrastrand constraints with labels at two adjacent residues. This also proposed the existence of a turn region in the residues 25-29. [73] The second paper combined ssNMR with other techniques

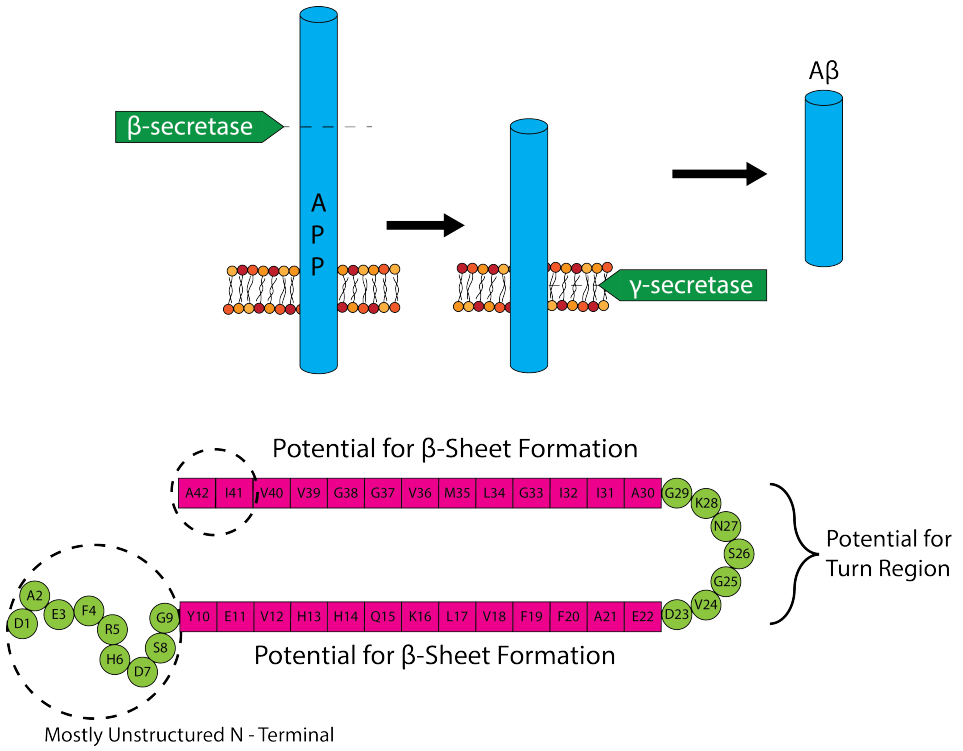

Figure 1.1: A schematic displaying the cleavage sites of APP which produce the variants of Aβ (top). The sequence of the 1-42 variant of Aβ is shown with regions in which secondary structure can be found within the fibrillar form indicated. The secondary structure varies with different polymorphs, however most indicate that two β-sheets exist either side of turn section. Those residues between D23 and G29 that are not included in the turn region are often found in one of the β-sheets.

(electron microscopy, small angle neutron scattering and others) to assign the three-dimensional form of the fibrils from $A\beta_{10\text{-}35}$. [74] In the same year, Tycko's group produced two reports, one structurally characterising a seven residue fragment of Aβ, 16-22, using 2D MAS ^{13}C-^{13}C ssNMR experiments to reveal the $A\beta_{16\text{-}22}$ fragment as the shortest (at the time) to form fibrils. [75] The other used a multiple quantum ^{13}C ssNMR technique to probe the β-sheet organisation in the full length peptide in fibrillar form; it revealed a parallel, not antiparallel, organisation of β-sheets. [76]

Several publications occurred in the amyloid-beta field in 2002 as interest continued to rise, a structural model for full length wild type (WT) Aβ based on ^{13}C and ^{15}N chemical shifts was proposed, [61] constraints on the supramolecular structure of $A\beta_{1\text{-}40}$ using intermolecular dipole-dipole couplings between ^{13}C spins at 11 carbon sites using MAS NMR were also reported, alongside the discovery of structural disor-

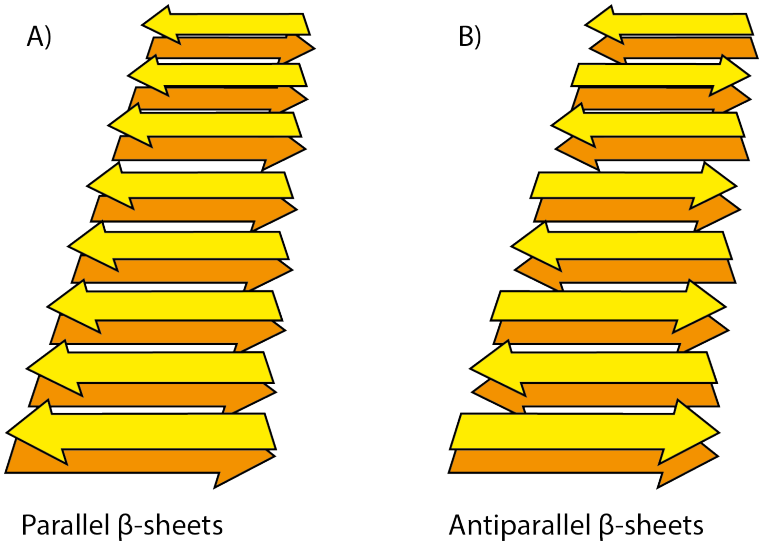

Figure 1.2: A schematic displaying a parallel β-sheet arrangement (A) and an antiparallel β-sheet arrangement (B). Adapted from [49]

der in the N-terminal segment. [77] An extensive investigation was also reported by the same group in the same year showing electron microscopy, scanning transmission electron microscopy and ssNMR data on $A\beta_{1\text{-}42}$ and $A\beta_{10\text{-}35}$ at varying pH, providing constraints for the supramolecular structure of the fibrils, and in particular on the β-sheet properties of the sample. The report also provided schematic structural models of the fibrils investigated. [78] A study using electron paramagnetic resonance (EPR) to identify in-register parallel arrangement of fibrils as well as confirm dynamic regions in the N- and C-termini was published. [79]

Further work into the locations of turn and β-sheet sections and the issue of parallel or anti-parallel arrangements of these β-sheets were published the following year, [80,81] with the turn section identified at residues G25, S26 and G29. The effect of pH on the structure of fibrils from the 11-25 fragment of the peptide was published in 2004; this work found that the registry of the intermolecular hydrogen bonds was well defined but varied due to pH and also different to the 16-22 fragment previously published. [82] A report investigating the importance of amphiphilicity on parallel or anti-parallel β-sheet formation using the 16-22 fragment was published in the same year. [83]

Tycko and co-workers then published a report showing that different fibril morphologies have different underlying molecular structures, and that these can be dictated by fibril growth conditions and that the morphology and structure can be propagated

from fibrillar seeds. These different morphologies were also shown as having different toxicities. [62] In a collaboration with Meredith, the group published findings that, with a secure Lactam bridge from D23 - K28, rapid self-association (1000 times faster than usual) without a lag phase occurs creating fibrils which are similar to WT Aβ fibrils. The lactam bridge Aβ also acted as a seed for fibrillisation of WT Aβ. [84] Ishii and Chimon reported the first site-resolved structural measurement of an intermediate species in fibril formation for $A\beta_{1\text{-}40}$, showing the spherical amyloid intermediate has a 15-30 nm diameter and exists prior to fibril formation. [85]

In 2006, intra- and intermolecular contacts were obtained such that a quaternary structure of $A\beta_{1\text{-}40}$ fibrils could be made using molecular dynamics simulations. [86] The morphology and molecular structure of fibrils of $A\beta_{10\text{-}40}$ grown under different conditions were shown to display polymorphism, and it was concluded that residues 1-9 did not necessarily dictate polymorphism. Seeds of $A\beta_{10\text{-}40}$ were shown to be able to produce fibrils in mixtures of $A\beta_{1\text{-}40}$. [87] Smith and co-workers reported the packing of M35 against G33 in $A\beta_{1\text{-}40}$ and against G37 in $A\beta_{1\text{-}42}$, and, from this structural displacement, they designed a new class of inhibitors that prevented fibril formation by disrupting sheet-to-sheet packing and reduced the toxicity of $A\beta_{1\text{-}42}$ on cultured rat cortical neurons. [88] Solution NMR was conducted alongside many solid-state NMR experiments; of interest is a hydrogen/deuterium exchange spectroscopy study of Aβ under physiological conditions, revealing two core regions 11-25 and 28-42. The 1-42 variant was found to be much more stable in intermediary conformations than the 1-40, possibly explaining its greater toxicity. [89]

The following year, Ishii and co-workers reported β-sheet structures in a neurotoxic amyloid intermediate of $A\beta_{1\text{-}40}$. The toxicity of the intermediate was shown to be higher than that of the fibril, but that the formation of the β-sheets within the intermediate's structure could trigger neurotoxicity. [90] In the same year, the Tycko group investigated the molecular structure of the fibrils formed by $A\beta_{14\text{-}23}$ and discovered that the fibrils contained antiparallel β-sheets with a registry of backbone hydrogen bonds aligning residue $17+k$ with residue $22-k$ of neighbouring molecules in the same β-sheet. [91]

In 2008, Tycko and Thurber investigated the implications of MAS NMR at very low temperatures, 25 K, on $A\beta_{14\text{-}23}$ in fibrillar form. It was found that a gain of roughly $1/T$ could be won in signal-to-noise. [92] The Tycko group also published a full structural model for amyloid fibrils formed from full length Aβ with a periodically twisted morphology, see Fig. 1.3. The structure has threefold symmetry about the fibril growth axis as opposed to the twofold symmetry found for a previously published

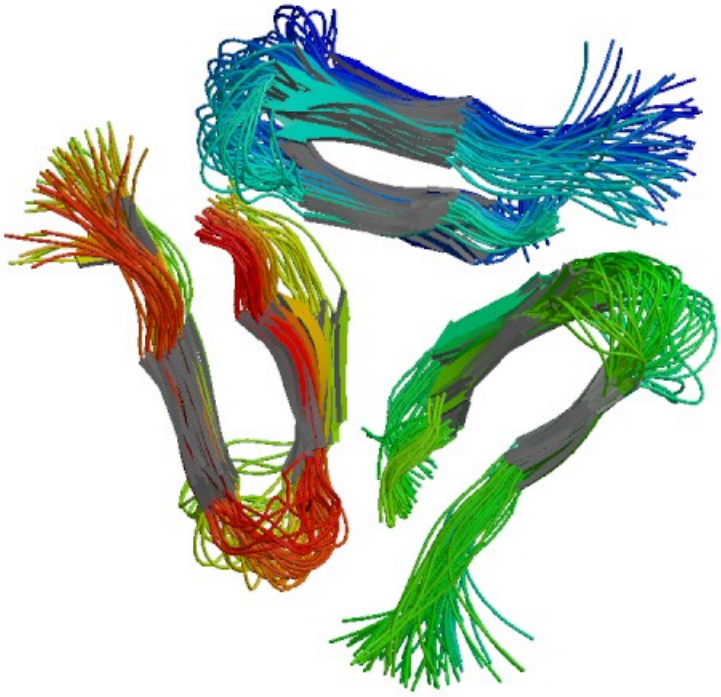

Figure 1.3: A three-fold symmetric fibril form of Aβ as revealed by the Tycko group. [93] Referred to as 'twisted pair' fibrils, this form is often found from quiescent growth conditions. [49] Fibril long axis is into the page. Obtained from the PDB.

model of striated ribbon fibrils, see Fig 1.4. [93]

A particularly exciting piece of research was published in 2009 by the Tycko group, reporting the investigation of the structure of fibrils seeded by extracts from an AD afflicted patient's brain. ^{13}C chemical shifts and other ssNMR data indicated that these fibrils were distinct when compared to previously characterised synthetic fibrils, though no model was produced. [64] Tycko and co-workers also investigated the structure of fibrils formed by the Iowa mutant (D23N). Fibrils formed faster than WT and without a lag phase, and only a minority of the fibrils contained in-register, parallel β-sheet structures with ssNMR data implying the existence of antiparallel fibrils. [94]

Ishii and co-workers then investigated the impact of Cu^{2+} on the structure of amyloid fibrils, as metals had previously been identified as an important factor in the activity of Aβ on membranes and their toxicity on neurons by the Barnham group. [95, 96]

Figure 1.4: A two-fold symmetric fibril form of Aβ as revealed by the Tycko group. [86] Referred to as 'striated ribbon' fibrils, these fibrils contain D23-K28 salt bridge interactions, which are thought to be important in fibril nucleation. In contrast to 'twisted pair' fibrils, this form is often found using gentle agitation during fibril growth. [49] Fibril long axis is into the page. Obtained from the PDB.

The ssNMR and UV-vis spectroscopy data revealed the binding sites as histidines-6,13 and 14, and also that the secondary structure was not disrupted by the Cu^{2+} binding. [97]

In 2011, Huster and co-workers determined the secondary structure in B10AP-stabilised $A\beta_{1\text{-}40}$ protofibrils at a single residue level using ssNMR. It was found that the β-sheet elements are formed in protofibrils but they elongate during conversion to mature amyloid fibrils to include residues 23-26 and G33. [98] Meredith and co-workers reported the instantaneous fibrillisation of the Japanese mutant (ΔE22) of Aβ. ssNMR measurements taken were not compatible with parallel, in-register β-sheet structures such as that of the WT fibrils, however when used as a seed in a mixture of WT Aβ, fibrils grew but in the fibrillar form of the Japanese mutant. [99] Tycko and co-workers then published an investigation into the effect of seeding using the Iowa

mutant, which had previously shown antiparallel and parallel β-sheet structures. It was shown that the sample increases homogeneity while undergoing repeated seeding attempts and, though starting from a sample containing both types of structure, the final structures contain only parallel β-sheets, indicating the metastable nature of an antiparallel β-sheet structure. [100] Following this, in 2012, a protocol was reported that regularly produced antiparallel β-sheet structure in the Iowa mutant, in spite of the less efficient propagation of the structure. [101] Also in 2011, the Bertini group published their new structural model of amyloid fibrils for $A\beta_{1\text{-}40}$ as found using ssNMR. [63] There were also chemical shifts reported for Aβ fibril samples with metals, and the effect of these metals on the aggregation properties of the fibrils by Ishii, investigating Cu^{2+}, and Madhu, investigating Zn^{2+}. [55, 102]

The Huster group then reported contacts found between E22 and I31 for protofibrils which were not found in fibrils. As these were also found in oligomers, the suggestion was put forward that protofibrils were closer to oligomers in structure than fibrils. If this were the case, some major structural re-organisation would be required to aggregate from protofibrils into fibrils. [103] In the same year, the same group revealed the dynamics of Aβ fibrils using ssNMR. [104] Many groups at this time were using solid phase peptide synthesis (SPPS) to produce synthetic samples for ssNMR, the Ishii group investigated the efficiency of this method for long peptide sequences, as it was known that for sequences 30-50 residues long the efficiency plummeted. It was found that Aβ underwent excessive misfolding while attached to the resin, and highly ordered β-structures were found over the entire sequence. [105] The Ramamoorthy group revealed that membrane disruption by Aβ is a two step process, with initial formation of ion-selective pores followed by nonspecific fragmentation of the lipid membrane during amyloid fiber formation. The study suggests zinc blockading is a possibility for solving the initial defects, but that amyloid formation on the membrane fragment surface cannot be impaired through the use of ions. It was shown also that gangliosides enhanced the pore formation and fiber elongation process. [106]

In 2013, the Madhu group investigated a central fragment of Aβ, residues 18-35, and found that the significant structural properties of full length Aβ fibrils were maintained, and that the secondary structure and tertiary contacts were also propagated. It was suggested that this fragment would be ideal for therapeutic investigations. [107] The Ishii group, now a leading ssNMR group in the investigation of the effect of metals on Aβ aggregation, reported the resolution enhancements achievable through use of fast spinning and rapid recycle delays available due to paramagnetic centres such as Cu^{2+} within samples. [108] The same group then investigated through ssNMR, a

biologically relevant amyloid intermediate of the highly toxic $A\beta_{1\text{-}42}$ peptide. [109] This was a particularly important piece of work as focus was beginning to shift to the oligomeric form of the peptide as this was thought to be the most toxic and therefore the most important for therapeutic remedies. The Tycko group then revealed a landmark paper; almost all previous work had used synthetic samples, however by seeding fibrils from samples of Aβ plaques obtained from pieces of AD brain tissue from different parts of the brain, several fibril samples were seeded. A single set of signals were found for all fibril samples seeded from plaques from all regions of the brain and a full structural model was produced from the brain-seeded fibrils. [110] This was then repeated with brain tissue from a different patient, and though patient two also had a single set of resolved signals the two sets were clearly different. The impressive homogeneity across all parts of the brain found for both patients implies that possibly Aβ forms in one part of the brain and then fragments and is transported to other regions. A review on this work was provided by Rienstra in the same year. [111]

The Huster group then studied several mutants of Aβ to better understand the influence of local physical variations on the fibril formation mechanism. Though fibrillation kinetics and local structure and dynamics were altered, the overall morphology and cross-β structure remained throughout. 7 of the 8 mutants investigated formed fibrils of very similar morphology. [112] Smith and co-workers investigated the Flemish mutant, A21G, which was found to emanate from an altered section of the C-terminal fragment of the amyloid precursor protein (APP). It was found to reduce the β-sheet component from L17-A21 and increase the α-helical structure from G25-G29, typically the turn section. It was also found that cholesterol increased Aβ secretion and that the incorporation of cholesterol into model membranes enhanced the structural changes induced by the Flemish mutant. [113] Ishii's group have recently continued their investigations into the effect of copper, by investigating the structure of fibrils without copper, then with Cu^{2+} added, and then with Cu^{+}, by reduction of the Cu^{2+} using ascorbate. The V12 carbon signals are lost upon Cu^{2+} addition, but recovered when ascorbate is added. It is suggested that the Cu^{2+} binding site is likely to be located at the Nδ of histidines-13 and 14. [114] Alongside the impact of metals, which has been known for a long time to effect the properties of Aβ, focus has moved to finding a substance that might be able to disrupt the toxic nature of the amyloid intermediate. A candidate, recognised over 10 years ago as a possible therapeutic target, for this is curcumin. [115, 116] Only recently has the ssNMR community started to investigate the effect of curcumin on amyloid fibrils, and the Madhu group reported,

in 2014, the disruption of the D23-K28 intrastrand contacts, alongside TEM images showing significant disturbance in the structure. Curcumin was also found to affect the C-terminal of the peptide. [117]

Alongside curcumin, other inhibitors have been investigated through ssNMR, such as those recorded in studies by the Reif group. [118] Binding of ligands and the molecular interfaces involved with protein folding and aggregation in an ssNMR context have also been recorded. [119]

Studies on Aβ, amongst other peptides, and membrane interactions are also numerous and have been investigated using: ^{31}P ssNMR - in such a study by the Seelig group, it was suggested that Aβ binds electrostatically to the outer envelope of the polar headgroup without penetrating between polar groups; ^{19}F ssNMR - a study by the Hong group proposed the oligomeric state of peptides bound to lipid bilayers; and ^{14}N ssNMR - in a study investigating the association of Aβ with membranes. [120–122]

The effect of metals on Aβ is of great interest as aggregates in the brain are found to have increased levels of metals such as copper, zinc and iron in them. [102] Zinc has been found to be protective in low concentrations, with mechanisms similar in effect to curcumin, but with high concentrations it increases the toxicity of Aβ. [123] EPR has also been used to investigate copper binding in Aβ, with TEM images suggesting that the fibrils before and after are the same, however the presence of copper induces fibril-fibril association. [124] Such studies have also taken place on other peptides. [125]

Molecular dynamics (MD) simulations is a complementary technique to ssNMR, and many groups are now obtaining data from ssNMR experiments and using MD simulations for modelling purposes. In 2005, MD simulations was used to probe the structural stability and conformational dynamics of several models of Aβ fibril structures. [126] In 2007 an investigation was performed into the effect of pH on the conformational processes of Aβ, as studied above in [78, 82], and the folding energy landscape was found to modulate strongly with pH and is most favourable for hydrophobically driven aggregation at pH 6. [127] Many other MD simulations publications have been made, on both Aβ and other peptides, but these will not be mentioned in more detail. [128–130]

Many other ssNMR studies has been published on interesting amyloid and other biological samples such as amylin, [131–134] HET-s prion, [135–137] α-synuclein, [53, 138] transthyretin fragments, [139] and Sup35p prion [140] to name just a few of

the impressive studies being carried out over the world. Moreover, work on the tau protein, also associated with Alzheimer's disease though with far less scientific attention currently focussed on it, is also ongoing. [141]

For further information on the vast library of ssNMR work on amyloid fibrils there are many review articles available: for a review on the progress made by ssNMR regarding Aβ see [142] (2000); for a review on structural investigations into fibrillogenesis see [143] (also 2000); for a review on what ssNMR can provide in terms of information regarding the structure and folding of Aβ see [144] (2003); for a review of the structures already found for amyloid fibrils using ssNMR, EPR, X-ray diffraction and electron microscopy see [145] (2005); for a short overview of ssNMR spectroscopic studies on amyloid fibrils see [146] (2008); and for a review by Tycko on amyloid and prion fibrils illustrating the vast array of structural issues which have been investigated by solid-state NMR amongst other techniques, see [147] (2013).

There are also a number of interesting reviews which concern various general aspects of Aβ science: for a review on the structure and function of AD amyloid deposits, their aggregation pathway and interaction of the structures along this pathway with cell biology see [148] (2004); for a review on the importance of, and progress made towards, conformation-dependent antibodies in tackling the aggregation of *in vivo* and *in vitro* amyloid proteins see [149] (also 2004); for a review of the progress made through using short peptide models to investigate amyloid self-assembly see [150] (2005); for a review of preparation techniques on Aβ see [151] (2006); for a review examining possible therapeutic directions for AD treatment see [152] (2007); for reviews on the impact of metals on Aβ aggregation and behaviour, or specifically on copper aided reactive oxygen species generation see [153] and [154] respectively (both 2009); and, for a review on intervention of amyloidosis and the achievement of inhibition of protein aggregation and amyloid formation see [155] (2012).

Solid-state NMR is an extremely powerful tool and has rapidly grown since its humble beginnings in the 1940s, with its ability to investigate the structure and dynamics of biomacromolecules which cannot be easily solved via other, more established, methods; as such, it is uniquely placed for use in this study of amyloid-β aggregates. The above shows that many groups across the world have put down sound foundations upon which this Aβ work is based.

1.3 Thesis Overview

The work presented in this thesis relies on using combinations of bio-NMR experiments to obtain chemical shift values for nuclear spins within the well defined structure of amyloid-beta aggregates. Experiments involving the most common biological nuclei, ^{1}H, ^{13}C and ^{15}N, constitute the bulk of the multidimensional ssNMR data, while 1D spectra of ^{31}P have also been recorded for investigating the stability of lipid membranes.

Chapters 2 and 3 provide the theoretical framework required to understand the fundamental workings of an NMR experiment. More specifically, Chapter 2 deals with the quantum mechanical foundations of NMR theory, and how these are manipulated in the methods employed to predict the behaviour of a system of many spins during an NMR experiment. Chapter 3 introduces the Hamiltonians responsible for the energy of spins in ssNMR experiments. Notably, a pertinent discussion of frame rotations and their use in NMR theory is offered.

Chapter 4 introduces the requirement for multidimensional NMR experiments for application to biological samples, and explains in detail the widely used techniques for obtaining nuclear-spin-specific chemical shift values from the spectra obtained from performing these experiments. The discussion also includes sign discrimination techniques and the manipulation of phase cycling for selective control over the coherences and multinuclear interactions that experiments investigate.

Chapter 5 introduces the specific bio-NMR experimental methods utilised in the work shown in this thesis. The pulse sequence coherence transfer pathway for, and data provided by, each experiment is presented, alongside a discussion of the techniques used for obtaining chemical shift values from the spectra produced by the experiments in the chapter. The decoupling and recoupling schemes used in the experiments are described. Chapter 6 contains all the experimental and computational details of the work shown in this thesis.

Chapter 7 presents the results of ssNMR investigation of a sample of U-[^{13}C, ^{15}N] A$\beta_{1\text{-}40}$ aggregates formed in the presence of copper. 2D ^{13}C-^{13}C homonuclear and ^{15}N-^{13}C heteronuclear spectra are shown alongside 2D and 3D inverse detection spectra involving both ^{13}C and ^{15}N with acquisition on ^{1}H. The chemical shift values obtained were submitted to the TALOS-N online program, and torsion angle predictions were obtained; secondary chemical shift analysis allowed reliable characterisation of the turn-region and two β-sheets.

Chapter 8 presents the results of the work performed on a cysteine-cysteine stabilised (following a mutation of A21C and A30C) oligomeric form of $A\beta_{1\text{-}42}$, a system which has previously been shown to be a particularly toxic species. 2D ^{13}C-^{13}C homonuclear spectra are shown for various amino acid labelling schemes, allowing accurate chemical shift values to be obtained for the residues in the hairpin turn section of the molecule, alongside some located in the β-sheets. 2D inverse detection spectra are also shown involving both ^{13}C and ^{15}N. 1D ^{31}P NMR was performed on samples containing combinations of the peptide, curcumin and cholesterol with lipid membranes and revealed that although individually each component disrupted the lipid membrane, curcumin appeared to reduce this destabilisation when combined with the oligomers, suggesting a therapeutic role for the molecule in the treatment of Alzheimer's disease.

This work will increase the level of structural knowledge regarding the interaction of curcumin with $A\beta_{1\text{-}42}$, alongside investigate the impact on the aggregated structure of $A\beta_{1\text{-}40}$ of copper when present during fibrillation. Important work in this area has been conducted previously (see § 1.2.1) however modern NMR techniques such as 2D and 3D inverse detection NMR will significantly increase the knowledge base; chemical knowledge of the environment of ^{1}H spins may allow a previously unobtainable level of understanding of the amyloid aggregation mechanism. Moreover, knowledge of the binding sites for copper will enable a greater understanding of why the ion is important in the formation of neuritic plaques.

2

Magnetic Resonance Theory

The bulk nuclear magnetism originating from the placement of nuclei into a magnetic field can be manipulated and observed, this is the fundamental approach of NMR spectroscopy. This chapter contains the quantum mechanical theory required to understand how a group of spins react to external magnetic fields, how radio frequency pulses can be used to carefully manipulate these systems and the theory required to predict the behaviour of an ensemble when the above are combined in a simple NMR experiment. This section, and § 3, draws upon the works of Levitt, [156] Duer, [157] and Mehring. [158]

2.1 Fundamental Quantum Mechanics

Nuclei possess important properties, which can be manipulated for experimental purposes: mass, electric charge, magnetism and spin. Spin angular momentum, $\hat{I}$, is an intrinsic property of a particle and is related to the particle's magnetic moment by the equation:

$$\hat{\mu} = \gamma \hat{I} \tag{2.1}$$

where $\hat{\mu}$ is the magnetic moment operator and γ is the gyromagnetic ratio of the material. Nuclei with $I > 0$ possess an intrinsic spin angular momentum given by:

$$|S| = \hbar\sqrt{I(I+1)} \tag{2.2}$$

Only two components of the nuclear spin angular momentum can be known simultaneously, convention dictates that these are the total angular spin, S, and the z-component, S_z:

$$S_z = m\hbar \tag{2.3}$$

where m is the azimuthal quantum number taking integer values $+I$, $+I-1$, ...,$-I$. A nuclear state with spin I is $(2I + 1)$-fold degenerate. If a magnetic field is applied, the degeneracy is broken. The splitting between the nuclear spin levels is called the nuclear Zeeman splitting. NMR is the spectroscopy of the nuclear Zeeman sublevels.

The Zeeman Hamiltonian, $\hat{\mathscr{H}}_Z$, is the perturbation to the Hamiltonian of a nucleus due to the presence of a magnetic field, B_0, which can be written:

$$\hat{\mathscr{H}}_{\mathrm{Z}} = -\hat{\mu}\mathrm{B}_0 = -\gamma\hat{I}\mathrm{B}_0 \tag{2.4}$$

The splitting of ^{1}H is about ten times greater than that of ^{15}N due to the ratio of gyromagnetic ratios ($\gamma_{\mathrm{H}}/\gamma_{\mathrm{N}}$), resulting in a proton nucleus being more magnetic than a ^{15}N nucleus. This energy level splitting, alongside other contributing factors, is responsible for the measurements taken in an NMR experiment.

2.2 Density Operator Theory

So as to have a generalised approach for understanding how a group of spins react to external magnetic fields and radio frequency (rf) pulses, which is essential for predicting the behaviour of a system during an NMR experiment, we turn to density operator theory. A collection of independent, identical systems is called an ensemble; an operator called the spin density operator is used to describe the entire quantum state of the ensemble.

A brief recap of quantum mechanics (QM) will smooth our transition into density operator theory. In QM, a state vector, $\langle\psi|$ or $|\psi\rangle$, represents the physical state of a system. This 'bra' and 'ket' notation is regularly used and they are related by complex conjugates:

$$\langle\psi| = (|\psi\rangle)* \tag{2.5}$$

State vectors can be expressed as a sum of a linear combination, or superposition, of unit vectors, ϕ_i:

$$|\psi\rangle = \Sigma_{i=1}^{i} c_i \, |\phi_i\rangle \tag{2.6}$$

where the coefficients c_i represent the contribution of each unit vector to the superposition. It can also be specified that the components belong to an orthonormal basis set:

$$\langle\phi_i \,|\, \phi_i\rangle = 1 \tag{2.7a}$$

$$\langle\phi_i \,|\, \phi_j\rangle = 0 \tag{2.7b}$$

where $\langle\phi \,|\, \phi\rangle$ represents a scalar product, or a projection of one vector onto another. More formally the coefficients, c_i, are related to the probability that when a measurement is performed on a system, the system will be found in the corresponding state. This probability can be calculated from multiplying c_i with its complex conjugate, c_i^*. Consider a two level system, such as a spin-$\frac{1}{2}$ nucleus with levels ϕ_1 and ϕ_2; the state vector can be expressed as:

$$|\psi\rangle = c_1 \, |\phi_1\rangle + c_2 \, |\phi_2\rangle \tag{2.8}$$

Operators can act on state vectors to give other state vectors (or a linear combination of different state vectors). In certain cases, however, the result is the original state vector multiplied by a constant:

$$\hat{A} \, |\psi\rangle = a \, |\psi\rangle \tag{2.9}$$

where $\hat{A}$ is an operator and a is the constant. In this case, $|\psi\rangle$ is referred to as an eigenfunction of $\hat{A}$, with eigenvalue, a. If the operator corresponds to a physical observable of a system, such as energy or angular momentum, the mean eigenvalue observed over several iterations of an experiment is given by the expectation value of

$\hat{A}$. This expectation value, $\langle \hat{A} \rangle$, is given by:

$$\langle \hat{A} \rangle = \langle \psi | \, \hat{A} \, | \psi \rangle \tag{2.10}$$

Consider a two level system, such as that used above, the basis vectors $|\phi_1\rangle$ and $|\phi_2\rangle$ are eigenfunctions of $\hat{A}$ when:

$$\hat{A} \, |\phi_1\rangle = a_1 \, |\phi_1\rangle \tag{2.11a}$$
$$\hat{A} \, |\phi_2\rangle = a_2 \, |\phi_2\rangle \tag{2.11b}$$

Therefore using eqn. 2.6

$$\hat{A} \, |\psi\rangle = a_1 c_1 \, |\phi_1\rangle + a_2 c_2 \, |\phi_2\rangle \tag{2.12}$$

Further using the result above and substituting eqn. 2.8 into eqn. 2.10 for the expectation value $\langle \hat{A} \rangle$, one finds:

$$\begin{aligned} \langle \hat{A} \rangle &= \langle \psi | \, \hat{A} \, | \psi \rangle \\ &= (c_1^* \langle \phi_1 | + c_2^* \langle \phi_2 |)(a_1 c_1 \, |\phi_1\rangle + a_2 c_2 \, |\phi_2\rangle) \\ &= a_1 c_1 c_1^* + a_2 c_2 c_2^* \\ &= a_1 |c_1|^2 + a_2 |c_2|^2 \end{aligned} \tag{2.13}$$

Now we have shown that each experiment on this wavefunction $|\psi\rangle$ produces the value a_1 or a_2 with the probabilities $|c_1|^2$ and $|c_2|^2$ respectively. Note, however, that the above relies on $|\phi_1\rangle$ and $|\phi_2\rangle$ being eigenfunctions of $\hat{A}$, and this is generally not the case, in which case eqn. 2.13 becomes:

$$\langle \hat{A} \rangle = c_1^* c_1 \langle \phi_1 | \, \hat{A} \, | \phi_1 \rangle + c_1^* c_2 \langle \phi_1 | \, \hat{A} \, | \phi_2 \rangle + c_2^* c_1 \langle \phi_2 | \, \hat{A} \, | \phi_1 \rangle + c_2^* c_2 \langle \phi_2 | \, \hat{A} \, | \phi_2 \rangle \tag{2.14}$$

Using the following notation,

$$A_{\phi_1 \phi_1} = \langle \phi_1 | \, \hat{A} \, | \phi_1 \rangle \tag{2.15}$$

eqn. 2.14 can be expressed as:

$$\langle \hat{A} \rangle = c_1^* c_1 A_{\phi_1\phi_1} + c_1^* c_2 A_{\phi_1\phi_2} + c_2^* c_1 A_{\phi_2\phi_1} + c_2^* c_2 A_{\phi_2\phi_2} \tag{2.16}$$

The matrix representation of $\langle \hat{A} \rangle$ is also used, this can be written by initially expressing $\mathbf{A}$, using eqn. 2.15:

$$\mathbf{A} = \begin{pmatrix} A_{\phi_1\phi_1} & A_{\phi_1\phi_2} \\ A_{\phi_2\phi_1} & A_{\phi_2\phi_2} \end{pmatrix} = \begin{pmatrix} \langle \phi_1 | \hat{A} | \phi_1 \rangle & \langle \phi_1 | \hat{A} | \phi_2 \rangle \\ \langle \phi_2 | \hat{A} | \phi_1 \rangle & \langle \phi_2 | \hat{A} | \phi_2 \rangle \end{pmatrix} \tag{2.17}$$

such that $\langle \hat{A} \rangle$ can now be expressed by:

$$\langle \hat{A} \rangle = \begin{pmatrix} c_1^* & c_2^* \end{pmatrix} \begin{pmatrix} A_{\phi_1\phi_1} & A_{\phi_1\phi_2} \\ A_{\phi_2\phi_1} & A_{\phi_2\phi_2} \end{pmatrix} \begin{pmatrix} c_1 \\ c_2 \end{pmatrix} \tag{2.18}$$

An expression for $\langle \hat{A} \rangle$ has now been obtained which involves the product of three matrices. This can be re-written to contain only two matrices, and the new matrix is of significant importance in density operator theory. It is called the density matrix, and can be expressed as:

$$\boldsymbol{\rho} = \begin{pmatrix} c_1 c_1^* & c_1 c_2^* \\ c_2 c_1^* & c_2 c_2^* \end{pmatrix} \tag{2.19}$$

So now expressing the expectation value with only two matrices we have:

$$\langle \hat{A} \rangle = \mathrm{Tr}[\boldsymbol{\rho} \boldsymbol{A}] \tag{2.20}$$

We now have two matrices: $\mathbf{A}$ which relates to the experiment or measurement on the spin system; and the other $\boldsymbol{\rho}$ which relates to the spin system. $\boldsymbol{\rho}$ is the matrix representation of the density operator, $\hat{\rho}$, which is formally written as:

$$\hat{\rho} = \overline{|\psi\rangle \langle\psi|} \tag{2.21}$$

where the overscore denotes an average over the whole system, referred to as an ensemble average. The result of this is that using the density matrix, $\boldsymbol{\rho}$, one can find the expectation value, $\langle \hat{A} \rangle$.

2.3 Introduction to Coherence

The density matrix for an isolated $I = \frac{1}{2}$ spin can more formally be expressed as:

$$\boldsymbol{\rho} = \begin{pmatrix} \overline{c_1 c_1^*} & \overline{c_1 c_2^*} \\ \overline{c_2 c_1^*} & \overline{c_2 c_2^*} \end{pmatrix} \tag{2.22}$$

where the overscore, once again, indicates an average over the system. The off diagonal elements reflect so called coherence between the states, with the diagonal reflecting the populations. In the case that the constants have uniformly distributed differing phases ϕ_i, with c_i=$|c_i|e^{i\phi_i}$, and noting the density matrix is an average over all $|\psi\rangle$s it is found:

$$\boldsymbol{\rho} = \begin{pmatrix} c_\alpha^2 & 0 \\ 0 & c_\beta^2 \end{pmatrix} \tag{2.23}$$

i.e. there is no coherence between the phases. Where there is a non-zero component off the diagonal in the density matrix, this implies an allowed and active transition between the two connected states. NMR spectroscopists can deliberately induce transfer between coherences through use of rf pulses of EM radiation on the sample. Quantum mechanically this is equivalent to acting on the state vector of the spin system with an operator, which corresponds to the rf pulse, which creates coherence.

2.4 The Liouville-von Neumann Equation

The time-dependent Schrodinger equation (TDSE) describes a system evolving with time:

$$\frac{\partial}{\partial t} |\psi(t)\rangle = -i\hat{\mathscr{H}} |\psi(t)\rangle \tag{2.24}$$

However, to use this to describe the behaviour of an NMR sample would require applying this equation to each spin within it, which is impractical. The density operator, however, contains information about the system as a whole and can be utilised. The time derivative of $\hat{\rho}$(t) can be written:

$$\frac{\partial}{\partial t}|\hat{\rho}(t)\rangle = \frac{\partial}{\partial t}(|\psi(t)\rangle) \cdot \langle\psi(t)| + |\psi(t)\rangle \cdot (\frac{\partial}{\partial t}\langle\psi(t)|) \tag{2.25}$$

Applying the TDSE, and its complex conjugate, to the time derivatives on the right hand side of the above equation, the below relation is found:

$$\frac{\partial}{\partial t}|\hat{\rho}(t)\rangle = -i[\hat{\mathscr{H}}, \hat{\rho}(t)] \tag{2.26}$$

where $[\hat{\mathscr{H}}, \hat{\rho}(t)]$ is the commutator of density operator and the Hamiltonian. This equation is the Liouville-von Neumann (LvN) equation, and the standard solution can be written:

$$\hat{\rho}(t) = e^{-i\hat{\mathscr{H}}t/\hbar}\hat{\rho}(0)e^{i\hat{\mathscr{H}}t/\hbar} \tag{2.27}$$

where the density operator, at $t = 0$, is $\hat{\rho}(0)$.

There are numerous NMR simulation programmes available, such as SpinEvolution and SIMPSON, which solve the density operator at various times, $\hat{\rho}(t)$, after specifying starting conditions, $\hat{\rho}(0)$, and the Hamiltonian, $\hat{\mathscr{H}}$. [159, 160] With over 1,300 citations together it is clear that these powerful programs are widely used within the NMR community.

2.5 Application of Liouville-von Neumann equation

A mathematical expression can be calculated for the FID by applying the LvN equation to an isolated spin-$\frac{1}{2}$ system under a resonance offset. Using the density operator at time, $t = 0$, as:

$$\hat{\rho}(0) = \hat{I}_x = \begin{pmatrix} 0 & \frac{1}{2} \\ \frac{1}{2} & 0 \end{pmatrix} \tag{2.28}$$

and the Hamiltonian being expressed as:

$$\hat{\mathscr{H}} = \Omega\hat{I}_z \tag{2.29}$$

where, $\Omega = \omega_0 - \omega_{\mathrm{rf}}$, is the resonance offset which can be described as the difference

between the Larmor frequency, the frequency at which the NMR signal oscillates, and the reference frequency, the frequency of the reference signal. Now with analogy to eqn. 2.20, to find the expectation value of the signal detected in the coil, the matrix form of the lowering operator of the spin angular momentum vector, $\hat{I}_- = \hat{I}_x - i\hat{I}_y$, is applied to $\hat{\rho}$(t); from eqn. 2.27:

$$\hat{I}_-^\dagger \hat{\rho}(\mathrm{t}) = \hat{I}_+ \hat{\rho}(\mathrm{t}) = \begin{pmatrix} 0 & 1 \\ 0 & 0 \end{pmatrix} \begin{pmatrix} 0 & \frac{1}{2}e^{-i\Omega t} \\ \frac{1}{2}e^{+i\Omega t} & 0 \end{pmatrix} = \begin{pmatrix} \frac{1}{2}e^{+i\Omega t} & 0 \\ 0 & 0 \end{pmatrix} \tag{2.30}$$

so that now, when a trace is taken, $s(t) = \mathrm{Tr}\ [\hat{I}_-^\dagger \boldsymbol{\rho}]$, and a simple substitution made, it is found that:

$$s(t) = \frac{1}{2}[\cos(\Omega t) + i\sin(\Omega t)] \tag{2.31}$$

It can be seen that a FID contains a real and imaginary signal which are 90° out of phase. This phenomenon is utilised for finding a difference between positive and negative values of the resonance offset, a process called quadrature detection, which will be expanded upon in § 4.3.1. In this chapter, the Hamiltonian describing the energy of the system has been represented simply by $\hat{\mathscr{H}}$, in the next chapter this will be expanded on and all the contributing factors to $\hat{\mathscr{H}}$ in an NMR experiment will be discussed.

3

HAMILTONIANS

This chapter contains details of the Hamiltonians of interest involved in an NMR experiment. The internal spin Hamiltonians describe the interactions between a spin and the environment around it, such that analysis of these provides a detailed description of the local physical and chemical landscape. Alongside the discussion of internal spin interactions, and the impact of these on NMR spectra, an important and relevant discussion of frame rotations involved in understanding these NMR interactions is presented. The impact of MAS on the spin interactions is also discussed.

3.1 Basics of an NMR Experiment

A brief overview of the basics of an NMR experiment will allow a smooth transition from the mainly theoretical approach of § 2 into this chapter, which begins to apply the theory to the practical application of the technique. NMR relies on the decaying precession around the static external magnetic field of the bulk magnetisation of a sample creating a Free Induction Decay (FID) in a coil wrapped around the vessel in which the sample is located. This FID, often referred to as the signal, contains information on the sample based on the atomic level environment of and interactions between spins within the sample.

Before performing ssNMR experiments, samples are packed into rotors [1] and placed into probes which enable rf irradiation to be applied onto the sample and the FID to be detected. The probes are then placed into a spectrometer, which is the piece of hardware housing the magnet which creates the large static external field. Once the

[1] Rotors are available in varying outer diameters, experiments in this thesis use 0.8 - 2.5 mm rotors

sample is placed within this field, the spins will begin to precess around this magnetic field (by convention named the z-axis), and a bulk magnetisation is created parallel to the field. This precession frequency around the z-axis is called the Larmor frequency; spectrometers are classed based on the Larmor frequency of ^{1}H, with larger magnetic fields generating higher Larmor frequencies. If rf irradiation is applied perpendicular to the external field (along e.g. the x-axis) and is oscillating at the Larmor frequency ('on resonance'), the bulk magnetisation vector will begin to precess anti-clockwise around the axis along which the irradiation is being applied. The frequency of this precession is called the nutation frequency, $\omega_1 = \gamma B_1$.

In a 'one pulse' experiment, a 90° pulse is applied such that the bulk magnetisation vector lies in the xy plane, i.e. an on resonance rf pulse is applied for a period of time suited to the nutation frequency, such that the bulk magnetisation vector is rotated through 90°. When left to evolve (a period of time when no rf irradiation is applied), this magnetisation will precess at the Larmor frequency. In addition, it will slowly dephase (as different spins will be in slightly different magnetic environments and therefore have slightly different Larmor frequencies), whereby the bulk magnetisation in the xy plane spreads out (this term is called transverse relaxation, and an important property in ssNMR is the transverse relaxation rate T_2 [161]) and the magnetisation will eventually return to thermal equilibrium along the z-axis (referred to as longitudinal relaxation, with T_1 as the longitudinal relaxation rate). As the magnetisation spirals back to the z-axis, precessing at the Larmor frequency, a signal will be generated in a nearby coil through induction, and this signal is recorded and analysed. For more on the hardware used in NMR experiments, and for an indepth explanation of signal acquisition see [156].

3.2 Interactions in an NMR Experiment

The full Hamiltonian for the energy of spins in ssNMR experiments can be written:

$$\hat{\mathscr{H}} = \hat{\mathscr{H}}_{\text{ext}} + \hat{\mathscr{H}}_{\text{int}} \tag{3.1}$$

where $\hat{\mathscr{H}}_{\text{ext}}$ depends on the external factors, the static field and the rf field, and $\hat{\mathscr{H}}_{\text{int}}$ depends on various internal factors of differing magnitudes of influence which will be discussed in detail later; in NMR experiments, $\hat{\mathscr{H}}_{\text{ext}}$ is by far the greater

factor.

The form of the Hamiltonian, in a general frame, for an interaction in Cartesian form is given by:

$$\hat{\mathscr{H}}_\Lambda = \hat{I}\tilde{A}\hat{S} \tag{3.2}$$

where $\tilde{A}$ is a second rank tensor specific for each individual interaction, Λ: chemical shift (CS); dipolar (D); J coupling (J); and, where appropriate, quadrupolar (Q). This can be expressed in spherical tensors as:

$$\hat{\mathscr{H}}_\Lambda = \sum_{j=0}^{2} C_j^\Lambda \sum_{m=-j}^{+j} (-1)^m A_{j,m}^\Lambda \hat{T}_{j,-m} \tag{3.3}$$

where A_{jm}^Λ corresponds to the spatial component of interaction Λ with rank j (e.g. if second rank then $j = 2$) and order m (where $m = j, j-1, ..., -j$), and $\hat{T}_{j-m}$ corresponds to the spin component of the Hamiltonian. C_j^Λ, here, represents a constant which varies for each interaction.

3.3 Frames and Rotations

There is an axes convention, which is of use for simplifying later Hamiltonian expressions, which will now be discussed. The principal axis system (PAS) of a Hamiltonian is one in which only the diagonal elements of the interaction tensor $\tilde{A}$ are non zero. The axes of this system often draw a parallel with local molecular structural features. To visualize this, consider a carboxylate group, the z-axis will often be perpendicular to the COO^- plane and the x- and y-axes are often approximately in the COO^- plane. However, in a powdered sample, not all the COO^- groups will be aligned and so the PAS frame for each nuclear site can be different; moreover, the PAS frame for each interaction involved in an NMR experiment can be different. A general transformation, taking each interaction from its PAS frame to a 'lab frame' where the signal is measured, is therefore required. By convention, the lab frame to which all interactions are mapped onto is the frame whereby the z-axis is parallel to the B_0 field; this is due to the Zeeman interaction, the strongest interaction in a NMR experiment, acting in this frame.

Spherical tensors, see eqn. 3.3, are often used, as the rank of a spherical tensor remains

the same under rotation. Remember in the PAS frame of an interaction that only the diagonal components of $\tilde{A}$ are non zero. In the PAS frame, eqn. 3.3 can then be written:

$$\hat{\mathscr{H}}_{\Lambda}^{PAS} = A_{00}^{P}\hat{T}_{00} + A_{20}^{P}\hat{T}_{20} + A_{22}^{P}\hat{T}_{2-2} + A_{2-2}^{P}\hat{T}_{22} \tag{3.4}$$

where A_{00}^{P} is the zero, zero matrix component of the interaction tensor $\tilde{A}$ in the PAS frame of the interaction, Λ.

The angles used to describe a rotation from one frame of reference to another are called Euler angles, α, β and γ. The operator for a rotation about these angles, conventionally α around the z-axis, β around the new y-axis and finally γ around the new z-axis, see Fig. 3.1, can be written:

$$\hat{R}(\alpha,\beta,\gamma) = \hat{R}_z(\gamma)\hat{R}_y(\beta)\hat{R}_z(\alpha) \tag{3.5}$$

where $\hat{R}_z(\alpha)$ is a rotation about the z-axis by an angle α. This is the first rotation of the above set to be applied and can be expressed:

$$\hat{R}_z(\alpha) = e^{(-i\alpha\hat{I}_z)} \tag{3.6}$$

As the spin tensor is constant under rotation, only an application of a rotation matrix on the spatial tensor is required to transform between frames; this rotation matrix, known as a Wigner D-matrix, can be written:

$$D_{kl}^{j}(\alpha,\beta,\gamma) = e^{-ik\alpha}d_{kl}^{j}(\beta)e^{-il\gamma} \tag{3.7}$$

where $d_{kl}^{j}(\beta)$ is a reduced Wigner rotation matrix, taking standard values e.g. see [162, 163]. The full transformation for a j^{th}-rank tensor can now be written:

$$A_{jm}^{end} = \sum_{m'=-j}^{+j} D_{m'm}^{j}(\alpha,\beta,\gamma)A_{jm'}^{start} \tag{3.8}$$

where $A_{jm'}^{start}$ is the initial frame and A_{jm}^{end} is the frame after transformation.[2] Note

[2]This is a generalised case. An example would be treating the 'start' frame as the principal axis system and the 'end' frame as the laboratory frame, using Euler angles α_{PL}, β_{PL} and γ_{PL}.

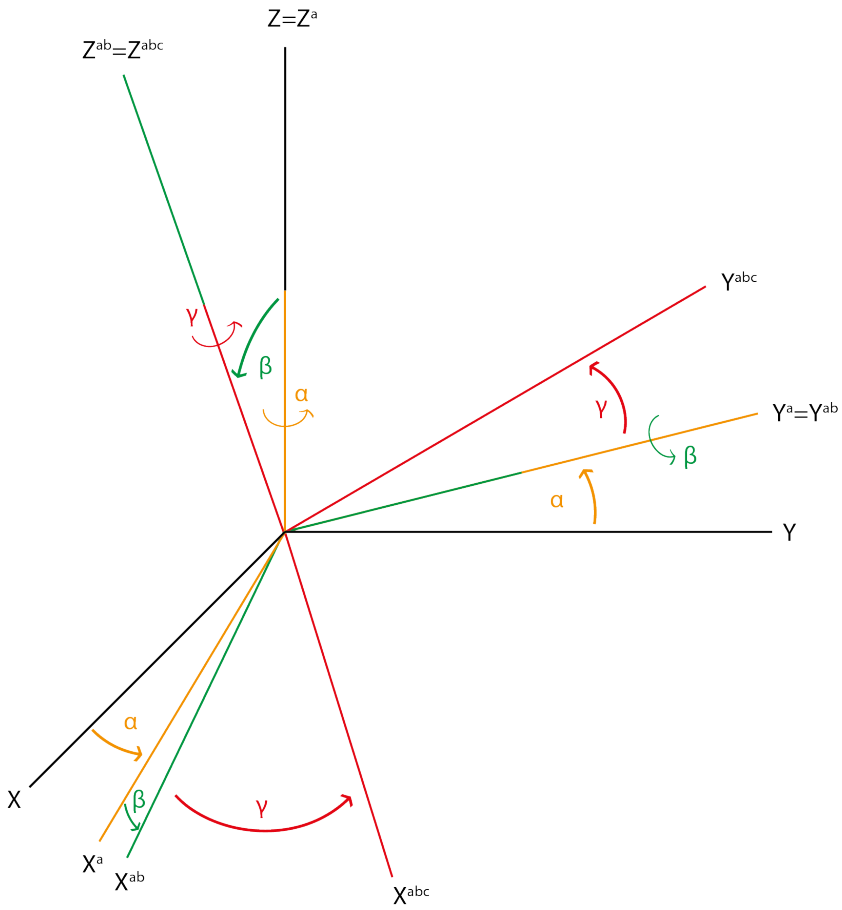

Figure 3.1: Illustration of the use of Euler angles, α, β and γ to describe a rotation between two reference frames.

that the rank has not changed, as expected, but the order has been changed upon rotation. Now an expression for the full Hamiltonian in the lab frame (L) for a static sample can be written:

$$\hat{\mathscr{H}}^L = \sum_{j=0}^{2} \sum_{m=-j}^{+j} (-1)^m A^P_{jm'} D^j_{m'm}(\alpha_{PL}, \beta_{PL}, \gamma_{PL}) \hat{T}_{j-m} \tag{3.9}$$

A quick look at the reduced Wigner rotation matrix from eqn. 3.7 will be informative at this stage. These matrices can be looked up in a table, such as Appendix A, and it can be seen that there is a relation from these to Legendre polynomials when $m = m' = 0$ which is often the case in NMR:

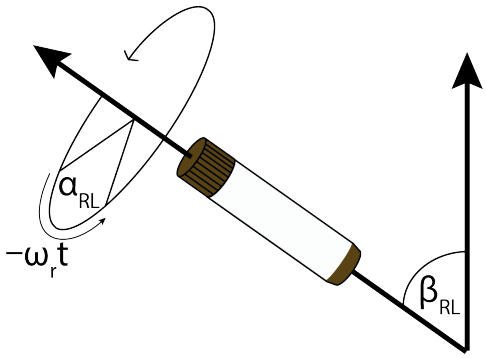

Figure 3.2: A graphic displaying MAS of a rotor. The material inside the rotor is rotated rapidly around the angle β_{RL}, $\simeq 54.74°$, to the static magnetic field. The angle α_{RL} is perpendicular to β_{RL} and is time dependent upon the spinning frequency, which nowadays can achieve upwards of 100 kHz. The angles here are the angles required to go from the rotor frame to the lab frame.

$$d^{j}_{00}(\beta) = P_j(\cos\beta) \tag{3.10}$$

β here is of great significance in solid-state NMR. It plays a role in the transformation of frames, whether the principal axis system or rotor frame (to be discussed later), into the laboratory frame (earlier assigned as the frame where the z-axis is considered that along which the B_0 magnetic field and hence the dominant Zeeman Hamiltonian act) as it describes the angle between those frames and this z-axis. The first Legendre polynomial is $P_0(\cos\theta) = 1$, which has a significance which will be discussed later. The $j = 2$ Legendre polynomial, which is of immediate relevance, can be written:

$$P_2(\cos\theta) = \frac{1}{2}(3\cos^2\theta - 1) \tag{3.11}$$

Such that the substitution of $\theta = \arccos\sqrt{\frac{1}{3}} \simeq 54.74°$ results in

$$P_2(\cos 54.74) \simeq 0 \tag{3.12}$$

This particular angle is called the magic angle, the angle at which rotors are spun so as to average out undesirable anisotropic effects, which will be described in detail later, see Fig. 3.2.

A useful frame for describing NMR experiments is called the rotating frame. In the rotating frame, the xy plane rotates at the rf frequency, ω_{rf}. The transformation (PAS

frame to lab frame), described above, occurs in the rotating frame, and the impact of this, called the secular approximation, will now be discussed. The secular, or high field, approximation, is where solely spin terms, $\hat{T}_{jm}$, that commute with the Zeeman interaction, $\hat{I}_z$, are preserved; resulting in only terms, A^L_{j0}, being considered in the lab frame. In this method, it is possible to visualise the spin interaction Hamiltonians as perturbations to the dominant Zeeman Hamiltonian and only consider first-order perturbations. This approximation will be used regularly in the following section on the internal Hamiltonians of a spin system.

To elaborate on the mathematical explanation of the MAS technique, a third frame, the rotor frame must first be introduced. Two transformations are now required, one from the PAS frame into the rotor frame, the frame in which the sample is spinning, and another from the rotor into the lab frame, see Fig. 3.3. The set of time-dependent Euler angles, see Fig. 3.2, used in the transformation from the rotor to the lab frame, $\Omega_{RL}(t)$, can be expressed:

$$\Omega_{RL}(t) = (\alpha_{RL}(t), \beta_{RL}, \gamma_{RL}) = (-\omega_{\mathrm{r}} t, \theta_m, 0) \tag{3.13}$$

where, physically, α_{RL} can be seen from Fig. 3.2 to be dependent on the spinning frequency and β_{RL} is the angle between the rotor frame and the large external magnetic field (the z-axis of the lab frame). Now using the time-dependent angle α_{RL} and the time-dependent part of eqn. 3.7 [3] an average over a rotor period is found by integrating:

$$\frac{1}{t_{\mathrm{r}}} \int_0^{2\pi/\omega_{\mathrm{r}}} e^{(im\omega_{\mathrm{r}}t)} \mathrm{d}t = \begin{cases} \frac{2\pi}{\omega_{\mathrm{r}} t_{\mathrm{r}}} = 1 & m = 0 \\ \frac{\cos(m2\pi) + i\sin(m2\pi) - 1}{im\omega_{\mathrm{r}} t_{\mathrm{r}}} = 0 & m = \pm 1, \pm 2, ... \end{cases} \tag{3.14}$$

with the rotor period expressed as $t_{\mathrm{r}} = 2\pi/\omega_{\mathrm{r}}$. Clearly in eqn. 3.7, under MAS, when one of the indices m is zero, the time-dependent part equates to unity after one full rotor period. Similarly when $m = \pm 1$, 2, ... the time-dependent part disappears after exactly one rotor period. By splitting interactions into components that are perpendicular and parallel to the rotor's long axis, it can be visualised why MAS averages out those that are perpendicular to the rotor over each full rotor period.

Eqn. 3.8 is the definition of a single frame transformation, such that a double frame rotation using two sets of Euler angles, as is now required to go through the PAS-

[3] replacing the notation k with m

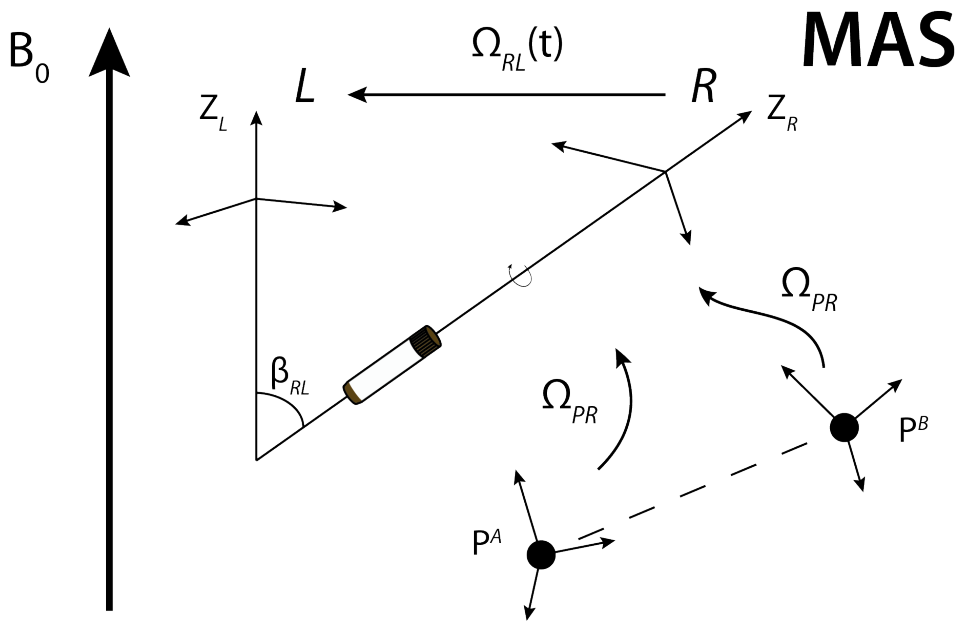

Figure 3.3: Illustration of the two frame rotations to go from the principal axis system to the lab frame via the rotor frame using the combined Euler angles Ω_{PR} and Ω_{RL}.

rotor-lab frames, can be written:

$$R(A^{lab}_{jn}) = \sum_{m=-j}^{+j} \sum_{m'=-j}^{+j} D^{j}_{nm}(\alpha_{RL}, \beta_{RL}, \gamma_{RL}) D^{j}_{mm'}(\alpha_{PR}, \beta_{PR}, \gamma_{PR}) A^{PAS}_{jm'} \tag{3.15}$$

This can be re-written, using the limits found in eqn. 3.14 and the D-matrix expressions for a second-rank ($j = 2$) tensor:

$$D^{2}_{m'n}(\Omega_{PL}) = D^{2}_{0n}(\Omega_{RL}) D^{2}_{m'0}(\Omega_{PR}). \tag{3.16}$$

Previously there would have been a sum from $m = -2$ to $+2$, however those five terms have been reduced to one through eqn. 3.14. Comparing this expression to eqn. 3.15 the remaining term can be seen as representing ${A^{\text{lab}}}_{2n}$, however under the secular approximation only the diagonal terms of the matrix are nonzero, i.e. only ${A^{\text{lab}}}_{2n} = {A^{\text{lab}}}_{20}$, such that eqn. 3.16 now becomes:

$$D^{2}_{m'0}(\Omega_{PL}) = D^{2}_{00}(\Omega_{RL}) D^{2}_{m'0}(\Omega_{PR}) \tag{3.17}$$

such that now only one angle describes the transformation of the surviving parallel components from rotor frame to the lab frame, and it is contained within Ω_{RL}. The angular dependence of the d^2_{00} term was revealed earlier in eqns. 3.10 and 3.11 as the dependence found in the second-order Legendre polynomial. As followed, the insertion of $\theta \simeq 54.74°$ reduced the polynomial and, therefore, also the above term to zero. It has now been shown that MAS can average some second-rank ($j = 0$) interactions to zero after a full rotor period, which is of great use in NMR so as to average out e.g. the heteronuclear dipolar coupling which can cause unwanted linebroadening in spectra.

A discussion of the internal interactions of an ensemble of spins is offered in the following section, and provides a detailed analysis of each interaction and the manipulation of these for extracting information from samples in ssNMR experiments.

3.4 Internal Hamiltonians

The internal Hamiltonian can be expressed as a sum of the contributing factors, which will be discussed in further detail below:

$$\hat{\mathscr{H}}_{int} = \hat{\mathscr{H}}_{CS} + \hat{\mathscr{H}}_D + \hat{\mathscr{H}}_J + \hat{\mathscr{H}}_P + \hat{\mathscr{H}}_K + \hat{\mathscr{H}}_Q^{(1)} + \hat{\mathscr{H}}_Q^{(2)} \tag{3.18}$$

In biological NMR the most common nuclei investigated are ^{1}H, ^{13}C and ^{15}N, all of which are spin-$\frac{1}{2}$ nuclei; this being the case only the first three terms are significant. $\hat{\mathscr{H}}_P$ only contributes in paramagnetic materials and so requires no further discussion in this report. $\hat{\mathscr{H}}_K$, the Knight shift, only contributes in metals and so will also be disregarded. $\hat{\mathscr{H}}_Q^{(1)}$ and $\hat{\mathscr{H}}_Q^{(2)}$ are quadrupolar terms and so are only relevant for spin $>\frac{1}{2}$ nuclei. $\hat{\mathscr{H}}_{CS}$ and $\hat{\mathscr{H}}_D$ are the Hamiltonians for the chemical shift and dipolar coupling which will be discussed in more detail below. $\hat{\mathscr{H}}_J$ represents the Hamiltonian for the J coupling which, along with the dipolar coupling, is the second type of nuclear coupling. The two are different in their mechanisms, electron mediated through-bond interaction for J coupling and a through-space interaction for dipolar coupling. The J coupling is too small to detect in the experiments shown in this work and so will not be discussed further.

Electrons surrounding a nucleus can have a current induced in them by an applied magnetic field. This circulating current in turn generates an additional magnetic field, with the result that in NMR experiments the magnetic field in certain locations can

slightly vary from that of the large, static, applied field, B_0. For example, the Cα and Cγ of a leucine molecule will experience slightly different magnetic fields although the induced field is typically only 10^{-4} of the external field B_0. This may seem small but is large enough to produce measurable differences in the spin precession frequencies: this effect is called the chemical shift. The Hamiltonian of this interaction can be written:

$$\hat{\mathscr{H}}_{CS} = \gamma \hat{I}.\boldsymbol{\delta}\mathrm{B}_0 \tag{3.19}$$

where $\boldsymbol{\delta}$ is the second rank chemical shift tensor, which in its PAS frame (discussed above), can be diagonalised and therefore gives an isotropic contribution which can be written as the mean of the 'principal values' of the chemical shift tensor for site j:

$$\delta^j_{iso} = \frac{1}{3}(\delta^j_{xx} + \delta^j_{yy} + \delta^j_{zz}) \tag{3.20}$$

where

$$\mathbf{B}^j_{induced} = \delta^j_{xx}\mathbf{B}_0 \tag{3.21a}$$
$$\mathbf{B}^j_{induced} = \delta^j_{yy}\mathbf{B}_0 \tag{3.21b}$$
$$\mathbf{B}^j_{induced} = \delta^j_{zz}\mathbf{B}_0 \tag{3.21c}$$

are relevant when B_0 is along the x principal axis (a), along the y principal axis (b), or the z principal axis (c). The isotropic chemical shift, $\delta^j{}_{iso}$, determines the positions of peaks in isotropic liquids when the three principal values are equal. When the values are not equal there is an anisotropic contribution; defined as the largest deviation from the isotropic value:

$$\delta^j_{aniso} = \delta^j_{zz} - \delta^j_{iso} \tag{3.22}$$

known as the Chemical Shift Anisotropy (CSA). The difference between the other two principal values is regularly denoted by η_j, which is known by many names, Spin Dynamics uses biaxiality, whereas other sources use asymmetry: [156, 164]

$$\eta_j = \frac{\delta^j_{yy} - \delta^j_{xx}}{\delta^j_{aniso}} \tag{3.23}$$

Evidently if ${\delta^j}_{yy} = {\delta^j}_{xx}$ then the asymmetry is equal to zero; the chemical shift tensor is then said to be axially symmetric.

The CSA depends on the orientation of the spins under consideration. In ssNMR, MAS can average out the CSA due to a $(3\ \cos^2\theta\ -1)$ dependence which has been discussed earlier, Fig. 3.4 illustrates how slowly increasing the MAS frequency can simplify a spectrum by removing a greater proportion of the sidebands due to the CSA.

From eqn. 3.19, it is clear that the induced magnetic field is directly proportional to B_0, however as the shift is taken with respect to the Larmor frequency of a reference compound tailored to the observed nuclei, ${\omega_0}^{ref}$, there is a relation which is a B_0 independent measure of the chemical shielding, σ[4]:

$$\delta_{ppm} = \frac{(1-\sigma^{CS}) - (1-\sigma^{ref})}{1-\sigma^{ref}} \times 10^6 = \frac{\omega_0^{CS} - \omega_0^{ref}}{\omega_0^{ref}} \times 10^6 \tag{3.24}$$

where δ_{ppm} is the isotropic chemical shift in parts per million (ppm). The isotropic chemical shift is a very small number and so is expressed in ppm; it is a direct measure of the electronic environment of the structure under investigation. That a B_0 independent value can be obtained is crucial for being able to perform experiments at different field strengths and use and compare all the data obtained.

3.4.1 Chemical Shielding under MAS

The chemical shielding tensor, $\boldsymbol{\sigma}$, is usually anisotropic and as such varies throughout a powdered sample as the different molecules within the sample are randomly oriented. Its value is dependent on the direction of its orientation with respect to the large static magnetic field. MAS, rotating a sample at $\sim$54.74° (the diagonal through a cube) to this static field, ensures any CSA vectors aligned with the z-axis then pass through both the x- and y-axes thereby averaging its contribution to the total CSA. The same process occurs to all orientations such that the CSA is no longer randomly distributed throughout the sample but reduced to an average value which applies equally to all

[4]Chemical shielding, σ, due to the effect of e.g. nearby electrons, is responsible for the effective field experienced by a nucleus

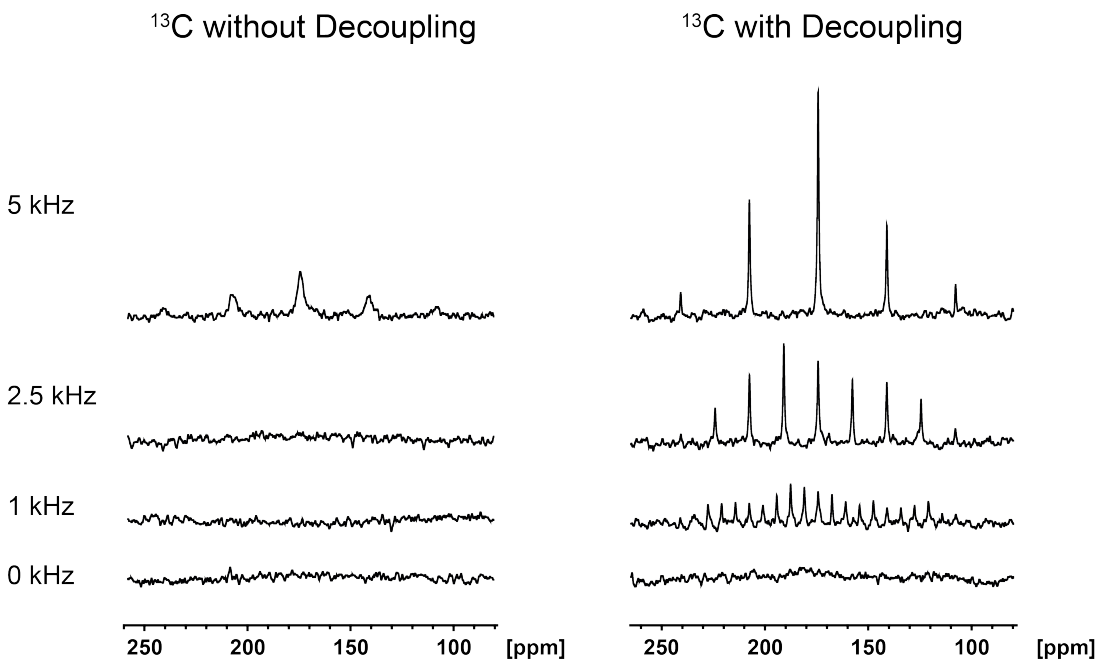

Figure 3.4: 1D ^{13}C spectra taken on a C′ labelled powder sample of alanine at a ^{1}H Larmor frequency of 600 MHz. The impact of decoupling and MAS on improving resolution is clear. A powder-like pattern can be seen for 2.5 kHz MAS frequency for the experimental setup with decoupling, this is due to the decoupling removing dipolar-coupling but not CSA, which is removed by increasing MAS frequencies. The combination of both techniques results in well resolved spectra. Data obtained by the author.

spins. The theory of this was discussed in § 3.3, and the magic angle is represented as β_{RL} in Fig. 3.3, the only angle describing the transformation of the surviving parallel components from the rotor frame to the lab frame. Slow spinning, as shown in Fig. 3.4, partially alleviates the CSA resulting in the presence of spinning sidebands in spectra with intensities based on the powder pattern as shown in Fig. 3.5, whereas rapid spinning removes this effect and significantly distances the sidebands from the main peak, resulting in the observation of distinct sites.

3.4.2 Dipolar Coupling

Direct dipole-dipole coupling between spins is the influence of one spin on the other acting through space. Each nuclear spin is magnetic thereby generating a magnetic field at the position of another spin; altering the total magnetic field experienced by the second spin. The full Hamiltonian form of the direct dipole-dipole interaction,

between spins I_j and I_k, is written:

$$\hat{\mathscr{H}}_D^{jk} = b_{jk}(3(\hat{\mathrm{I}}_j \cdot e_{jk})(\hat{\mathrm{I}}_k \cdot e_{jk}) - \hat{\mathrm{I}}_j \cdot \hat{\mathrm{I}}_k) \tag{3.25}$$

where e_{jk} is a unit vector parallel to the line joining the centres of the two nuclei and b_{jk} is the dipole-dipole coupling constant (in units of rad/s):

$$b_{jk} = -\frac{\mu_0}{4\pi}\frac{\gamma_j\gamma_k\hbar}{r_{jk}^3} \tag{3.26}$$

where γ_j and γ_k represent the gyromagnetic ratios of spins j and k respectively, and r_{jk} is the distance between spins j and k. b_{jk} is a constant and so is not dependent on molecular orientation whereas $\hat{\mathscr{H}}_D^{jk}$ in eqn. 3.25 is orientation dependent, since the vector e_{jk} changes direction as the molecule rotates. Eqn. 3.26 contains a negative sign since the coupling energy is minimised between two spins when both are pointing in the same direction along the internuclear vector; an analogous system is two bar magnets arranged in a line, head to tail. When one rotates, the other will move so as to minimise the energy of the system as a whole. Since the direct dipole-dipole coupling only depends on known physical constants and the reciprocal of the cubed internuclear distance, it is extremely useful for molecular structural studies. If an estimate for the coupling between two spins can be obtained, a value for the distance between them can also be obtained; repeat this for many pairs and an overall structure of the sample can be built.

Eqn. 3.25 can now be fully expressed as:

$$\hat{\mathscr{H}}_D^{jk} = -\left(\frac{\mu_0}{4\pi}\right)\gamma_I\gamma_S\hbar\left(\frac{\hat{\mathrm{I}}_j \cdot \hat{\mathrm{I}}_k}{r_{jk}^3} - 3\frac{(\hat{\mathrm{I}}_j \cdot \mathbf{r}_{jk})(\hat{\mathrm{I}}_k \cdot \mathbf{r}_{jk})}{r_{jk}^5}\right) \tag{3.27}$$

where $\mathbf{r}_{\mathrm{jk}}$ is the vector equivalent of e_{jk}. This can now be re-written, after having made the PAS to lab frame transformation as in § 3.3, in terms of Abragam's 'dipolar alphabet', see [165]:

$$\hat{\mathscr{H}}_D^{jk} = -\left(\frac{\mu_0}{4\pi}\right)\frac{\gamma_I\gamma_S\hbar}{r_{jk}^3}[A + B + C + D + E + F] \tag{3.28}$$

whereby:

$$A = \hat{\mathrm{I}}_{jz}\hat{\mathrm{I}}_{kz}(3\cos^2\theta - 1) \tag{3.29a}$$

$$B = -\frac{1}{2}(\hat{\mathrm{I}}_{jx}\hat{\mathrm{I}}_{kx} + \hat{\mathrm{I}}_{jy}\hat{\mathrm{I}}_{ky})(3\cos^2\theta - 1) \tag{3.29b}$$

$$C = -\frac{3}{2}[\hat{\mathrm{I}}_{jz}\hat{\mathrm{I}}_{k+} + \hat{\mathrm{I}}_{j+}\hat{\mathrm{I}}_{kz}]\sin\theta\cos\theta\, e^{-i\phi} \tag{3.29c}$$

$$D = -\frac{3}{2}[\hat{\mathrm{I}}_{jz}\hat{\mathrm{I}}_{k-} + \hat{\mathrm{I}}_{j-}\hat{\mathrm{I}}_{kz}]\sin\theta\cos\theta\, e^{+i\phi} \tag{3.29d}$$

$$E = -\frac{3}{4}[\hat{\mathrm{I}}_{j+}\hat{\mathrm{I}}_{k+}]\sin^2\theta\, e^{-2i\phi} \tag{3.29e}$$

$$F = -\frac{3}{4}[\hat{\mathrm{I}}_{j-}\hat{\mathrm{I}}_{k-}]\sin^2\theta\, e^{+2i\phi} \tag{3.29f}$$

The Zeeman interaction is significantly larger than typical dipolar coupling values ($\sim$500 MHz cf. $\sim$50 kHz) so the high field approximation can still be used, first established on p. 34, such that the full dipole-dipole coupling becomes approximately equal to the secular dipole-dipole coupling. Under this regime only terms that commute with the Zeeman interaction remain, i.e. A and B. Moreover, whether or not term B remains depends on whether spins I_j and I_k are of the same isotropic species or not. This is because term B is only relevant when $\omega_\mathrm{j} \approx \omega_\mathrm{k}$, which is not the case in e.g. ^{1}H-^{13}C. In the homonuclear case, the secular part of the dipole-dipole spin Hamiltonian is given by:

$$\hat{\mathscr{H}}_D^{homo}(\theta_{jk}) = -\left(\frac{\mu_0}{4\pi}\right)\frac{\gamma_I\gamma_S\hbar}{r_{jk}^3}(3\cos^2\theta - 1)\left[\hat{\mathrm{I}}_{jz}\hat{\mathrm{I}}_{kz} - \frac{1}{2}(\hat{\mathrm{I}}_{jx}\hat{\mathrm{I}}_{kx} + \hat{\mathrm{I}}_{jy}\hat{\mathrm{I}}_{ky})\right] \tag{3.30}$$

whereas in the heteronuclear case, thereby losing term B, the Hamiltonian can be written: [166]

$$\hat{\mathscr{H}}_D^{hetero}(\theta_{jk}) = -\left(\frac{\mu_0}{4\pi}\right)\frac{\gamma_I\gamma_S\hbar}{r_{jk}^3}(3\cos^2\theta - 1)\hat{\mathrm{I}}_{jz}\hat{\mathrm{I}}_{kz} \tag{3.31}$$

The B term which is lost going from the homonuclear to the heteronuclear case is also known as the flip-flop term, which represents the exchange of magnetisation between two spins where, as one spin is raised, the other is lowered.

The orientation dependence found above results in a characteristic lineshape for a powder sample encompassing all possible orientations of a spin-$\frac{1}{2}$ nuclei. In a 1948

investigation of the proton resonance lineshape on hydrated gypsum ($CaSO_4.2H_2O$) samples, with the externally applied magnetic field being applied in various directions, Pake, at the time a graduate student at Harvard, calculated the superposition of the resulting lineshapes and produced his famous doublet. [15] The Pake doublet is the lineshape produced by the dipole-dipole interaction of a powder sample of a pair of spin-$\frac{1}{2}$ nuclei, and is composed of two subspectra which result from the α and β spin states of the coupled nuclei, see Fig. 3.5. Note the locations, in the spectra, of $\theta = 0$ and 90°, the intensities of these peaks result from a $\sin\theta$ weighting of the spectrum. At a certain value of θ, the line position of both the α and β states must be coincident. As has probably become already apparent, this value is $\approx 54.74°$, the magic angle.

3.4.3 Dipolar Coupling under MAS

MAS can remove unwanted dipolar coupling [5] alongside 2nd rank tensor interactions including CSA, as shown earlier, and any weak quadrupolar interaction e.g. ^{2}H, through the angular dependence of eqn. 3.30. In this instance, a transformation is required from the PAS frame into the rotor frame, the frame in which the sample is spinning, and then a further transformation into the lab frame, see Fig. 3.3 and eqns. 3.15-3.17. The Hamiltonian including this can be written:

$$\hat{\mathscr{H}}_D^{jk}(\theta_{jk}) = b_{jk}(\frac{1}{4}(3\cos^2\beta_{PR} - 1)(3\cos^2\beta_{RL} - 1) - \frac{3}{4}\sin 2\beta_{PR}\sin 2\beta_{RL}\cos(\gamma_{PR} - \omega_r t) + \frac{3}{4}\sin^2\beta_{PR}\sin^2\beta_{RL}\cos(2\gamma_{PR} - 2\omega_r t))(3\hat{I}_{jz}\hat{I}_{kz} - \hat{I}_j \cdot \hat{I}_k) \tag{3.32}$$

However when $\beta_{RL} = 54.74°$, the $3\cos^2\beta_{RL} - 1$ term equals zero, and the rest of the equation can be re-written:

$$\hat{\mathscr{H}}_D^{jk}(\theta_{jk}) = b_{jk}(-\frac{1}{\sqrt{2}}\sin 2\beta_{PR}\cos(\gamma_{PR} - \omega_r t) + \frac{1}{2}\sin^2\beta_{PR}\cos(2\gamma_{PR} - 2\omega_r t))(3\hat{I}_{jz}\hat{I}_{kz} - \hat{I}_j \cdot \hat{I}_k) \tag{3.33}$$

[5] More precisely, MAS removes all heteronuclear dipolar coupling, as for a homonuclear coupled system of three ^{1}H nuclei which are non linear, MAS is unable to fully remove the dipolar coupling, [167]

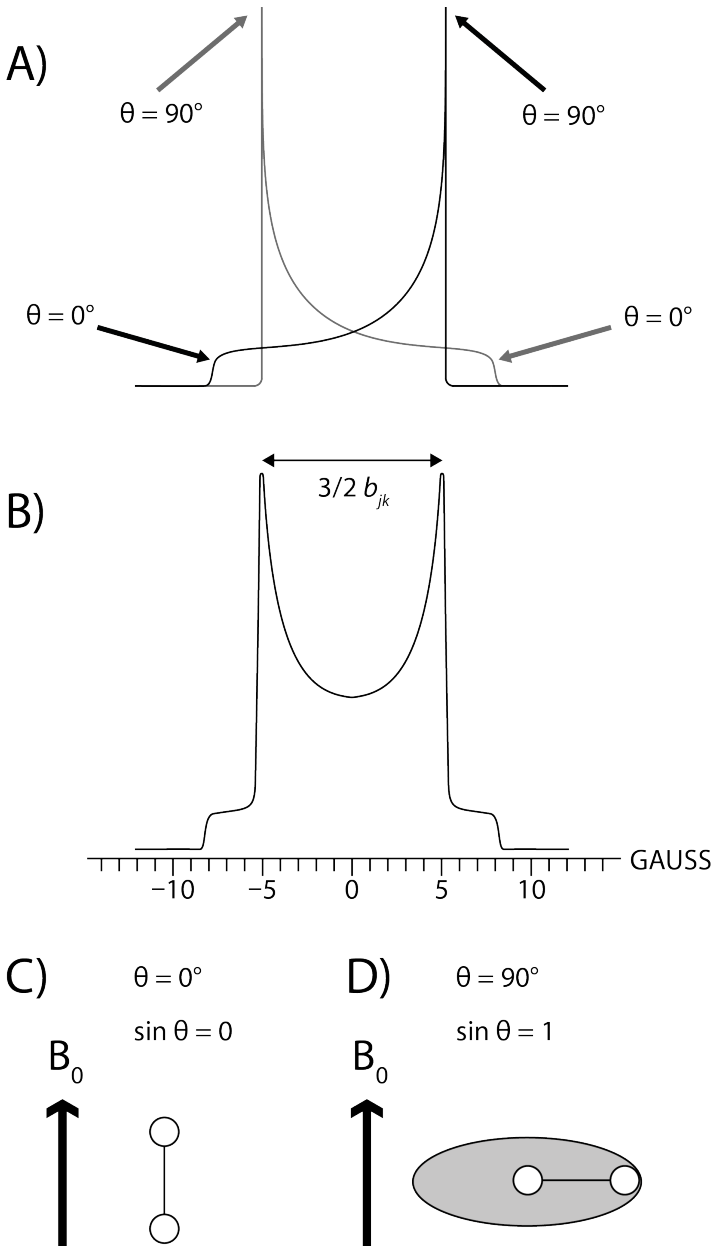

Figure 3.5: Illustration of the Pake doublet and its cause. A) shows the two subspectra (one black and one grey) which result from the α and β spin states of the coupled nuclei, the different frequencies within one spectra arise from the $(3\cos^2\theta - 1)$ orientation dependence and that a powder sample will encompass all possible orientations. B) shows the Pake doublet formed from the combination of the two subspectra in A). The Pake doublet shown is for a pair of homonuclear spins. C) and D) illustrate the $\sin\theta$ dependency of the intensities of the peaks; for $\theta = 0°$ there is only one possible orientation of the dipolar vector, whereas for $\theta = 90°$ there are many.

Using eqn. 3.13, the integral over a full rotor period is zero. In this manner dipolar coupling, a second-rank interaction, can be averaged to zero over a full rotor period, see Figs. 3.4 and 3.6 for an illustration of increasing MAS frequency providing more resolved spectra.

As the dipole-dipole interaction contains useful information regarding distance between like nuclei but can be removed due to averaging of the Hamiltonian under the effect of high frequency MAS, spectroscopists use homonuclear recoupling, see § 5, to reintroduce this effect and therefore make this information available. [168]

In certain circumstances a spectroscopist may wish to fully remove homonuclear dipole-dipole interaction, as MAS alone may not achieve this, see Fig. 3.6,[6] so one can use homonuclear decoupling, sequences, such as WAHUHA and MREV8, exist to achieve this. Homonuclear decoupling will also be expanded upon in § 5.

3.4.4 Paramagnetic Relaxation Enhancement

A paramagnetic ion, such as copper, will contribute free electrons to the sample and these will affect the magnetic moment of the local environment in which they are situated. Electrons are spin half and therefore can align parallel or antiparallel to the field, B_0. The chemical potential of electrons aligned with the field is decreased by $\mu_B B_0$ and those antiparallel to the field are increased by the same amount; μ_B is the Bohr magneton.

Free electrons increase the shielding of spins within the local environment and the crucial result, for an NMR spectroscopist, is that the relaxation times of these spins are drastically shortened. Therefore, when NMR experiments are conducted with typical relaxation times the spins that are within the proximity of the ion will relax quickly and so the signals from these spins will be lost. These signals are said to be 'quenched'. It is therefore possible to determine the binding sites of paramagnetic ions by isolating these lost resonances.

Such a paramagnetic effect is displayed by the sample examined in § 7.

[6] The difference in eqns. 3.30 and 3.31, the B term in eqn. 3.29b, is the reason for the difficulty in fully removing homonuclear when compared to the heteronuclear case

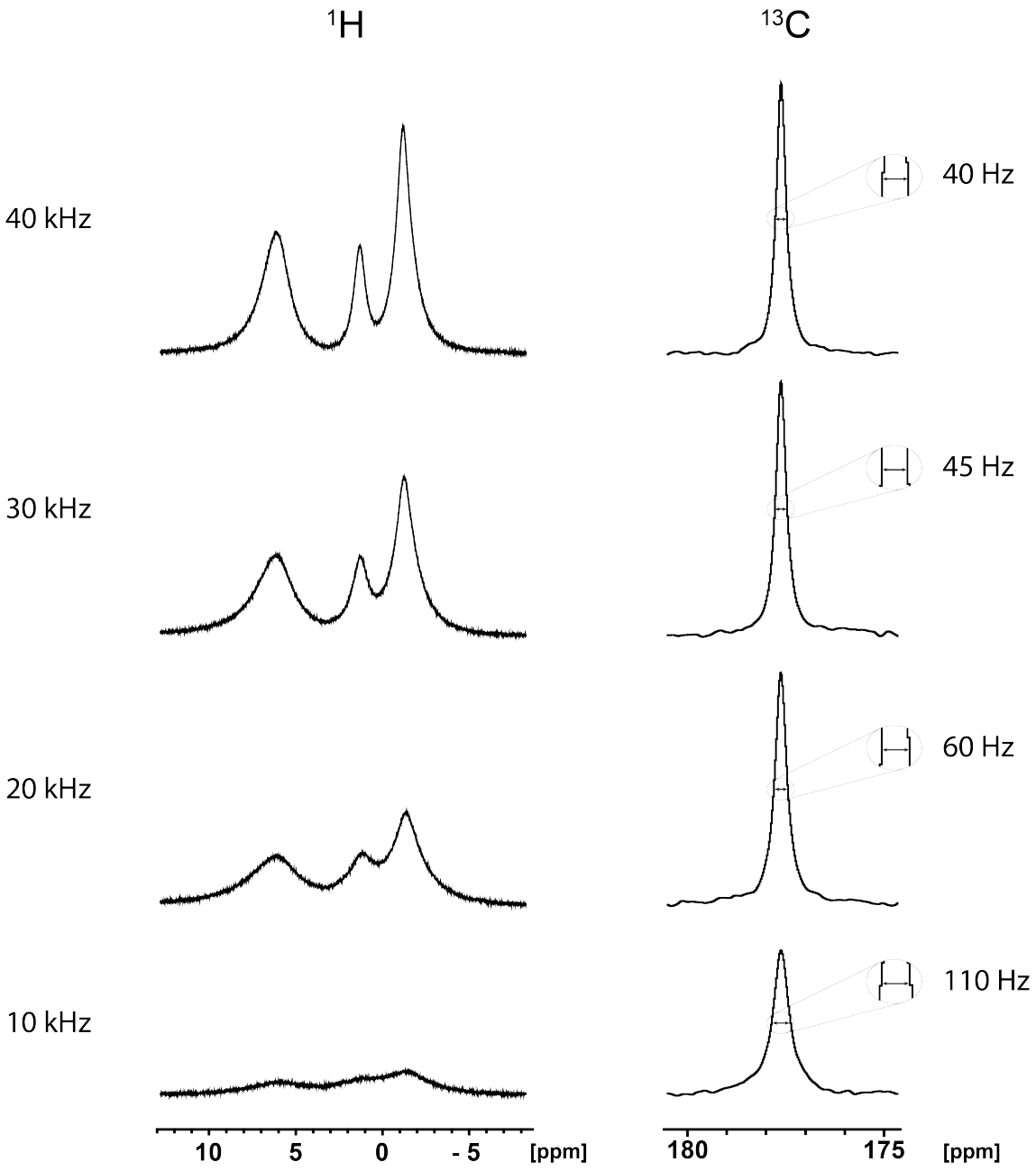

Figure 3.6: 1D ^{1}H and ^{13}C spectra taken at varying MAS frequencies on C′ labelled alanine at a ^{1}H Larmor frequency of 600 MHz. The improvement of higher MAS frequencies on the ^{13}C linewidths is much less than the improvement of the ^{1}H spectra, which are, at 10 kHz MAS, very poor and, at 40 kHz MAS, are fairly well resolved. Data taken by the author.

4

Multidimensional NMR for Biological Studies

This chapter contains details of 1D, 2D and 3D NMR experiments, which are crucial for investigating peptides and proteins. Phase cycling, which is required to selectively excite desired coherences, is also discussed. Techniques for sign discrimination in 2D experiments are given a thorough explanation and are compared. The importance of 3D ssNMR experiments in the investigation of biological samples with many isotopic labels is explained, and the method for processing 3D experiments is elucidated.

4.1 Multidimensional NMR: Benefits and Drawbacks

Biological NMR focuses on the elucidation of structure and dynamics for important biomolecules, notably proteins for which the main constituent elements are H, C, N and O. To this end, several pulse sequences have been created for the transfer of magnetisation from ^{1}H to other nuclei, usually ^{13}C and ^{15}N. [169] In A$\beta_{1\text{-}40}$, there are many carbon nuclei, and in a uniformly labelled ^{13}C sample there would be far too many resonances for successful assignment from a simple 1D experiment. Therefore there is a need to use sequences which can separate these resonances, i.e. through the use of multidimensional spectra, such that assignments can be made. The first step towards this goal is the use of 2D experiments. These experiments contain an additional FID acquisition section over 1D experiments, the time period over which this occurs is usually referred to as t_1, see Fig. 4.1. 2D experiments are suitable for assignment of biomacromolecules, despite the spectral sensitivity in a 2D experiment typically being three to five times lower than 1D, because polarization transfer efficiencies are typically 30-60%, and another factor of two is lost as a result of hypercomplex sampling of the indirect chemical shift dimension. [169] Once chemical

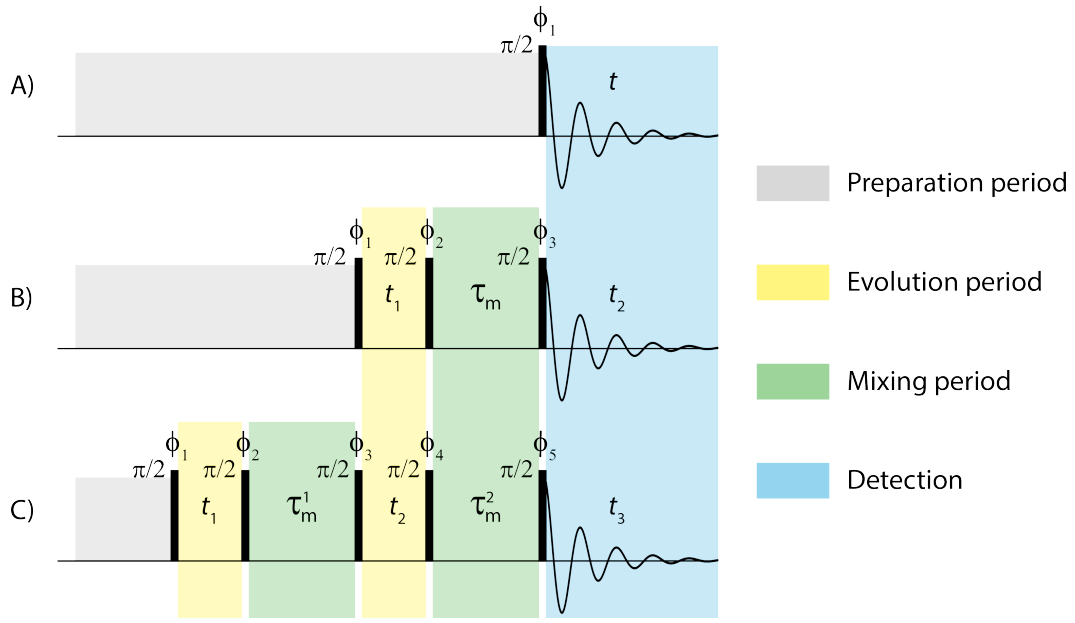

Figure 4.1: An illustration of the most basic pulse sequences required to obtain multidimensional data. The black rectangles are 90° pulses on an unspecified nucleus, each with their own phase, ϕ. t_x refers to a period of acquisition for dimension F_x and τ_m refers to a mixing time, whereby nuclei are allowed to communicate with one another and therefore exchange magnetisation. The preparation period can include anything required before the acquisition begins e.g. cross polarisation from an abundant spin to a dilute one. A), B) and C) show 1D, 2D and 3D experiments respectively.

shift values have been obtained from 2D experiments, they can be used in empirical databases such as TALOS, which allow semi-quantitative secondary structure determination. [170] Finally and crucially, to ascertain the global fold of a protein, several long range internuclear distances are required; such information can be obtained using spectra obtained from the use of intelligent pulse sequences, for more on the sequences used in this study see § 5.

Fig. 4.1 illustrates the basic pulse sequences required for multidimensional experiments. The sequences shown are only for an illustrative purpose, and are exacted on one nuclear species whereas pulse sequences that will be shown later are often applied to two or more nuclear species. In the preparation period, denoted by the grey block, it is usual in ssNMR to prepare magnetisation on ^{1}H then transfer this to the nucleus under investigation via a technique called CP, see § 5, although this is not always the case.

4.2 1D Spectroscopy

Before discussing 2D NMR experiments, a brief segue into 1D experiments will provide a solid understanding of certain experimental NMR aspects which can quickly become complicated in 2D. A complex time-domain NMR signal $s(t)$ recorded with quadrature detection, derived previously for a simplistic case without relaxation in eqn. 2.31, can be written:

$$s(t) = e^{i\Omega t}e^{-t/T_2} = \Big[\cos(\Omega t) + i\sin(\Omega t)\Big]e^{-t/T_2} = e^{i\Omega t}.e^{-t/T_2} \tag{4.1}$$

and this expression can be Fourier transformed to provide a NMR frequency signal from the NMR time-domain signal of the above equation, such that:

$$S(\omega) = \int_0^{+\infty} s(t)e^{-i\omega t}\mathrm{dt} \tag{4.2}$$

The signal from a 1D experiment can be further defined by the real (absorptive) and imaginary (dispersive) parts:

$$S(\omega)^{Re} = A(\Omega) = \frac{(\frac{1}{T_2})}{\left(\frac{1}{T_2}\right)^2 + (\omega - \Omega)^2} \tag{4.3a}$$

$$S(\omega)^{Im} = D(\Omega) = \frac{(\omega - \Omega)}{\left(\frac{1}{T_2}\right)^2 + (\omega - \Omega)^2} \tag{4.3b}$$

As a 1D spectrum has two components of the produced signal, real or imaginary, as shown in Fig. 4.2, when discussing 2D spectra there are, therefore, four combinations of signal possible. So that the best resolution is achieved, the lineshapes in both the F_1 and F_2 dimensions are absorptive is most desirable.

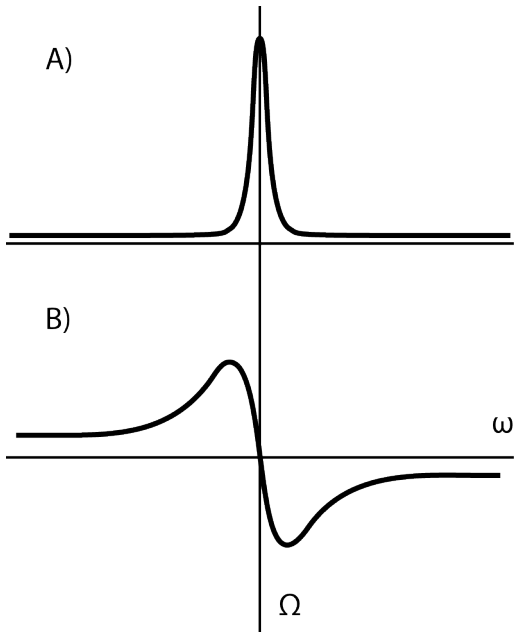

Figure 4.2: Illustration of lineshapes for a 1D NMR experiment. A) shows a real absorptive and B) an imaginary dispersive lineshape.

4.3 2D Spectroscopy

4.3.1 Phase and Amplitude Modulation

During the characteristic t_1 period of a 2D experiment, see Fig. 4.1, the signal $s(t_1,t_2)$ can be modulated by two different properties: phase and amplitude. Fig. 4.3 shows the coherence transfer pathways for a phase (top) and amplitude (bottom) modulated, with respect to t_1, simple experiment. The phase modulation only allows passage of one of the two pathways, whereas the amplitude modulation allows passage of both.

The time-domain signal produced from the amplitude modulated experiment illustrated in Fig. 4.3 is of the form: [171]

$$\begin{aligned} s(t_1,t_2) &= \{e^{-i\Omega t_1} + e^{+i\Omega t_1}\} e^{\left(-\frac{t_1}{T_2^{(1)}}\right)} e^{(+i\Omega t_2)} e^{\left(-\frac{t_2}{T_2^{(2)}}\right)} \\ &= 2\cos(\Omega t_1) e^{\left(-\frac{t_1}{T_2^{(1)}}\right)} e^{(+i\Omega t_2)} e^{\left(-\frac{t_2}{T_2^{(2)}}\right)} \end{aligned} \tag{4.4}$$

where $T_2{}^{(1)}$ and $T_2{}^{(2)}$ are the transverse relaxation rates during the evolution periods

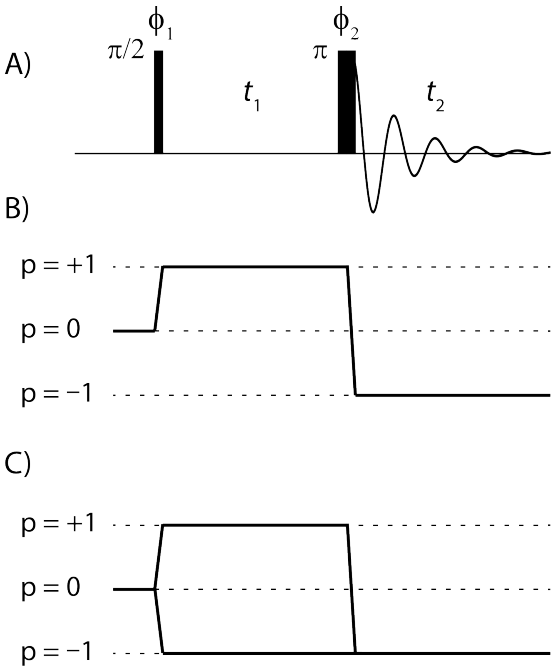

Figure 4.3: Simple 2D experiment pulse sequence to illustrate coherence transfer pathways: A) the pulse sequence; B) coherence transfer pathway for t_1 phase-modulated signal; and C) coherence transfer pathway for t_1 amplitude-modulated signal.

t_1 and t_2, as mentioned previously. When Fourier transformed over t_2 the signal can be written:

$$S(t_1, \omega_2) = 2\cos(\Omega t_1) e^{\left(-\frac{t_1}{T_2^{(1)}}\right)} (A_2^+ - iD_2^+) \tag{4.5}$$

where $A_n^{\pm}$ and $D_n^{\pm}$ correspond to the absorptive and dispersive lineshapes centred at the frequency $\pm\Omega$ in the F_{n} dimension. Separating the real and imaginary parts of eqn. 4.5 before performing the complex Fourier transforming in the F_1 dimension, so as to obtain pure absorption-mode lineshapes is known as a hypercomplex two-dimensional Fourier transform, and is shown below. Removing the imaginary part of eqn. 4.5:

$$S(t_1, \omega_2) = 2\cos(\Omega t_1) e^{\left(-\frac{t_1}{T_2^{(1)}}\right)} (A_2^+) \tag{4.6}$$

$$= \{e^{-i\Omega t_1} + e^{+i\Omega t_1}\} e^{\left(-\frac{t_1}{T_2^{(1)}}\right)} (A_2^+) \tag{4.7}$$

now performing the Fourier transformation over t_1:

$$S(\omega_1,\omega_2)^{Re} = [(A_1^- - iD_1^-) + (A_1^+ - iD_1^+)](A_2^+) \tag{4.8}$$
$$= A_1^- A_2^+ + A_1^+ A_2^+ - i[D_1^- A_2^+ + D_1^+ A_2^+] \tag{4.9}$$

Then repeating, but discarding the real portion of eqn 4.5, ultimately leads to:

$$S(\omega_1,\omega_2)^{Im} = A_1^+ D_2^+ + A_1^- D_2^+ - i[D_1^+ D_2^+ + D_1^- D_2^+] \tag{4.10}$$

However from the last two equations it can be seen that there is no sign discrimination in ω_1 due to the mixture of positive and negative A and D terms; determining if the resonance offset is positive or negative is not possible. There are several techniques, however, which achieve sign discrimination; two examples are 'States' and 'TPPI'.

4.3.2 States-Haberkorn-Ruben Method: States

The States method relies on acquiring two FIDs which are 90° out of phase with one another for every t_1 value, such that there then exists a cosine or a sine modulation with respect to t_1. [172] The form of the cosine modulated signal is from eqn. 4.4:

$$\begin{aligned} s_{\cos}(t_1,t_2) &= \{e^{-i\Omega t_1} + e^{+i\Omega t_1}\} e^{\left(-\frac{t_1}{T_2^{(1)}}\right)} e^{(+i\Omega t_2)} e^{\left(-\frac{t_2}{T_2^{(2)}}\right)} \\ &= 2\cos(\Omega t_1) e^{\left(-\frac{t_1}{T_2^{(1)}}\right)} e^{(+i\Omega t_2)} e^{\left(-\frac{t_2}{T_2^{(2)}}\right)} \end{aligned} \tag{4.11}$$

and the sine modulated signal takes the form:

$$\begin{aligned} s_{\sin}(t_1,t_2) &= \{e^{+i\Omega t_1} - e^{-i\Omega t_1}\} e^{\left(-\frac{t_1}{T_2^{(1)}}\right)} e^{(+i\Omega t_2)} e^{\left(-\frac{t_2}{T_2^{(2)}}\right)} \\ &= 2i\sin(\Omega t_1) e^{\left(-\frac{t_1}{T_2^{(1)}}\right)} e^{(+i\Omega t_2)} e^{\left(-\frac{t_2}{T_2^{(2)}}\right)} \end{aligned} \tag{4.12}$$

Now apply a Fourier transform in F_2 (FT_2) to the cosine modulated equation above:

$$S_{\cos}(t_1,\omega_2) = 2\cos(\Omega t_1)e^{\left(-\frac{t_1}{T_2^{(1)}}\right)}(A_2^+ - iD_2^+) \tag{4.13}$$

and now taking just the real part:

$$S_{\cos}^{\mathrm{Re}}(t_1,\omega_2) = 2\cos(\Omega t_1)e^{\left(-\frac{t_1}{T_2^{(1)}}\right)}(A_2^+) \tag{4.14}$$

and now take the sine modulated equation and performed FT_2:

$$S_{\sin}(t_1,\omega_2) = 2i\sin(\Omega t_1)e^{\left(-\frac{t_1}{T_2^{(1)}}\right)}(A_2^+ - iD_2^+) \tag{4.15}$$

and taking the imaginary component:

$$S_{\sin}^{\mathrm{Im}}(t_1,\omega_2) = 2\sin(\Omega t_1)e^{\left(-\frac{t_1}{T_2^{(1)}}\right)}(A_2^+) \tag{4.16}$$

Such that summing eqns. 4.14 and 4.16:

$$\begin{aligned} S_{\cos}^{\mathrm{Re}}(t_1,\omega_2) + i\ S_{\sin}^{\mathrm{Im}}(t_1,\omega_2) &= 2(\cos(\Omega t_1) + i\sin(\Omega t_1))e^{\left(-\frac{t_1}{T_2^{(1)}}\right)}(A_2^+) \\ &= 2e^{(+i\Omega t_1)}e^{\left(-\frac{t_1}{T_2^{(1)}}\right)}(A_2^+) \end{aligned} \tag{4.17}$$

Such that when FT_1 is performed, we find:

$$S(\omega_1,\omega_2) = 2(A_1^+ - iD_1^+)(A_2^+) = 2(A_1^+A_2^+ - iD_1^+A_2^+) \tag{4.18}$$

such that sign discrimination has been achieved and the real part, $2A_1^+A_2^+$ is purely absorptive.

4.3.3 Time-Proportional Phase Incrementation Method: TPPI

TPPI was first used in 1983 in a seminal paper using the COSY sequence for finding ^{1}H-^{1}H couplings in proteins, [173] it was based on Redfield's work on obtaining quadrature detection from 1975, see [174]. The basic idea of TPPI is similar to States,

Table 4.1: Comparison of the t_1 increments and pulse phases used in the States and TPPI methods for quadrature detection.

A TPPI Experiment			A States Experiment		
Row	t_1	Pulse Phase	Row	t_1	Pulse Phase
1	0	0	1	0	0
2	1/(2SW)	90	2	0	90
3	1/(SW)	180	3	1/(SW)	0
4	3/(2SW)	270	4	1/(SW)	90
5	2/(SW)	0	5	2/(SW)	0
⋮	⋮	⋮	⋮	⋮	⋮

but whereas States takes two FIDs for each Δt_1 increment, TPPI takes one FID every $\Delta t_1/2$ increment. TPPI also increases ϕ_1 from Fig. 4.3 by 90° every $t_1/2$ interval,[1], hence the name time-proportional phase incrementation, see Table 4.1. So as to make the following easier it is useful to redefine Δt_1 in the case of TPPI as half that in States, so now when referring to t_1 in one scheme it is a different value to the t_1 in the other.

The explanation for the technique of TPPI lies in the addition of half the spectral width (SW/2) to each point in the spectrum. This ensures that peaks which would have appeared between −SW/2 to 0 now appear between 0 and SW/2, and the signals that occupied those frequencies have been shifted to SW/2 to SW. Therefore, aliasing about zero frequency is prevented, for peaks in this region, and quadrature detection is achieved. The same process can be used in the F_1 dimension. [171] As mentioned in the table above, t_1 is incremented in steps of 1/(2SW), where SW is the spectral width in F_1, also shown is the phase incrementation which imposes a t_1 dependent phase modulation, $e^{-i\phi}$, where:

$$\phi = \frac{\pi}{2} \cdot t_1 \cdot \frac{1}{\Delta t_1} = \frac{\pi}{2} \cdot t_1 \cdot (\mathrm{SW} \cdot 2) = \pi \mathrm{SW} t_1 \tag{4.19}$$

Now the time domain signal, $A_2\cos(\Omega t_1)$, includes an extra term such that:

$$S(t_1, \omega_2) = A_2 \cos(\Omega_1 t_1 + \pi \mathrm{SW} t_1) \tag{4.20}$$

[1]The shift is 90° provided the coherence order of the experiment, p, in Fig. 4.3 is ±1. If the experiment were a double-quantum coherence experiment, $p = \pm 2$, the shift would be 45°, i.e. phase change, $\Delta\phi_1 = \frac{\pi}{2|p|}$.

where currently SW is in units of Hz, however if SW is put in rad/s the additional term applies now as the addition of half a spectral width to each signal in the range ±SW/2 as described above. The similarity between TPPI and States can be emphasised by considering the hypothetical case whereby the signals measured on the odd and even increments of t_1 are kept separate. We are able to express the signals obtained during these as:

$$\begin{aligned} S_e(t_1, \omega_2) &= A_2 \cos(\Omega_1 t_1) \cos(\mathrm{SW} t_1/2) \\ S_o(t_1, \omega_2) &= -A_2 \sin(\Omega_1 t_1) \sin(\mathrm{SW} t_1/2) \end{aligned} \tag{4.21}$$

and now, for ease of notation replacing SW/2 with Ω_c, using product-to-sum trigonometric identities we obtain: [171]

$$\begin{aligned} s_e(t_1) &= A_2 (\frac{1}{2} \cos[(\Omega_1 - \Omega_c) t_1] + \frac{1}{2} \cos[(\Omega_1 + \Omega_c) t_1]) \\ s_o(t_1) &= -A_2 (\frac{1}{2} \cos[(\Omega_1 - \Omega_c) t_1] - \frac{1}{2} \cos[(\Omega_1 + \Omega_c) t_1]) \end{aligned} \tag{4.22}$$

Such that now if both s_e and s_o are Fourier transformed the spectra produced contain lines at $\Omega_1 \pm \Omega_c$. Looking at s_e, it is clear that both lines will be positive, whereas in s_o one is positive and one is negative. So now when the two spectra are summed one pair of lines will cancel and one, located at $\Omega_1 + \Omega_c$, will be left. Sign discrimination via TPPI has now been achieved.

4.4 Phase Cycling and Coherence

The term coherence, as introduced in § 2.3, has been mentioned many times above and used synonymously with the term magnetisation, e.g. this is the case in a 1 pulse experiment. Coherence is linked to the important idea of transverse magnetisation, and can be seen as relating to the transition between two spin-states $|\alpha\rangle$ and $|\beta\rangle$ with a coherence order being denoted as:

$$p_{\alpha,\beta} = m_\alpha - m_\beta \tag{4.23}$$

with m representing the magnetic quantum number. Transverse magnetisation corresponds to a specific type of coherence whereby $p = \pm 1$. [175] Relating this idea to fundamental sections of a pulse sequence, initially the magnetisation will be aligned

with the z-axis of the magnet, and the population state that exists ($\hat{I}_z$) is considered as having no coherence, i.e. $p = 0$; this is the state at which all NMR experiments begin. $p = 0$ also represents zero-quantum coherence ($\hat{I}^+\hat{S}^-$) and longitudinal scalar or dipolar spin order. [175] As mentioned in § 2.3, pulses are the spectroscopist's method to create or alter coherence, with a 90° pulse exciting all possible coherence orders and a 180° pulse converting all p to $-p$. All experiments must end with in-phase single-quantum coherence so as to be detectable, as only transverse magnetisation can generate an EMF.

Phase cycling is a flexible approach allowing specific coherence transfers to be collected by the spectrometer; from the above description it seems using just 90° and 180° pulses denies the finesse required to excite only particular transfers such that when analysing the signal, all coherences would be contribute equally. When a coherence undergoes a change in coherence order, Δp it will experience a phase shift of $-\Delta\phi\Delta p$. By matching the receiver phase, often denoted ϕ_{rec}, to that of the above, one selects only that particular coherence, the remaining undesired coherences will be summed to zero over the full phase cycle. This technique is often guided by the 'Golden Rules' of Phase Cycling: [176]

i: A phase cycle of N steps ensures selection of pathways Δp and $\Delta p + nN$ (where $n = 1, 2, 3, ...$) while all other pathways are blocked.

ii: If the phase of a pulse(s) is shifted by $\Delta\phi$, then a coherence undergoing a change in coherence order Δp experiences a phase shift $-\Delta\phi\Delta p$ as detected by the receiver.

Phase cycles for the multidimensional experiments used in this study will be explicitly stated and the coherence pathways will be represented diagrammatically.

4.5 Examples of 2D Spectroscopy for Biological Solid-State NMR

Clearly 2D spectroscopy is a powerful tool, one which is regularly used in this study. As Fig. 4.4 illustrates, two dimensional experiments are very important in establishing the chemical shift values of the many nuclei in the numerous residues in a fully labelled protein. A 2D ^{13}C-^{13}C experiment can produce spectra similar to that in Fig. 4.4 B), provided various precise conditions are met e.g. the experiment used to obtain the spectra in Fig. 4.4 is a dipolar-assisted rotational resonance (DARR) experiment

(for more detail see § 5) which requires careful preparation, though other types of 2D homonuclear experiments are available. In homonuclear 2D experiments, there will usually exist a diagonal resonance line, due to a resonance possessing a correlation with itself, either side of which will exist cross peaks; it is these cross peaks that are of particular interest as they arise from two nuclei which are within a certain proximity so as to be able to exchange magnetisation during a user-defined mixing period, see Fig. 4.1. As typical biological ssNMR nuclei are ^{1}H, ^{13}C and ^{15}N but, as acquiring signal on ^{1}H is troublesome, see § 5, though exploited in this thesis, see § 7, and due to the dilute nature of ^{15}N spins even in labelled proteins and the small chemical shift range for most ^{15}N nuclei when compared to ^{13}C,[2] ^{13}C-^{13}C correlation experiments are by far the most common biological 2D homonuclear ssNMR experiment.

2D heteronuclear experiments also exist, and these regularly involve ^{15}N and ^{13}C and can take the form of NCA and NCO experiments, see Fig. 4.4. These are experiments whereby the first acquisition is performed on ^{15}N and the second on either Cα or C$'$. As can be seen from Fig. 4.4, these are complementary techniques whereby the NCA experiment provides a correlation between the nitrogen and Cα in residue i, and the NCO experiment provides a correlation between the nitrogen in residue i and C$'$ in residue i$-$1. Though many assignments can be made using a suite of 2D experiments, there is often a need for a third dimension for complete assignment. Occasionally regions of a 2D experiment can become cluttered due to the number of residues with nuclei in a similar magnetic environment, such as would be the case with a protein containing many valines in typical valine chemical shift regions,[3] so, as shown in Fig. 4.4, extending an experiment into a third dimension can be necessary, and is becoming regular practice in the community. [37, 42, 177, 178]

4.6 3D Spectroscopy

3D solid-state NMR experiments can be used to obtain complete chemical shift assignments. A variety of experiments exist involving all three typical biological nuclei, however experiments including ^{1}H detection (also known as inverse detection experiments) are less common than experiments involving acquisitions on the other two, this will be expanded upon in § 5. The magnetisation transfers involved in NCACX

[2] Chemical shift ranges for ^{1}H, ^{13}C and ^{15}N in amino acids are ∼0-10 ppm, ∼0-190 ppm and ∼100-135 ppm respectively, although ^{15}N nuclei in lysine, arginine and histidine are outliers which typically exist around 30, 70 and 190 ppm, however the vast bulk of ^{15}N spins exist in the region stated

[3] See http://www.bmrb.wisc.edu/ref˙info/statful.htm

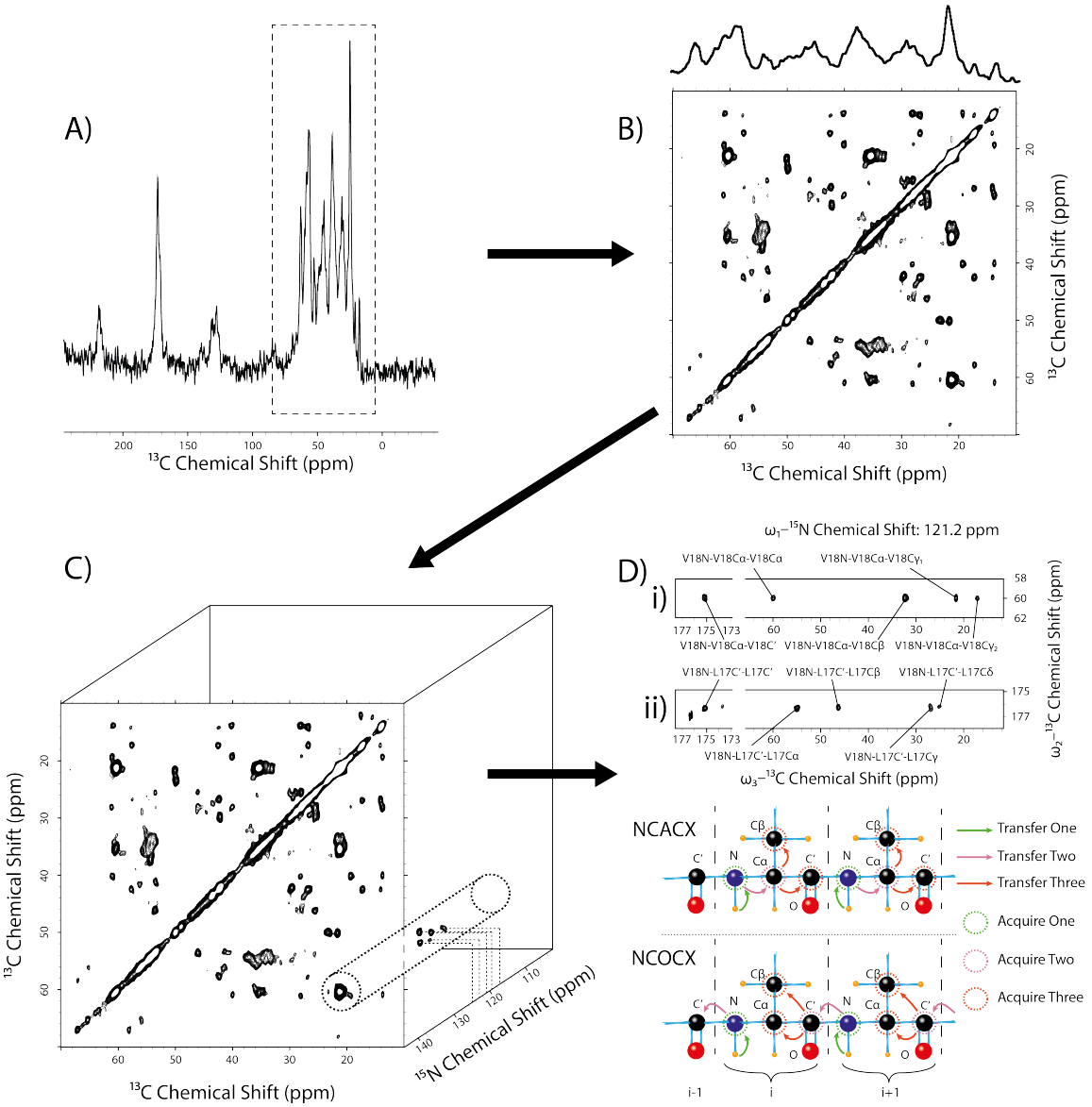

Figure 4.4: Illustration of the improvement in resolution provided by extra dimensions in a NMR experiment. A) shows a simple 1D ^{13}C spectrum, B) shows a homonuclear 2D ^{13}C-^{13}C experiment, C) shows a ^{13}C-^{13}C-^{15}N 3D experiment, and D) shows two strip plots taken from two 3D experiments, and highlights the separation of signals that is possible, under ideal conditions, via the third dimension. Both strips are taken at ^{15}N = 121.2 ppm. The sequences used here are A) Cross Polarisation, B) Dipolar-Assisted Rotational Resonance and C) NCACX and NCOCX experiments. For more on these see § 5. All data shown here was recorded and processed by the author.

and NCOCX experiments are shown in Fig. 4.4, and the data provided by each is demonstrated in D) i) and ii). Clearly, once again, these techniques are complementary and, when combined, allow the assignment of many residues by simultaneously proceeding through the ^{15}N dimension in both spectra and assigning carbon chemical shifts from the same residue, using the NCACX spectrum, and from residue i$-$1, using the NCOCX spectrum. In this manner, cluttered, and therefore unassignable, spectral regions in 2D become dispersed throughout the third dimension and assignment can take place. The obvious drawbacks to using 3D experiments are those mentioned in § 4.1 regarding 2D experiments, though there is often three magnetisation transfers and three or more evolution periods as opposed to two, emphasising the loss in spectral sensitivity. [169] If the nitrogen signals are also overlain, experiments can be altered to include a ^{1}H dimension or even a fourth dimension, though these experiments are not yet standard practice in biological ssNMR. [39, 47, 179]

4.6.1 Strip Plots

The typical technique to process 3D spectra is to find the experiment-dependent correlations (i.e. an NCOCX experiment provides different correlations to an NCACX experiment as described above) by progressing along one axis, and then taking a strip which includes those resonances at a certain value on that axis, shown in Fig. 4.4. For an NCACX spectrum, a strip can be taken, at a set chemical shift value on the ^{15}N axis and covering a small section of the Cα region as the width of the strip, showing a residue-specific set of chemical shifts along the second ^{13}C axis that provides the length of the strip. This can be seen as complementary with NCOCX where the width of the strip is a small section of the C$'$ region, while the other two dimensions remain the same. By proceeding through the ^{15}N dimension and discovering in-line resonances in both the NCACX and NCOCX spectra many, if not all, residues can be assigned. The same process can be used even if the axes of the experiment differ from this example. 3D experiments are used in this study and will be processed using strip plots, for more see [39, 42, 180, 181].

5

Pulse Sequences for Biological Solid-State NMR

This chapter contains details of the experiments performed to obtain high-resolution ssNMR spectra presented in this thesis. Fundamental spectroscopic techniques used in experiments such as the Dipolar-Assisted Rotational Resonance, [182] Double Cross Polarisation [183] and inverse detection sequences [184] are described and explained. The pulse sequences of, coherence pathways belonging to and type of data provided by each experiment are shown and explained. The decoupling and recoupling used in the experiments are also described and compared, and, where appropriate, pulse sequences are shown.

5.1 Cross Polarisation-Based Techniques

5.1.1 Cross Polarisation

In an NMR experiment, coherence is created within the sample under investigation using finely tuned rf pulses. Often in biological ssNMR this coherence will be created on ^{1}H then transferred to other nuclei of interest, for reasons explained below. The original Hartmann-Hahn matching condition, found for the static case, [20] states:

$$\nu_1(^1\mathrm{H}) = \nu_1(\mathrm{X}) \tag{5.1}$$

while the Hartmann-Hahn condition during sample rotation, an experiment known as Cross Polarisation with MAS (CPMAS) which was first demonstrated by Schaefer and Stejskal, [23] states:

$$\nu_1(^1\mathrm{H}) = \nu_1(\mathrm{X}) \pm n\nu_\mathrm{R} \tag{5.2}$$

where $\nu_1(^1\mathrm{H})$ is the nutation frequency of the transferring species (usually ^{1}H), $\nu_1(\mathrm{X})$ is the nutation frequency of the receiving species (e.g. ^{13}C or ^{15}N), ν_R is the MAS frequency and n is an integer: for efficient polarisation transfer $n = 1, 2$. This condition specifies that with nutation frequencies that differ by integer multiples of the spinning frequency irradiating the sample, efficient polarisation transfer between nuclear species is achieved provided there exists a dipole-dipole coupling between the nuclei. Sensitivity enhancement is exacted in this manner for two reasons: upon polarisation transfer, there is a maximum gain in magnetisation of the ratio of gyromagnetic ratios which, in the case of carbon and nitrogen receiving magnetisation from proton, are $\sim$4 times and $\sim$10 times respectively, see below for an explanation of this effect; and dilute spins, e.g. ^{13}C and ^{15}N, tend to have very long relaxation times, because the dipolar couplings, which are largely responsible for relaxation transitions, are smaller than for protons. If relaxation times are long then large time delays need to be left between each experiment, to ensure a return to thermal equilibrium of the system, and an experiment requiring many repetitions to achieve a suitable signal-to-noise ratio takes an extremely long time. However as the proton-proton dipolar interaction is strong, the time required to return to thermal equilibrium for protons, $T_{1\mathrm{H}}$, is usually less than that for other nuclei e.g. carbon, $T_{1\mathrm{C}}$, so that a reduced recycle delay can be used. This is the rationale for the use of the classic solid-state NMR technique called Cross Polarisation.

The 'classical description' of this technique used the concept of a spin temperature, $\mathcal{T}_\mathrm{H}$ and $\mathcal{T}_\mathrm{C}$ for proton and carbon, respectively, as illustrated in Fig. 5.1. It can be used to explain why CP provides a gain in polarisation on the dilute spin system when compared to direct excitation. The approach is valid provided the system contains a large number of spins and provided that strong homonuclear proton dipolar networks exist. When a solid is placed into a large magnetic field, B_0, the protons will occupy Zeeman levels with energies $\pm(\gamma_\mathrm{H}/2\pi)B_0/2$, corresponding to parallel and antiparallel alignment of the z-angular momentum with the external field. This network of strongly dipolar coupled spins exhibits 'spin diffusion', in that if one proton changes Zeeman levels through energy exchange with the lattice, surrounding protons will propagate this by also changing energy states in a timeframe of $<$100 μs. This results in a rapid propagation of the spin temperature of the lattice reservoir throughout the proton network, and, after several spin lattice relaxation times ($T_{1\mathrm{H}}$), the proton reservoir enters thermal equilibrium with the lattice, $\mathcal{T}_\mathrm{H} = \mathcal{T}_\mathrm{L}$. The proton magnetisation can now be written, according to a Curie law: [185]

$$M_{0\mathrm{H}} = C_\mathrm{H} B_0 / \mathcal{T}_\mathrm{L} \tag{5.3}$$

where C_{H}=$N_{\mathrm{H}}\gamma^2{}_{\mathrm{H}}\hbar^2/4k_{\mathrm{B}}$ is the proton Curie constant, N_{H} is the number of protons and k_{B} is the Boltzmann constant. CP consists of two steps, creation of transverse magnetisation of proton spins using a 90° pulse and then spin lock Hartmann-Hahn matched pulses on proton and the dilute spin, the physics of which was elucidated by Redfield [186] who presented an argument stating that the equilibrium in this state should be viewed in a rotating frame (as first suggested by Bloch in [161]), negating the time dependence of the external B_1 field, which rotates at ν_{rf} and results in the corresponding spin state energy values $\pm(\gamma_{\mathrm{H}}/2\pi)\ B_{1\mathrm{H}}/2$. Redfield also concluded that the states were populated based on a Boltzmann distribution characterised by a spin temperature in the rotating frame.[1] Therefore it can be stated that the proton magnetisation under the spin lock field can now be expressed as:

$$M_{0\mathrm{H}} = C_{\mathrm{H}}B_{1\mathrm{H}}/\mathcal{T}_{\mathrm{H}} \tag{5.4}$$

with $\mathcal{T}_{\mathrm{H}}$ the proton temperature in the rotating frame, which can be expressed using the two expressions for $M_{0\mathrm{H}}$ eqns. 5.3 and 5.4:

$$M_{0\mathrm{H}} = C_{\mathrm{H}}B_{1\mathrm{H}}/\mathcal{T}_{\mathrm{H}} = C_{\mathrm{H}}B_0/\mathcal{T}_{\mathrm{L}} \tag{5.5}$$

Giving:

$$\frac{\mathcal{T}_{\mathrm{H}}}{\mathcal{T}_{\mathrm{L}}} = \frac{B_{1\mathrm{H}}}{B_0} \tag{5.6}$$

Such that with typical values of $B_0 \gtrsim 1$ T and $B_{1\mathrm{H}} \approx 10$ mT, and with the sample at room temperature ($\mathcal{T}_{\mathrm{L}} \approx 300$ K), $\mathcal{T}_{\mathrm{H}} \approx 3$ K. However, it is worth noting that within a few $T_{1\mathrm{H}}$ of the spin lock being turned off, the proton magnetisation will decay back to thermal equilibrium with the lattice. In an analogue of eqn. 5.4, the carbon spin temperature can be written as $\mathcal{T}_{\mathrm{C}} = C_{\mathrm{C}}B_0/M_{\mathrm{C}}$, where C_{C} is the ^{13}C Curie constant as defined previously for ^{1}H. Just before the beginning of the spin lock pulse on proton, the carbon magnetisation has yet to build up and so M_{C} is very small, resulting in a high spin temperature. It can now be seen why a well ordered and polarised spin system is seen as having a low spin temperature while a disordered, non-polarised spin system has a high spin temperature. The systems are brought into contact by Hartmann-Hahn matched, to the spin lock pulse on proton, irradiation on carbon. This ensures that, in the rotating frame, the energy levels of the proton and

[1] This work relied on the seminal work by Felix Bloch in deriving the Bloch equations, [161] however re-examined the validity of that work under the consideration of a solid at greater rf field intensities

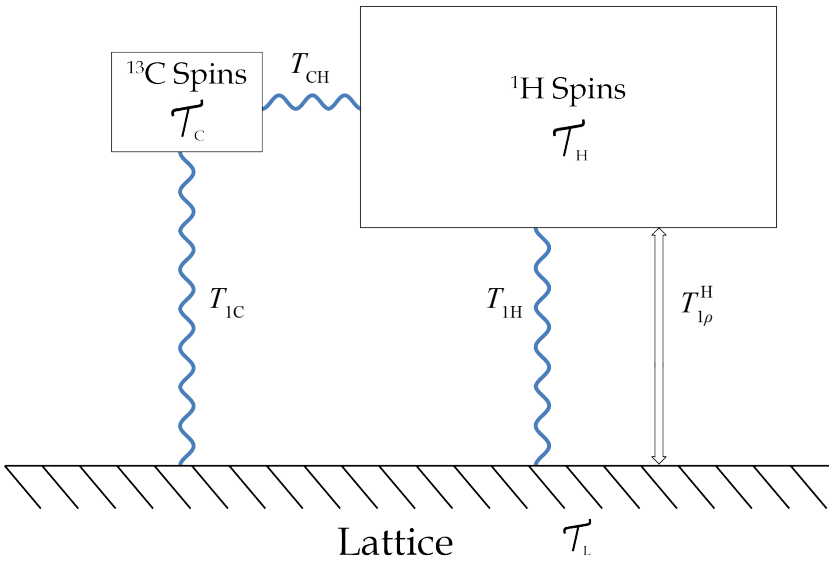

Figure 5.1: Simple thermodynamic picture for double resonance, based on [187]. The two spin systems, abundant I spin (^{1}H) and dilute S spin (^{13}C), initially have spin temperatures $\mathcal{T}_H$ and $\mathcal{T}_C$, long nuclear spin-lattice relaxation times T_{1H} and T_{1C}, and a cross-relaxation time T_{CH}. As the two spin systems are brought into contact, energy flows from one state to the other at a rate of $\sim\epsilon/T_{CH}$, where ϵ is the ratio of the S to I heat capacities. This creates a heating and partial destruction of the I spin order, and a creation of order within the observed S spin order. Relaxation of the polarised I spins occurs over a timescale $T_{1\rho}^H$.

carbon spin levels match:

$$(\gamma_C/2\pi)B_{1C} = \nu_1(^{13}C) = \nu_1(^1H) = (\gamma_H/2\pi)B_{1H} \tag{5.7}$$

As shown in Fig. 5.1, after several T_{CH}, the proton and carbon reservoirs will have equilibrated and share a temperature which is close to the original temperature of the proton reservoir as the carbon reservoir is small and therefore does not have a large enough heat capacity to significantly raise the proton reservoir temperature. Assuming that the relaxation effects on the proton magnetisation occur over a long timescale, i.e. $T_{1\rho}^H >> T_{CH}$, both temperatures at the end of the Hartmann-Hahn matched pulses will be the same, ≈ 3 K as shown previously from eqn. 5.6, i.e., $\mathcal{T}_C = \mathcal{T}_H = \mathcal{T}_L(B_{1H}/B_0)$. This reduction of spin temperature equates to an increase in the magnetisation of the carbon spins along the direction of the rf field B_{1C}. The magnetisation that would be created on carbon through direct excitation can be

written as in eqn. 5.3:

$$M_{0\mathrm{C}} = C_{\mathrm{C}}B_0/\mathcal{T}_{\mathrm{L}} = C_{\mathrm{C}}B_0B_{1\mathrm{H}}/\mathcal{T}_{\mathrm{C}}B_0 = C_{\mathrm{C}}B_{1\mathrm{H}}/\mathcal{T}_{\mathrm{C}} \tag{5.8}$$

and, using eqn. 13 from [187] whereby the x component of the magnetisation of a spin species, C, in the rotating frame along the B_1 field can be written:

$$M_{\mathrm{C}} = \gamma_{\mathrm{C}}\hbar\langle I_x\rangle = \gamma_{\mathrm{C}}\hbar\mathrm{Tr}\{\rho_R I_x\} = \beta_{\mathrm{C}}C_{\mathrm{C}}B_{1\mathrm{C}} = C_{\mathrm{C}}B_{1\mathrm{C}}/\mathcal{T}_{\mathrm{C}} \tag{5.9}$$

where ρ_R is the density matrix in the rotating frame. Now the enhanced magnetisation, M_{C}, due to using CP on the spin species C can be written:

$$M_{\mathrm{C}} = C_{\mathrm{C}}B_{1\mathrm{C}}/\mathcal{T}_{\mathrm{C}} = M_{0\mathrm{C}}(B_{1\mathrm{C}}/B_{1\mathrm{H}}). \tag{5.10}$$

Due to the Hartmann-Hahn matching condition the nutation frequencies of the spins are equal, see eqn. 5.7, which means the above can be re-written as $M_{\mathrm{C}} = (\gamma_{\mathrm{H}}/\gamma_{\mathrm{C}})M_{0\mathrm{C}}$ $\approx 4M_{0\mathrm{C}}$. Therefore, by using CP, one can gain an increase of the ratio of gyromagnetic ratios in total polarisation on the dilute spin species. This technique was first combined with observation on the S spin and proton decoupling, so as to produce higher resolution NMR spectra in the lab of Professor John S. Waugh at M.I.T.; its originally suggested acronym was not accepted widely and so this crucial technique is known as CP. [22, 187] Fig. 5.2 shows a CP sequence with the coherence pathway for both the observed nuclei and protons. The main drawback with CP is that relative signal intensities often cease to be quantitative; [157] the strength of the heteronuclear dipolar interaction determines the efficiency of magnetisation transfer, and so different chemical groups exhibit varying CP build-up rates.

During CP, ν_1, from eqns. 5.1 and 5.2, of the pulse on either nuclei can be varied, and often is; this is done as the ramp broadens the match condition, making it easier to find. The Hartmann-Hahn matching condition while spinning, eqn. 5.2, implies that matches exist in narrow bands, this narrowness is emphasised when investigating samples with weak dipolar couplings or under fast MAS. Moreover, the locations of these resonant bands are dependent on the resonance offset. [188] The result is that transferring magnetisation from abundant spins to dilute spins can be troublesome. It was found that varying the rf field strength during CP facilitated the location of these resonant bands, and actually enhanced the signal. [189] This 'ramping' of pulses is typically performed on the proton pulse and can be ramped in many different ways; complicated ramps involving trigonometric functions, or that have been optimised

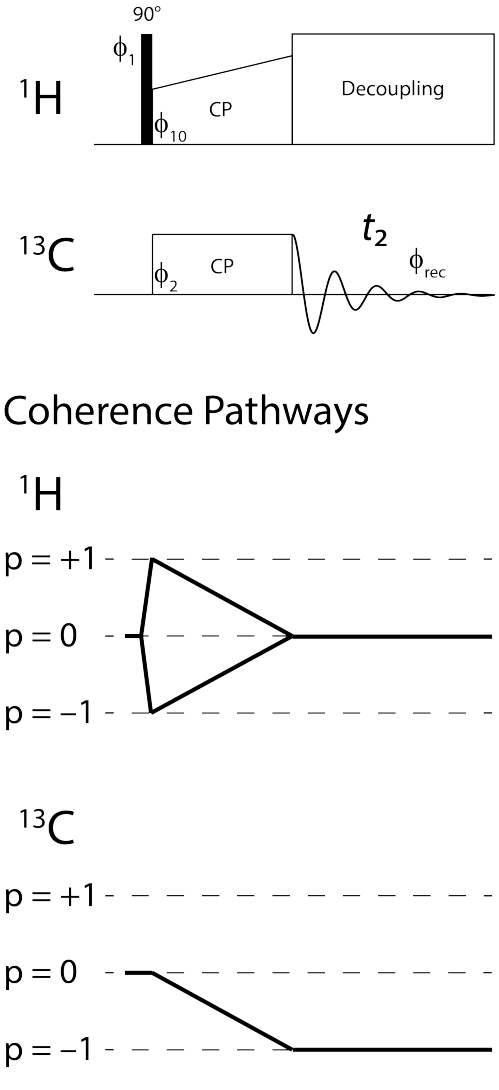

Figure 5.2: Pulse sequence for CP from ^{1}H to ^{13}C. The coherence pathway for ^{13}C and ^{1}H is also shown. The initial 90° pulse on ^{1}H creates magnetisation which is transferred to ^{13}C through ramped (for ^{1}H), Hartmann-Hahn matched pulses. Phase cycling: $\phi_1 = (+y\ -y)$, $\phi_2 = (+x+x-x-x+y+y-y-y)$, $\phi_{10} = (+x)$, $\phi_{\mathrm{rec}} = (+x-x-x+x+y-y-y+y)$.

through simulations, exist, however many spectroscopists use a simple X% to 100% linear ramp. In the experiments performed in this thesis, the majority use a 70 or 80% to 100% ramp for CP.

The contact time for CP can be optimised depending on which nuclei, or which type of nuclei, is of interest. For example, the contact time for a typical ^{1}H-^{13}C CP is often shorter than that of a typical ^{1}H-^{15}N CP, 1.0 ms and 1.5 ms respectively. Moreover, it is possible to optimise for carbonyl over aliphatic carbons by using shorter contact times to favour aliphatic sites at around 800 µs as opposed to 1.5 ms, which is better suited for carbonyl sites. This is a direct consequence of the size of the dipolar coupling between the nuclei mentioned and the local ^{1}H spins; typical dipolar coupling values between ^{1}H and Cα and ^{15}N are ∼25 and ∼10 kHz. [190] In all experiments in this thesis, contact times similar to those above have been used.

5.1.2 Double Cross Polarisation

The spectroscopic rationales for using CP have been discussed in detail above; briefly, there is a significant increase in total coherence produced on the receiving nuclei due to the ratio of the gyromagnetic ratios, and a decrease in total time of experiment due to faster relaxation when compared to direct excitation on the nuclei of interest (when the donating nuclei is ^{1}H, as is the most common case).

Double Cross Polarisation (DCP), introduced by Schaefer, McKay and Stejskal in 1979 in a paper investigating ^{15}N-^{13}C correlations in glycine, [183] involves the creation of coherence on ^{1}H before transferring to one spin species then to a second spin species, with a correlation spectrum produced between the two heteronuclear spin species; a pulse sequence and coherence pathway [2] for DCP is shown in Fig. 5.3. During periods of evolution on either nucleus under investigation, high power decoupling is applied on ^{1}H to achieve high resolution, which will be expanded on later in this chapter.

In biological ssNMR, typical nuclei under investigation are ^{15}N and ^{13}C allowing variations of the DCP experiment such as NCO and NCA, where the carbons involved (i.e. polarisation transfers) are differentiated via the resonance offset (for either carbonyl or aliphatic carbons). These experiments are valuable as they can provide sequential assignment of the backbone nuclei of proteins which allows investigation of structural and dynamical properties of important biomolecules. [191, 192] In the experiments

[2] For the observed nuclei, in this example ^{15}N and ^{13}C

performed in this study, the first CP is from ^{1}H to ^{15}N and the second is from ^{15}N to ^{13}C such that the final acquisition is on ^{13}C, shown in Fig. 5.3. The experiment is performed in this order as the sensitivity of an NMR experiment is proportional to γ^3, due to γ factors appearing from the Boltzmann distribution, the magnetic moment of a spin and from Faraday's law of induction of the signal in the coil. The magnetic moment of ^{13}C is greater than that of ^{15}N as is ν_0, thereby increasing the EMF induced in the coil and providing a more sensitive experiment than for that when acquisition is performed on ^{15}N. Secondarily, the spectral width of the carbon aliphatic region is greater than that of the nitrogen so that ^{13}C acquisition is more suited to t_2, than the incremented t_1 time, and once the experiment is optimised for Cα it can more easily be altered for C$'$ than to change F_1 and F_2.

An illustration of the coherence transfer in DCP experiments is shown in Fig. 5.4; from this it is easy to see that the correlations produced in NCA experiments (Fig. 5.4 top) are intra-residue and those in NCO (Fig. 5.4 bottom) are inter-residue, from ^{15}N in residue i to C$'$ in residue i$-$1. Illustrative NCA and NCO spectra are shown in Fig. 5.5. NCA (Fig. 5.5 left) and NCO (Fig. 5.5 right) experiments can easily be visualised as complementary techniques from the figure. The amino acid (primary) sequence of the protein is known, and can be used to aid assignment of the spectra obtained by these experiments, though an issue arises for the two terminal residues, NCO will not provide signals for either residue due to there being, for N-terminus, no C$'$ to receive magnetisation or, for C-terminus, no ^{15}N to provide it.

When assigning DCP spectra, previously obtained carbon assignments (from multidimensional homonuclear spectra) can be used to significantly accelerate analysis. If Cα resonances have been assigned, from e.g. experiments in § 5.5, it is trivial to locate the previously assigned Cα resonance, as few Cα resonances will have identical chemical shift values. As ^{15}N chemical shifts exist in residue-specific regions, separation of ^{15}N resonances should be possible, and so finding the corresponding ^{15}N resonance to the previously assigned Cα resonances enables analysis of DCP NCA spectra. Fewer C$'$ chemical shift values will have been found compared to Cα from earlier 2D ^{13}C-^{13}C spectra, as the C$'$ region is often cluttered, so the analysis method for NCO spectra differs to that described above. Here, the ^{15}N chemical shift values found from NCA spectra can be used to locate the C$'$ chemical shifts. Certain amino acids have characteristically low ^{15}N chemical shifts ($\sim$110 ppm), such as glycine, which facilitates assignment. As mentioned in § 4, there are other ^{15}N chemical shifts which are significant outliers such as lysine Nz, at $\sim$30 ppm, or histidine Nδ_1 and Nϵ_2 at $\sim$ 190 ppm, which would be easily assigned however it is unusual to attempt to

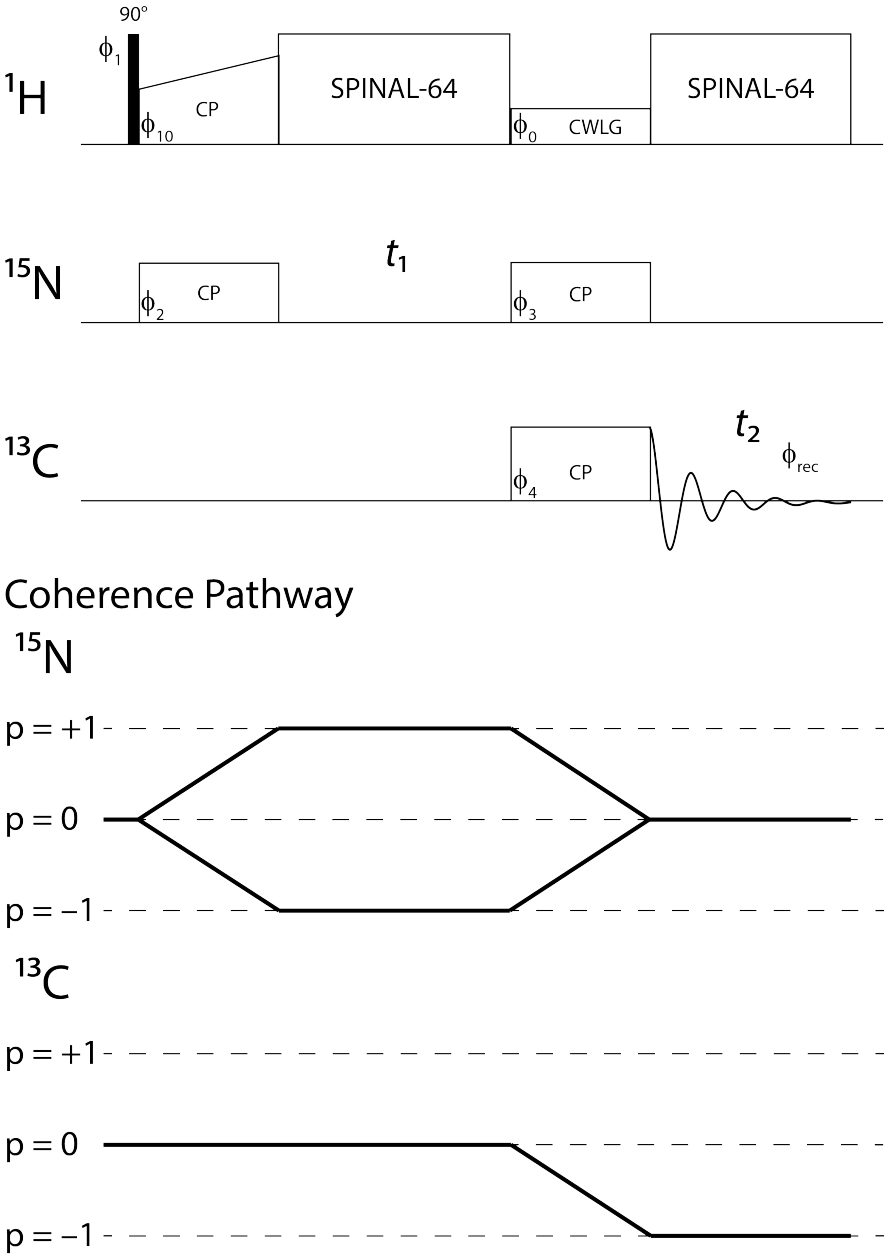

Figure 5.3: Pulse sequence for DCP, where initial CP is to ^{15}N and the second CP is to ^{13}C. The coherence pathways for ^{15}N and ^{13}C are also shown. The decoupling used on ^{1}H will be explained in § 5.3. Phase cycling: $\phi_1 = (+y-y)$, $\phi_2 = (+x)$, $\phi_{10} = (+x)$, $\phi_0 = (+x)$, $\phi_3 = (+x+x+x+x-x-x-x-x)$, $\phi_4 = (+x+x+x+x+y+y+y+y-x-x-x-x-y-y-y-y)$, $\phi_{\mathrm{rec}} = (+y-y+y-y+x-x+x-x-y+y-y+y-x+x-x+x)$.

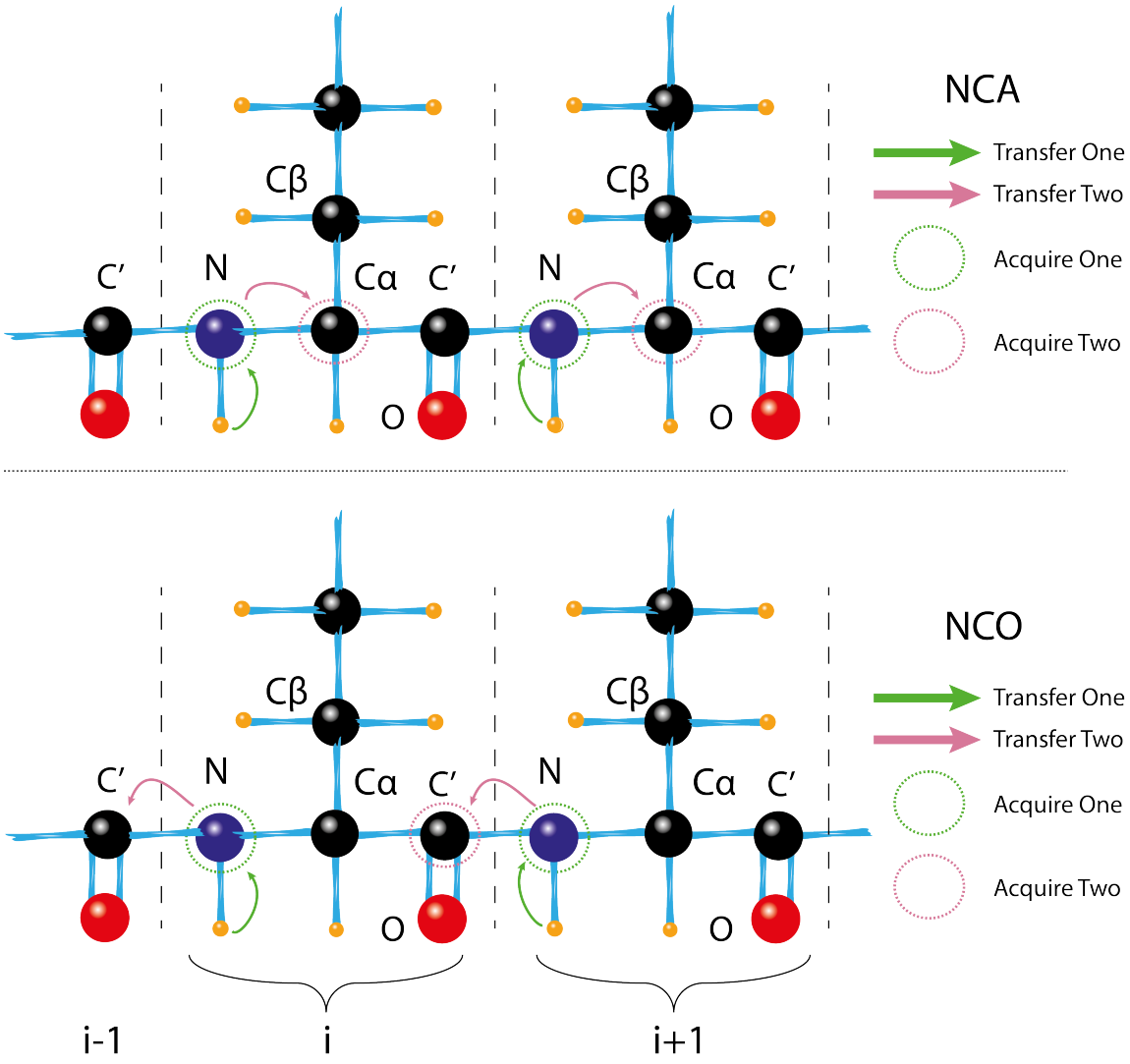

Figure 5.4: Illustration of coherence transfer during NCA (top) and NCO (bottom) DCP experiments. It is illustrated why NCA experiments reveal intra-residue connectivities while NCO experiments identify inter-residue connectivities.

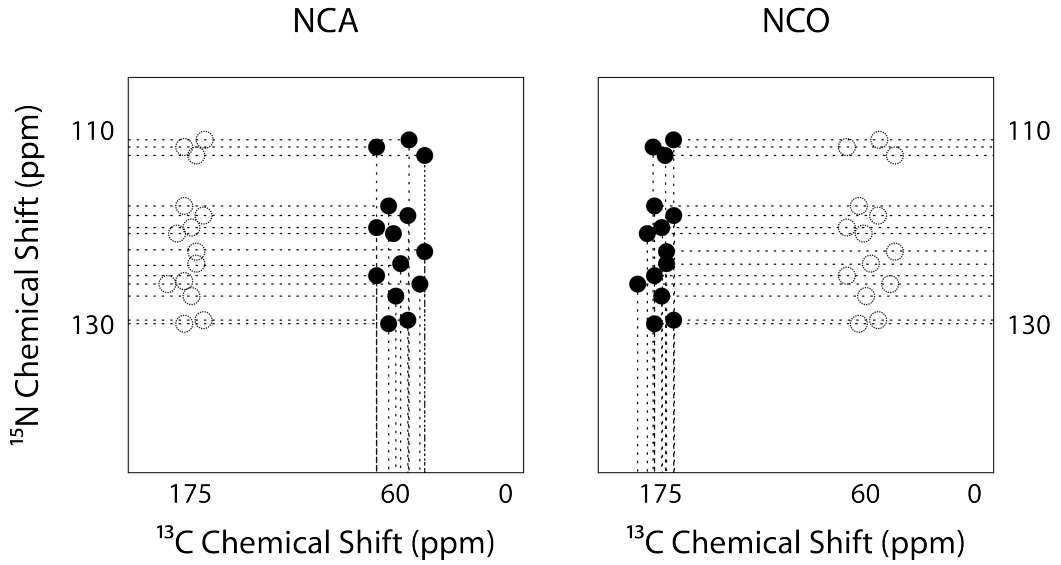

Figure 5.5: Illustrative spectra produced by a DCP experiment, NCA (left) and NCO (right). Notably low ^{15}N chemical shifts (∼110 ppm) can often be assigned to glycine residues, or secondary nitrogens in amino acids such as glutamine. Full circles represent signals obtained by the experiment while dotted circles represent the signals obtained by the other experiment. When the two spectra are combined, the aliphatic ^{13}C signal in the same residue as the ^{15}N signal and the carbonyl ^{13}C signal of the preceding residue will be horizontally aligned.

detect these while detecting the main block at ∼120 ppm due to the spectral width required.

Performing DCP experiments at high MAS frequencies is impractical as CP gets less efficient at high rf amplitudes, so throughout this study DCP experiments are performed between 7.0 and 15.0 kHz; if the MAS spinning frequency was set to 40 kHz, irradiating at a moderate 40 kHz on one channel, during the carbon-nitrogen CP, results in the corresponding pulse on the other channel needing to be 80 kHz. Triple channel probes (HXY) are required for DCP experiments and achievable nutation frequencies are lower for a triple- rather than for a double-resonance configuration, which can cause difficulty in efficiently producing rf irradiation with a high nutation frequency.

5.2 Inverse Detection

The techniques mentioned up to now for obtaining high resolution ssNMR data rely on acquiring signals on dilute spins, such as carbon or nitrogen, as better resolution is achievable on these spins than, e.g., ^{1}H due to the larger chemical shift range and the narrow linewidths as a result of less homonuclear dipolar broadening. However, with the advance in technology of solid-state NMR equipment, such as commercially available 1.0 mm probes and Ago Samoson's 0.8 mm probe allowing up to 100 kHz MAS frequencies, proton detection on large peptides is now a viable option. [193–196] Proton detection, or inverse detection, is highly desirable in ssNMR as protons can act as a sensitive probe of local structure due to the location of protons at the edges of molecules resulting in protons being useful in examining long range contacts. Moreover, proton detection allows a gain in sensitivity of $(\gamma_H/\gamma_X)^{3/2}$, corresponding to a factor of 8 and 31 when compared to ^{13}C- and ^{15}N-detected experiments respectively, however, due to the strong homonuclear dipole-dipole coupling network, fast MAS is required to ensure resolution is achieved; [197] the residual dipolar linewidth is inversely proportional to the MAS frequency. A drawback to proton detection is that high MAS frequencies are only available in rotors of small diameter (see above) which naturally restrict the sample volume, which in turn reduces the inherent signal-to-noise achievable, although the sensitivity per sample volume is much higher for smaller rotors as the coil is nearer the sample. [198] Perdeuteration of samples, combined with back-exchange of amide protons, has been used by many groups [194, 199, 200] as a solution to attenuating the strong dipolar network although this technique is often not an applicable solution to the problem. Another problem that requires solving for inverse detection of hydrated biological samples is that the strong H_2O resonance can dominate signals within the 4-5 ppm region;[3] this issue can be negated using intelligent water suppression schemes, which will be discussed in detail later, see § 5.3.

Two pulse sequences for a 2D and 3D inversely detected experiment are shown in Figs. 5.6 and 5.7, respectively. Notable features, some of which are discussed later, include the use of a low nutation frequency solution state NMR decoupling scheme, WALTZ-16, on ^{13}C during t_2 acquisition, H_2O saturation sequences to suppress the water peak, tangentially ramped CP pulses on ^{1}H, and, as is the definition of an inversely detected experiment, a final acquisition on ^{1}H.

[3] The position of the H_2O ^{1}H resonance shifts with sample temperature, but within workable biological temperatures the water peak will exist around these values

Fig. 5.8 shows an illustration of the magnetisation transfer pathways within the 3D Cα-Hα-HX sequence, shown in Fig. 5.7. This produces a 3D spectrum, see Fig. 5.9, with Cα against Hα against HX, which can be assigned using Cα assignments obtained from homonuclear spectra. The 2D sequence, Fig. 5.6, results in a correlation between aliphatic or carbonyl ^{13}C and ^{1}H. In the 3D spectra, some resonances may not be detectable due to the nature of 3 dimensional experiments, namely time constraints due to incrementing both t_1 and t_2 dimensions, and poor sensitivity due to the extra magnetisation transfer. However, many proton resonances will be assignable using previously assigned Cα resonances, from e.g. 2D homonuclear spectra and simpler 2D inversely detected spectra, such that further ^{1}H chemical shifts, including, but not limited to, Hβ and H, can be assigned. All the sequences shown here for inverse detection using carbon can also be performed replacing carbon with nitrogen, provided some nitrogen chemical shifts have been obtained from earlier spectra, such as DCP NCA and NCO. Once these assignments have been made, there will be a large number of ^{13}C, ^{15}N and a few ^{1}H assignments from which computer programs can be employed to estimate torsion angles and secondary chemical shifts; the program used in this study is TALOS-N, [170] however there are a wide array of programs available; [201, 202] the functionality of TALOS-N will be discussed in the next chapter.

Resolution in the proton dimension is dependent on many factors: high-frequency MAS (>30 kHz) and high field homogeneous magnets (>17.6 T) are technological advances which have enabled the employment of inverse detection in the solid state, [184] the greater these two factors, the narrower ^{1}H linewidths become. Moreover, the application of WALTZ-16 decoupling on the X nucleus during ^{1}H evolution has been shown to improve ^{1}H linewidths; [195] perdeuteration with back-exchange of the amide protons, as mentioned earlier, has been shown to be effective in reducing ^{1}H linewidths by reducing the strong proton-proton dipolar couplings. [200] Note that pulsed field gradients (PFGs) can be used to attenuate problems due to the solvent resonance in solid-state NMR. [194] Variation in site to site intensity of peaks in 2D inversely detected experiments has been recorded, this has been attributed to the differential CP efficiency (discussed above in § 5.1.1) which is exacerbated in these experiments due to the use of two CP steps. [195]

Fig. 5.9 shows an illustrative spectrum obtained by performing the Inverse Detection pulse sequence in Fig. 5.7 on a three amino acid sequence. Dashed lines have been used to illustrate how chemical shifts can be obtained from 3D spectra. There are resonances in the spectrum resulting from magnetisation which has transferred, after

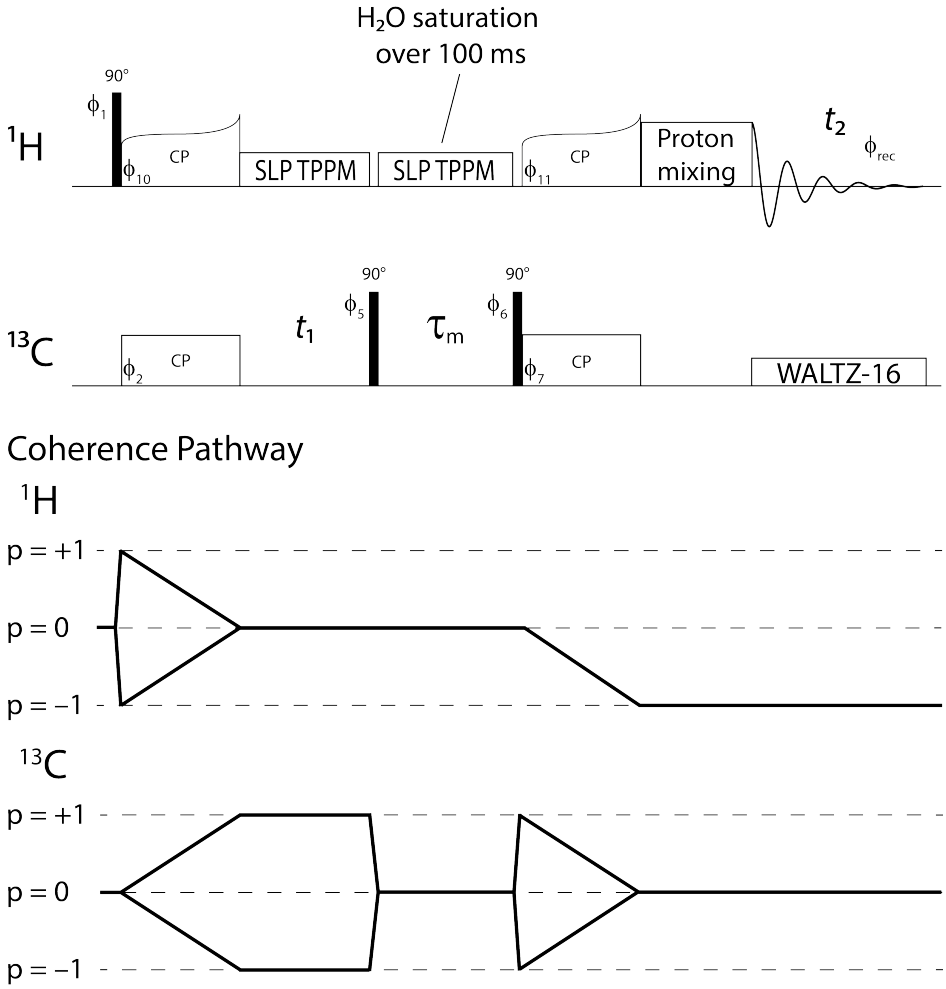

Figure 5.6: A 2D Inverse Detection pulse sequence. There is an initial CP from proton to carbon before t_1 evolution on ^{13}C. After the t_1 period, a pair of 90° pulses are applied on ^{13}C, after which an inverse CP occurs from ^{13}C to ^{1}H before t_2 acquisition. Water saturation ensures ^{1}H peaks in the 4-5 ppm region are not overwhelmed; slpTPPM is a decoupling sequence first used by Lewandowski et al. [203] The coherence pathway for ^{1}H is also shown. Phase cycling: $\phi_1 = (+y+y+y+y)$, $\phi_{10} = (+x+x+x+x)$, $\phi_2 = (+y+y+y+y-y-y-y-y)$, $\phi_5 = (+x+x-x-x)$, $\phi_6 = (-x-x+x+x)$, $\phi_{11} = (+y+y-y-y)$, $\phi_7 = (+y-y+y-y)$, $\phi_{\mathrm{rec}} = (+y-y-y+y-y+y+y-y)$.

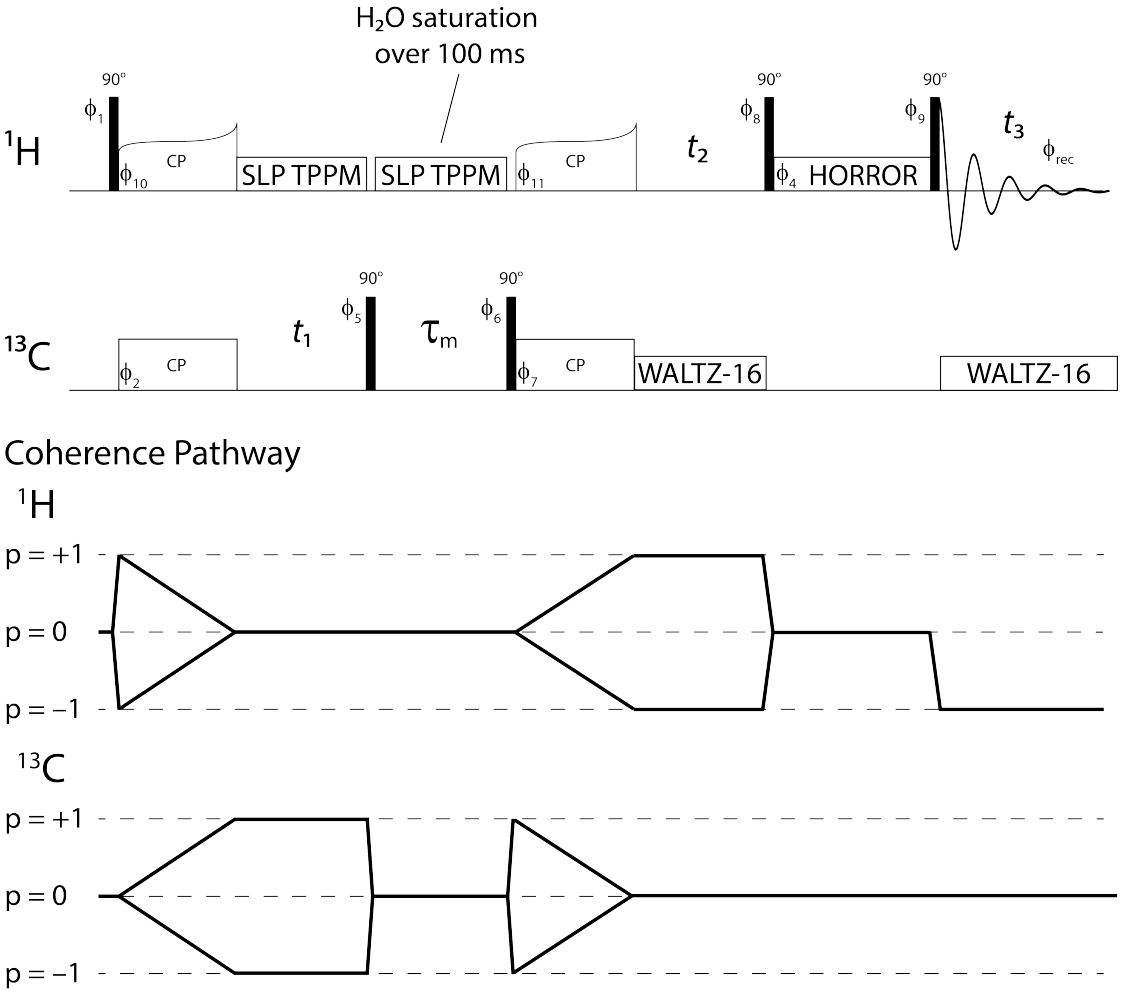

Figure 5.7: A 3D Cα-Hα-HX Inverse Detection pulse sequence. A HORROR sequence is used for proton-proton mixing. [204] The coherence pathway for ^{1}H is, again, shown. Phase cycling: $\phi_1 = (+y+y+y+y)$, $\phi_{10} = (+x+x+x+x)$, $\phi_2 = (+y+y-y-y)$, $\phi_5 = (+x+x)$, $\phi_6 = (-x-x)$, $\phi_7 = (+y-y)$, $\phi_{11} = (+y+y)$, $\phi_8 = (-x-+x+x)$, $\phi_4 = (+x+y+x+y+y+x+y+x-x-y-x-y-y-x-y-x)$, $\phi_9 = (+x+x-x-x)$, $\phi_{\text{rec}} = (+y-y-y+y-y+y+y-y)$.

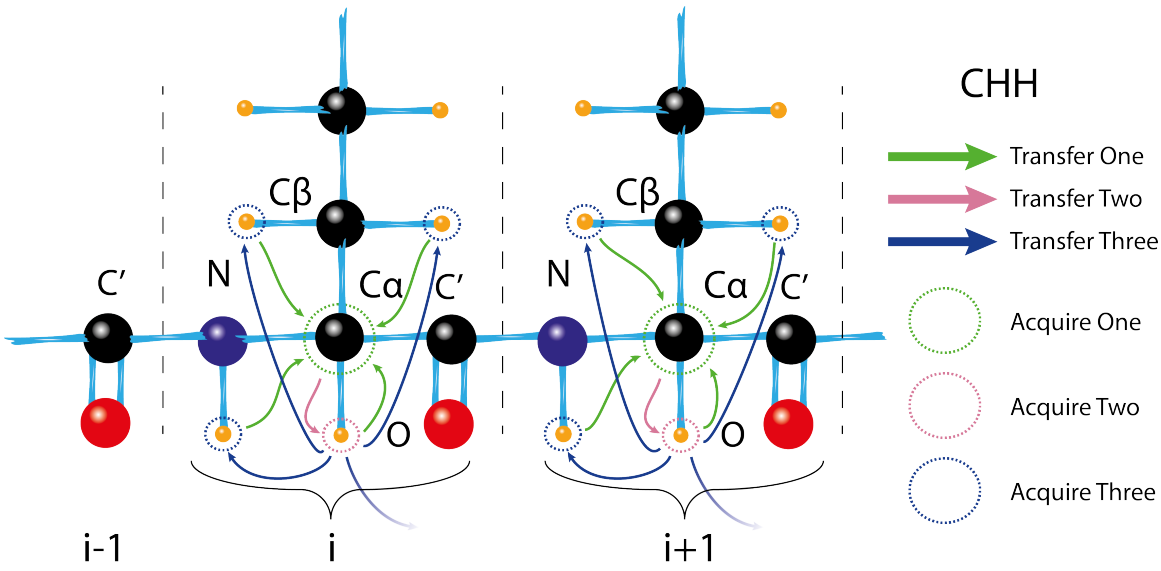

Figure 5.8: Illustration of the magnetisation transfer pathways achieved in a 3D Cα-Hα-HX Inverse Detection pulse sequence, see Fig. 5.7. The faded transfer three arrows indicate transfer to other protons not in residues i or i+1, such as those across the β-hairpin structure found in aggregated forms of amyloid-beta.

CP, from the Cα of a residue to the Hα of that residue and which has then transferred to Hβ. Transfers to H have been omitted in this spectrum as the chemical shift values of amide protons are typically high (∼9 ppm) and to represent this accurately in the spectrum would require considerable amounts of empty space, although such transfers are very possible in the sequence as shown in Fig: 5.8.[4] Provided the Cα chemical shift is known, this spectrum can easily be analysed and proton shifts can be found. The distinction between Hα and Hβ can be made based on the typical chemical shifts regions where the shifts for either exist and the location in which they are found in the spectrum. For example, the typical chemical shift for Hα in an alanine residue is ∼4 ppm whereas the Hβ chemical shift is typically ∼1 ppm. These values can be found in the BMRB. The two protons will be aligned at the carbon chemical shift value, and, therefore, pairs of proton chemical shifts can be found and assigned. If the carbon dimension was compressed into one plane, there would be a diagonal line made of proton signals in the remaining 2D proton-proton spectrum which results from the self-correlation of the Hα resonance.[5]

[4]Transfers to extra-residue protons have also been omitted due to the unnecessary complications such an inclusion would cause.

[5]If the spectral widths of the two proton dimensions were different, which is likely to be the case so as to include the amide and sidechain protons in the HX dimension while maintaining a suitable spectral width in the Hα dimension, the diagonal might be skewed, but there would still be

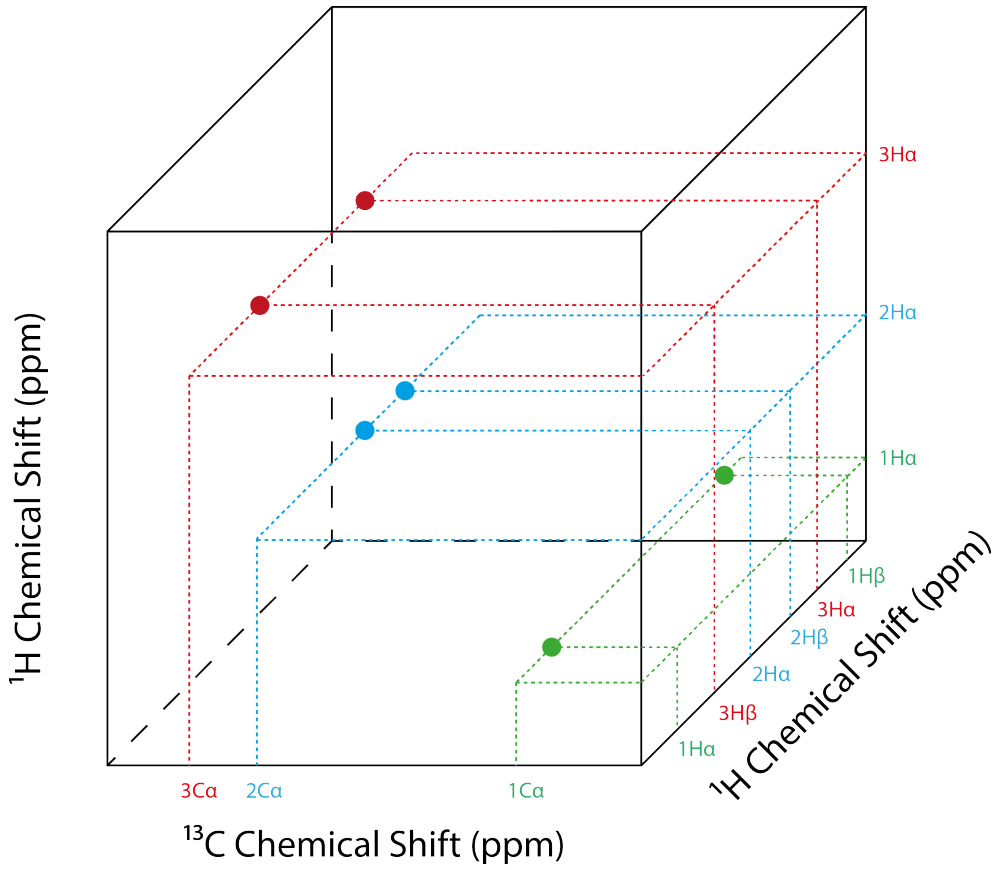

Figure 5.9: Illustrative spectrum produced by a 3D CHH Inverse Detection experiment. Certain residues show both Hα and Hβ resonances correlating with Cα from the same residue, this will be dependent on the mixing times involved.

The two spectroscopic techniques of DCP and inverse detection can be combined in one experiment. The pulse sequence in Fig 5.10 shows such an experiment; the correlations produced by the sequence are Cα-N-H, where the final H is the amide proton and will be referred to throughout this thesis simply as H, e.g. S26H refers to the amide NH of the Ser 26 residue. This sequence is one of those which are used in later chapters to obtain proton and nitrogen chemical shifts of samples which have already had many of the carbon chemical shifts assigned. All of the features of this sequence can be seen in the previous sequences from § 5.1.2 and 5.2 such as WALTZ decoupling on the dilute spin and slpTPPM decoupling on protons.

5.3 Dipolar Decoupling

5.3.1 Introduction to Decoupling

Solid-state NMR differs from solution NMR in many ways, one of which is due to the absence of rapid molecular tumbling which averages out anisotropic interactions. The strong dipolar interaction between abundant spins, such as ^{1}H, as well as between ^{1}H and a dilute spin such as ^{13}C can lead to factors which adversely affect spectral resolution, as mentioned in § 3.4.2 and 3.4.3, so techniques utilising rf irradiation called dipolar decoupling have been developed so as to remove this interaction. Homonuclear and heteronuclear decoupling exist however in most experiments in this study only heteronuclear decoupling is used.

5.3.2 Continuous Wave: cw

A basic heteronuclear decoupling sequence is on-resonance continuous wave (cw) irradiation which provides a simple method of decoupling for many solids, and was first described in 1955. [205] For low MAS frequencies (<20 kHz) and moderate decoupling nutation frequency (∼60 kHz), effective decoupling can be shown via the sharpening of linewidths. [206] An interesting phenomenon was noticed in the form of ^{13}C linewidths increasing as MAS frequencies increased over ∼10 kHz, and was explained in the form of a weakening of the homonuclear coupling network due to MAS. [207, 208] This strong homonuclear coupling for ^{1}H provides a 'self decoupling' effect from the rare spin species, which is then disturbed by MAS. [158, 209] Had the

a characteristic line in the projection of the carbon dimension, this complication has been omitted here.

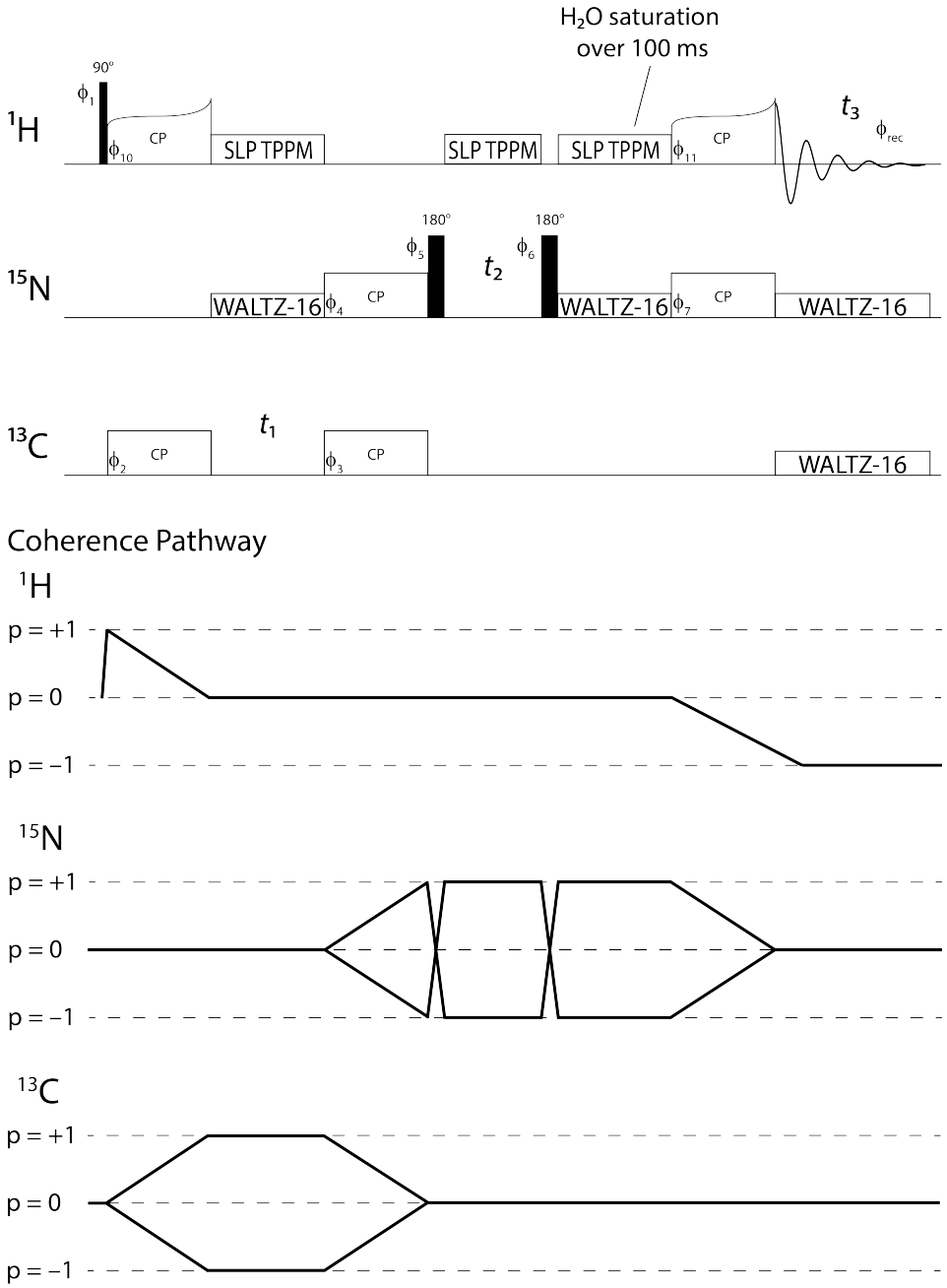

Figure 5.10: A 3D Cα-N-H Double Cross Polarisation, Inverse Detection pulse sequence. Pulse sequence involving both the DCP and inverse detection, which produces a spectrum with ^{13}C-^{15}N-^{1}H correlations. The coherence pathways for all three nuclear species are shown. Phase cycling: $\phi_1 = (+y+y+y+y)$, $\phi_{10} = (+x+x+x+x)$, $\phi_2 = (+y+y+y+y)$, $\phi_3 = (+y+y+y+y)$, $\phi_4 = (+y+y+y+y-y-y-y-y)$, $\phi_5 = (+x+x-x-x)$, $\phi_6 = (-x-x+x+x)$, $\phi_7 = (+y-y+y-y)$, $\phi_{11} = (+y+y-y-y)$, $\phi_{\mathrm{rec}} = (+y-y-y+y-y+y+y-y)$.

MAS frequency achievable been large enough to fully average out the ^{1}H homonuclear dipolar couplings, the only decoupling required would be to remove the effect of any J couplings, however such MAS frequencies are today still not obtainable. [210–212] The increase in MAS frequency is necessary at high magnetic field strengths to remove the increased ^{13}C CSA, which scales proportionally with B_0, however this ensured a more efficient decoupling method was required as simply increasing the nutation frequency of the cw decoupling was not a long term solution. Recent work by Kentgens and co-workers has been investigating the properties of microcoil detectors, and the advantages to be gained through use of these in terms of senstivity while maintaining high resolution. Moreover, the use of microcoils allows the generation of extremely high rf fields, such as claimed in [213]; using an rf power of 270 W for ^{1}H at 400 MHz (9.4 T) a B_1-field strength of 4.7 MHz was achieved, with B_1-field strengths of 1.9 MHz and 3 MHz found for aluminium at 14.1 T using 380 and 850 W of rf power respectively. These extremely high frequencies may become more widely used in the future for highly effective decoupling.

5.3.3 Wideband, Alternating-phase, Low-power Technique for Zero-residual-splitting: WALTZ

A homonuclear decoupling sequence originally designed for solution state NMR in 1983, WALTZ-16, [214] can be used in the solid state at very high MAS frequencies, such as used in the later parts of this study during the inverse detection experiments from § 5.2, see Figs. 5.6−5.7. The basic block for WALTZ decoupling, R, is:

$$R = 90^\circ(\phi)180^\circ(-\phi)270^\circ(\phi) = 1\bar{2}3 \tag{5.11}$$

with WALTZ-4, the primitive cycle, taking the form $RR\overline{RR}$. WALTZ-8 benefits from supercycling which eliminates an undesirable small-angle rotation about an axis close to the z-axis, for more detail on this see [214], and takes the form:

$$K\overline{KK}K = \bar{2}4\bar{2}3\bar{1} \quad 2\bar{4}2\bar{3}1 \quad 2\bar{4}2\bar{3}1 \quad \bar{2}4\bar{2}3\bar{1} \tag{5.12}$$

From this sequence there are many options of further expansion but Shaka et al found the best performance was offered by, what is now known as, WALTZ-16: [214]

$$Q\overline{QQ}Q = \bar{3}4\bar{2}3\bar{1}2\bar{4}2\bar{3} \quad 3\bar{4}2\bar{3}1\bar{2}4\bar{2}3 \quad 3\bar{4}2\bar{3}1\bar{2}4\bar{2}3 \quad \bar{3}4\bar{2}3\bar{1}2\bar{4}2\bar{3} \tag{5.13}$$

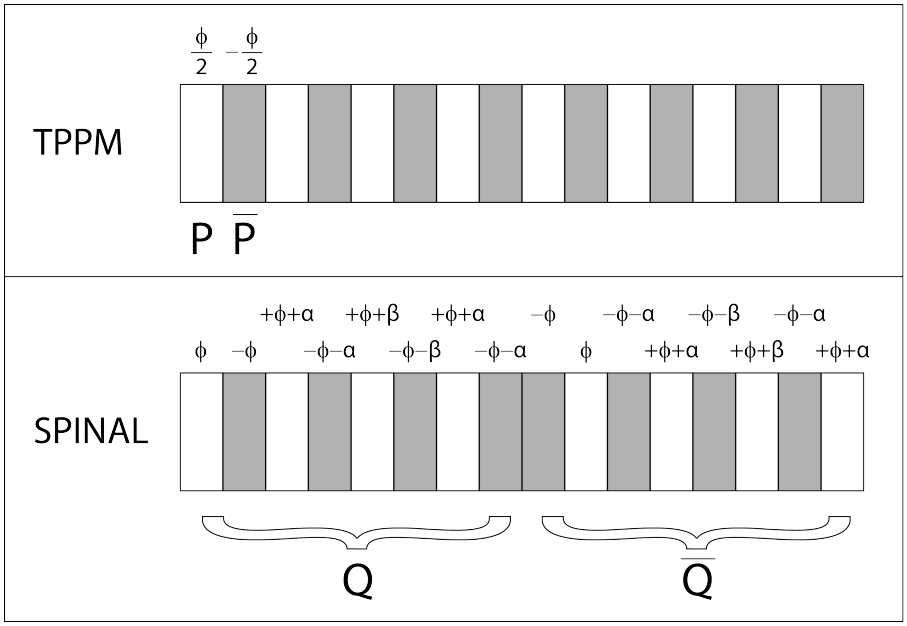

Figure 5.11: Pulse sequences for TPPM [215] and SPINAL [216] decoupling schemes. Phase varies between $+\frac{\phi}{2}$ and $-\frac{\phi}{2}$ in the TPPM scheme and follows the scheme $+\phi$, $-\phi$, $+\phi+\alpha$, $-\phi-\alpha$, $+\phi+\beta$, $-\phi-\beta$, $+\phi+\alpha$ and $-\phi-\alpha$ for Q in the SPINAL sequence. SPINAL-64 supercycling exists through use of the Q $\overline{\text{Q}}$ $\overline{\text{Q}}$ Q $\overline{\text{Q}}$ Q Q $\overline{\text{Q}}$ scheme. During use of the TPPM scheme a value of $\phi = 15°$ was used, and during the SPINAL scheme values of $\phi = 10°$, $\alpha = 5°$ and $\beta = 10°$ were used.

WALTZ-16 offers broadband decoupling and can be performed in the solid state using relatively low nutation frequencies, which is desirable when pulsing on already rapidly rotating biological samples so as to limit any further sample heating due to the decoupling.

5.3.4 Two Pulse Phase Modulation: TPPM

Under cw decoupling, as MAS frequency increased over ∼10 kHz the ^{13}C linewidths increased, moreover, with higher magnetic field strengths, greater MAS frequencies are required to average out the CSA; specifically, cw showed poor performance for CH_2 groups for MAS frequencies around 15 kHz. Therefore, a new heteronuclear decoupling sequence was needed as cw was unable to cope with emerging high magnetic field strengths and MAS frequencies. [206] The task was as follows, create a sequence which: provided efficient decoupling over a wide range of MAS frequencies; accounted for variations in the proton resonance offset due to the sample containing many protons over a chemical shift range of ∼10 ppm; utilised a shorter decoupling

sequence than e.g. WALTZ-16, as it had been noticed that as the cycle time of the sequence approached that of the rotor period decoupling efficiency degraded; and which exploited, if possible, the line-narrowing effect of the network of strong homonuclear couplings from which cw decoupling benefited, mentioned earlier in the chapter. The breakthrough was found in 1995 in the form of Two Pulse Phase Modulation (TPPM). [215] It had been found earlier that simple modulations of the decoupler phase could significantly improve the performance of decoupling in comparison to standard cw irradiation, [217–219] and this was the starting point for the discovery of TPPM. TPPM decoupling takes the form of rapidly alternating, equal length blocks of decoupling, with the phase of the rf irradiation switching from $+\frac{\phi}{2}$ (for block i) to $-\frac{\phi}{2}$ (for block i+1), see Fig. 5.11. Experimental optimisation found values of $\sim$7 μs for pulse length (τ_p), with a ν_1 optimised around 63 kHz, and 15° for ϕ. When cw and TPPM decoupling were performed on a sample of tyrosine hydrochloride monohydrate spinning at 10 kHz with ν_1 = 75.8 kHz ^{1}H decoupling, the Cα and Cβ linewidths narrowed from 85 and 120 Hz to 52 and 48 Hz, respectively. [215] This discovery led to many variants on the TPPM sequence, including TPFM, FMPM$^{\mathrm{L}}$, FMPM$^{\mathrm{R}}$ (variants with frequency and/or phase modulated decoupling), AM-TPPM (an additional amplitude modulation), CPM (a continuous cosine phase modulation) and CM (single-frequency continuous modulation), [220–223] however none show significant and consistent improvements over TPPM. In 2006 however, a sequence was introduced by the Madhu group called swept-frequency two-pulse phase modulation (SW$_{\mathrm{f}}$-TPPM) which was shown to outperform TPPM when performed on U-^{13}C labelled tyrosine for MAS frequencies up to 14 kHz at ^{1}H decoupling rf nutation frequencies of 70, 90 and 100 kHz. [224] The sequence increments the pulse durations of the usual TPPM sequence causing a sweep in the modulation frequency, while the phase alternation remains constant. A family of decoupling sequences has emerged from this initial finding using linear (SW$_{\mathrm{f}}^{\mathrm{lin}}$-TPPM) and tangential (SW$_{\mathrm{f}}^{\mathrm{tan}}$-TPPM) sweep profiles alongside other minor alterations (SW$_{\mathrm{f}}^{\mathrm{inv}}$-TPPM). [225, 226] Another sequence similar to this family is swept low power TPPM (slpTPPM) created by the Emsley group, [203] this sequence is used in inverse detection sequences in § 5.2. slpTPPM contains a linearly varied duration of pulses achieving a frequency sweep through the low power TPPM condition in a manner analogous to SW$_{\mathrm{f}}$-TPPM. The lengths of the pulses in the middle of the decoupling cycle are set to twice the rotor period. The phase of decoupling pulses alternates as in TPPM, though between ϕ and $-\phi$, and their amplitude is set to $\frac{1}{4}\nu_{\mathrm{R}}$.

5.3.5 Small Phase Incremental Alternation Decoupling: SPINAL

Another sequence that shows significant and consistent improvements over TPPM is SPINAL-64. [216] Though initially developed for use on liquid crystals, its application on solid samples is widespread due to the efficient decoupling provided on rigid samples at high MAS frequencies. Fig. 5.11 shows the form the decoupling takes. If TPPM can be represented by two pulses with alternating phase (as described above) with notation P and $\overline{\mathrm{P}}$, as used in Fig. 5.11, then SPINAL-64 can be represented by eight pulses with phases alternating as in Fig. 5.11 with the use of supercycling such that the overall structure of the sequence is: Q $\overline{\mathrm{Q}}$ $\overline{\mathrm{Q}}$ Q $\overline{\mathrm{Q}}$ Q Q $\overline{\mathrm{Q}}$, where Q represents a block of eight pulses, as shown in Fig. 5.11. Fung and co-workers first discovered the effectiveness of supercycling in a publication on SPARC-16 (small phase angle rapid cycling with 16 steps); [227] SPARC-16 was a supercycled version of the basic TPPM scheme. SPINAL-64 was shown to have an increased decoupling efficiency over TPPM and cw, but was also shown as being less affected than TPPM when the decoupler offset was altered. [216] Although Fung refers to a detailed theoretical analysis of the sequence as extremely difficult if not impossible, due to the complex nature of decoupling heteronuclear couplings which themselves are part of a strong homonuclear network which itself is disrupted by any decoupling, a qualitative analysis as to its effectiveness at high magnetic field strengths and MAS frequencies was suggested; [216] as the sequence was developed on liquid crystals, where molecular motion reduces the effective strength of the dipolar interactions, when performed at high magnetic fields, which promotes the effects of chemical shift offsets over dipolar couplings, it is unsurprising that SPINAL-64 displays efficient decoupling. [228] SPINAL-64 is regularly used in the experiments in this thesis as shown in the DCP pulse sequences in § 5.1.

5.4 An Introduction to Probing Dipolar Couplings and Dipolar Truncation

As mentioned above, a combination of MAS and decoupling can achieve a significant reduction in the linewidths of ssNMR spectra by inducing a spatial averaging of anisotropic interactions which then enables the acquisition of high-resolution ssNMR data, for an in-depth discussion see [167]. By averaging second rank tensor interactions such as the chemical shift anisotropy and the heteronuclear dipolar interaction, experiments then provide solely isotropic chemical shift information. In this manner,

ssNMR is able to mimic (though without completely averaged interactions) solution NMR. This is not always the desired outcome, however, as e.g. a suppressed dipole-dipole interaction would provide useful distance information if it could be selectively re-introduced, and so techniques were developed to re-introduce specific interactions. Diligently prepared sequences of rf pulses were shown to be able to selectively and coherently re-introduce the dipole-dipole interaction, a technique known as dipolar recoupling. [229]

In the last decade, solid-state NMR spectroscopists have been faced with a significant task; enable precise long-range contacts (>3 Å) to be obtained on samples that are fully-labelled or, at least, have many sites labelled. The structural information provided by these contacts is vital in biological NMR as it can reveal the overall fold of a peptide or protein which is crucial in modelling and often has great implications on functionality. Extracting long range contacts, however, is no mean feat due to the phenomenon of dipolar truncation, which describes the attenuation of polarization transfers over weak couplings in the presence of strong interactions. [166, 230]

There are 3 main groups into which spectroscopic methods developed to combat dipolar truncation can be placed: Frequency-selective methods which avoid recoupling strong one and two bond interactions; Second-order spin diffusion-type experiments including PDSD and DARR, see § 5.5; and techniques which utilise ^{1}H-^{1}H spin diffusion such as the CHHC experiment. Dipolar truncation can also be partially alleviated, in biological NMR, by using biochemical methods which generate alternatingly labelled proteins, [35, 231–233] however this study does not use these labelling techniques and so no further detail will be provided.

5.5 Nuclear Overhauser Effect Spectroscopy: NOESY and NOESY-like experiments

In solution NMR, dipolar interactions lead to dipolar cross-relaxation and the nuclear Overhauser effect (NOE) which carry information on molecular structure and dynamics. The NOE is the fractional change in intensity of one NMR line when another resonance is perturbed, [176] and is an invaluable tool for structural studies in solution NMR of small molecules. A common solution NMR experiment is the NOESY experiment developed by Ernst and co-workers in 1979, [29] which can establish correlations between physically close homonuclei. The basic 2D NOESY pulse sequence takes the form shown in Fig. 5.12: a sequence of three 90° pulses between the first

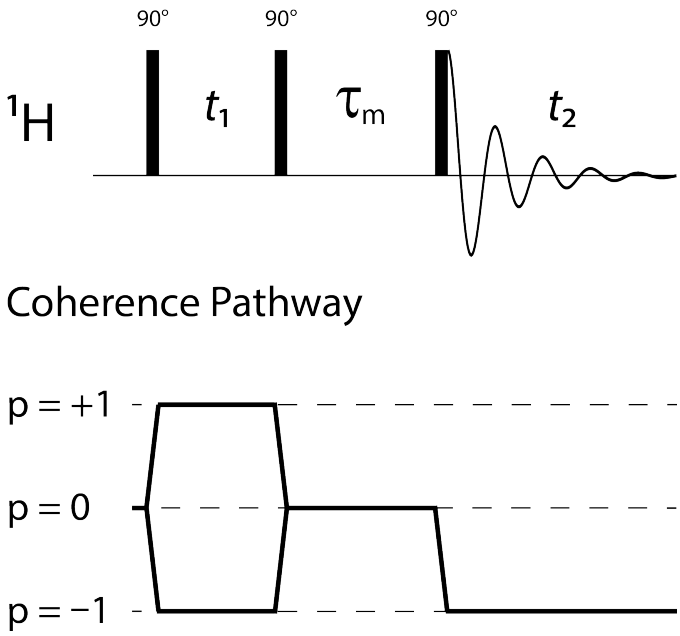

Figure 5.12: Pulse sequence for a NOESY experiment. Three 90° pulses on the ^{1}H channel are separated by a t_1 acquisition time and a mixing time, τ_m.

and second of which there is a period of magnetisation evolution (t_1), between the second and third there is a mixing time (τ_m), and acquisition following the final pulse (t_2). During t_1, the magnetisation components are frequency-labelled, and during τ_m cross-relaxation results in local magnetisation exchange between dipolar coupled protons. As is usual in a 2D experiment, t_1 is incremented linearly between set values, such that a 2D Fourier transformation produces the desired frequency domain spectrum.

Solid-state NMR analogues of the NOESY experiment rely on a phenomenon known as spin diffusion. The transfer of magnetisation between two dipolar coupled spins has been shown to be oscillatory, however, as the number of spins in the system increases, the network of coupled spins reduces this oscillatory behaviour to a diffuse transfer of magnetisation. The magnetisation transfer occurring in a network of dipolar coupled ^{1}H spins is referred to as ^{1}H spin diffusion. [234] 2D homonuclear NOESY-like spin diffusion experiments, shown in Fig. 5.13, performed under MAS, can be used to obtain through-space proximities between spins in the solid state from the analysis of the 2D correlation spectra obtained through use of the experiment, for more on this see Chapter 3 in [234].

A schematic NOESY spectrum is shown in Fig. 5.14 where spin A is coupled to

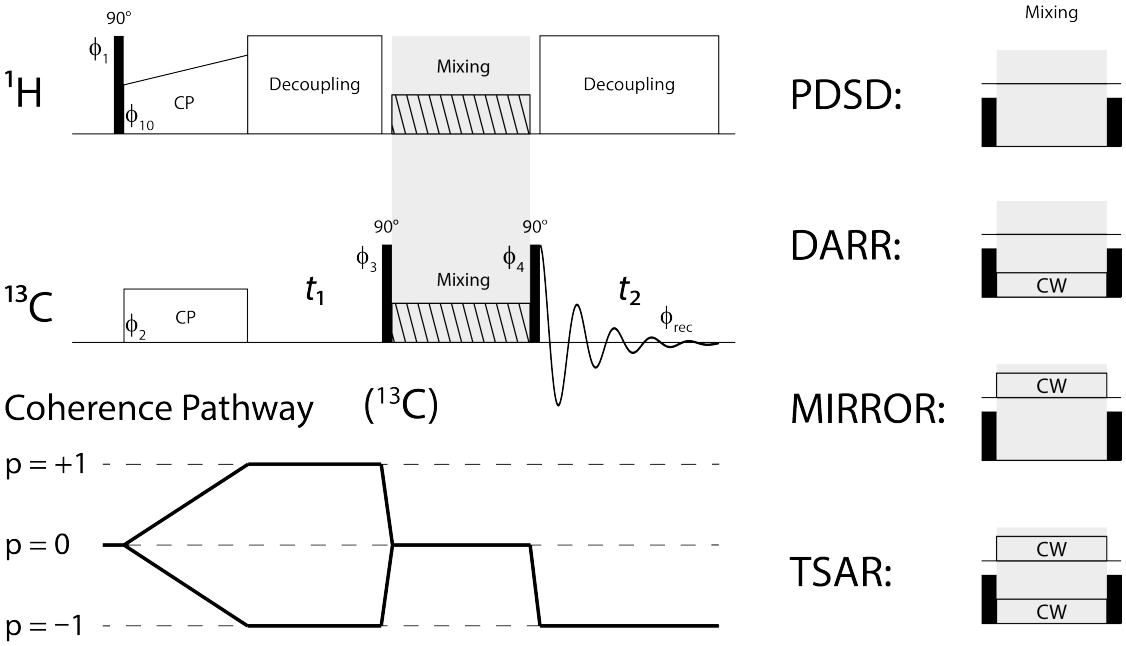

Figure 5.13: Pulse sequence for 2D NOESY-like experiments. The coherence pathway for ^{13}C is also shown. The application of rf pulses in the mixing time differentiates one experiment from the other as shown on the right. The DARR cw pulse obeys $\nu_1 = \nu_R$. Phase cycling: $\phi_1 = (+y-y)$, $\phi_{10} = (+x)$, $\phi_2 = (+x+x-x-x+y+y-y-y)$, $\phi_3 = (+y+y-y-y-x-x+x+x)$, $\phi_4 = (-y-y+y+y+x+x-x-x)$, $\phi_{rec} = (+x-x-x+x+y-y-y+y)$.

spins C and E, and spin B is coupled to spin D. The figure shows the cross peak pattern produced by such a, albeit simplistic, system and it is quite clear that A, C and E are separated from B and D. The existence of equivalent cross peaks at the corresponding position on the opposite sides of the diagonal is a reliable marker for the veracity of a signal. As the τ_m of the NOESY experiment is increased, the greater the number of cross peaks that become visible in the spectrum; these new longer range contacts are produced due to spin diffusion, which will be expanded on in detail later, effects. τ_m can be increased up to >500 ms, such that there would be many long-range contacts in the spectrum however, in payment for these extra signals, the overall peak intensities of the shorter range contacts, due to direct dipolar coupling between nearby protons, decreases. In this way, a range of τ_m experiments provides a range of structural and dynamical information on the sample. There are

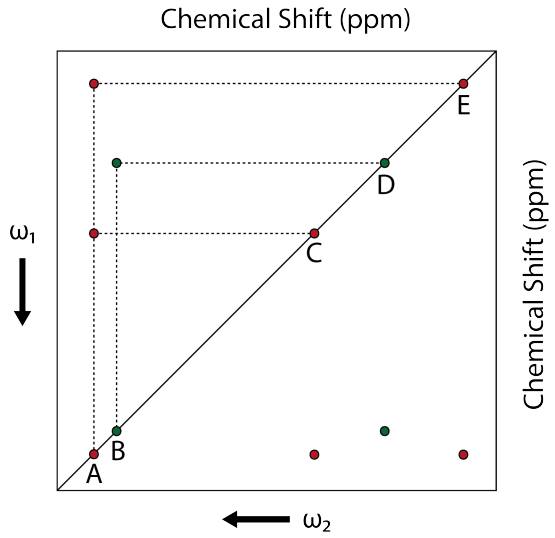

Figure 5.14: Schematic NOESY spectra of a simple five spin system whereby spins A, C and E, and B and D are dipolar coupled. Cross peaks on both sides of the diagonal are a reliable indication for a true correlation between spins.

many analogues of this solution NMR experiment used in ssNMR, see Fig. 5.13, for homonuclear correlation of biological nuclei e.g. ^{13}C-^{13}C, a few of these will be described below.

5.5.1 Spin Diffusion

Before solid-state NMR analogues of the NOESY experiment are discussed, the phenomenon of spin diffusion will be briefly considered. In general, spin diffusion techniques perform well and NOESY-like sequences, such as proton-driven spin diffusion (PDSD) [36] and dipolar-assisted rotational resonance (DARR) [182], are widely used, however at high MAS frequencies and high magnetic fields a different method is preferential: TSAR-based experiments (third spin-assisted recoupling) such as PAR [235] and PAIN-CP [236], see Fig. 5.13. These more sophisticated experiments are not used within the study however and so will not be discussed here. The basic solid-state analogue to the NOESY experiment involves storing a spin's magnetisation in the z-direction and then allowing MAS to average carbon-carbon, carbon-proton and proton-proton dipolar interactions to the zeroth order, such that the spin evolution during the mixing time is governed by first order terms (for a full mathematical interpretation see [237]). Briefly, the first order dipolar Hamiltonian can be represented by:

$$\overline{\mathscr{H}}_D^{(1)} = \{\frac{-i}{36\omega_r}\sum_{a,k\neq l} d^{(1)}_{k,l,a} I_{az}(S_k^+ S_l^- - S_l^- S_k^+)$$
$$-\frac{-i}{36\omega_r}\sum_{k,a\neq b} d^{(2)}_{k,a,b} S_{kz}(I_a^+ I_b^- - I_a^- I_b^+)$$
$$+\frac{i}{72\omega_r}\sum_{k\neq l\neq m} 2d^{(3)}_{k,l,m} S_{kz}(S_l^+ S_m^- - S_m^- S_l^+)$$
$$+\frac{i}{72\omega_r}\sum_{a\neq b\neq c} 2d^{(4)}_{a,b,c} I_{az}(I_b^+ I_c^- - I_b^- I_c^+)\}$$

where the proton and carbon spins are represented by the operators I and S, respectively. The dipolar coefficients, $d^{(1)}_{k,l,a}$, $d^{(2)}_{k,a,b}$, $d^{(3)}_{k,l,m}$ and $d^{(4)}_{a,b,c}$ have a complex relationship with the I-S, I-I and S-S couplings within the spin system - for more detail see [229, 237]. The consequence of the form of this Hamiltonian can be understood as such: the first and third terms control polarization transfer between two coupled S-spins; while the second and fourth homogenously broadens the zero quantum (ZQ) transition by virtue of coupling the S-spins to the strongly coupled I-spin network. This ZQ transition broadening is crucial for efficient polarisation transfer between carbon spins. The factors determining the broadening are the homonuclear proton-proton and the heteronuclear carbon-proton dipolar couplings and also the MAS frequency. PDSD, see below, is a sequence which functions well at slow spinning speeds, but at higher MAS frequencies the frequency-dependent homogeneous width of the ZQ transition becomes smaller than the chemical shift-generated energy mismatch. This can be overcome by irradiating the protons at the $n = 1$ or 2 rotary resonance (R^3) condition [238] and selectively reintroducing the heteronuclear dipolar spin interaction into the zeroth order average Hamiltonian, but without affecting the polarisation transfer which is controlled by the effectively unchanged first-order Hamiltonian. [229] When the $n = 1$ condition is met, the experiment is referred to as a dipolar-assisted rotational resonance (DARR) experiment, [182] the employment of which will be expanded upon later. With this understanding of spin diffusion, we may now move on to discussing NOESY-like experiments.

5.5.2 Proton-Driven Spin Diffusion: PDSD

In 1982, Szeverenyi and co-workers introduced a solid-state analogue of the NOESY experiment for application to a typical CPMAS experiment. [36] A CP section re-

placed the first ^{1}H 90° pulse at the start of the NOESY sequence, for the benefits previously discussed. Fig. 5.13 shows the pulse sequence for this experiment, and the family of experiments that then followed. t_1 now signifies the evolution period whereby the magnetisation of the dilute spins is allowed to evolve under participating Hamiltonians, notably here the chemical shift interactions. During τ_{m} there is no decoupling on proton spins and this is an opportunity for the ^{13}C-^{13}C spins to communicate. This communication can take the form of chemical exchange, if ^{13}C spins relocate in the sample and experience a different chemical shift environment, or spin diffusion, discussed above; in this manner the major problem of dipolar truncation is overcome in these experiments. This 'Proton-Driven Spin Diffusion' experiment can then provide homonuclear correlation spectra which show increasing distance proximities as τ_{m} increases, from very close resonance pairs to long range proximities. The importance of PDSD cannot be understated as it was used to solve the first 3D structure of a protein in ssNMR. [35] The efficiency of this mechanism is inversely proportional to spinning frequency and therefore suffers when exacted at high magnetic fields >15 Tesla, whereby high MAS frequencies are required to account for the increased CSA.

5.5.3 Dipolar Assisted Rotational Resonance: DARR

Dipolar-Assisted Rotational Resonance (DARR) was first introduced in 2001 by Takegoshi, Nakamura and Terao. [182] It is a homonuclear recoupling mechanism which occurs under MAS. As the name suggests the experiment involves the rotational resonance (R^2) mechanism to broaden transition lineshapes of the carbon spins such that polarisation transfer can occur, however, confusingly, it also utilises the R^3, rotary resonance, phenomenon so as to recouple the ^{13}C-^{1}H dipolar interaction. This recoupling is achieved by continuous wave (cw) irradiation on ^{1}H which satisfies the rotary resonance condition, [238]

$$\nu_1 = n\nu_R \tag{5.14}$$

where ν_1 is the nutation frequency of the rf irradiation, ν_R is the MAS frequency and $n = 1$ or 2, the most efficient of the integer matching conditions. Different integer values recouple different interactions, thus DARR uses $n = 1$ where HORROR uses $n = 1/2$. [204] These recoupling mechanisms will be expanded on later in this section.

When created, the DARR sequence had various advantages over previous sequences; [239–241] as mentioned above, the popular PDSD mechanism is inversely proportional

to spinning frequency and so, as magnetic fields and MAS frequencies increased, a sequence without this drawback was required. That the DARR experiment is better suited to higher MAS frequencies was the main advantage,[6] however the requirement for the recoupling pulse to be set at the nutation frequency equivalent to the MAS frequency is a reason why the DARR experiment is limited in this attribute; as mixing times, τ_m, regularly reach 500 ms, irradiating at e.g. >50 kHz for this length of time could damage the probe. At the time of conception, however, this was still an improvement on the PDSD experiment.

As in NOESY and PDSD, the τ_m used dictates the distance over which carbon spins can communicate, so a spectroscopist can perform a series of DARR experiments varying τ_m, thereby selecting which proximities are seen in the spectra produced. Short τ_m spectra typically contain only intra-residue contacts whereas longer τ_m spectra can contain both intra- and inter-residue contacts; with such spectra, a spectroscopist can begin to assign the sample, see Fig. 5.15.

Fig. 5.15 shows schematic spectra corresponding to a short and long τ_m DARR experiment on two small peptides. Fig. 5.15 (a) and (c) show the spectra obtained by performing a short τ_m DARR experiment on two amino acids (both alanines) and three amino acids (two alanines and a valine) respectively, (b) and (d) show the spectra obtained by performing a longer τ_m DARR experiment on the same systems. It is possible to see a fuller set of correlations in the longer τ_m experiment whereas the short τ_m spectrum only has a smaller set, for the reason discussed above (as a note, in (b), for 1Cβ - 2Cβ contacts a very long τ_m would be required, however such contacts can be found). Dashed circles (d) indicate lack of contacts between nuclei, dashed lines are used to illustrate chemical shifts of certain nuclei and solid lines are used to illustrate a sequential walk through the contacts between residues. Although Fig. 5.15 indicates that transfer is based on the number of connecting bonds or distance, in reality polarisation transfer is extremely complex and depends on many factors such as the dipolar interaction, the CSA and also the orientation of the dipolar and CSA tensors within the sample; for a detailed theoretical approach to the spin diffusion process, see [242].

The assignment process begins by assigning individual residues using a less-cluttered, short τ_m spectrum in which it is possible to see the characteristic patterns for different amino acids, see Fig. 6 in [243], before identifying the Cα-Cα connections in a longer τ_m spectrum so as to assign neighbouring residues. In biological ssNMR

[6] the authors in [182] mention that the DARR experiment is well suited to MAS frequencies of up to 30 kHz

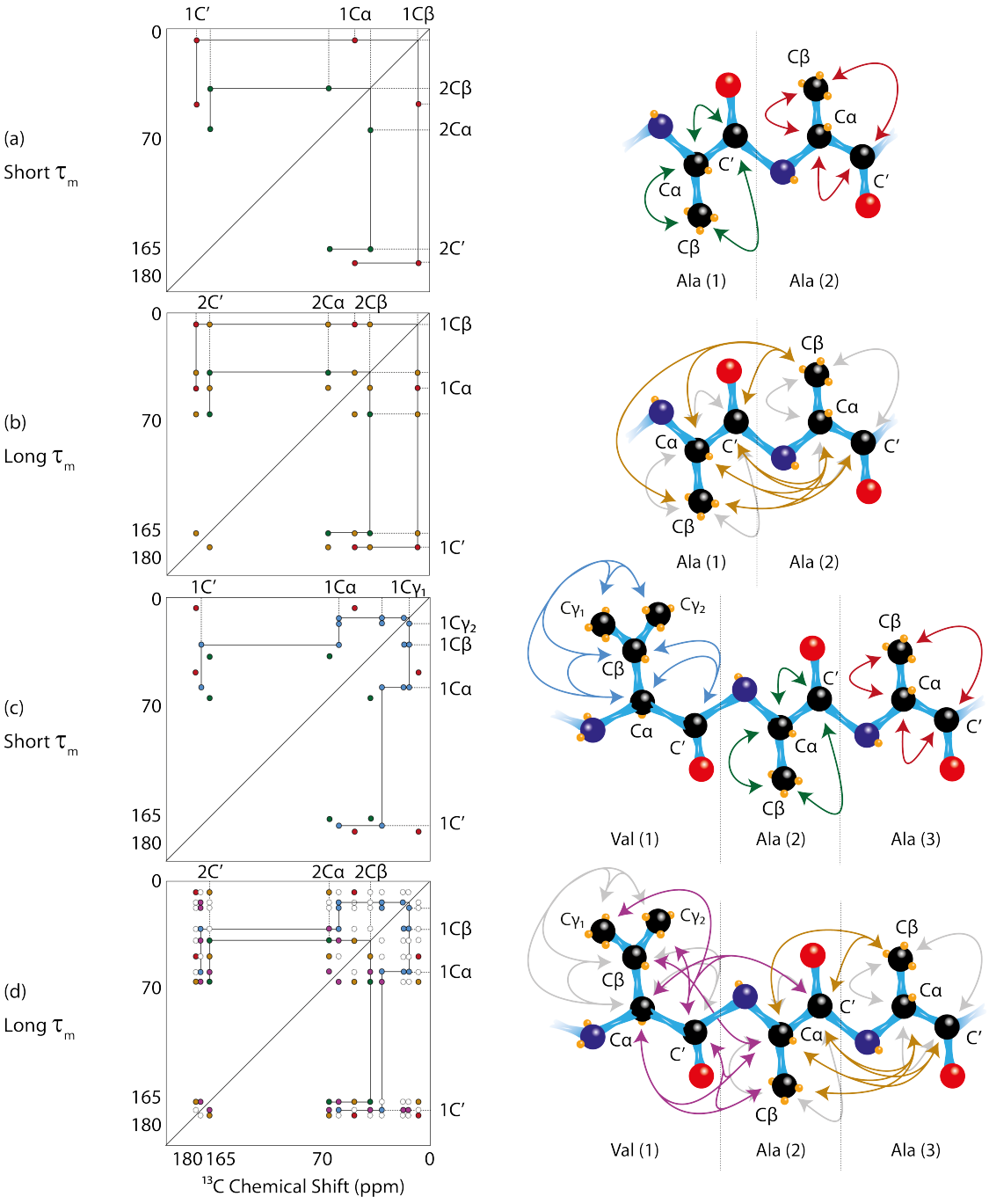

Figure 5.15: Schematic short and long τ_m DARR spectra for two- and three-amino acid systems. In (a) and (b) residues 1 and 2 represent alanine residues, in (c) and (d) residue 1 represents a valine residue and residues 2 and 3 represent alanine residues. Arrows indicate permitted coherence transfers between nuclei; the arrow colour helps to identify contacts in the spectra. Grey arrows represent previous, but still present, transfers, so as to emphasize the 'newer' longer-range transfers.

studies, the amino acid sequence of the sample is already known, which facilitates assignment as the spectroscopist knows how many of which residues to expect and to what each residue is connected. In this way many carbons can be assigned from the sample, however for a more complete assignment (including ^{15}N and ^{1}H chemical shifts) other experiments, such as those described in § 5.1.2 and § 5.2, are required. Further ^{13}C assignment can be required due to reasons such as spectral crowding; if a sample has 5 valines for example [7] carbon resonances will exist in similar locations, due to the similarity of their magnetic environments, such that resolving them is troublesome. This is why a suite of experiments is required for detailed chemical shift assignment.

5.6 Dipolar Recoupling

Initial work in this area focussed on the recoupling of dipolar interactions between isolated (via selective labelling) heteronuclear spin pairs. However as ssNMR has grown, it has become more important to extract significant amounts of data, both homo and heteronuclear, using a single fully labelled protein sample, whereby there are many competing interactions attempting to truncate weaker, long-range interactions. These long-range proximities are the key to extracting long-range distance constraints which are crucial in modelling the tertiary and even quaternary structure of biological samples. Sequences in § 5.1 and § 5.5 included recoupling sequences which, so far, have been left unexplained. This section will elucidate recoupling mechanisms such as R^2, R^3, RFDR and HORROR.

Rotational resonance (R^2) is one of the most common frequency-selective recoupling methods, and provides a simple introduction to this type of method. Initially discovered by Andrew and co-workers in 1966, its use for structural measurements was only realised many years later by the Griffin group. [43, 244, 245] R^2 recoupling can be achieved by matching the chemical shift difference of two homonuclear spins to a small multiple (1 or 2) of the spinning frequency. Clearly this relies on the isotropic chemical shift difference of the two spins in question being well suited to this technique (as MAS frequencies are not unlimited). It was soon discovered that carbonyl and aliphatic side chain ^{13}C spins were suited to this technique, and could be matched at moderate spinning frequencies. Under an exact matching R^2 condition, the $|\alpha\beta\rangle$ and $|\beta\alpha\rangle$ energy levels of the two spins become degenerate, and the transitions generated

[7] Such as Aβ, at positions 12, 18, 24, 39 and 40

by the zero-quantum dipolar Hamiltonian become exactly energy conserving. [229] Even near the matched condition, polarisation transfer can still occur provided that the mismatch is smaller than the effective dipolar coupling strength. Many articles provide detailed descriptions of the mechanics of R^2 involving average Hamiltonian theory, see e.g. [246–248].

Rotary resonance recoupling (R^3) is a heteronuclear dipolar recoupling sequence for use with MAS introduced in 1988 by Levitt and co-workers, [238] whereby one can selectively reintroduce the dipolar coupling between two spins. If there are two dilute, heteronuclear spins, I and S, and the signal on S is observed while irradiating at the Larmor frequency of the I spin, if the frequency of the irradiation field is such to elicit rotary resonance, i.e. eqn. 5.14, a recoupling effect is observed. In the original experiment, this took the form of broadening previously sharp ^{31}P centreband and spinning sidebands into lineshapes resembling the Pake powder pattern. The splittings observed were then used to measure the ^{31}P-^{15}N dipolar interaction, and therefore reveal the internuclear distance. Both R^2 and R^3 are incorporated into the DARR experiment in § 5.5.

In the following two years, rotational-echo double-resonance (REDOR) NMR and dipolar recoupling at the magic angle (DRAMA) were developed. [24, 26] REDOR is a heteronuclear recoupling sequence which was initially used to recouple ^{13}C-^{15}N interactions. The dephasing of ^{13}C echoes due to ^{15}N π pulses, compared to the ^{13}C signal without the pulses, can be used to measure the ^{13}C-^{15}N coupling. This technique is still very popular today, although it is not used in this study. DRAMA was the first broadband homonuclear dipolar recoupling sequence, and though it has mostly been superseded by other sequences it is deserving of mention in a brief history of recoupling.

DRAMA led the way for the more popular homonuclear sequences such as radio frequency-driven dipolar (RFDR) recoupling, developed by the Griffin group in 1992, [249] and homonuclear rotary resonance (HORROR), developed by Levitt and co-workers in 1994. [204] RFDR utilises a series of rotor-synchronised π pulses during a longitudinal mixing period on the S spins to act as a compensated echo sequence while simultaneously decoupling on the I spins; through this mechanism it is possible to reintroduce the flip-flop part of the dipolar coupling. The result is a time-independent interaction which causes magnetisation transfer between coupled homonuclear spins. It is important that the RDFR π pulses do not match the frequency of the proton decoupling, else rapid depolarisation of the carbon signal occurs. HORROR was developed with the intention of use on large biomolecules as previously developed se-

quences, R^2, R^3, DRAMA and REDOR did not have efficient double quantum filtering (2QF). One advantage of a 2QF experiment is greater discrimination to distinguish between the signals obtained in experiments from the desired, intentionally-labelled ^{13}C and those from randomly distributed, natural ^{13}C. The developers of HORROR claimed that by first exciting double-quantum coherence, a correlation between the polarisations of neighbouring spins, and then reconverting it back into observable signal these signals could be distinguished. With a 2QF efficiency of 27% for DRAMA and 25% for R^2, HORROR seemed like a front runner (efficiency of 60%), however it had two drawbacks; a dependence on the rf field and chemical shift. [204] The rf field dependence is not serious for spins in close proximities, and the chemical shift dependence can be minimized by rapid MAS frequencies (hence the use of this sequence at 100 kHz MAS), however the sequence performs very poorly over a wide chemical shift range and is therefore classified as a 'narrowband' recoupling sequence. Both these techniques are used in the pulse sequences in § 5.2.

6

Experimental & Computational Methods

6.1 NMR Data Acquisition

This chapter contains experimental and computational details for the work performed in obtaining and processing high-resolution solid-state NMR data presented in this thesis. Included in this chapter are details on spectrometers, probe and rotor type, pulse sequences and temperatures used alongside the software employed post-acquisition.

6.1.1 Spectrometers

Experiments were performed on Bruker spectrometers with ^{1}H Larmor frequencies of 850.2 MHz (^{13}C Larmor frequency 213.7 MHz), the Avance III, and 600.1 MHz (^{13}C Larmor frequency 150.8 MHz), the Avance II+, using TopSpin 2.1 as the interface for acquisition. A Chemagnetic InfinityPlus spectrometer with ^{1}H Larmor frequency of 359.2 MHz (^{31}P Larmor frequency 145.4 MHz) was used for ^{31}P NMR experiments using SpinSight for acquisition.

6.1.2 Probes and Rotors

2.5 mm HX and HXY, 1.3 mm HXY, 1.0 mm HX and 0.8 mm HX probes were used in either ^{1}H-^{13}C or ^{1}H-^{15}N double resonance (DR) modes, or ^{1}H-^{13}C-^{15}N or ^{1}H-^{1}H-^{15}N triple resonance (TR) mode, although the set up used will be stated explicitly for each experiment. The range of rotor sizes (all made of ZrO_2 with vespel top

and bottom caps) used corresponds to the range of MAS frequencies available: most experiments are performed in 2.5 mm rotors with MAS frequencies of 7.0 to 15 kHz; some experiments are performed in 1.3 mm rotors with MAS frequencies of up to 62 kHz; some experiments are performed in 1.0 mm rotors with MAS frequencies of up to 80 kHz; and, finally, some are performed in 0.8 mm rotors with MAS frequencies of up to 100 kHz. This range of MAS frequencies directly affects the experiments one can perform; the lower frequencies are suited to DARR and DCP experiments and the higher frequencies are suited to experiments such as inverse detection, and the decoupling/recoupling sequences included therein (see § 5.4). A 10 mm PFG NMR probe was used for experiments investigating ^{31}P.

6.1.3 Pulse Sequence Details

^{1}H decoupling in DARR experiments in this study was performed using the SPINAL64 technique with 6 or 5 μs pulses at a ^{1}H nutation frequency at $\nu_1(^{1}H)$ of either 83 or 100 kHz depending on the concentration of salt within the sample. Proton and carbon nutation frequencies of 100 kHz and 50 kHz are used for π pulses. Short mixing experiments have τ_m of 20-50 ms and long mixing experiments have τ_m of 200-500 ms.

^{1}H decoupling in DCP experiments in this study was performed using the SPINAL64 technique as described above during acquisition periods, with CWLG decoupling during ^{15}N-^{13}C CP applied on ^{1}H, with a nutation frequency at $\nu_1(^{1}H)$ of 83 kHz. [250] Proton, carbon and nitrogen nutation frequencies of 100, 50 and 50 kHz are used for π pulses.

Inverse Detection experiments use slpTPPM, RFDR, WALTZ-16 and HORROR sequences: using slpTPPM with 20 μs pulses of 15 kHz; RFDR with 5 μs pulses of 100 kHz; WALTZ-16 with 16 μs pulses of 10 kHz; and HORROR with 40 μs pulses of 30 kHz (exciting DQ transitions). Proton, carbon and nitrogen nutation frequencies of either 100 or 83 kHz are used for π pulses.

^{31}P one pulse experiments were performed with 30 μs pulses at a ^{31}P nutation frequency of 8.3 kHz.

6.1.4 Referencing

Often carbon referencing is made to tetramethylsilane (TMS) which contains four carbons in equivalent magnetic environments, or TSP which is favoured by certain groups. Nitrogen referencing is often made to liquid ammonia however other references used are nitromethane, urea, NH_4Cl and NH_4NO_3. [251] Though the differences in most of the common ^1H references (DSS, TSP and TMS) are trivially small the variations in carbon and nitrogen standards can be substantial; under the conditions shown in eqn. 6 of [252], there is a 2.01 ppm difference between a carbon signal referenced to TMS compared to DSS. Moreover in [251] it is claimed that a dioxane signal can be found at 66.6 ppm (when measured with respect to external DSS), at 67.5 ppm (with respect to internal TMS) or at 69.4 ppm (when measured against internal TSP). Detailed conversion tables for most standards can be found in [253, 254]: if a TSP referenced signal is located at 0.00 ppm, then a DSS referenced signal would exist at 0.15 ppm and a TMS signal at 2.81, although factors such as pH, temperature and solvent are responsible for minor variations around these figures.

For the work presented here referencing has been taken from an alanine C′ resonance of 177.8 ppm, unless otherwise stated. [252,253] Other methods include use of histidine ^{13}C and ^{15}N resonances and internal reference to DSS, by setting the DSS ^1H peak to 0 ppm, though alanine and DSS referencing is more prominent throughout this study.

Chemical shifts of nuclei in amino acids in a protein can vary due to the secondary structure, for example the Cα resonances will have higher chemical shifts in regions of α-helix and lower chemical shifts in regions of β-sheet, whereas Cβ resonances have the opposite dependence. Deviations from this typical behaviour can occur due to e.g. the presence of additional local fields from aromatic rings or charged neighbours. [255] The 'random coil' chemical shift value has been defined as the chemical shift of an amino acid residue within a peptide which is free to access all sterically allowed regions of its conformational space. [251] Often this value is taken as the average value of all the carbon entries for that residue in the BMRB, and it is to this value that the terms 'higher...' and 'lower chemical shifts' apply. [256, 257] In this manner an estimate for the secondary structure of the sample can be made using the chemical shift values obtained and the sequence of the protein.

For referencing in certain samples, measures of an aqueous solution of 5% DSS were added. The proton DSS peak could then be set to zero and using relations from [253] and [252], the carbon and nitrogen chemical shift references could be found. The

water proton peak shifts by virtue of the temperature and the chemical shift of this peak when compared to the DSS peak, which was always set to zero, can be used to obtain the temperature within the sample.

6.1.5 Temperature

Due to the biological nature of the samples in this study, the temperature at which the samples are studied is important. Many experiments in this study use a BCU-Xtreme with flow rates of 670 - 800 l/h to maintain a steady temperature of ∼2 °C. This flow rate ensures that, during decoupling, which can significantly heat a hydrated sample, the temperature does not exceed that which might result in denaturing the samples. The gas source used is N_2 so as to avoid any chance of icing within the BCU.

6.2 NMR Data Analysis

6.2.1 CCPN

The Combined Computing Project for NMR, known as CCPNmr, CcpNmr or just CCPN, is a series of programs for macromolecular NMR spectroscopy. [258] The modules CcpNmr Analysis, ChemBuild, Format Converter, SpecView, Data Model alongside web based applications constitute this rapidly developing open-source tool. This thesis work utilised the interactive NMR assignment and project management program CcpNmr Analysis. Format Converter allows data from sources such as TopSpin to be imported into and exported out of the CCPN framework. It can also read/write/edit NMR acquisition and processing parameters. SpecView allows rapid visualisation of 1D, 2D or 3D NMR spectra and peak data from many different input file formats. In this thesis work, the Analysis and Format Converter are most regularly used from the CCPN suite. In the Analysis window, several 2D spectra can be displayed, contour levels can be adjusted and peaks can be assigned. The amino acid sequence of the sample can be input and CCPN will make intelligent suggestions for unassigned peaks based on both the sequence and the current assignments, moreover any assignment made in an unusual location (e.g. if a user attempted to assign a glycine Cα at 60 ppm whereby a far more typical chemical shift value is ∼45 ppm) is queried by the software providing a level of security when assigning.

6.2.2 SPARKY

SPARKY is an NMR assignment and integration program for use on proteins, nucleic acids, and other polymers. [259] Bruker output files can be used in SPARKY alongside, NMRPipe, Felix and Varian VNMR data, though these generally need to be converted which can be done using the command line and a few simple instructions. In this analysis work, SPARKY is used for processing and analysis of 2D and 3D spectra. SPARKY features include: adjusting contour levels; visualisation of several spectra at once with mouse controlled axes appearing at equivalent locations on all spectra to aid assignment; automated and manually controlled peak picking; output of peak file with intensities and S/N; extraction of strip plots from 3D spectra; intelligent assignment software able to suggest assignments based on previous assignments.

6.2.3 TALOS-N

TALOS-N is a software package for the prediction of protein backbone and sidechain torsion angles from NMR chemical shifts. [170] The program's previous iterations TALOS (Torsion Angle Likelihood Obtained from Shifts and sequence similarity) and TALOS+ worked on the basis that secondary chemical shifts (the difference between the chemical shift value for a specific nucleus and its random coil value as mentioned in § 6.1.4) are highly correlated with aspects of protein secondary structure. Briefly, TALOS-N uses secondary chemical shift alongside sequence information to derive predictions for the backbone angles ϕ and ψ and sidechain angles χ^1 with a measure of the uncertainties in each of these predictions, and also the secondary structure.

It has been shown that secondary chemical shifts for Cα and Cβ of a given residue correlate closely with its ϕ and ψ torsion angles, which therefore permits TALOS to perform this analysis. [260–262] When given an input file of the amino acid sequence and chemical shifts for nuclei within the residues, TALOS will analyse the sequence in triplets and searches a database for triplets of adjacent residues with chemical shifts and a sequence similar to those input, to attempt to find a best match to the current triplet of interest. The database contains backbone torsion angles of proteins solved using crystal structures to a resolution of $\leq$2.2 Å, and which also have nearly complete resonance assignments. TALOS will then select the 10 triplets with the closest matches to the input sequence for each triplet in the query sequence. If the 10 triplets exhibit similar ϕ and ψ backbone angles, their averages can be used

as angular restraints for the sequence under investigation. The paper introducing TALOS showed a root-mean-squared deviation of the TALOS output angles and X-ray derived backbones angles as $\sim$15°, and that only 3% of predictions from TALOS are found to be erroneous. [263]

The TALOS database contained 20 proteins with over 3,000 residues, but when TALOS+ was released 10 years later, the database used contained 200 proteins and had improved the backbone angle prediction fraction from 65 to 74%, simultaneously reducing the error from 3 to 2.5%. The accuracy of the angles predicted also increased, ignoring the 2.5% of residues for which TALOS+ made erroneous predictions, as the error in angle dropped to $\pm$13°. TALOS+ contains a two-layer neural network filter to the database fragment selection process, which is found to increase the overall prediction rate to 88.5%. [264]

TALOS-N then provided a prediction rate of $\geq$90% with an error of less than $\sim$3.5% and an error in angle of $\pm$12°, alongside the prediction of sidechain χ^1 angles for around 50% of residues with a consistency to reference structures of 89%. The criteria for a valid prediction were also tightened by nearly two-fold for TALOS-N, and yet it reports the same fraction of residues as TALOS+, without increasing the error rate. Where TALOS-N cannot produce a reliable prediction, it will produce a 'generous' prediction, which match reference backbone angles for $\sim$77% of predictions.

A more simplistic web-based version of the TALOS-N program exists whereby inputting sequence and chemical shift data, in the form exported by NMRPipe, [265] can produce the data mentioned above.

6.3 Samples

Samples of Aβ_{1-40} are provided by collaborators in Umeå University and selectively labelled Aβ_{1-42} peptides are synthesised using solid-phase synthesis at Luleå University of Technology with fully labelled Aβ_{1-42} peptides being provided by collaborators in Uppsala. Further details are offered in § 7 and 8, which show and discuss the work performed on these systems.

7

Solid-State NMR Analysis of Amyloid-β_{1-40} Aggregates Formed in the Presence of Copper Ions

This chapter contains the results from the work performed on U-[^{13}C, ^{15}N] A$\beta_{1\text{-}40}$ aggregates which were formed in the presence of copper. 2D ^{13}C-^{13}C DARR spectra with a variety of mixing times illustrate short and long distance connectivities and proximities within the sample, and enable ^{13}C chemical shift values to be determined. 2D ^{15}N-^{13}C DCP spectra allow chemical shift values for ^{15}N to be obtained. Multidimensional inverse detection spectra are also shown, and allow ^{1}H and additional ^{15}N chemical shift values to be obtained. TALOS-N provides torsion angle predictions and secondary chemical shift analysis is performed, with the secondary structure being compared to previously published models for Aβ fibrils.

7.1 Introduction

Structural studies of amyloid fibrils are currently of significant scientific interest due to their involvement in amyloidogenic diseases such as Alzheimer's disease and Parkinson's disease. During Alzheimer's disease, Aβ begins to misfold and aggregate into plaques within which higher concentrations of endogenous metals can be found. [49, 102] The presence of metals has already been shown to alter the structure of amyloid fibrils, [55] notably for Cu^{2+} when introduced after fibril formation in previous studies. [102] In this work, aggregates have formed in the presence of Cu^{2+} ions and solid-state NMR and electron microscopy (EM) is used to investigate the resulting structure.

As plaques in the brain contain higher concentrations of metals, and these metals have

been shown to alter the structure of $A\beta_{1-40}$ it seems logical that a ssNMR structural study of plaques, which are formed in the presence of metals, is performed, however so far one has yet to be published; although a study has been performed investigating the effect of copper on fibril structure after formation has taken place, [102] providing an interesting comparison for this work.

7.2 Experimental Details

7.2.1 Sample Preparation

Recombinant $A\beta_{1-40}$-[U-^{13}C, ^{15}N] was prepared, using standard minimum U-[^{13}C,^{15}N] media growth and purification protocols [266] and then lyophilized from an ammonium acetate buffer, by Anders Olofsson in Umeå University. The peptide was dissolved in an aqueous solution at a high pH to obtain a purely monomeric form of the peptide, as described in [266]. The pH was adjusted to 7.0 and NaCl was added at a physiological concentration of 150 mM. A solution of $CuCl_2$ was added to this sample of the peptide and the pH was adjusted again to 7.0. The peptide concentration was 50 μM, with a two-fold molar excess of $CuCl_2$. After the Cu^{2+} had been added to $A\beta_{1-40}$-[U-^{13}C,^{15}N], the peptide precipitated instantly. These $A\beta_{1-40}$/Cu aggregates appear completely stable in aqueous suspensions; the sample has not yet degraded over 50 months.

The sample was packed into a Bruker 2.5 mm rotor and NMR experiments were performed. The sample was then allowed to hydrate in an aqueous environment for a few days with the cap removed (see Fig. 7.1) before further NMR experiments were performed. After nearly two years, the sample was partly transferred into a 0.8 mm Samoson rotor to enable high frequency MAS experiments to be performed (unlocking MAS frequencies up to 100 kHz); the sample appeared to dry out during this process, therefore both 2.5 mm and 0.8 mm rotors were placed into a hydrated environment so as to ensure that a similar level of hydration, to that previously obtained, was achieved.

7.2.2 Solid-State NMR Measurements

2D ^{13}C-^{13}C DARR, ^{15}N-^{13}C DCP and ^{1}H-^{13}C, ^{1}H-^{15}N, ^{1}H-^{13}C-^{15}N and ^{1}H-^{1}H-^{15}N inverse detection experiments were performed on a Bruker Avance II+ wide-bore

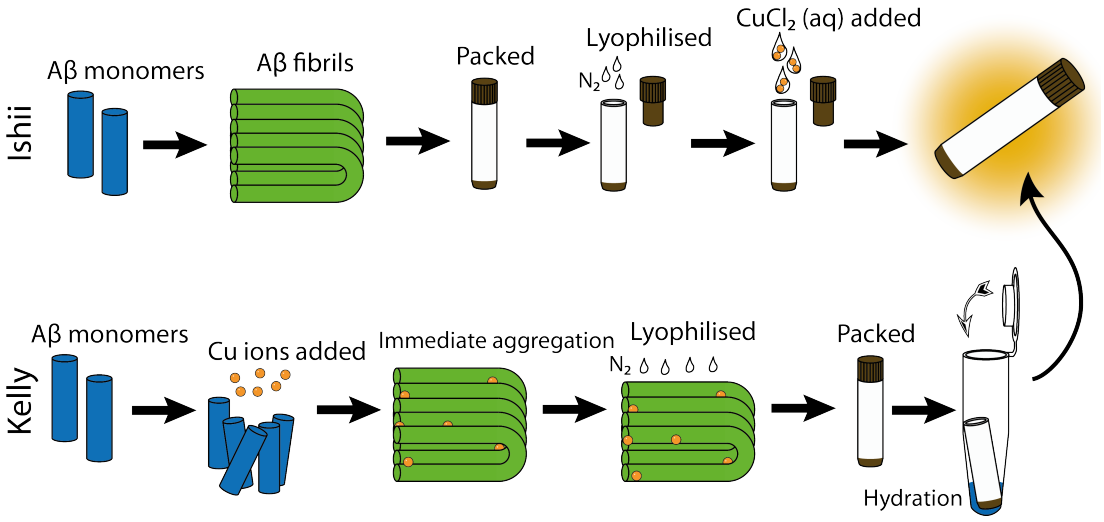

Figure 7.1: Sample preparation pathways for sample studied by the Ishii group [102] and sample studied in this thesis. These differences result in different polymorphs being created; the one in this study could well be more physiologically relevant due to the introduction of copper ions before aggregation.

spectrometer (600 MHz ^{1}H Larmor frequency and 150.8 MHz ^{13}C Larmor frequency) and a Bruker Avance III wide-bore spectrometer (850 MHz ^{1}H Larmor frequency and 213.7 MHz ^{13}C Larmor frequency). A 2.5 mm DVT MAS probe head in double- and triple-resonance modes was used for DARR and DCP experiments, respectively. The MAS frequency for these experiments was 10.0 kHz unless otherwise stated. In DARR experiments, mixing times of 20 (short mixing) to 200 ms (long mixing) were used with cw ^{1}H irradiation at a nutation frequency of 10.0 kHz. SPINAL64 ^{1}H decoupling at a nutation frequency of 83.3 kHz was used during t_1 and t_2 acquisition. An 80-100% ramp was applied on the ^{1}H channel during cross polarisation, and contact time of this pulse was 1000 µs. A 0.8 mm Samoson MAS probe head in double- and triple-resonance mode was used for inverse detection experiments. MAS frequencies of ∼100 kHz were used. Low power WALTZ-16 decoupling at a nutation frequency of 25 kHz was applied on ^{13}C and ^{15}N during ^{1}H acquisition. Experiments were performed at a sample temperature of 2℃, target temperature −8℃, maintained by a dry, cold air flow of 600 l/h generated by a Bruker Cooling Unit Xtreme.

7.2.3 Electron Microscopy

Negatively stained aggregates were prepared by re-suspending 0.5 mg of Aβ_{1-40}/Cu aggregates in 100 µl of deionised water. Copper grids were activated with UV light for

1 minute and 2.5 µl of re-suspended sample was then added to the copper grids. After adsorption for 30 seconds, the grids were blotted off, and then counter-stained twice with 2 wt% uranyl acetate aqueous solution. Grids were blotted after 30 seconds and left to dry in air. Electron microscopy was performed on a JEOL 2010F TEM 200 kV Field Emission Gun fitted with a Gatan UltraScan 4000 camera.

7.3 Results

7.3.1 Effect of Hydration

Samples of U-[^{13}C,^{15}N] Aβ_{1-40}/Cu aggregates were prepared and hydrated as described above and TEM images were taken of both dry and hydrated aggregates, see Fig. 7.2. TEM images of the dry aggregates reveal very short aggregates, possibly protofibrils or some related building block of the larger final-state aggregates, which are likely to be attracted to one another shown by the inhomogenous distribution of aggregates throughout the image. By comparison, TEM images of the hydrated aggregates reveal a homogeneous sample consisting of large networks of aggregated material in the hydrated state. When compared to previous TEM images of Aβ fibrils, [63, 64, 93, 102] there is a considerable amount of disorder in the alignment of these aggregates, which is likely to be due to the speed at which the aggregates precipitated from the peptide solution upon introduction of the Cu ions.[1] It is clear from the TEM images in Fig. 7.2 that hydration has increased both the length of aggregate strands, which can only be caused by encouraging further aggregation, and the overall homogeneity of the sample. It is difficult to state whether the aggregates are striated ribbon or twisted pair, it is more likely that the sample contains both types of structure.

The sample had over two years to re-order into the current hydrated form, and this gradual re-ordering to a less energetic, more homogeneous and fibril-like form would explain the increase in resolution with time as shown by the 1D NMR spectra in Fig. 7.3. The ^{13}C aliphatic region has been selected to demonstrate the increase in resolution as it is more dramatic than within the cluttered carbonyl region. Various studies have shown an amyloidogenic re-ordering with time similar to the one shown here, albeit without the effect of a paramagnetic ion within the sample. [267] Notable regions of resolution increase include: the two peaks with lowest chemical shift values,

[1] As mentioned in § 7.2.1 the aggregates precipitated from the solution instantaneously with the introduction of the Cu^{2+} ions

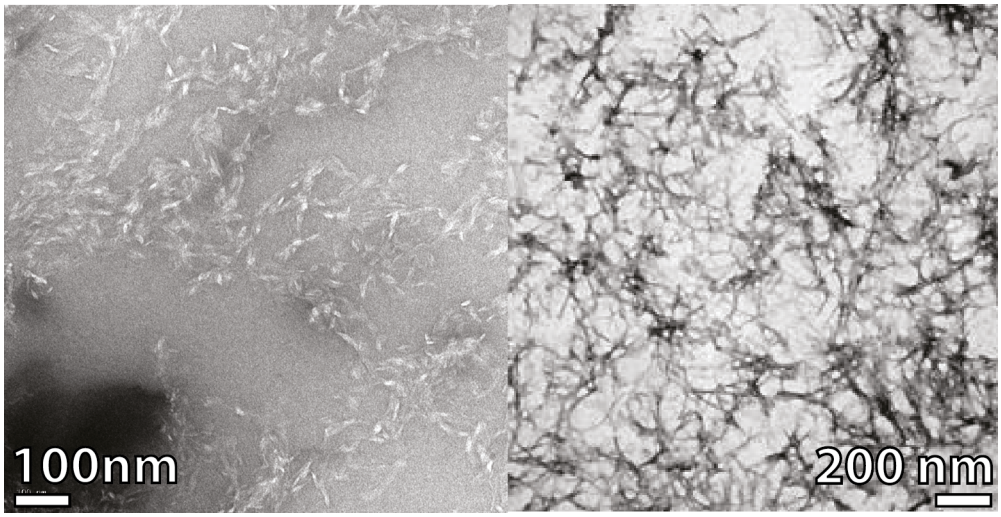

Figure 7.2: Electron microscopy images of, left, dry (lyophilised) and, right, hydrated aggregates. Hydration causes aggregates to become longer and more mesh-like where previously aggregates are short and not in networks of aggregates.

which, in Fig. 7.3 a), appear as one peak and one shoulder to a more intense peak but which slowly become more well defined as time passes and are clearly two separate peaks in Fig. 7.3 f); and the block of signals in the 55 ppm region which only really begin to show some resolution in the most recent CP spectrum obtained using the 0.8 mm probe. Alongside the overall improvement in resolution which has occured over time, the two left most peaks in Fig. 7.3 a) which are well defined and unlike most of the remaining spectrum in (a), seem to disappear over time (for the peak at the higher chemical shift value) or be replaced with a slightly shifted peak which is less defined (for the peak at the lower chemical shift value). The residues containing carbons at the highest chemical shifts are later found to be the serine residues at positions 8 and 26, and both these Cβ chemical shift values are assigned, which then asks the question as to what the peak was that seems to disappears. This might imply that the sample contained serine residues which initially were in two environments, suggesting, therefore, that the sample contaied two polymorphs. If this were the case, that the leftmost peak is much less intense implies that the other of the two forms was favoured during aggregation and when the sample was hydrated this less-favourable form was lost in the re-ordering to a less energetic state.

^{13}C DARR spectra recorded at 850 MHz lend support to the above claims that hydration has led to a more homogeneous sample. Fig. 7.4 compares identical experiments taken before and after hydration. There is a noticeable increase in the resolution

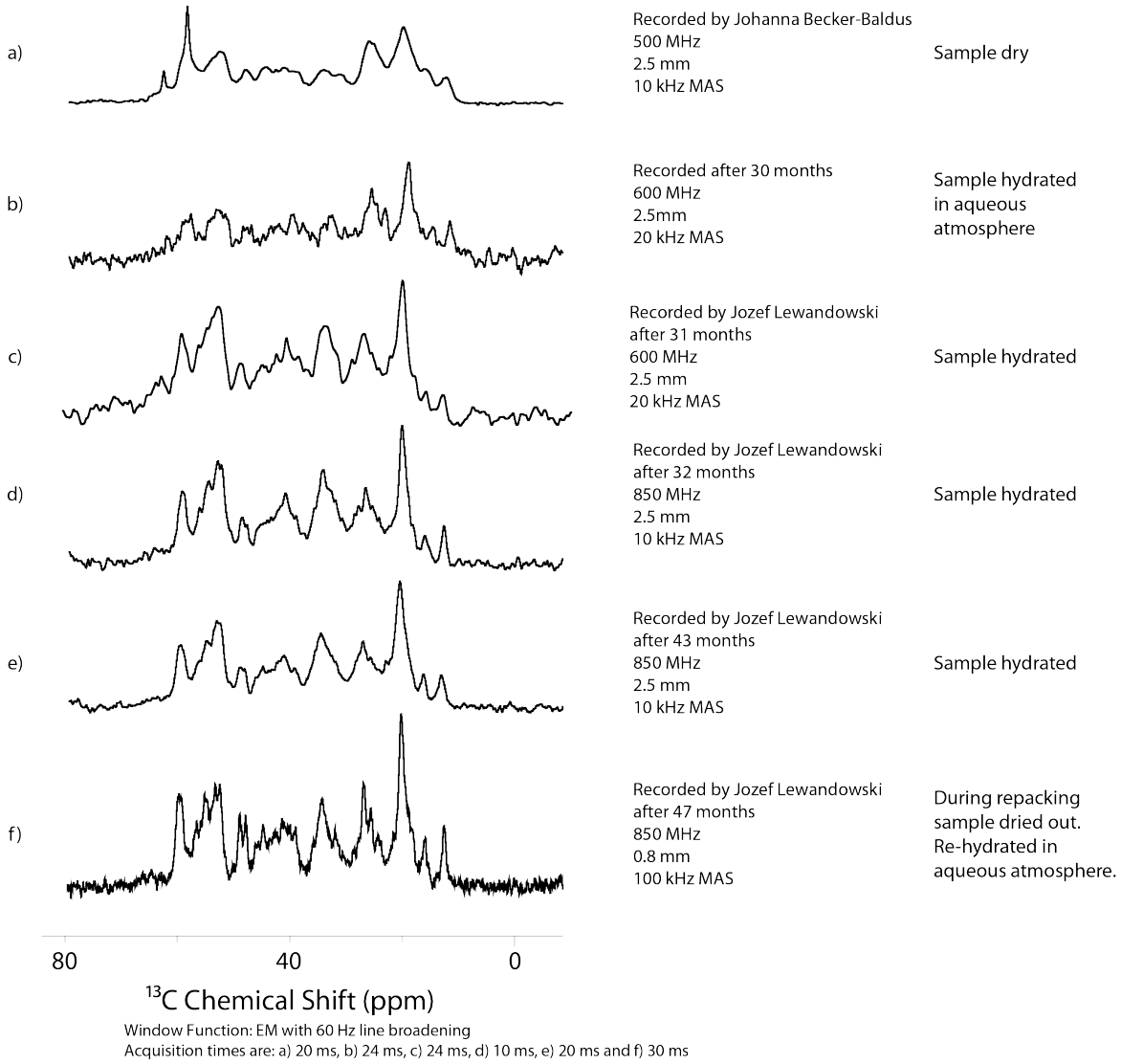

Figure 7.3: Comparison of ^{1}H-^{13}C CPMAS spectra taken on Aβ_{1-40}/Cu aggregates over time. Spectra were recorded with 128 (a), 8 (b, c, d), 16 (e) and 1024 (f) co-added transients. The sample has been packed into two different rotor sizes as stated in the figure. Sample was hydrated as in Fig. 7.1 when mentioned on the figure.

of the spectrum when the sample has been hydrated; two areas which particularly emphasize this have been enlarged and overlaid, with the thick dashed line in the comparison panels indicating the hydrated sample and the thin unbroken line indicating the dry sample. Both regions have improved from an unresolved region of signal into several distinct peaks which enable assignment, this improvement can be noticed throughout the aliphatic regions. Moreover the serine peaks (lower left zone of aliphatic region), which were previously non-existent, are very clear after hydra-

tion. A similar statement can be made for the two isoleucine residues, at locations 31 and 32, which can be seen at the characteristically low chemical shift values (<22 ppm) of the two Cδ_1. Although certain regions remain cluttered, e.g. typical valine chemical shift regions (∼20, ∼35 and ∼60 ppm), due to the existence of 6 valines in the Aβ sequence, there is much greater definition in these areas post-hydration.

7.3.2 Effect of Field

To investigate the effect of field on the resolution of ssNMR spectra, the hydrated sample had two identical 20 ms mixing DARR experiments performed on it, one at a ^{1}H Larmor frequency of 600 MHz and one at a ^{1}H Larmor frequency of 850 MHz. The comparison of the spectra in Fig. 7.5 clearly shows a significant improvement in resolution. The overlain sections in particular highlight regions of improved resolution, with many regions improving from extended wide areas of un-assignable signal to assignable peaks, e.g. in the first comparison box, two individual, almost completely resolved peaks appear from a previously broad single signal. The second comparison box reveals a possible four peaks from a previously unassignable region. Alongside these, many other regions have become more resolved as can be seen in Fig. 7.5. Moreover, signals that were already resolved at 600 MHz are sharper in the 850 MHz spectrum. More specifically, the linewidth for the peak corresponding to the I31Cβ-Cδ_1 connectivity (39.9 ppm, 13.7 ppm) improves from 220 Hz to 190 Hz, while the linewidth for the peak corresponding to the connectivity for S26Cβ-Cα (65.2 ppm, 55.9 ppm) improves from 170 Hz to 140 Hz showing that there is an increase in the resolution of the spectrum across the entire aliphatic region. The L17Cβ-Cδ_2 (46.1 ppm, 25.5 ppm) and L17Cγ-Cβ (28.6 ppm, 46.1 ppm) peaks become resolved allowing the full assignment of residue L17, and also the K16Cδ-Cϵ (29.3 ppm, 41.9 ppm) peak becomes resolved from surrounding signals. Once again, the densely packed valine region has not improved to the point that 6 individual resonances can be found, but, through the combination of hydrating the sample and the use of the higher magnetic fields, some valine assignments can be made. Nonetheless, these spectra indicate the significant level of improvement available through increasing the magnetic field used in experiments from 14.1 T to 20.0 T.

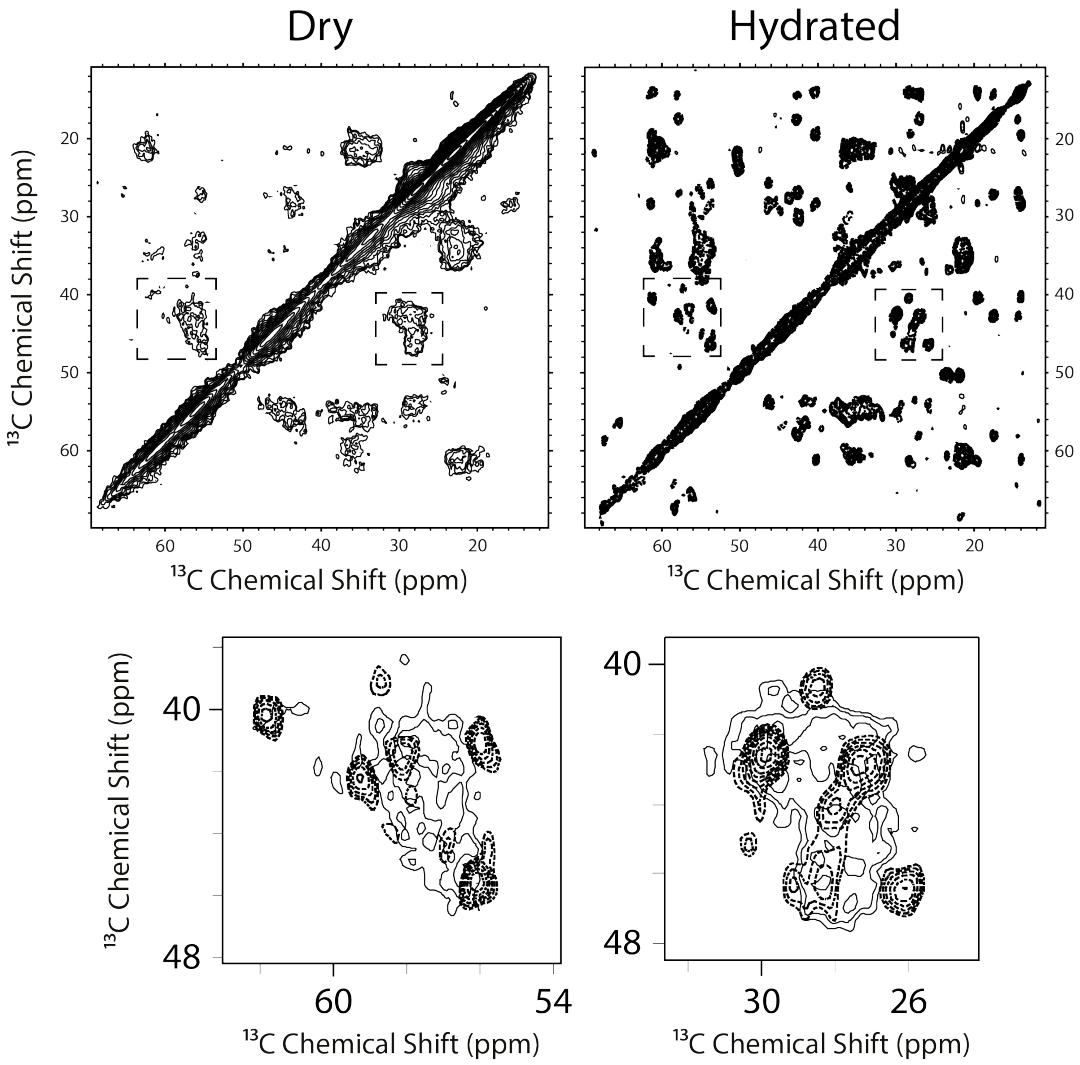

Figure 7.4: Comparison of ^{13}C spectra recorded using the DARR experiment with a mixing time of 20 ms at a ^{1}H Larmor frequency of 850 MHz and a MAS frequency of 10 kHz of U-[^{13}C,^{15}N] Aβ_{1-40}/Cu aggregates before and after hydration. Regions of particularly increased resolution have been highlighted and overlaid. Unbroken lines are from the before hydration spectra, dashed lines are from the after hydration spectra. 72 (dry) and 64 (hydrated) transients were co-added for each 546 (dry) and 640 (hydrated) t_1 FIDs, with a recycle delays of 1.5 s (dry) and 1.6 s (hydrated), corresponding to experimental times of ∼16.5 hours (dry) and ∼18 hours (hydrated). Base contours for both spectra are 3%.

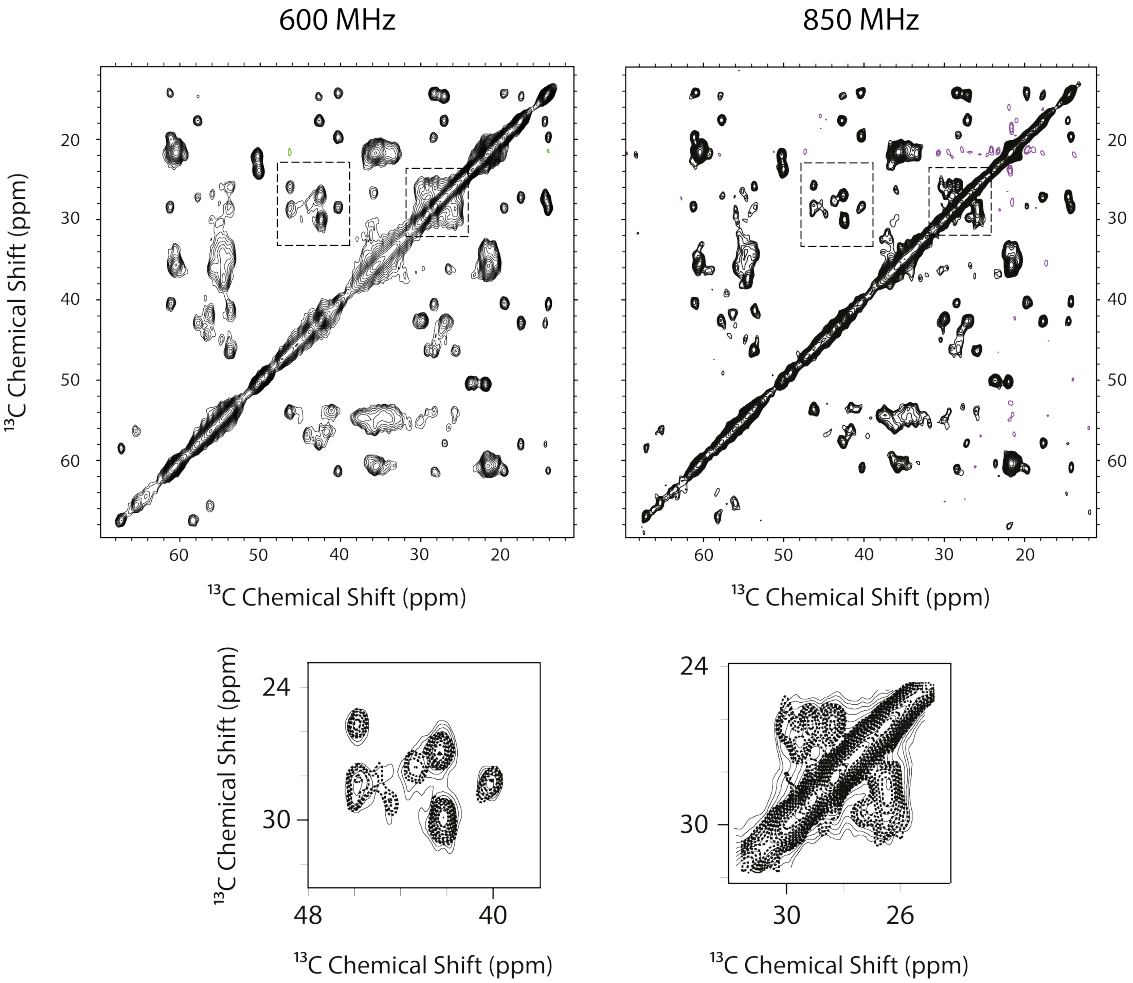

Figure 7.5: Comparison of ^{13}C spectra recorded using the DARR experiment with a mixing time of 20 ms taken at ^{1}H Larmor frequencies 600 MHz and 850 MHz, on a Bruker Avance II+ and Avance III spectrometer respectively, using 10 kHz MAS frequency on U-[^{13}C,^{15}N] Aβ_{1-40}/Cu aggregates. Regions of particularly increased resolution have been highlighted and overlain. Unbroken lines are from the spectra taken at 600 MHz, dashed lines are from the spectra taken at 850 MHz. 256 (600 MHz) and 64 (850 MHz) transients were co-added for each 512 (600 MHz) and 640 (850 MHz) t_1 FIDs, with a recycle delays of 1.5 s (600 MHz) and 1.6 s (850 MHz), corresponding to experimental times of ∼54.5 hours (600 MHz) and ∼18 hours (850 MHz). Base contour for the spectra are 3% (600 MHz) and 4% (850 MHz).

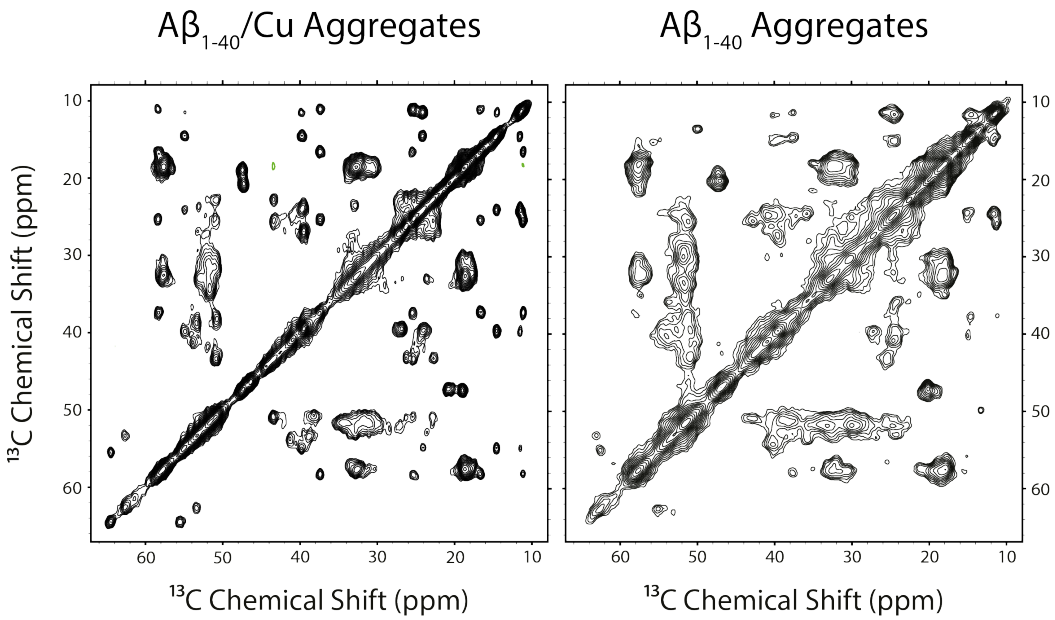

Figure 7.6: Comparison of ^{13}C-^{13}C 2D 20 ms mixing time DARR spectra of Aβ_{1-40}/Cu aggregates and Aβ_{1-40} aggregates recorded at 600 MHz ^{1}H Larmor frequency and 10 kHz MAS frequency. 128 transients were co-added for each 512 t_1 FIDs, with recycle delays of 2 s, corresponding to experimental times of ∼36.5 hours. Signal/noise for the highest peak in the spectrum = 107 (Aβ_{1-40}/Cu aggregates) and 43 (Aβ_{1-40} aggregates). Base contour level: 5% (Aβ_{1-40}/Cu aggregates) and 3% (Aβ_{1-40} aggregates).

7.3.3 2D DARR Spectra

Short mixing time DARR spectra were taken on both the Aβ_{1-40}/Cu aggregates sample and a sample of Aβ_{1-40} aggregates, which were prepared simultaneously and with all the same preparative steps excluding obviously the introduction of the copper, so as to provide a simple comparison and allow an instantaneous view on the effect of the copper; these spectra are displayed in Fig. 7.6. The spectra differ significantly in terms of resolution, there are large regions which are fairly well defined in the spectrum obtained on the Aβ_{1-40}/Cu aggregates which are not at all well defined in the spectrum taken on Aβ_{1-40} aggregates: for a specific example see the region (∼40 ppm, ∼25 ppm). Moreover, the signal/noise ratio for the highest peaks in each spectrum are quite different, 107 for Aβ_{1-40}/Cu aggregates and 43 for Aβ_{1-40} aggregates. Alongside the difference in resolution, certain resonances have shifted chemical shifts such as the serines at locations 8 and 26 to name a clear example. The signal from these residues can be seen in the high chemical shift region (∼55

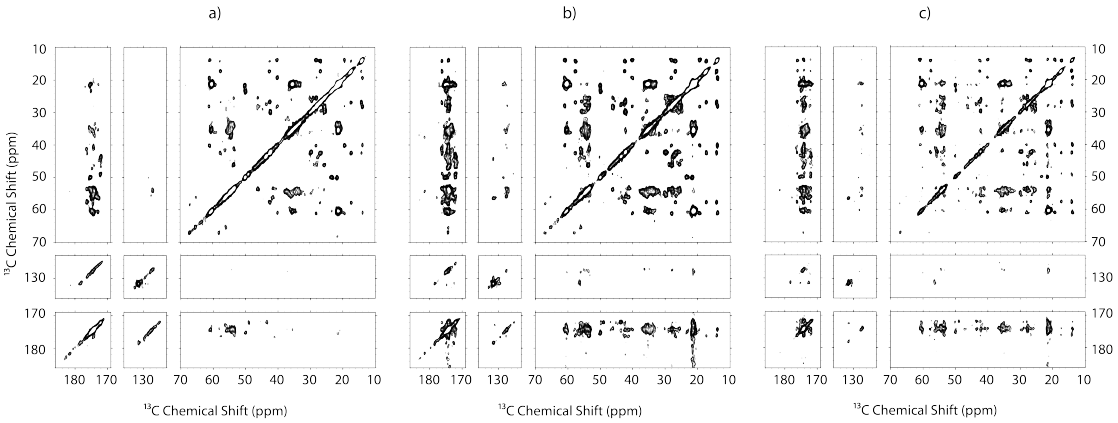

Figure 7.7: Comparison of ^{13}C-^{13}C 2D 20 (a), 100 (b) and 200 (c) ms mixing time DARR spectra of Aβ_{1-40}/Cu aggregates recorded at 850 MHz ^{1}H Larmor frequency and 10 kHz MAS frequency, 32 months after initial packing. 128 (a,b) and 152 (c) transients were co-added for each 512 (a) and 640 (b,c) t_1 FIDs, with recycle delays of 2 s (a, c) and 1.6 s (b), corresponding to experimental times of ∼36.5 hours (a,b) and ∼43 hours (c). Signal/noise for the highest peak in the spectrum = 107 (a), 75 (b) and 56 (c). Base contour level: 5% (a), 4% (b) and 3% (c).

ppm, ∼65 ppm). Quite clearly the copper is having an effect on the aggregation of the peptide and the result is a highly ordered state (indicted by the narrow linewidths) which has a different structure to that formed without the ion (indicated by the shift in chemical shifts).

Short and long mixing time DARR spectra were obtained on U-[^{13}C,^{15}N] Aβ_{1-40}/Cu aggregates. The spectra in Fig. 7.7 show intra- ($\tau_m = 20$ ms) and both intra- and inter-residue cross peaks ($\tau_m = 100$ and 200 ms). Peak intensity decreases with increasing mixing time which is expected due to T_1 relaxation during the mixing time, [182] but there is a gain in the number of cross peaks, as spin diffusion effects occur over greater distances. Fig. 7.7 a) displays a short mixing time DARR spectrum which contains fewer cross peaks than b) or c) but with better sensitivity - maximum signal-to-noise (S/N) values for the spectra are a) 107, b) 75 and c) 56. Although the spectrum in Fig. 7.7 a) contains 124 peaks, it still contains areas which are quite cluttered, e.g. the previously mentioned valine Cα, Cβ and Cγ regions. It is, therefore, very probable that even with well-resolved 2D ^{13}C-^{13}C ssNMR spectra such as these, a full assignment for the ^{13}C nuclei cannot be made by these spectra alone: identifying the six individual valines within those cluttered spectral regions will be particularly troublesome. Moreover, it can be seen in all the spectra in Fig. 7.7 that assignment of C$'$ resonances would be very difficult due to the nature of C$'$ chemical shifts existing

in similar regions for all residues. Fig. 7.7 c) contains several cross peaks which do not appear in the shorter mixing time spectra which can be used for inter-residue assignment; a particularly useful region of this spectrum is that between ∼50 to ∼70 ppm which contains the Cα-Cα cross peak region, and can be used for determining sequential residues. Additionally, it should be mentioned that the spectral regions in Fig. 7.7 b) exhibit diluted aspects of both the advantages and disadvantages of the other two spectra, however the 100 ms mixing time spectrum has high value in showing which longer range cross peaks appear first. In this way, long and very long range cross peaks can be distinguished.

Fig. 7.8 highlights specific areas of interest, where long-range cross peaks appearing only in the 200 ms mixing time DARR spectrum exist. Cross peaks found in the (48 ppm, 48 ppm) to (62 ppm, 62 ppm) region are likely to be Cα-Cα cross peaks, though extra peaks can occur between distant carbons within one residue, for example Cϵ and Cα in lysine, however these are easily recognised if most carbons from the residue in question have been previously assigned from the 20 ms DARR spectrum. Longer range contacts, appearing on the longer τ_m spectra, are very important in establishing the overall fold of a protein and are therefore of significant interest during assignment. In this work, individual residues were located on the short mixing time DARR spectrum, then adjoining residues were determined using the Cα-Cα cross peak region on the long mixing time DARR spectrum, highlighted in the figure. As the amino-acid sequence for the sample under investigation is known, this technique was the fastest and most reliable method of assignment, since assignment from the short mixing DARR spectrum of large amino acids could be verified by the existence of longer range intra-residue cross peaks appearing in the long mixing DARR spectrum, again such as lysine Cϵ and Cα cross peaks, alongside investigation of inter-residue cross peaks. This is precisely the processing technique for 2D spectra discussed in § 5.

As also detailed earlier in § 5, and as metioned above, when assigning residues in a molecule such as Aβ, using DARR spectra, it is easiest to start on a shorter mixing time spectrum as they are usually less cluttered. Specific residues are likely to occupy certain chemical shift regions within a spectrum, and one can look up typical values within the Biological Magnetic Resonance Data Bank (BMRB); as such, the initial search begins by examining these regions and identifying assignments for the carbons within the residues which are located in these regions, for an informative discussion of this see [243]. As the sequence of the peptide or protein under investigation is known, assignment is made easier as it is known how many of what residue there are in the

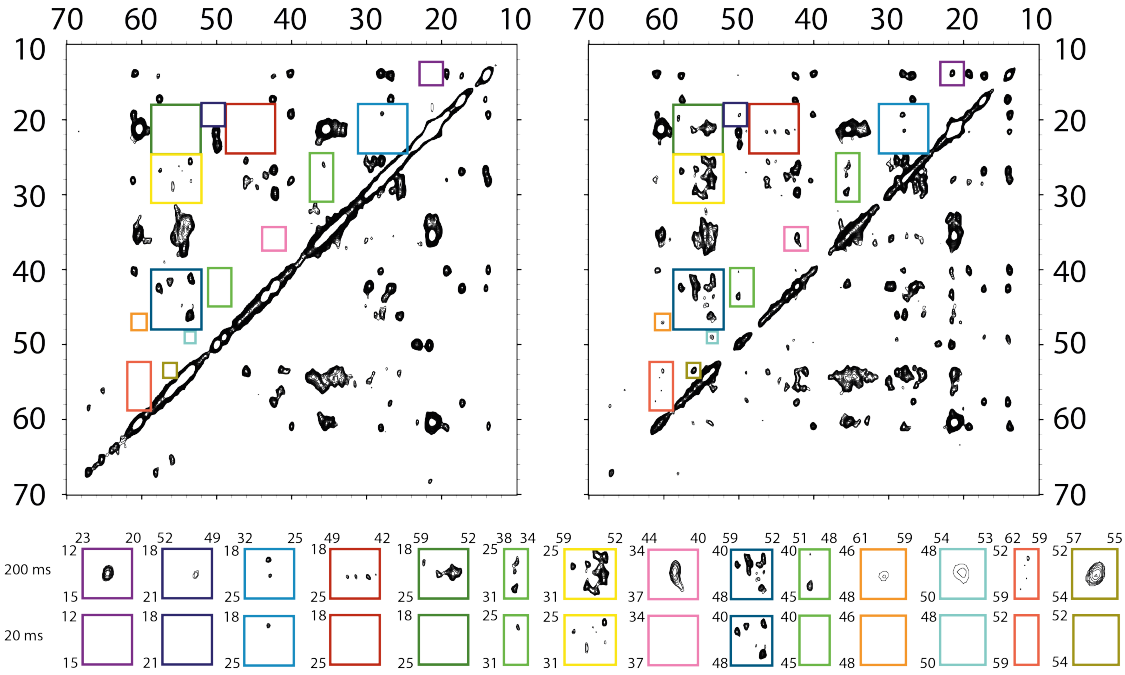

Figure 7.8: Comparison of 20 ms (left) and 200 ms (right) mixing time DARR spectra of Aβ_{1-40}/Cu aggregates recorded at 850 MHz ^{1}H Larmor frequency and 10 kHz MAS frequency with the aliphatic regions displayed. Spectral regions corresponding to new peaks that appear in the 200 ms spectrum are shown as insets below. In the way, it is possible to differentiate between intra- and inter-residue contacts. Experimental details are the same as those listed in Fig. 7.7.

sequence, with this information (and applying it specifically to Aβ_{1-40}) the chemical shift values for e.g. both of the two isoleucines and two serines can easily be found in Fig. 7.7 a); isoleucines contain a Cδ which typically has a very low chemical shift ($\sim$14 ppm) and serines contain a Cβ which has a notably high chemical shift ($\sim$66 ppm). Other, less easily located residues are found through recognising the pattern generated by the residue due to the number of carbons it contains, e.g. if a residue contains four carbons there should be a pattern of four horizontally aligned peaks at four corresponding vertical values of chemical shift, with the diagonal accounting for one of the peaks at each level, provided all intra-molecular carbons have exchanged magnetisation with all other intra-molecular carbons. Moreover for each residue, it is known both how many carbons to expect and at what chemical shift values to expect them which again aids assignment. Although spectra of larger peptides and proteins can become very crowded which increases assignment difficulty, especially as separating e.g. several of a particular residue which will be located at very similar chemical shifts can seem near to impossible and that with increased peptide length

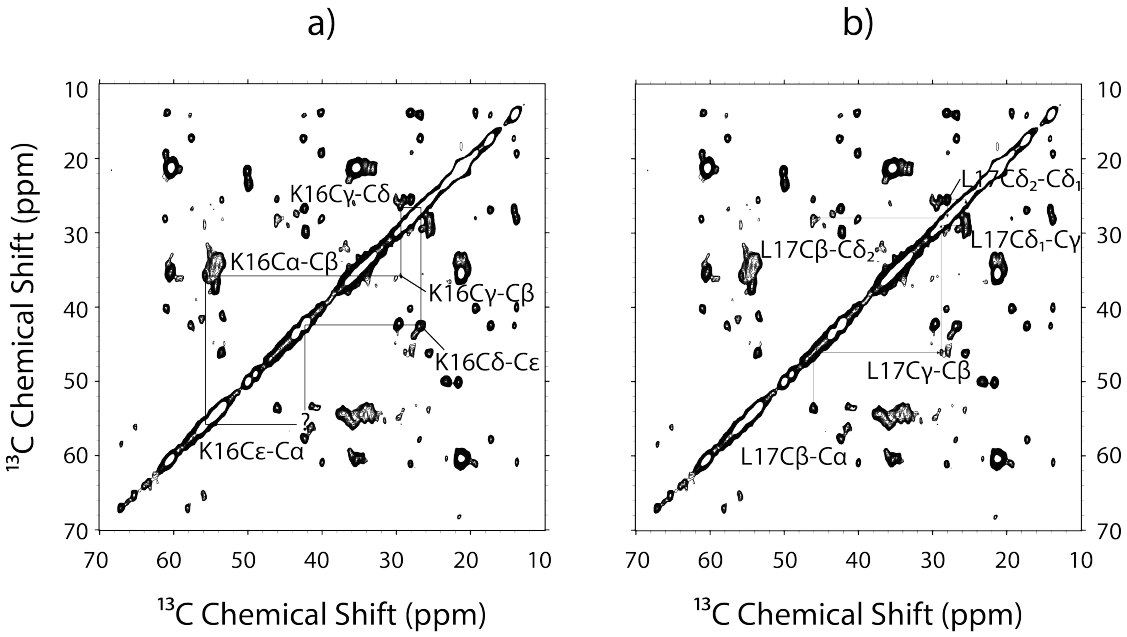

Figure 7.9: Assignment of two individual residues on the aliphatic region of the 20 ms mixing time DARR spectrum of Aβ_{1-40}/Cu aggregates recorded at 850 MHz ^{1}H Larmor frequency and 10 kHz MAS frequency. Lysine-16, a), and leucine-17, b), have all sidechain carbons assigned. The location of a long range peak which has not appeared in the short mixing spectrum, K16Cϵ-Cα has been marked with a question mark. Experimental details are the same as those listed in Fig. 7.7.

this is more likely to occur, this is still the easiest method for residue recognition and assignment. Note that typically in the larger molecules successfully investigated by ssNMR, the homogeneity of the sample is greater than the sample here, which results in narrower linewidths and, therefore, easier assignment. [41, 268, 269]

Individual residue assignment, as described above in a general case, has been illustrated in Fig. 7.9 a) and b) for the carbons in a lysine residue and a leucine residue respectively. The sequential walk along the sidechain has also been illustrated for each residue. Lysines have two characteristically low chemical shift value carbons, Cγ and Cδ, which are in close proximity to a medium-high chemical shift value carbon, Cϵ. The strong and characteristic K16Cδ-Cϵ cross peak in Fig. 7.9 a) is a suitable starting point for attempting to assign lysine residues. Starting from the Cδ-Cϵ peak, one is able to move vertically to the diagonal and then horizontally to a Cγ-Cδ cross peak and another assignment can be made. Though the process of returning to, and, while tracing lines towards peaks for assignment, remaining on one side of, the diagonal is conventional, it is expected that a peak that appears on one side of the diagonal will

also appear on the other so, when presenting spectra of the type shown here, it is easiest to maintain order if all assignments are on one side of the diagonal, however crossing the diagonal is no less correct a manner for assignment. From the Cγ-Cδ cross peak, the Cγ-Cβ cross peak can be found directly below (after crossing the diagonal). Subsequently, moving horizontally thereby remaining at the chemical shift value for Cβ, we find the cross peak for Cα-Cβ, which completes the assignment. It is possible to check the total assignment of a residue if there are any long range peaks that have appeared, e.g. in the case of a lysine residue, the Cϵ-Cα peak would provide a very strong argument for the veracity of the earlier assignments. This location has been included in Fig. 7.9 a), even though the peak is missing, with the label '?' for future use.

Leucines have three characteristically low chemical shift value carbons, Cγ, $C\delta_1$ and $C\delta_2$, which all have similar typical values. Leucines can therefore be recognised by a cluster of peaks around the diagonal in the ∼25 ppm region, which is precisely what can be seen in Fig. 7.9 b), where these three carbons have been assigned. For clarity, the assignment tracks for L17 have been broken in half, with one half starting at L17$C\delta_2$-$C\delta_1$, which then descends to the diagonal before extending horizontally out to L17Cβ-$C\delta_2$, which as a two-bond intramolecular connectivity, is visible in the 20 ms mixing time DARR spectrum. The second route begins at L17$C\delta_1$-Cγ, which, when ascending, joins the diagonal in line with the first peak from the first route (L17$C\delta_2$-$C\delta_1$ at the chemical shift value of L17$C\delta_1$ which displays the validity of this two route approach) but also moves horizontally to the diagonal before descending to L17Cγ-Cβ. Following this is another horizontal return to the diagonal and a descent to the final assignment L17Cβ-Cα, which is directly beneath the final assignment of the first route, which is also a good confirmation of the veracity of the assignments. In this manner, individual residues were assigned from the short mixing DARR spectrum before the longer mixing DARR spectra were fully analysed; occasionally the longer mixing spectra were used for confirmation of assignments made in the short mixing DARR spectrum as mentioned above.

Once all residue recognition and chemical shift assignment that can be achieved from the short mixing DARR spectra has been carried out, the following step is to uncover which residues (e.g. isoleucines in $A\beta_{1-40}$) that have been assigned correspond to which residues (either position 31 or 32) in the molecule; this can be done by using the longer mixing time DARR spectra. Once the Cα chemical shifts have been assigned, the longer mixing time DARR spectra show which Cα is in a proximity to which other two Cα (and accordingly the Cα of one residue will be spectrally linked to the

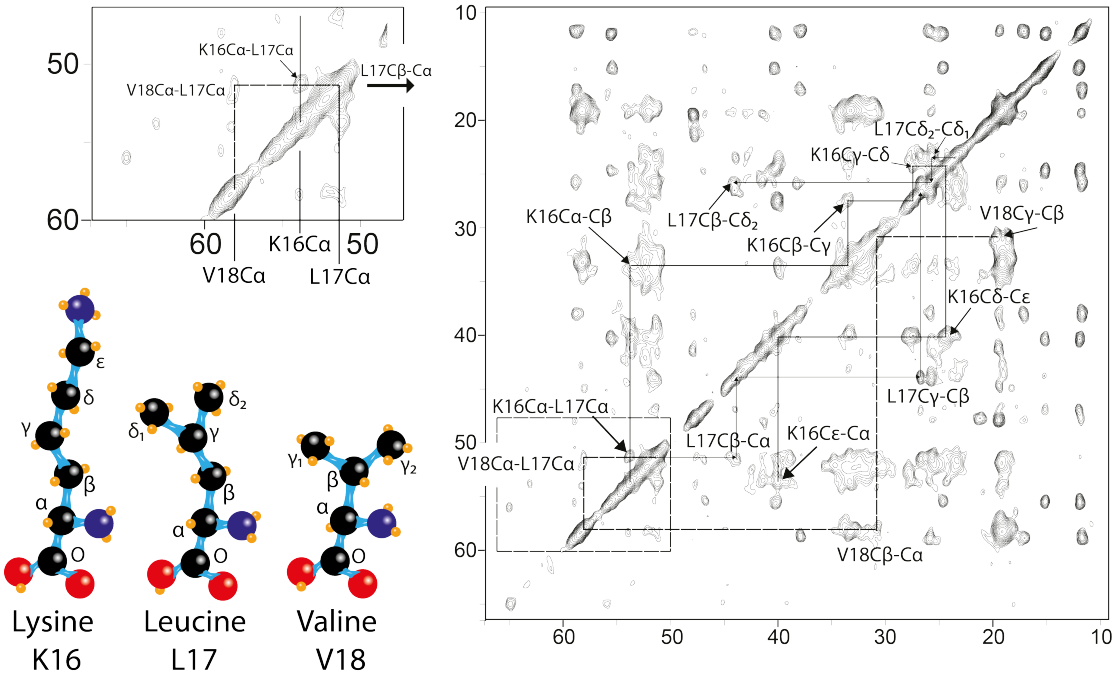

Figure 7.10: Assignment of three residues using the aliphatic region of the 200 ms mixing time DARR spectrum of $A\beta_{1-40}$/Cu aggregates recorded at 850 MHz ^{1}H Larmor frequency and 10 kHz MAS frequency with the Cα-Cα region enlarged for clarification. Residues are the previously assigned lysine-16, leucine-17, see Fig. 7.9, and an additional valine-18. The structures of the three amino acids are also shown: black spheres represent carbon; blue spheres represent nitrogen; red spheres represent oxygen; and smaller orange spheres represent protons. Experimental details are the same as those listed in Fig. 7.7.

other carbons located within that residue which by this point should be assigned, but, as stated earlier, this can be used for confirmation), and once this information has been found it is trivial to find which residue is the one that has been assigned. As an example, if the assigned isoleucine has a connectivity to another isoleucine this does not differentiate between positions 31 or 32, however if it has a connectivity to an alanine residue the isoleucine under investigation must be I31, similarly if not alanine but glycine then the isoleucine is I32, as the order of the peptide in that region is A30 - I31 - I32 - G33.

Fig. 7.10 illustrates the method described above using the two residues, a lysine and a leucine, from Fig 7.9 and the following valine in the Aβ sequence, K16 - L17 - V18. The individual assignments for each residue have been combined on the full aliphatic spectrum and the Cα-Cα region, located within the dashed rectangle on the main spectrum, has been enlarged such that inter-molecular Cα-Cα cross peaks

can be seen. As a note on the individual assignments, the K16Cϵ-Cα peak, which was denoted using a '?' in Fig. 7.9 a) due to its omission on the spectrum, has now become apparent on the longer mixing DARR spectrum and has been labelled accordingly. This is a clear example of using the longer mixing spectrum to find long range intra-molecular cross peaks which corroborate earlier assignments. For assignment of inter-molecular Cα-Cα cross peaks a suitable approach is to e.g. from the K16Cα-Cβ peak trace a line vertically down to the diagonal and identify where this line crosses with the horizontal line extended from the L17Cβ-Cα cross peak which has to cross the diagonal. The peak which exists in this location is clearly the inter-molecular K16Cα-L17Cα connectivity as assigned. A similar technique has been used for assigning the V18Cα-L17Cα cross peak, however as both lines have been extended horizontally, one needs to reach the diagonal then move vertically to ensure the lines meet. This can be seen on the diagram. It is equally valid to have either line reach the diagonal and then move vertically, and it can be seen that had it been chosen such that the leucine Cα line reached the diagonal and descended, the two lines would still have intersected at a peak. Fig. 7.10 also shows the structures of the three residues assigned in the figure so as to illustrate the distance between the various carbons, it can easily be seen why the K16Cϵ-Cα peak only appeared on the longer mixing time spectrum. Valine residues contain two Cγ carbons, however differentiating between the two resonances on a 2D DARR spectrum is often very difficult due to the similarity of their chemical shift values,[2] and so here only one Cγ value has been assigned.

7.3.4 ^{15}N-^{13}C Correlation DCP Spectra

Figs. 7.11 and 7.12 show Double Cross Polarisation NCA and NCO experiments performed on hydrated Aβ_{1-40}/Cu aggregates. Residues with lower chemical shifts for Cα, such as those in glycines, facilitate assignment of nitrogen chemical shifts, as illustrated on the figure, due to the resolved nature of the resonances in these lower ^{13}C chemical shift regions. In regions of crowded Cα chemical shifts, e.g. 53 to 62 ppm, it is very difficult to unambiguously assign nitrogen chemical shifts. The NCA spectrum in Fig. 7.11 also shows signals appearing in the C$'$ chemical shift region, with a few strong, partially resolved peaks, however as so few carbonyl carbons were assigned previously using the 2D ^{13}C-^{13}C DARR spectra, it is very difficult to unambiguously assign these. The DCP-NCO spectrum, Fig. 7.12, is also very crowded and so further

[2]The average values, as provided by the BMRB, for valine Cγ_1 and Cγ_2 are 21.52 and 21.30 ppm respectively

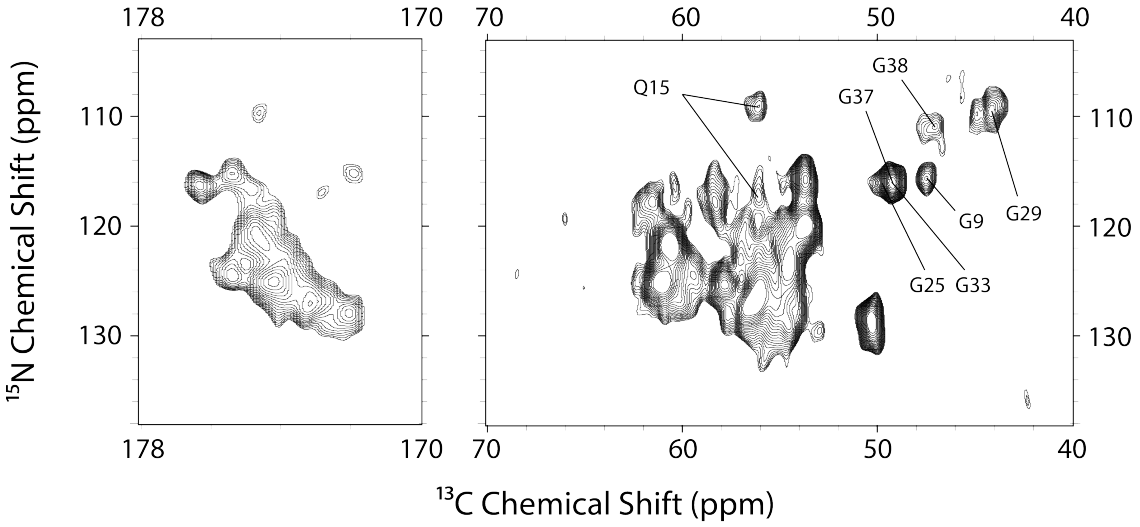

Figure 7.11: 2D NCA DCP spectrum of Aβ_{1-40}/Cu aggregates recorded at a ^{1}H Larmor frequency of 600 MHz and 10 kHz MAS, 32 months after initial packing. Signal/noise for the highest peak in the spectrum = 15. Assignment of well resolved peaks are shown. Glycine assignment is possible due to low Cα chemical shift, and the distinct ^{15}N chemical shifts in those regions. Contact time for the ^{15}N to ^{13}C CP pulse was 4 ms. 512 transients were co-added for each 40 t_1 FIDs, with a recycle delay of 1.5 s, corresponding to an experimental time of ∼8.5 hours. Base contour level is 3%.

assignment is particularly difficult. Glutamine has two nitrogens within its structure, and within Aβ_{1-40} there is only one glutamine residue (at location 15), so these can be found vertically aligned at one Cα chemical shift value. The Q15 carbon chemical shifts had already been assigned using the 2D DARR spectra and so, using the BMRB to indicate that the Nϵ_2 had a typically low chemical shift, isolating a set of peaks at ^{13}C chemical shift 56.0 ppm and with two nitrogen peaks with one at a distinctively low value, it was possible to assign the Q15 ^{15}N chemical shifts. Moreover, the backbone nitrogen in glutamine has a lower chemical shift than the majority of residues, so it is easily located at the top of the block of signals, as shown on Fig. 7.11. Alanines 21 and 30 are likely to be the nuclei resonating at the strong peak at (∼50 ppm, ∼130 ppm) as few other carbon shifts are assigned in this low carbon Cα region, however unambiguous assignment is difficult due to the broad nature of the peak, and so this peak has remained unassigned. Further doubt is cast upon this as alanine nitrogen chemical shift values are not usually as high as 130 ppm. Although these spectra surrendered little more information they demonstrated that DCP experiments could be semi-successfully run on this

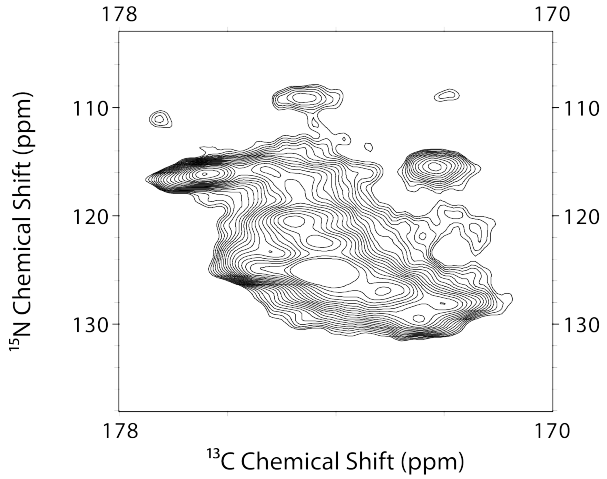

Figure 7.12: 2D NCO DCP spectrum of Aβ_{1-40}/Cu aggregates recorded at a ^{1}H Larmor frequency of 600 MHz and 10 kHz MAS, 32 months after initial packing. Signal/noise for the highest peak in the spectrum = 16. Further assignment is difficult due to spectral crowding. Contact time for the ^{15}N to ^{13}C CP pulse was 4 ms. 512 transients were co-added for each 40 t_1 FIDs, with a recycle delay of 1.5 s, corresponding to an experimental time of ∼8.5 hours. Base contour level is 4%.

sample within sensible time-scales, with less than a day required to take both spectra. With the addition of a third dimension so as to separate out the peaks over this third dimension, further assignment could be possible, so the option of using inverse detection was investigated.

7.3.5 Inverse Detection Experiments

Inverse detection experiments investigating both ^{13}C and ^{15}N were performed at a ^{1}H Larmor frequency of 850 MHz with a MAS frequency of ∼100 kHz using double- and triple-channel 0.8 mm Samoson probes. Experiments of this type were performed so as to permit residues with previously assigned Cα, C$'$ and ^{15}N chemical shifts to have corresponding ^{1}H and, where not already assigned, ^{15}N chemical shifts assigned.

Fig. 7.13 shows a spectrum obtained from a 2D ^{1}H-^{13}C correlation experiment displaying the aliphatic region of the ^{13}C dimension. The mixing time used was quite short such that the correlations displayed are most likely to be intra-residue. The peak located at the lowest carbon chemical shift value appears at ∼14 ppm which is to be expected as this is the location of the characteristically low Cδ_1 chemical shift values for the isoleucine residues at positions 31 and 32 as found from the earlier 2D ^{13}C-^{13}C DARR spectra. The peak directly above this, in terms of chemical shift,

at ∼17 ppm, is the 31/32 isoleucine Cγ_2 peak which was also found from earlier DARR spectra. In this way assignments of ^{1}H chemical shift values for protons in specific residues bonded to specific carbons can be made; that the spectrum is very likely to only contain intra-residue correlations validates this assignment technique. Certain regions are, again, cluttered and so assignment within these areas is difficult, for example see the typical valine regions (∼20, ∼35 and ∼60 ppm), and so further inverse detection experiments, potentially involving a third dimension, were required to isolate the ^{1}H chemical shift values within these areas. In spite of this spectral crowding, Fig. 7.13 illustrates that inverse detection experiments can be performed on amyloidogenic samples, provided rapid MAS is employed, to extract certain ^{1}H chemical shift values without requiring deuteration of the sample.

Fig. 7.14 shows a 2D ^{1}H-^{13}C correlation spectrum obtained from a similar experimental set up to Fig. 7.13 but with a longer ^{13}C to ^{1}H CP duration and proton-proton mixing time. These alterations allow magnetisation to transfer over greater distances and therefore the spectrum shows a greater number of correlations, in a similar way to long mixing DARR spectra showing more peaks than short mixing DARR spectra. This enables assignment of longer distance proximities, however, as with DARR spectra, areas that are cluttered in the shorter mixing experiment will be equally cluttered, or moreso, in the longer mixing experiment; this can easily be seen in the large block of overlapping signals between ∼0-2 ppm for proton and ∼13-30 ppm for carbon. The most informative peaks that are displayed in this spectrum are the isolated peaks between 2.5-6 ppm in the ^{1}H dimension and 20-50 ppm on the ^{13}C chemical shift axis. Mostly these are new peaks when compared to Fig. 7.13, but are also well resolved such that assignment is possible. Alongside these useful peaks, any resonances between 8-9 ppm, which is the typical chemical shift region for amide protons and which were not visible in the earlier spectra, can be assigned. There are at least 4 strong, well-resolved peaks in this region which can be assigned. The protons that can be assigned from this spectra are no longer necessarily directly bonded to the carbons at the chemical shift values of which the resonances appear. For example, the peak at (∼21.5 ppm, ∼8.7 ppm) cannot have occured from a directly bonded spin pair as the proton shift is too well suited to be anything other than an amide proton, moreover the carbon chemical shift value is too low to be even a nearby Cα; this peak is later assigned as V24Cγ-V24H. Therefore clearly this spectrum shows various long range correlations which can be of significant use, as the greater number of peaks there will be on the spectrum which correspond to previously assigned carbons, though not all carbons have been assigned, and so all the protons with connectivities

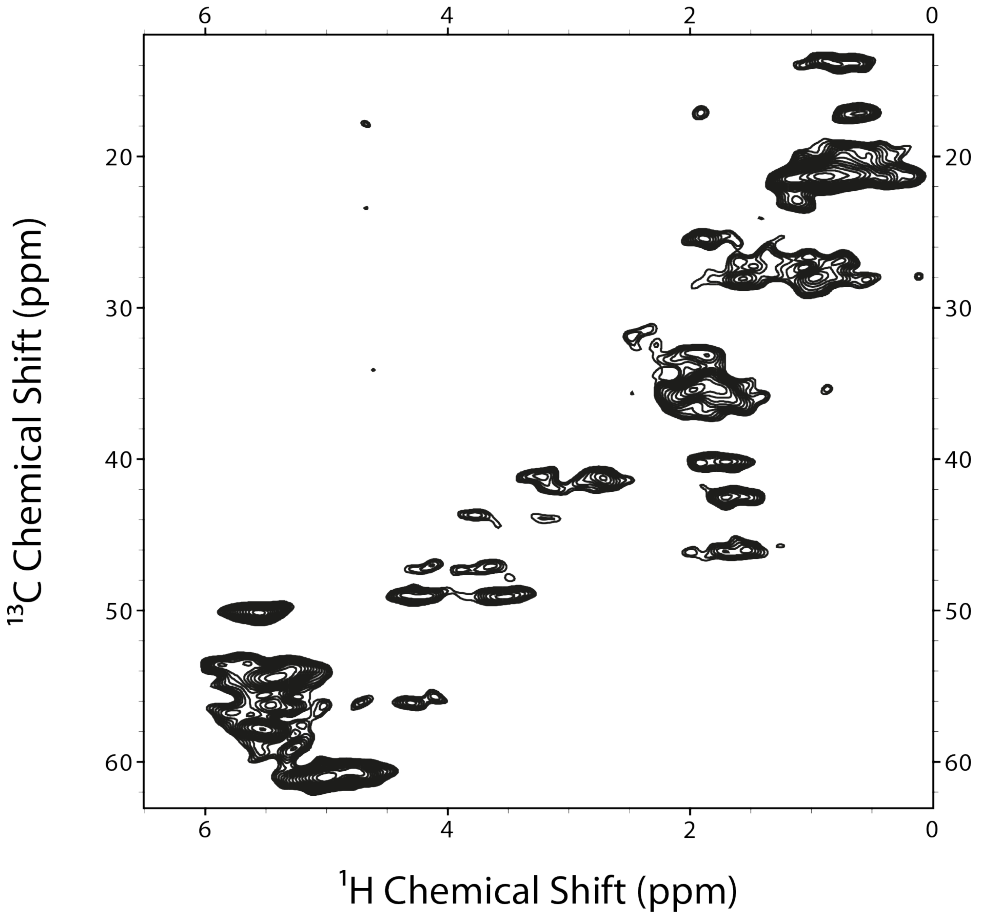

Figure 7.13: 2D ^{1}H-^{13}C inverse detection spectrum of A$\beta_{1\text{-}40}$/Cu aggregates recorded at 850 MHz ^{1}H Larmor frequency and 100 kHz MAS frequency. A ^{13}C to ^{1}H CP duration of 200 µs was used. 32 transients were co-added for each 200 t_1 FIDs, with a recycle delay of 0.3 s, corresponding to an experimental time of ∼30 mins. Base contour level: 3%.

to previously assigned carbons can be assigned. In this way, although some carbons in a residue may not have been assigned, this will not limit the number of protons that can be assigned from a residue provided at least one carbon has been assigned. Long range connectivities, such as the one mentioned above, are often well resolved as they exist in sparsely populated spectral environments, provided the experimental setup is such that the signal does not decay before acquisition which can occur during particularly long mixing times.

A collection of 2D ^{1}H-^{13}C inverse detection spectra were taken with varying ^{13}C to ^{1}H CP durations and proton-proton mixing times so as to obtain an overview of the order in which, and the timescales over which, long range signals begin to appear. Four such spectra are shown in Fig. 7.15, with all assigned peaks labelled.[3] From A) to D), the ^{13}C to ^{1}H CP durations increase, though the ^{1}H-^{1}H mixing times differ in no order. 37 assignments were made using previously assigned chemical shift values and Fig. 7.15 A), with 37, 58 and 26 assignments made using Fig. 7.15 B), C) and D) respectively. Clearly these spectra are somewhat complementary and allow for significant numbers of protons to be assigned; in total, 64 ^{1}H chemical shifts were assigned from the spectra. It can be seen that with the reduced amount of assignments (26) available from analysis of Fig. 7.15 D), 4000 μs for a ^{13}C to ^{1}H CP duration is too long and that relaxation has occurred during this time. S/N ratios for the I31Cδ_1-Hδ_1 peak, which is common to all the spectra, are A): 7.3, B): 15.7, C): 15.3 and D): 13.5, with ^{13}C linewidths for the same peak as 265, 240, 160 and 200 Hz and ^{1}H linewidths measured as 670, 560, 420 and 660 Hz respectively. Although a total of 64 ^{1}H assignments have been made, there remains 97 peaks, as recognised by the SPARKY software, across all four spectra which are yet to be assigned.[4] Further carbon assignments are required to enable these proton assignments to be made reliably.

Fig. 7.16 shows a 2D ^{1}H-^{15}N inverse detection spectrum, obtained from a short mixing inverse detection experiment and displaying the amide chemical shift region in the proton dimension. There are a number of resonances that can be assigned due to the dilute nature of ^{15}N chemical shift values outside the main block of signals in the 120-130 ppm region, reminiscent of the DCP spectra from § 7.3.4; glycine and glutamine have particularly low ^{15}N chemical shifts which result in simpler assignment for these residues. Within the dense block of ^{15}N chemical shifts, it is particularly difficult to obtain assignments because typical proton linewidths are larger than car-

[3] Peaks were identifed through the use of the SPARKY peak picking function

[4] Where peaks have clearly been corresponding to the same resonance across multiple spectra these have been counted only once in the tally

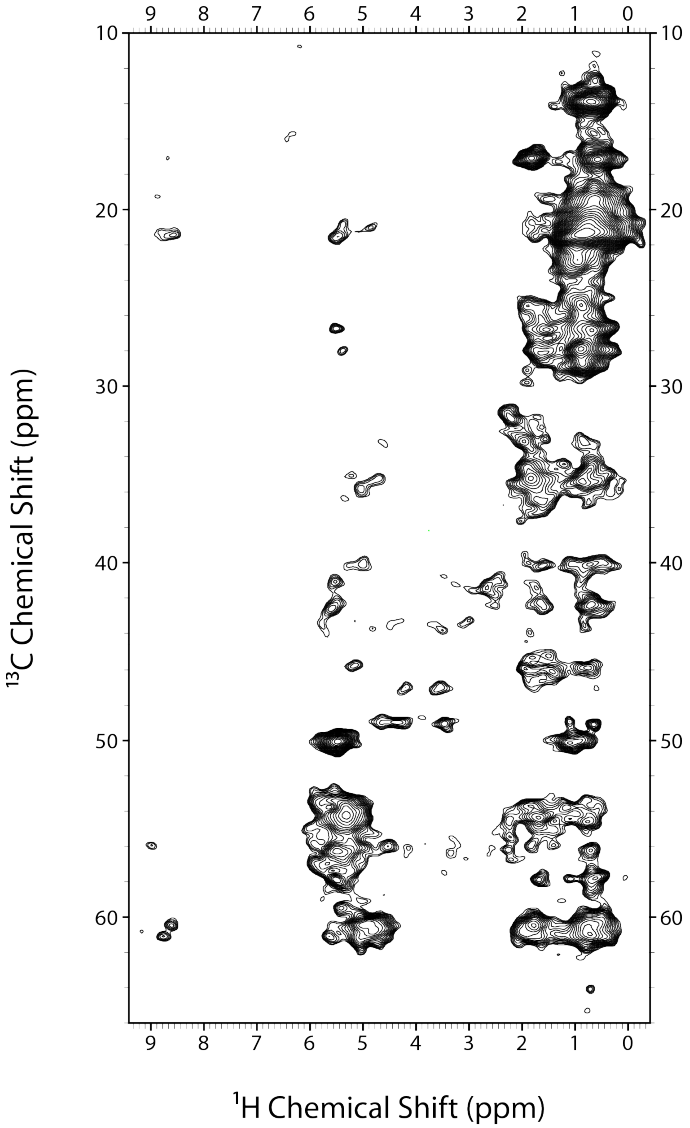

Figure 7.14: 2D ^{1}H-^{13}C inverse detection spectrum of A$\beta_{1\text{-}40}$/Cu aggregates recorded at 850 MHz ^{1}H Larmor frequency and 100 kHz MAS frequency. The ^{13}C to ^{1}H CP duration was 2 ms and the ^{1}H-^{1}H mixing time was 1 ms. 48 transients were co-added for each 200 t_1 FIDs, with a recycle delay of 0.3 s, corresponding to an experimental time of $\sim$50 mins. Base contour level: 4%

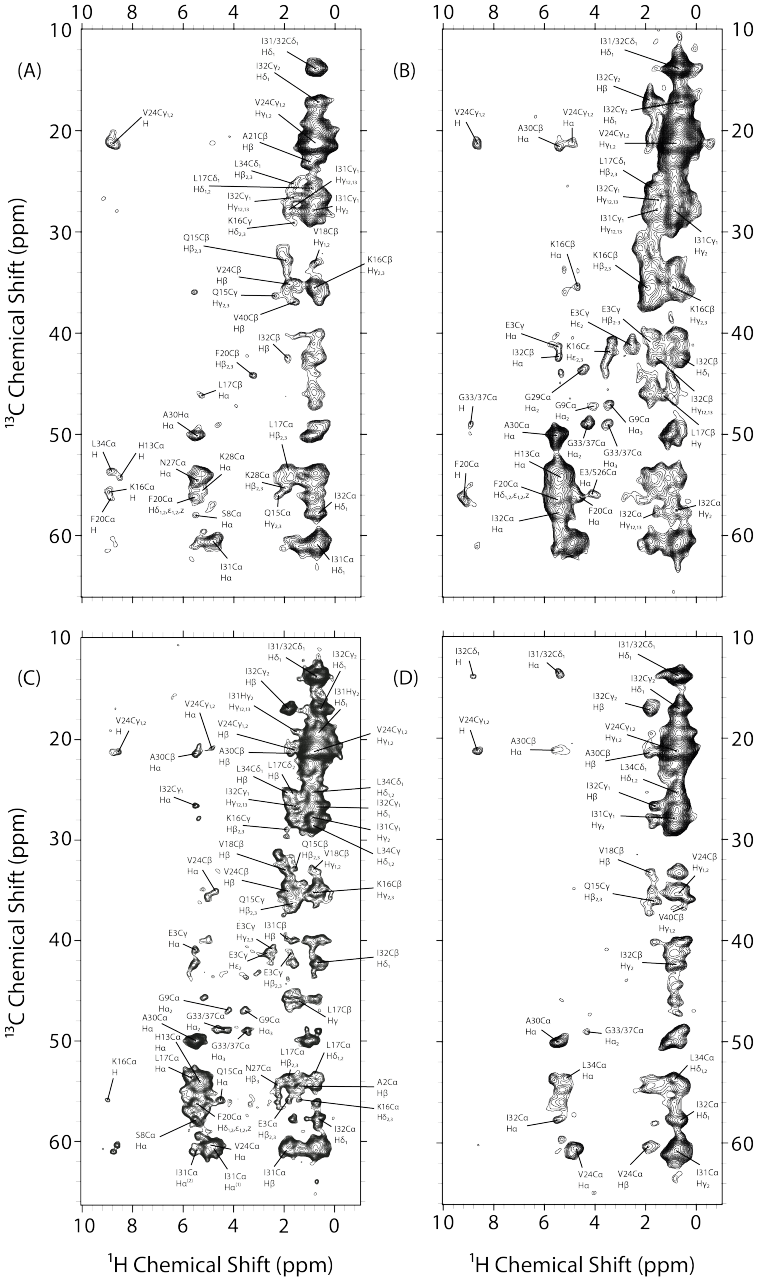

Figure 7.15: 2D ^{1}H-^{13}C inverse detection spectra of A$\beta_{1\text{-}40}$/Cu aggregates recorded at 850 MHz ^{1}H Larmor frequency and 100 kHz MAS frequency. ^{13}C to ^{1}H CP durations of 200 (A), 1500 (B), 2000 (C) and 4000 µs (D) and ^{1}H-^{1}H mixing times of 1200 (A), 2 (B), 1000 (C) and 2 µs (D) were used. Assignments have been made where possible, totalling 64 assignments, and a further 97 peaks have been recognised but remain unassigned. 32 (a, b, d) and 48 (c) transients were co-added for each 120 (a, b, d) and 200 (c) t_1 FIDs, with a recycle delay of 0.3 s, corresponding to experimental times of ∼20 mins (a, b, d) and ∼50 mins (c).

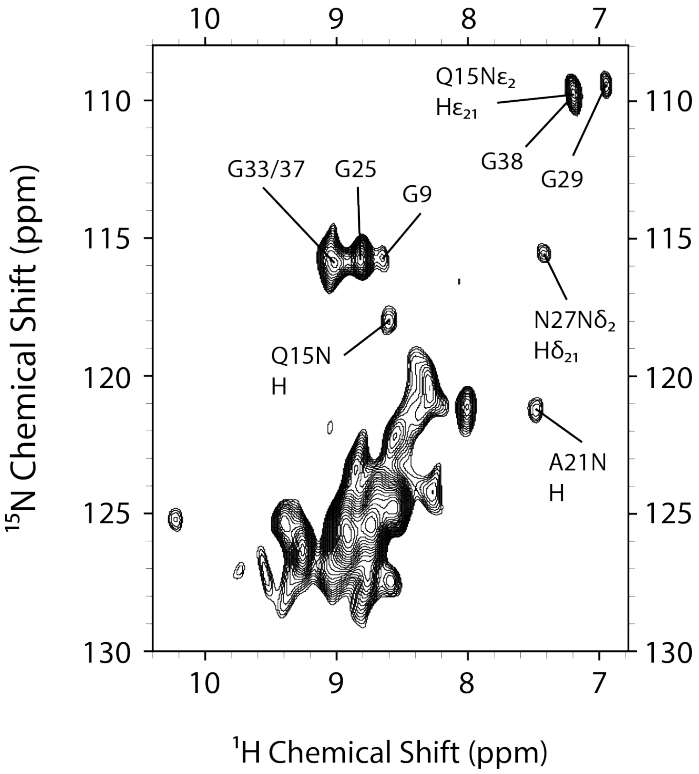

Figure 7.16: 2D ^{1}H-^{15}N inverse detection spectrum of A$\beta_{1\text{-}40}$/Cu aggregates recorded at 850 MHz ^{1}H Larmor frequency and 100 kHz MAS frequency. Showing only the amide region. A ^{15}N to ^{1}H CP duration of 200 µs was used. 8 transients were co-added for each 50 t_1 FIDs, with a recycle delay of 0.3 s, corresponding to an experimental time of ∼2 mins.

bon linewidths (400 Hz vs 150 Hz) so a task that is difficult using ^{15}N-^{13}C correlation spectra is all the harder when using ^{15}N-^{1}H spectra, as can be seen in Fig. 7.16. In spite of this, using the SPARKY automated peak picking function, 21 peaks were recognised and 5 of these were matched to nitrogen chemical shift values previously obtained, with a further 4 assigned through analysis of the spectrum. An interesting outlier, N27Nδ_2-Hδ_{21} was tentatively assigned, and is labelled on the figure. The chemical shift location of the peak is characteristically distinctive and is unlikely to be another correlation, however further experiments were used to corroborate this assignment. The correlation A21N-H was also assigned in this manner, and is labelled on the figure.

Fig. 7.17 shows five strip plots taken from two 3D spectra, one, obtained from a C-N-H correlation experiment, and the other, from a N-H-HX correlation experiment. The C-N-H sequence used provides intra-residue correlations for the aliphatic carbon, the

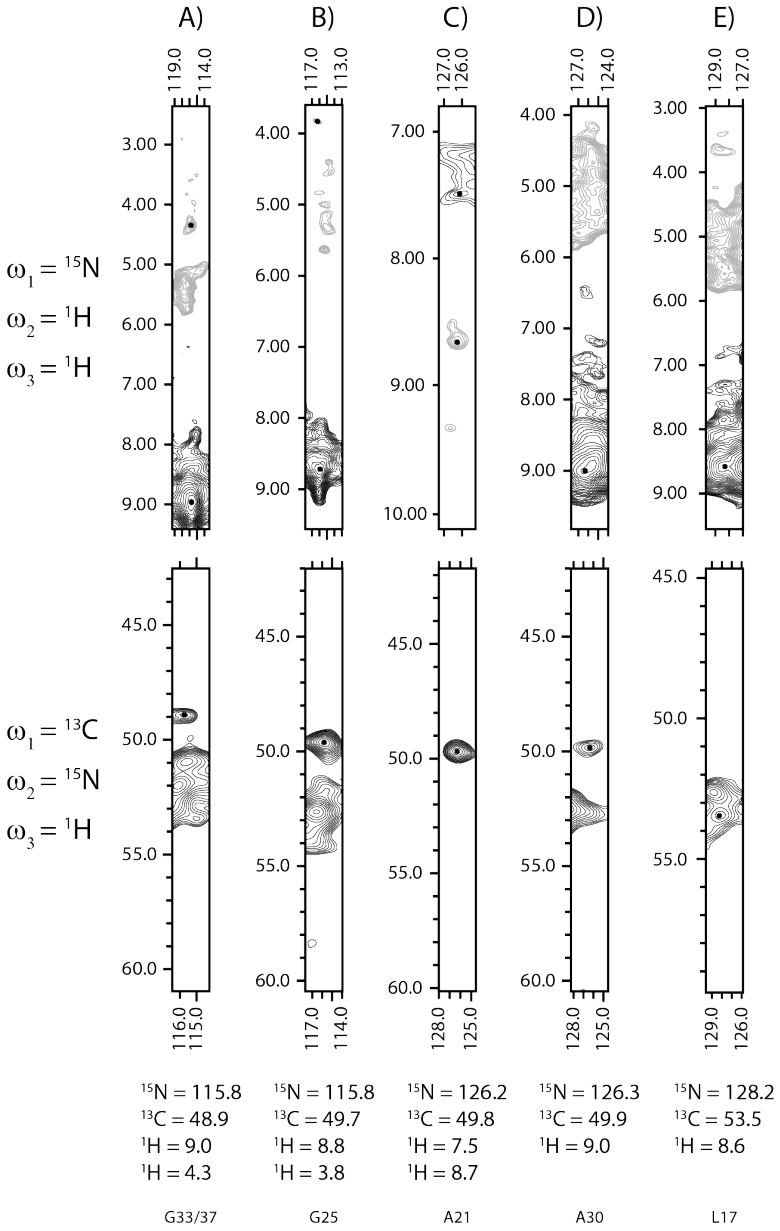

Figure 7.17: Strip plots of 3D ^{15}N-^{1}H-^{1}H and ^{13}C-^{15}N-^{1}H inverse detection spectra of Aβ_{1-40}/Cu aggregates recorded at 850 MHz ^{1}H Larmor frequency and 100 kHz MAS frequency. Correlations found across the two spectra revealing both intra-residue C-N-H connectivities and the proton connectivites to amide protons are shown. Chemical shift values of the peaks are included below the strip plots and the corresponding assignments below that. Positive contours, corresponding to the diagonal of a 2D plot, are in black and negative contours, corresponding to a one-bond connectivity, are in grey. 64 (NHH) and 112 (CNH) transients were co-added for each 80 (NNH) and 56 (CNH) t_1 and 34 (NNH) and 24 (CNH) t_3 FIDs, with a recycle delay of 0.3 s, corresponding to an experimental time of ∼14.5 (NNH) and ∼12.5 (CNH) hours.

nitrogen and amide proton, and the N-H-HX sequence provides correlations between the nitrogen, amide proton and then protons with a connectivity to the amide proton. The third dimension in Fig. 7.17 is the amide proton chemical shift value, which is common to both spectra, such that pairs of cross peaks in the two spectra located at the same amide proton and nitrogen (horizontal axis) chemical shift values offer an aliphatic carbon and a secondary proton chemical shift value to be assigned. The result of this, and the manner in which the spectra are displayed, is that pairs of vertically aligned peaks share a common nitrogen chemical shift value and amide proton. Proton values that are on the H-HX diagonal, are self-correlations, and therefore only offer a Cα-N-H correlation, and are represented by positive contours, resulting from the use of the HORROR sequence, and the one-bond proton-proton correlations that lie off the H-HX diagonal are shown as negative contours, for the same reason. The strips taken from the N-H-HX spectrum are shown above those taken from the C-N-H spectrum.

As previously, there are cluttered regions in both spectra which hinders assignment for correlations that are located in both the main block of ^{13}C signals, $\sim$50 - 55 ppm, and the typical ^{15}N chemical shift region $\sim$120 - 128 ppm, for the C-N-H spectrum, and lastly, the same spectral crowding can be found along the ^{1}H diagonal formed in the N-H-HX spectrum. Therefore, the assignments from the C-N-H spectrum are often made from outliers from the main ^{13}C chemical shift value block of signals, as can be seen in the assignments of carbons with chemical shifts mostly around 49 - 50 ppm. The carbon assignment displayed within this region, L17Cα (Fig. 7.17 (E)) is possible as the ^{15}N chemical shift value for this residue is found to be higher than most surrounding signals, reducing the spectral crowding in the carbon dimension.

Fig. 7.17 (A), (B) and (C) display assignments where a secondary proton (i.e. one with a one-bond connectivity to the amide proton) has been identified for assignment. The secondary proton assignment in (A) has been assigned as the Hα of either the G33 or G37 residue. As can be seen from the N-H-HX row of strip plot (A) there are a number of secondary protons excited in the HX = 5-6 ppm region, however they were not found to align with the ^{15}N chemical shift value of 115.8 ppm assigned to G33/37; clearly, there are further assignments that can be made within this region (though these have not been displayed in the figure) in spite of the overlain signals present. Fig. 7.17 (B) has had a secondary proton assigned which occurs at a ^{1}H chemical shift value suitable to G25Hα, though, admittedly, the peak is not intense. The Cα-Hα correlation that would occur from this assignment does not appear in Fig. 7.15, although this does not mean the correlation is incorrect. Therefore, the

assignment has been made and is found later to be valid. Fig. 7.17 (C) is a strip taken at the other end of the ^{15}N spectrum (126.2 ppm cf. 115.8 ppm) and displays two proton resonances, the self correlation, located at 7.5 ppm, and the secondary proton, located at 8.7 ppm. Though the 7.5 ppm is likely to be the A21H resonance, also found earlier in Fig. 7.16, the 8.7 ppm proton cannot be within the same alanine residue. This is an example of the inter-residue ^{1}H-^{1}H correlation, and the proton may well belong to F20, or even to a residue on the opposite side of the β-hairpin. Strip (C) shows that isolated resonances can be found in spectrally uncrowded regions, and that particularly interesting assignments are available from these regions. Fig. 7.17 (D) and (E) display a broad collection of peaks occuring within crowded ^{1}H regions while the ^{13}C regions are fairly clear. As can be seen, there are many options for a secondary proton assignment in (D) and (E), however any assignment would be extremely tentative and so it would be unwise to suggest a single secondary proton in these cases. The correlations that were found were clearly assigned as A30Cα-N-H and L17Cα-N-H.

The SPARKY peak picking function provided many correlations, with only a representative set shown in Fig. 7.17, all of which were critiqued before inclusion in the final data, shown in Table 7.1. In total ten ^{15}N assignments were made through use of this spectrum when combined with the data previously shown, with new assignments including A30, L17 and S26 (data not shown).

7.3.6 Chemical Shift Analysis

54% of aliphatic carbons have been assigned and all chemical shift assignments are listed in the right-most column of Table 7.1, further experiments are ongoing to complete the assignment. There is a high confidence in the assignments made. Previously published assignments have also been listed in Table 7.1. [55,63,64,101,102,110] The approach for assignment of ^{13}C chemical shifts is illustrated in Figs. 7.9 and 7.10, while Figs. 7.11 and 7.15 to 7.17 illustrate how ^{15}N and ^{1}H assignments were made. The differences between these chemical shifts lend support to the claim that this is a novel structure. Root mean squared average deviations from the published chemical shifts have been calculated and, interestingly, the closest match to the sample under investigation is the Tycko and Meredith brain-extract seeded fibrils with an average deviation of <1 ppm. None of the studies listed in the table were able to

[5]The assignment technique used to obtain these values can be seen in Figs. 7.9, 7.10, 7.11 and 7.15 to 7.17 as discussed above in § 7.3.6. There is a high confidence in the assignments made.

Table 7.1: Table of combined chemical shifts from all experiments included in the right-most Kelly(Cu) column, with comparisons to previously published models where possible.

Residue	Ishii (Cu)	Ishii	Madhu	Bertini	Tycko (Iowa)	Tycko 2009	Tycko 2013	Kelly[5] (Cu)
2 - Ala								
Cα				49.9			50.1	54.5
Cβ				22.0			24.1	26.8
Hβ								1.4
3 - Glu								
Cα				53.3			54.4	55.9
Cβ				32.3			33.7	35.6
Cγ							35.7	41.2
Hα								5.4
$H\beta_{23}$								1.8
$H\epsilon_2$								2.5
6 - His								
C′				173.5			171.7	174.2
Cα				53.7			50.6	56.7
Cβ				33.9			31.5	39.0
8 - Ser								
C′			173.7	172.3			175.1	174.3
Cα			57.6	55.9			54.7	58.0
Cβ			62.7	65.6			65.8	67.0
Hα								5.5
9 - Gly								
Cα				43.7			47.1	47.1
N				111.4			112.6	115.8
H								8.7
$H\alpha_2$								4.1
$H\alpha_3$								3.4
10 - Tyr								
Cα				56.5			56.4	59.9
13 - His								
Cα	54.2	54.1		53.4			50.9	54.2
Cβ	31.7	32.1		33.7			31.6	34.9
H								8.5

Residue	Ishii (Cu)	Ishii	Madhu	Bertini	Tycko (Iowa)	Tycko 2009	Tycko 2013	Kelly (Cu)
13 - His								
$H\alpha$								5.3
14 - His								
$C\alpha$		60.8		53.4				60.3
15 - Gln								
C'			173.6	172.6	173.1		173.8	174.7
$C\alpha$			53.5	53.8	53.3		54.0	56.0
$C\beta$			31.2	31.2	32.8		33.0	32.8
$C\gamma$			33.0	33.1	34.1		31.1	36.2
$C\delta$			177.9	176.4	177.2		176.3	181.6
N				126.2			123.2	117.6
$N\epsilon_2$							107.9	109.6
H								8.6
$H\alpha$								4.5
$H\beta_{2/3}$								1.7
$H\beta_{2/3}$								1.9
$H\gamma_{2/3}$								2.2
$H\gamma_{2/3}$								2.4
$H\epsilon_{21}$								7.2
16 - Lys								
C'				172.6	172.7		173.5	174.4
$C\alpha$				53.8	54.7		54.2	55.7
$C\beta$				33.7	36.4		36.0	35.5
$C\gamma$				26.4	24.5		25.0	26.3
$C\delta$				28.5	29.3		29.4	29.3
$C\epsilon$				41.1	40.8		42.0	41.9
H								8.9
$H\alpha$								4.7
$H\beta_{2/3}$								1.9
$H\gamma_2$								0.8
$H\gamma_3$								0.8
$H\delta_{2/3}$								1.6
$H\epsilon_{3/2}$								3.4
17 - Leu								
C'	174.8	174.9		173.8			174.2	174.1
$C\alpha$	54.5	54.8		52.0			53.6	53.5
$C\beta$	46.7	46.1		43.2			43.7	46.1

Residue	Ishii (Cu)	Ishii	Madhu	Bertini	Tycko (Iowa)	Tycko 2009	Tycko 2013	Kelly (Cu)
17 - Leu								
$C\gamma$	29.0	29.2		26.6			29.3	28.6
$C\delta_1$	26.9	27.4		24.6			24.2	27.9
$C\delta_2$	25.1	24.5		18.9			22.6	25.5
N							126.3	128.2
H								8.6
$H\alpha$								5.3
$H\beta_{2/3}$								1.8
$H\gamma$								1.3
$H\delta_{1/2}$								0.9
18 - Val								
C'				171.7	172.2		172.0	174.8
$C\alpha$	60.9	60.8		60.1	60.2		61.2	60.2
$C\beta$	35.0	35.1		33.6	34.6		33.2	33.1
$C\gamma$	21.0	21.1		21.0	20.8		21.4	21.6
$H\beta$								2.0
$H\gamma$								0.8
20 - Phe								
C'	172.9	173.1	170.6	172.6	171.8		176.8	172.6
$C\alpha$	56.5	56.6	54.1	52.4	55.0		57.0	56.4
$C\beta$	43.8	43.8	41.7	41.5	42.3		34.2	44.3
$C\delta_1$	131.5	131.6	129.8				127.2	131.6
H								9.2
$H\alpha$								4.6
$H\beta$								3.2
$H\delta_{12}\epsilon_{12}z$								5.5
21 - Ala								
C'	175.2	175.4		172.6	174.0		176.3	175.0
$C\alpha$	49.8	49.9		49.1	49.7		57.0	49.8
$C\beta$	23.6	23.7		19.8	23.5		18.5	23.3
N				125.5			117.0	126.2
H								7.5
$H\beta$								0.9
24 - Val								
C'	176.4	176.3		175.6		176.6	178.3	174.1
$C\alpha$	59.0	59.0		59.0		58.7	59.7	60.3

Residue	Ishii (Cu)	Ishii	Madhu	Bertini	Tycko (Iowa)	Tycko 2009	Tycko 2013	Kelly (Cu)
24 - Val								
Cβ	35.8	35.8		32.7		35.8	34.6	35.3
Cγ	21.5	21.5		19.8		22.7	20.7	21.2
H								8.6
Hα								5.6
Hβ								1.9
$H\gamma_{1/2}$								0.7
$H\gamma_{1/2}$								0.8
25 - Gly								
Cα	42.5	42.4		45.5		47.1	46.8	49.7
N				110.3			110.1	115.8
H								8.8
Hα								3.8
26 - Ser								
C′				171.2			173.5	174.3
Cα				55.1			56.9	55.9
Cβ				65.0			64.8	65.2
N				110.5			111.2	119.1
27 - Asn								
Cα				52.2			52.5	54.5
Cβ				42.8			42.9	44.5
$N\delta_2$							120.7	115.4
Hα								5.4
$H\beta_3$								2.2
$H\delta_{21}$								7.4
28 - Lys								
Cα			54.6	54.1	55.5	55.9	53.8	55.5
Hα								5.2
Hβ								1.9
29 - Gly								
C′				173.0		171.5	171.9	171.9
Cα				39.6		45.0	48.6	43.5
N				105.4			113.8	109.2
H								6.9
$H\alpha_2$								4.5

Residue	Ishii (Cu)	Ishii	Madhu	Bertini	Tycko (Iowa)	Tycko 2009	Tycko 2013	Kelly (Cu)
30 - Ala								
C′	174.2	174.2	174.3	172.8	174.6	174.2	175.1	175.2
Cα	49.9	50.0	48.7	51.2	50.4	50.5	50.3	49.9
Cβ	23.0	23.2	20.9	22.7	22.1	21.6	23.5	21.5
N				122.2			119.6	126.3
H								9.0
Hα								5.5
Hβ								1.7
31 - Ile								
C′				172.7	173.5	174.2	172.8	174.2
Cα	61.3	61.4		59.7	59.3	60.8	56.3	60.8
31 - Ile								
Cβ	40.2	40.2		38.5	41.0	40.3	38.4	39.9
$C\gamma_1$	28.3	28.3		27.0	26.9	27.6	27.8	27.9
$C\gamma_2$	19.4	19.4		16.0	16.6	18.8	14.5	19.2
$C\delta_1$	13.9	13.9		12.9	13.5	15.0	15.2	13.7
Hα								4.8
Hβ								1.9
$H\gamma_{12/13}$								1.6
$H\gamma_2$								0.9
$H\delta_1$								0.7
32 - Ile								
C′				174.1	173.7	176.8	175.9	176.1
Cα	58.2	57.9		58.0	58.4	58.3	58.5	57.6
Cβ	42.5	42.4		38.9	41.2	42.2	41.1	42.4
$C\gamma_1$	27.1	27.2		25.3	27.1	27.4	27.1	26.8
$C\gamma_2$	18.5	18.4		15.8	16.9	18.0	16.5	17.2
$C\delta_1$	14.5	14.6		13.2	13.4	15.0	14.7	14.0
H								8.8
Hα								5.5
Hβ								1.8
$H\gamma_{12/13}$								1.6
$H\gamma_2$								0.8
$H\delta_1$								0.7
33 - Gly								
Cα	45.0	45.2		44.2			48.6	48.9

Residue	Ishii (Cu)	Ishii	Madhu	Bertini	Tycko (Iowa)	Tycko 2009	Tycko 2013	Kelly (Cu)
33 - Gly								
N				115.4			113.9	115.8
H								9.0
$H\alpha_2$								4.3
$H\alpha_3$								3.5
34 - Leu								
C'			173.1	172.3	173.2	173.7	173.8	174.0
$C\alpha$	54.3	54.3	52.7	52.2	53.1	54.6	54.2	53.6
$C\gamma$	29.0	29.1	45.1	27.6	25.9	28.9	27.7	28.7
$C\delta_1$	26.5	26.4	24.9	26.0	24.9	24.4	25.9	25.4
H								8.8
$H\alpha$								5.1
$H\beta_{2/3}$								1.6
$H\delta_{1/2}$								0.9
$H\delta_{1/2}$								0.7
37 - Gly								
$C\alpha$	44.7	45.2		44.9			47.8	48.9
N				109.5			116.1	115.8
H								9.0
$H\alpha_2$								4.3
$H\alpha_3$								3.5
38 - Gly								
C'	172.3	172.5	170.3	168.9	170.0		169.8	176.8
$C\alpha$	44.6	45.1	42.4	42.8	44.8		44.9	46.0
N				104.5			106	110.6
40 - Val								
$C\alpha$				60.1	60.3		59.4	60.2
$C\beta$				33.7	33.7		33.2	36.8
$C\gamma$				19.7	20.1		21.7	22.7
$H\beta$								1.6
$H\gamma_{1/2}$								0.5

take ^{1}H chemical shift values so a comparison with those taken in this study is not possible.

Secondary chemical shift analysis has been performed, see Fig. 7.18, which indicates there exists two β-sheet sections between residues 15 to 22 and 28 to 32 which could well be linked by a turn section; most previously published models have a β-sheet−turn−β-sheet motif, so the break in β-sheet structure has been identified as a turn section in the sequence. Further assignment will enable a more detailed picture of the structure of these aggregates to be produced.

TALOS-N predictions

Chemical shift values were input into the TALOS-N online system [170] and predictions of torsion angles were obtained, and are displayed in Table 7.2. Here ϕ and ψ are standard torsion angles, with $\Delta\phi$ and $\Delta\psi$ the estimated standard deviations of the prediction errors in ϕ and ψ. 'Dist' is the TALOS-N database matching score, 'S2' is the Wishart random coil index chemical shift order parameter [253], 'Count' is the number of database triplets used to form the torsion angle predictions and 'Class' is the classification of the prediction result where STRONG/GENEROUS have a majority consensus in database matches and so the prediction is very likely to be good and WARN means there was no consensus in database matches. 18 'strong' fits were found, 3 'generous' fits and 3 'warn' fits were found. Interestingly all fits with warnings were based on data from glycine residues.

Table 7.2: TALOS-N torsion angle predictions.

Residue	ϕ	ψ	$\Delta\phi$	$\Delta\psi$	Dist	S2	Count	CS Count	Class
7 - Asp	−70.8	114.2	11.4	35.2	2.04	0.73	25	6	STRONG
8 - Ser	−144.1	151.1	10.2	10.1	1.92	0.74	25	5	STRONG
9 - Gly	142.5	145.1	51.6	76.3	4.14	0.74	5	6	WARN
14 - His	−69.9	−36.2	11.7	7.6	0.70	0.85	8	11	GENEROUS
15 - Gln	−146.0	146.3	12.6	10.1	0.47	0.86	25	8	STRONG
16 - Lys	−120.5	142.1	29.2	12.2	0.52	0.87	25	10	STRONG
17 - Leu	−116.8	137.4	15.9	12.5	0.45	0.87	25	9	STRONG
18 - Val	−105.1	126.5	12.0	10.2	0.41	0.86	25	6	STRONG
19 - Phe	−93.5	132.7	12.2	9.5	0.42	0.87	25	6	STRONG
20 - Phe	−131.5	149.9	10.4	10.9	0.48	0.88	25	6	STRONG
21 - Ala	−139.2	151.2	14.8	11.1	0.48	0.88	25	6	STRONG
24 - Val	−118.7	118.8	12.0	17.4	0.82	0.85	25	5	STRONG
25 - Gly	65.9	−121.8	6.1	8.1	0.78	0.84	25	9	STRONG
26 - Ser	−107.3	14.0	12.1	12.2	1.02	0.82	25	8	STRONG
27 - Asn	−112.6	145.9	21.4	10.6	1.20	0.87	25	9	STRONG
28 - Lys	−125.6	144.3	20.2	14.0	1.14	0.89	25	9	STRONG
29 - Gly	153.8	−169.1	49.2	14.1	0.77	0.81	8	7	WARN
30 - Ala	−120.2	139.0	18.7	16.2	0.80	0.87	25	9	STRONG
31 - Ile	−98.5	131.9	13.6	8.5	0.71	0.88	25	9	STRONG
32 - Ile	−127.2	146.3	10.2	14.0	0.72	0.88	25	8	STRONG
33 - Gly	63.6	−123.9	6.2	7.2	0.71	0.84	10	7	GENEROUS
34 - Leu	−106.0	131.0	12.7	17.8	1.27	0.87	9	7	GENEROUS
37 - Gly	−5.6	10.5	76.8	72.9	1.29	0.77	25	4	WARN
38 - Gly	−64.1	−29.03	5.5	10.6	1.30	0.77	25	4	STRONG

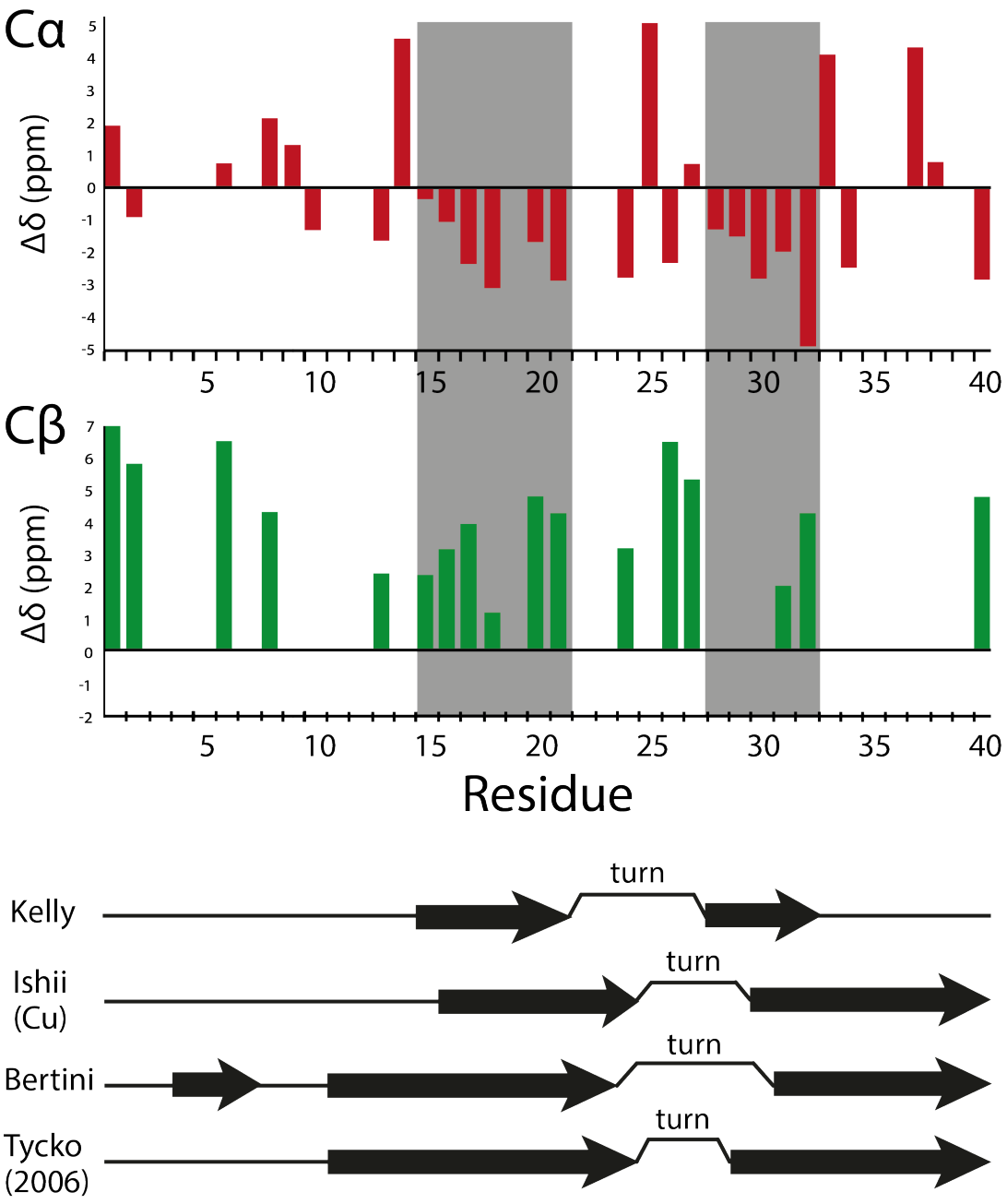

Figure 7.18: Chemical shift analysis indicates the presence of two sections of β-sheet between residues 15 to 21 and 28 to 32. Here $\Delta\delta$ is the difference in chemical shift to random coil chemical shift values for the respective residues obtained from the BMRB. The secondary structure as indicated by the chemical shift analysis has been illustrated below the graphs. Previously published secondary structures are shown for comparison [63, 86, 102].

7.4 Discussion

Amyloid-beta plaques found within Alzheimer's-disease-affected patient's brains are often found with higher-than-normal concentrations of copper, zinc and iron within them. In this chapter, solid-state NMR and electron microscopy data are presented of amyloid aggregates created upon introduction of copper ions to an amyloid suspension; a relevant and interesting form of aggregate yet to have been studied by ssNMR. It is found that the chemical shifts differ to previous models, that the microscopy images show substantial linked networks of aggregates, and that secondary chemical shift analysis suggests the existence of two β-sheets between residues 15-21 and 28-32. The TALOS-N software for torsion angle prediction was utilised and suggested 18 'strong' fits and 3 'generous' fits.

Though the precipitation of Aβ aggregates by metal ions has been reported, [270] to the best of our knowledge this precise sample protocol has not been previously documented and so, combining this with the slow re-ordering of these aggregates to a more fibril-like form following hydration, these $A\beta_{1-40}$/Cu aggregates are a novel species. Moreover, these networks of $A\beta_{1-40}$/Cu aggregates have not been observed, making them also a novel sample. Of the previously documented samples, included in Table 7.1, of Aβ fibrils it is interesting to note the most similar in chemical shift values, as calculated using the root-mean-square deviation of chemical shift values, is a sample seeded from brain-extracted plaque fragments. [64] This clearly supports a claim that this sample is extremely physiologically relevant, and therefore of significant importance especially if potential treatments for the disease, which aim to target the pathological structures involved in AD, characterised here by these plaques, are to work on a biological and structural level.

7.4.1 Hydration

The hydration of the sample was shown to significantly increase the resolution of the spectra obtained from 2D ^{13}C-^{13}C correlation experiments performed on the sample, see Fig. 7.4. Hydration has been shown to effect the resolution achievable on biological systems previously, with a study on α-synuclein revealing 36% (mass of water/total mass) as the optimal level of hydration for fibrils of this type, [53] however groups working on Aβ often fully hydrate their samples before commencing ssNMR experiments. The Tycko, Ishii and Madhu groups use the same protocol of hydrating by 0.5 μl of deionised water per mg of fibrils, [55, 90, 93] with Tycko's group noting that

the signals for A2 and G9 are reduced in the hydrated state relative to the volume of the V12 Cα-Cβ cross peak from the unhydrated state to the hydrated one, which is explained in the form of dynamics in the N-terminal. The group reports the same hydrated-sample signal reduction for S8 which is not the same as was found for the sample in this chapter; Fig. 7.4 clearly shows that signals from S8 are far stronger in the hydrated state, even when compared to the volume of the V12 Cα-Cβ peak. The Bertini group simply refer to their fibril as remaining fully hydrated throughout all steps, and no data is shown from the sample in a lyophilised state. [63] The brain extract samples from the Tycko and Meredith collaboration were hydrated with 0.5-1.0 µl of deionized water per mg of $A\beta_{1\text{-}40}$, in the 2009 work, or simply 'hydrated', for the 2013 report. [64, 110] Clearly it is important for ssNMR studies of amyloid proteins that the sample is hydrated to some extent before experiments are begun, with the data here supporting this viewpoint.

7.4.2 Effect of Magnetic Field

It is clear from the spectra within this chapter, shown in Fig. 7.5, that increasing the magnetic field increases the resolution of 2D carbon-carbon correlation spectra on small proteins. That the linewidths of peaks from both extremes of the aliphatic region have been identified as having reduced linewidths in the spectra obtained at the higher magnetic field (I31Cβ-$C\delta_1$ for the low chemical shift region and S26Cβ-Cα for the high chemical shift region) suggests a level of improvement across the entire spectrum, which, here, enabled the assignment of correlations which were previously obscured. A report from the Ishii group corroborates the findings shown in this chapter, [108] whereby with increasing magnetic field one can increase the resolution of 2D and 3D spectra taken on biological samples (the group show results taken on samples of GB1 and copper-bound $A\beta_{1\text{-}40}$ fibrils). Alongside altering the two fields used (from 400 to 750 MHz), the Ishii investigation changes the MAS frequency (from 40 to 98 kHz) and pulse sequence used (which is necessary by virtue of the use of greater MAS frequency), whereas in this study the field was altered separately so as to see the direct effect on resolution of increasing the field from 600 to 850 MHz. When comparing the two spectra produced by the two experimental setups well resolved spectra were obtained after 21.9 h, for the setup with 400 MHz field and 40 kHz MAS, but only 5.4 h, for the setup with 750 MHz and 98 kHz MAS. Clearly there are significant gains to be had when using high fields and rapid MAS frequencies.

7.4.3 Effect of Copper Ions

The effect of copper ions on the aggregation of the $A\beta_{1\text{-}40}$ is significant. Such an extrapolation is clear from Fig. 7.6 wherein the linewidths are far narrower and certain residues have had shifts in the chemical shifts of spins within them. A further interesting note is that seeding of amyloid fibril samples, a technique specifically done so as to increase the homogeneity of the sample, has previously provided linewidths of 1.5 to 2.5 ppm [62,93] wherein the fibrils investigated were from seeded generation 12 to 15.[6] In contrast the linewidths of the sample investigated in this chapter were <0.5 ppm. It can therefore be suggested that copper plays the role of a 'directing' agent towards a very well defined supramolecular structure of $A\beta_{1\text{-}40}$ aggregates. It can be presumed that the copper is 'locking' these $A\beta_{1\text{-}40}$ aggregates in a specific conformation, whereas a 'multiple seeding' procedure is a less selective protocol and so leads to a larger dispersion of the secondary (and side-chain) structures in $A\beta_{1\text{-}40}$ amyloid fibrils. This could also provide an explanation for the immediate precipitation of the aggregates observed duing the sample preparation.

7.4.4 Use of 0.8 mm Probe

The use of rotors with small diameters allows rotation at rapid MAS frequencies which in turn can enable inverse detection experiments, with sufficient ^{1}H resolution for assignment, to be performed. This type of experiment is routinely used in solution NMR however its use in a solid-state context is limited due to the difficulty in attaining suitable proton resolution for chemical shift assignment. The experiments performed here using inverse detection complemented the work on ^{13}C and ^{15}N taken at much lower MAS frequencies. The inverse detection experiments (H-C, H-N, C-N-H and N-H-H) account for ∼46% of the chemical shift assignments in Table 7.1.

Furthermore, due to the use of proton-detected experiments and the paramagnetic sample, the recycle delay used could be much less than half a second (0.2 s) which allowed rapid acquisition of spectra. For comparison, a sequence that typically takes ∼9 hours to obtain a well resolved spectrum when using a 2.5 mm HX probe took less than 2 hours with the 0.8 mm probe. Of course such a short recycle delay would not be possible without the relaxation effects of the paramagnetic Cu, however this experimental set up is particularly exciting due to this factor, and paramagnetic doping in biological samples is now being widely used so as to allow such rapid acquisition

[6] Wherein generation n+1 was formed from sonicated fibril fragments taken from generation n

studies to be performed. [108] Further experiments will be run in this arrangement and are likely to include 3D NCOCX and NCACX experiments, which will provide further information on ^{15}N-^{13}C correlations displayed in Figs. 7.11 and 7.12 which, although these 2D spectra display significant spectral crowding, will provide well resolved spectra through use of the third dimension which should separate out many of the overlapping correlations.

Improvements in NMR hardware are clearly important for increasing the ability of solid-state NMR to structurally solve biologically relevant and interesting samples, with the use of high magnetic fields and rapid MAS frequencies producing a number of impressive spectra as shown here, and in other published work. [271–273] Increasing acheivable MAS frequencies, however, cannot continue indefinitely, there is a limit set by the speed at which the gas can flow over the rotors (although current gas sources are typically air or nitrogen, so this has not been exhausted as of yet), a mechanical limit to the stresses that the rotors (currently made of ZrO_2 with vespel caps) can take, and a practical size limit, packing a 0.8 mm rotor is troublesome and smaller rotors will only become harder to pack (unless a reliable method is developed for packing by centrifuge, however this will place the rotor under significant mechanical stress).

Hardware will continue to improve and increase the structure-solving ability of ssNMR, however there will come a limit to this increase through the improvement of hardware alone. Though ssNMR will still be the prefered tool for investigating biological samples with local order, experimental techniques will be required for obtaining high resolution data on samples such as large proteins, proteins incorporated in lipid membranes and even whole cells as improvement in hardware will not, solely, be sufficient to achieve this for the majority of samples.

7.4.5 Assignment

Table 7.1 contains the chemical shift assignments obtained in this work for A$\beta_{1\text{-}40}$/Cu aggregates. In total, there are 174 assignments, with 16 C$'$, 67 aliphatic ^{13}C, 13 ^{15}N and 78 ^{1}H assignments.

In the entire sequence of A$\beta_{1\text{-}40}$ there are 237 protons; in Fig 7.15 there are a total of 161 peaks, as recognised by the SPARKY software, which is understandable due to the amount of overlap that is to be expected due to the similar chemical shifts among the protons in the peptide and the relatively broad linewidths. More-

over, it has been claimed that the N-terminus of Aβ is unstructured and possibly dynamic and, therefore, that signals from the residues within these regions are often significantly broadened. [104] With the 78 proton assignments made using the inverse detection experiments, the percentage of total proton assignments made is ∼33%, with the percentage for proton assignments made from the total number of proton correlations observed using inverse detection experiments reaching over 48%. The remaining 83 correlations require further aliphatic carbon assignments before they can be accurately assigned from Fig. 7.15, or additional nitrogen assignments are required if further proton assignments are to be obtained from Fig. 7.17. Clearly the limiting factor is not in the proton assignments but the assignments from the other nuclei.

The total number of carbon nuclei within the sequence of $A\beta_{1\text{-}40}$ is 194, with the total number of carbons assigned here equalling 83, or ∼43%. A significant number of carbonyl assignments are missing alongside almost all aromatic carbons from the phenylalanine (4, 19 and 20), histidine (6, 13, and 14) and tyrosine (15) residues, with the details of these carbon assignments reading: for carbonyl, 16 assignments from a total of 40; and for aromatic, 2 assignments from a total of 33. Though these regions require significantly more assignment, the aliphatic region shows reasonable assignment with 65 assignments from a total 121. Although these may appear to show a poor overall level of assignment, there are two major factors to consider: as mentioned above, there are studies which have shown the dynamic nature of the N-terminus, [104] which would hinder any significant assignment of this region; secondarily, the binding sites of the copper will cause nearby signals to be quenched due to the enhanced paramagnetic relaxtion. Ishii's group reported binding sites located at the Nϵ in H13 and 14, alongside the side chains of E3, E11 and E22 and a binding site at the end of the C-terminus, V40. As can be seen in Fig. 7.19 the binding sites at E11, H13, H14 and E22 correlate well with the regions of low assignment percentage, though a similar quenching is not found for the E3 and V40 suggested binding sites. The assignments made for H13 and 14 here are Cα (for both) and Cβ, H and Hα (for H13), which are mostly backbone nuclei and as such would be located the furthest distance from the quenching effect of the copper, if it were binding to the significant sidechain of the histidine residues. No assignments were able to be made for E11 and 22 which corelates well with the suggested binding sites in these regions, especially as both have neighbouring residues with poor assignment, possibly by virtue of the proximity of the copper molecules. In comparison to this, several assignments were made for residues E3 and V40, which are also suggested binding sites. However, as

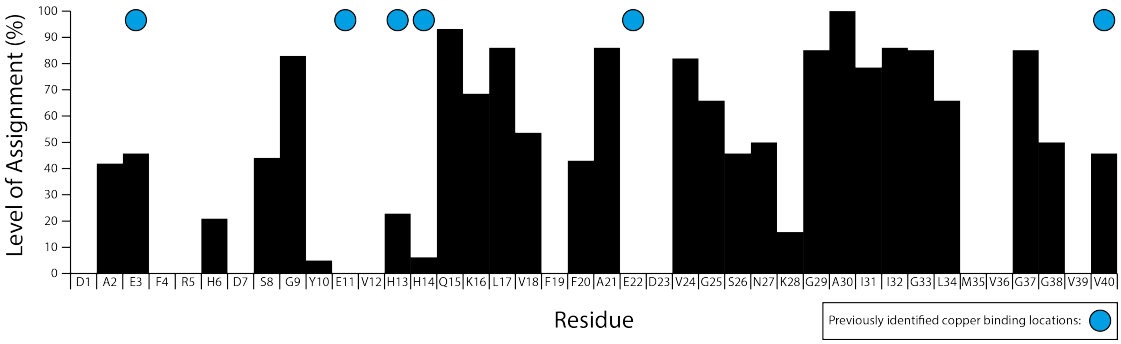

Figure 7.19: The level of assignment for each residue in this work is shown alongside the binding sites identified by the work from the Ishii group. [102] The level of assignment is measured as the percentage of chemical shifts assigned over the total number of distinct chemical shifts within the residue.

the sample preparation differed from that of previous samples, it is not unexpected that some variations are found in the behaviour of the sample.

Any prediction for the stoichiometry of the copper-peptide complex can only be based on the chemical shifts that have not been found during the investigation and the assumption that some of these missing chemical shift values are likely to be due to the quenching effect of the copper. This prediction would also utilise the likely binding residues, which previously have been shown to be D, E, H and V: a number of which exist in the $A\beta_{1\text{-}40}$ sequence. As illustrated in Fig. 7.19 there are clear locations of poor assignment which may be due to binding of copper to these residues, and it is from this alone that a prediction can be made. Such a claim however would be most tentative and therefore one will not be provided here.

That roughly a third of all protons have been assigned is impressive for an amyloid-β aggregate considering none of the other Aβ structures in Table 7.1 have proton assignments. There are 83 peaks left to be assigned on the spectra in Fig. 7.15, but these can be assigned once further ^{13}C assignment has occured. There are 111 remaining carbons to be assigned, which could be investigated through the use of 3D DCP experimenets such as NCACX, which will provide more ^{13}C assignments for residues with ^{15}N and Cα assignments already made. The discovery of further carbon and nitrogen assignments is currently the rate limiting factor for finding proton chemical shifts, and therefore experiments such as those proposed here will offer a chance for assigning chemical shifts from all three nuclei.

7.4.6 Chemical Shift Analysis & TALOS-N Predictions

The predictions made by the TALOS-N online program, which included secondary chemical shift analysis, imply that the overall secondary structure of the aggregates investigated in this study is similar to that found for many of the previously published models. The β-sheet−turn−β-sheet structure has been reported for many fibrillar forms of Aβ and so provides a reassuring check on the validity of the chemical shifts found for the sample investigated in this chapter, see Fig. 7.18. Moreover, the turn region is located in the typical Aβ region, residues 22 - 28. The structure shares features with some of the previously published models, as shown in Fig. 7.18, such as: the starting region of the first β-sheet with the Ishii model [102] (residues Q15 and K16 for this model and the Ishii mode,l respectively); the concluding region in the first β-sheet (or start of the turn section) with the Bertini model [63] (residues E21 and D23, respectively); and the beginning of the second β-sheet (and conversely the end of the turn region), which is in a similar region to the Tycko model (residues K28, for this sample, and G29, for the Tycko model).

Though the β-sheets found for this sample are shorter than all previous models, this is likely to be due to a lack of assignment in the first β-sheet region, and a lack of specifically Cβ assignments for the second β-sheet. More Cβ assignments for residues 32 and onwards may well imply that the β-sheet extends, however due to the positive $\Delta\delta$ of the Cα chemical shift assignment for G33 it must be assumed that the β-sheet finishes at residue 32. A similar shortening occurs due to the positive $\Delta\delta$ of H14Cα, which otherwise could be assumed to continue through to Y10 (which would then compare well to the β-sheet starting points of the Bertini and Tycko models, both E11). Furthermore, the β-sheet between residues 15 - 22, could be extended up to the positive $\Delta\delta$ value for G25, as the $\Delta\delta$ values for V24 are those typically associated with a β-sheet; this would then agree with the starting location of the turn with both the Tycko and Ishii models, with Ishii's model obtained from the sample Aβ with Cu^{2+}. It has been claimed the structure is as shown in Fig. 7.18 because without the chemical shift values of the residues inbetween, it is impossible to say for certain that a β-sheet exists between these residues (22 and 24). If the β-sheet was shown to include those residues, not only would the location of the turn but the size of the turn would then be very similar to both the Tycko and Ishii models.

The Bertini model proposes a short section of β-sheet in the N-terminus, which had previously thought to be disordered, between the residues F4-D7. The chemical shift analysis in Fig. 7.18 for the sample investigated in this chapter could be interpreted as

suggesting a similarly short section of β-sheet between residues H6-G9 which would not encompass all the same residues as the Bertini model, but would agree with the proposed small section of ordered N-terminus within the aggregated form of the peptide. This has not been included here as it was felt a continuous set of chemical shifts suggesting the existence of a β-sheet was required to claim that a β-sheet occured between certain residues.

The torsion angle predictions made by the TALOS-N program, shown in Table 7.2, contain 18 'strong', 3 'generous' and 3 'warn' classifications. The 21 'strong' and 'generous' predictions are found to agree well with the vast database used by the program and can be assumed to be indicative of reasonable assignment for the chemical shifts values of those residues. The 3 'warn' classifications, which all occur on glycine residues (G9, 29 and 37), are indicators that there was no correlation to the database, which may imply the assignments for these need revisiting. The assignments for the glycine residues however, as can be seen in Figs. 7.16 and 7.11, are not within spectrally clutttered regions but are found as well defined resonances. The percentage of classifications in the 'strong' category is 75%, with 'generous' and 'warn' classifications sharing the remaining 25%. It is interesting to note, therefore, that between the residues which have been identified as maintaining a certain type of structure (either β-sheet or hairpin-turn), residues 15 to 32, the amount of strong classifications increases to ∼94%. Moreover, the 3 'generous' classifications (which, as mentioned in § 7.3.6, still have a majority consensus in database matches) are directly linked to these structured regions, residues 14, 33 and 34. This implies that certainly the central section of the sample has been well characterised, and possibly that the N- and C-terminal require further assignments. This may also indicate however, a level of molecular dynamics within these regions as mentioned earlier which have resulted in uncharacteristic predictions for the torsion angles.

The TALOS-N online program was also used to generate torsion angle predictions for a second group of chemical shifts. The second group contained none of the ^{1}H chemical shift values obtained but retained all others from the group of chemical shifts which were used to produce Table 7.2. This was performed so as to enable a quantitative view as to the impact of proton chemical shifts on torsion angle predictions. In short, 6 of the 24 torsion angle predictions decreased in quality by at least one grade[7] or were unable to be made. Specifically, for H14, N27, K28 and L34 no predictions were made and for D7 and G38 the prediction quality decreased from strong to warn

[7]Whereby the TALOS-N grading system for predictions, in order of decreasing reliability, is strong, generous and then warning

and from strong to generous, respectively. That, here, a quarter of predictions suffer from the omission of proton data clearly shows that the proton chemical shift values are of significant importance in producing high quality torsion angle predictions for structures. It is suggested that, where possible, ssNMR structural studies conducted on biological samples utilise ^{1}H chemical shift values so as to enable high quality structures to be made. The work shown herein has indicated that obtaining ^{1}H chemical shift values is possible on semi-ordered samples, and that the benefit that such data brings is well worth the effort made to obtain it.

7.4.7 Chelation of Aggregates and its Impact

Finally, a previously unmentioned interesting aspect of this sample is that these aggregates are likely to be some sort of kinetic trap, 'trap' because they decompose completely into monomers when a copper(II)-chelating agent, such as EDTA, is added to the solution of Aβ_{1-40}/Cu; this phenomena (complete decomposition into the monomeric form) has not been documented in such an extreme form, though Fischer and co-workers have reported a reduction of aggregate diamter size from 2.5 μm to 250 nm. [270] This implies that the overall stability of the aggregates is linked to, and probably dependent on, the presence of the copper. The pathology of Alzheimer's disease is linked to the aggregation of monomeric Aβ of various forms (mostly the 1-40 and 1-42 variant, with the 1-42 variant particularly cytotoxic) and this aggregation creates toxic structures, such as oligomers, protofibrils and finally fibrils. That this sample can be decomposed by chelating the copper, suggests a method for therapeutic treatment via the removal of the metals which are found to congregate in the plaques during aggregation and many groups around the world are investigating this avenue of thought. Some developments that support this endeavour include: a report detailing the decrease in brain Aβ deposition by 49% in transgenic mice treated with a bioavailable Cu/Zn chelator, though this increased the overall level of soluble Aβ; [274] a report revealing that high levels of copper in aging mice brain capillaries reduces low-density lipoprotein receptor-related protein 1 (LRP1), which is responsible for the transportation of Aβ, which consequently leads to high Aβ levels in the brain, whereas high levels of copper in the parenchyma (neurons and glial cells) increases Aβ production and neuroinflammation, stressing the importance of chelators which can cross the blood brain barrier, such as PBT2; [275,276] work on chelators that avoid allowing copper to re-distribute back into the local medium after attaching to the chelator, which is crucial for long-term effective treatment; [277] a report detailing the behaviour of PBT2 in collecting metals from plaques and redis-

tributing them back into the cell, such that the deposited metal can then activate neuroprotective cell signalling pathways. [278]

7.5 Outlook

ssNMR has been used by many groups to structurally investigate amyloid fibrils of Aβ, with the many results reinforcing a view of polymorphism adopted during the various aggregatory stages. The work presented in this chapter has included standard biological ssNMR techniques, such as the DARR and DCP experiments, alongside the more exotic 2D and 3D inverse detection experiments performed at 100 kHz MAS. These experiments have enabled the sample to have chemical shift assignments made and compared to previously published models. The chemical shifts are found to be most similar to a sample of brain-extract-seeded fibrils which gives weight to the hypothesis that this sample is physiologically relevant, a particular goal for synthetic samples to strive to achieve; studies have shown that Alzheimer's plaques in the brain are found with increased level of copper, which this sample contains possibly explaining the similarity with the brain-extract-seeded sample. This study, therefore, signifies the importance of copper during fibrillisation in the creation of Aβ fibrils, the structures of which may be used for the development of therapeutic treatments.

The work presented here is clearly not complete, further chemical shift assignments are required to fully characterise the structural form adopted by these aggregates, and insights into the functional locations within the sample can be found through investigations into the dynamics of the sample. Once chemical shift assignments are closer to completion a more precise indication of the location of the binding sites for the copper ions can be extracted; the final signals that evade assignment are likely to be those that are having their signals quenched by nearby paramagnetic ions. It is thought that such information will be obtained from 3D experiments investigating combinations of correlations of the nuclei investigated here, ^{1}H, ^{13}C and ^{15}N.

8

Amyloid-β_{1-42} protofibrils stabilised by cross-linked cysteine replacements at positions 21 and 30

This chapter contains the results of work performed on a stabilised intermediate of the particularly toxic A$\beta_{1\text{-}42}$ variant of amyloid-beta. Cysteine mutations at locations A21 and A30 result in a sulphur bridge across the β-hairpin conformation, adopted by aggregating Aβ, forcing the aggregation to be halted at an oligomeric form. In this manner, 2D ^{13}C-^{13}C DARR spectra were recorded on an interesting system which is otherwise transient and therefore difficult to study using ssNMR; specifically, the chemical shifts of specific residues in selectively labelled samples have been obtained allowing the turn region of the β-hairpin to be characterised. 1D ^{31}P NMR indicates the destabilising effect of these oligomers, as well as cholesterol and curcumin, on phospholipid membranes; however, when the oligomers are combined with curcumin before addition to the membranes, this destabilisation is not observed, suggesting that curcumin has a role as a potentially therapeutic molecule.

8.1 Introduction

Amyloid-beta is known to aggregate *in vivo* towards fibrils and that significant damage can be done to neurons within the brain during this process, however current belief is that the most cytotoxic conformation could well be a transient form which is either on- or off-pathway to these fibrils. [279–283] As the current targets for pharmacological treatment, soluble pre-fibrillar oligomeric and protofibrillar forms of the peptide, are not stable, studying such a form through solid-state NMR is indeed a

difficult task; after a few months of obtaining data, variations in previously assigned chemical shifts might be seen before finding, via EM, that the sample is now no longer homogeneously oligomeric or protofibrillar but rather a further aggregated form. An ingenious solution to this problem is to stabilise this transient species using a sulphur bridge across the β-turn section of the molecule by replacing alanines at positions 21 and 30 with cysteines. This mutated Aβ peptide was shown to be able to form soluble oligomers and protofibrils, but is unable to adopt the cross-β structure observed in mature fibrils; this work was performed initially by Härd and co-workers. [60] These $A\beta_{1-42}$CC oligomers are stable over long time periods enabling solid-state NMR to be used to study their structure, however once the disulphide bond is broken by reduction, further fibrillation can occur indicating that the stabilisation is sufficient to halt aggregation temporarily at the oligomeric form without fully re-structuring the peptide and producing a physiologically irrelevant sample. [60] If it could be shown that these stabilised oligomers had the same behaviour as naturally occurring oligomers, this approach would become invaluable in investigating what was previously thought to be unobtainable. A further study by the Härd group has shown that many similarities exist such as morphology and size, surface properties and exposed antibody epitopes, protein binding and effect on synaptic activity in neurons, between naturally occurring $A\beta_{42}$ protofibrils and those formed from $A\beta_{42}$CC samples. [284]

Aβ oligomers are known to structurally damage cell membranes, therefore the efficacy of potential remedies regarding membrane protection can be investigated using a set of ^{31}P NMR experiments; by comparing the phosphorus spectrum from the membrane alone, the spectrum from a sample of lipid membranes and the destructive Aβ sample, and then finally the spectrum from a mixture of both the Aβ peptide and the remedy. The order in which these three are combined is also an interesting variable, as the binding order could impact significantly on the structures. Analysis of the ^{31}P lineshapes indicates whether any changes to the vesicles have occurred. Moreover, 2D ^{13}C-^{13}C DARR experiments investigating the structure of the oligomeric/protofibrillar form of the peptide can be performed, so as to gain an understanding of the variation in the structure of the peptide that might be responsible for the increased toxicity of this species over species from earlier or later in the aggregation pathway.

A potential remedy of significant scientific interest currently is curcumin, a major component of the traditional spice turmeric. It has long been used for medicinal purposes in India and China, and has recognised pharmacological properties such as being antioxidant, anticancer, antibiotic, antiviral, antifungal, antiamyloid, antidia-

betic, anti-apoptotic and anti-inflammatory. [285] Due to the significant diversity in the effect of curcumin, it was postulated that its effect was unlikely to be directly on the causes of each of the diseases and disorders from the above list, but rather on a factor that they held in common. As such, significant work has gone into investigating the effect of curcumin on cell membranes and whether an alteration by a molecule to such a surface could create such a varied range of beneficial effects. [286] So far, however, there is no consensus on a particular trait belonging to curcumin that could lead to its important, but varied, medical properties.

8.2 Experimental Details

8.2.1 Sample Preparation

Samples of selectively labelled A$\beta_{1\text{-}42}$CC were prepared in Luleå University of Technology under the supervision of Andrei Filippov, or by Christofer Lendel (recombinant U-[^{13}C, ^{15}N] A$\beta_{1\text{-}42}$CC) at the Swedish University of Agricultural Sciences in Uppsala. The work performed by Dr. Lendel used many samples of U-[^{13}C, ^{15}N] A$\beta_{1\text{-}42}$CC oligomers, including lyophilised and rehydrated oligomers and oligomers sedimented from a buffer solution using ultra-centrifugation into a rotor.

Selectively Labelled A$\beta_{1\text{-}42}$CC Samples

Samples of selectively labelled A$\beta_{1\text{-}42}$CC oligomers were produced from peptides which were synthesized by the standard fast F-moc SPPS on an automated peptide synthesizer (Applied Biosystems Model 433A) with HBTU activation, cleaved by TFA with radical scavengers and precipitated in *tert*-MBE, for ssNMR experiments such that an unambiguous assignment of NMR signals and a precise characterisation of the turn section were possible. The various labelling schemes, and their shorthand names which will be used later in the chapter, are described below:

'Crys 1' - A$\beta_{1\text{-}42}$CC with U-[^{13}C, ^{15}N] labels at D23, V24, G25, S26 and K28.

'Crys 2' - A$\beta_{1\text{-}42}$CC with U-[^{13}C, ^{15}N] labels at L17, V18, G29 and M35.

'Crys 3' - A$\beta_{1\text{-}42}$CC with U-[^{13}C, ^{15}N] labels at K16, N27, V36 and G37.

'F19I32' - A$\beta_{1\text{-}42}$CC with U-[^{13}C, ^{15}N] labels at F19 and I32.

'F20I31' - A$\beta_{1\text{-}42}$CC with U-[^{13}C, ^{15}N] labels at F20 and I31.

U-[^{13}C, ^{15}N] - uniformly labelled A$\beta_{1\text{-}42}$CC.[1]

Lipid Membrane Preparation

^{2}H labelled and non-labelled lipid mixtures were dissolved in ethanol within glass test tubes, to ensure that ^{2}H labelled lipids intersperse with non-labelled lipids, and were then centrifuged, to ensure all material was compacted at the end of the tube. The glass test tube was then placed under a gentle stream of dry nitrogen, to further mix the solution and to evaporate any excess liquid before being freeze dried. The lyophilised material was then redissolved in water and the material was, again, centrifuged. Following this, the tubes were sealed using a micro torch, to form pods. To ensure any fully- or partially-formed lipid networks were disrupted, the pods were subjected to alternating submersions into liquid nitrogen and warm water (freeze-thaw section). This ensured the lipids rapidly underwent phase transitions (around 20 °C) so that membrane formation only occurred when the sample was fully prepared (i.e. with all components equally dispersed throughout the sample), alongside making the lipid layers smaller and more homogeneous.

Amyloid-Beta Oligomerisation Protocol:

Four solutions were required for the oligomerisation protocol employed in this work:

'Solution 1': 2.2 g CH_6ClN_3 (GuHCl),[2] 3.3 ml H_2O

'Solution 2': 20 mM Na_3PO_4, 50 mM NaCl, 5 mM EDTA, 3 L H_2O

'Solution 3': 20 mM Na_3PO_4, 50 mM NaCl, 3 L H_2O

'Solution 4': 5 mM Na_3PO_4, 5 L H_2O

The peptide was dissolved in Solution 1 in a falcon tube to ensure the sample of A$\beta_{1\text{-}42}$CC peptide was in monomeric form; GuHCl facilitates disaggregation of pre-formed aggregates of A$\beta_{1\text{-}42}$CC and encourages a randomly coiled conformation. The material was pipetted from the falcon tube into a partially permeable membrane with the molecular weight cut off at 1000 Da, and the membrane was clipped shut.[3]

[1] Produced by expression from *E. Coli*.

[2] GuHCl is known as guanidine hydrochloride

[3] The molecular weight cut-off refers to the lowest weight solute or molecule for which 90% of the solute/molecule is retained within the membrane

The membrane was placed into Solution 2 alongside a magnetic stirrer to maintain a gradual flow. This dialysis was left for 4 hours. The buffer was then changed to Solution 3 and dialysed for at least 4 hours; this, and the following, dialysis step can be left overnight if necessary. The following dialysis was against Solution 4 and then finally to Milli Q or distilled water to remove traces of salts which can otherwise lead to complications in the tuning of NMR probes when performing experiments on samples of rehydrated A$\beta_{1\text{-}42}$CC oligomers. The amount of peptide remaining in the membrane should equal that placed into the membrane at the start of the protocol. Therefore, a fraction of the total volume contained within the membrane which corresponds to the amount of peptide in mg required can be calculated. A small amount of sodium azide was added to the solution to act as a preservative. This oligomer and sodium azide solution was placed directly into the open glass test tubes for oligomer samples with lipid membrane, see VIII and IX in the sample list below. The amount of solution to be placed into the tubes was often large enough such that any attempt to directly perform the freeze-thaw section of the protocol (above) would result in a shattered pod due to expansion of the solution within it, so, when sealing the tube, it was beneficial to make the pod quite long. In this way the risk of losing the sample during this phase is decreased. Further to this, the tube was placed under a stream of nitrogen so as to gradually evaporate some of the solution from the sample, thereby reducing the risk of the solution expanding and breaking the vessel upon submersions in liquid nitrogen and warm water.

Lipid Membrane and Aβ, Curcumin and Cholesterol Samples

A variety of samples were produced so as to investigate the effect on the structure of lipid membranes of three biologically relevant substances: Aβ, curcumin and cholesterol. The effect of the potential remedy curcumin was examined against the toxic behaviour of both the monomeric and oligomeric form of Aβ_{1-42}CC, and also the effect of cholesterol; therefore, samples were made to: collect a lipid membrane ^{31}P ssNMR base level signal (I); compare the impact of cholesterol and curcumin on the membrane under identical conditions (II, III); investigate the impact of increasing the amount of curcumin on the membrane (III, IV, V); discover and compare the base level of membrane disruption caused by both the monomeric and oligomeric forms of the peptide (VI, VIII); and investigate any alteration to the membrane disruption caused by the peptide when the peptide was combined with a possibly therapeutic molecule (VII, IX); and finally, investigate the impact of the molecule on a different membrane so as to uncover its effect over different lipids (X). The list below describes

the samples produced and the sample number by which they will be referred to later in the chapter:

I: Dimyristoylphosphatidylcholine (DMPC) ^{1}H (75%) DMPC ^{2}H (25%)

II: I + Cholesterol (5 mol %)

III: I + Curcumin (5 mol %)

IV: I + Curcumin (15 mol %)

V: I + Curcumin (30 mol %)

VI: I + Aβ monomer (0.5 mg)

VII: III + Aβ monomer (0.5 mg)

VIII: I + Aβ oligomer (0.5 mg)

IX: III + Aβ oligomer (0.5 mg)

X: Dioleylphosphatidylcholine (DOPC) ^{1}H (100%) + Curcumin (15 mol %)

8.2.2 Solid-State NMR Measurements

2D ^{13}C-^{13}C DARR experiments were performed on a Bruker Avance II+ wide-bore spectrometer (600.1 MHz ^{1}H Larmor frequency and 150.8 MHz ^{13}C Larmor frequency) and a Bruker Avance III wide-bore spectrometer (850.2 MHz ^{1}H Larmor frequency and 213.7 MHz ^{13}C Larmor frequency) equipped with a 2.5 mm DVT MAS probe head operating in double-resonance mode. The MAS frequency was varied from 10 to 13 kHz. Mixing times of 20 (short mixing) to 400 ms (long mixing) were used with ^{1}H irradiation at a nutation frequency of 10.0 kHz. SPINAL64 decoupling at a nutation frequency of 83.3 kHz was used during t_1 and t_2 acquisition. An 80-100% ramp was used during cross polarisation. 2D ^{13}C-^{1}H inverse detection experiments were performed on a Bruker Avance III wide-bore spectrometer (850.2 MHz ^{1}H Larmor frequency) equipped with a 1.0 mm MAS JEOL probe head in double-resonance mode. The MAS frequency was ∼78 kHz and low power WALTZ-16 decoupling at a nutation frequency of 10 kHz was applied on ^{13}C during ^{1}H acquisition. ssNMR experiments were performed at a sample temperature of 2℃, target temperature −8℃, maintained by a dry, cold air flow of 600 l/h generated by a Bruker Cooling Unit Xtreme.

8.2.3 Electron Microscopy

Negatively stained aggregates were prepared by re-suspending 0.5 mg of Aβ_{1-42}CC oligomers in 100 µL of deionised water. Copper grids were activated with UV light for 1 minute and 2.5 µL of re-suspended sample was then added to the copper grids. After adsorption for 30 seconds, the grids were blotted off, and then counter-stained twice with 2 wt% uranyl acetate aqueous solution. Grids were blotted after 30 seconds and left to dry in air. Electron microscopy was performed on a JEOL 2010F TEM 200 kV Field Emission Gun fitted with a Gatan UltraScan 4000 camera.

8.3 Results

8.3.1 Electron Microscopy

Fig. 8.1 shows an EM image of the oligomeric species contained within the 'F20I31' A$\beta_{1\text{-}42}$CC oligomer sample. The EM image here is similar to the EM image shown in the publication introducing the AβCC system. [60] In the EM image shown in ref. [60], small protofibrils can be seen which do not appear so prevalently in Fig. 8.1, however the oligomeric species both show diameters of ∼3 nm, which is to be expected as they are the same system. The EM image shown here was obtained by Dr. A. A. Sousa, NIH, USA.

8.3.2 2D ^{13}C-^{13}C Correlation Experiments

Short and long mixing time DARR spectra were obtained on uniformly and selectively-labelled [^{13}C, ^{15}N] Aβ_{1-42}CC stabilised oligomers. Labelling schemes used were entitled 'Crys 1, 2 and 3' and U-[^{13}C, ^{15}N], as described in § 8.2.1. Figs. 8.2-8.7 show various DARR spectra displaying intra- and inter-residue cross peaks for the different selectively-labelled samples. That most samples are selectively-labelled results in much clearer DARR spectra being obtained when compared to the spectra obtained from uniformly labelled samples of recombinant Aβ in this and the previous chapter, which, in turn, facilitates assignment. The residues chosen for labelling were selected such that the various resonances would not overlap in the spectra, again increasing the ease of assignment, e.g. the three selected glycines, G25, G29 and G37 are likely to contain nuclei which exist in similar chemical shift regions to one another and

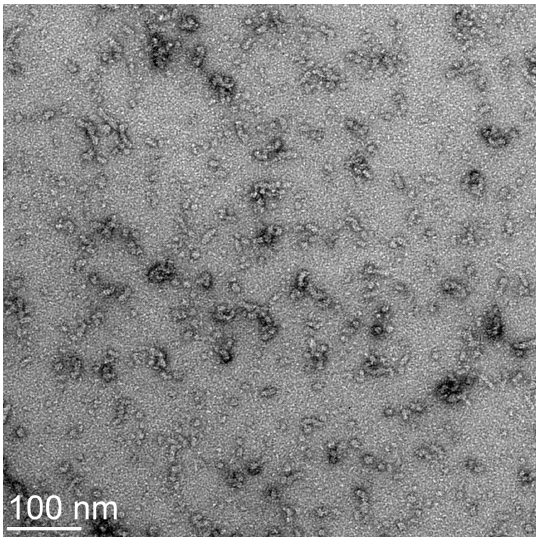

Figure 8.1: Negatively stained EM image of 'F20I31' A$\beta_{1\text{-}42}$CC oligomers, showing an average diameter for the structures in the figure of ∼6 nm. The TEM here shows similar structures to those seen in [60]. Figure obtained by Dr. A. A. Sousa, NIH, USA.

therefore were included individually in the schemes of 'Crys 1', 'Crys 2' and 'Crys 3' respectively.

Fig. 8.2 shows 2D ^{13}C-^{13}C, 50 ms (A) and 400 ms (B) mixing time DARR spectra obtained on A$\beta_{1\text{-}42}$CC 'Crys 1', with the aliphatic and carbonyl regions displayed. Fig. 8.2 C) shows the colour key used to identify the labelled residues and the inter-residue correlations during assignment on A) and B). V24 can be assigned based on the characteristically low chemical shift of the C$\gamma_{1,2}$ nuclei, the lowest of all the chemical shift values in this labelling scheme. From V24Cγ, again here as in § 7 assigning both Cγ nuclei is difficult due to their linewidths being wider than the separation in ppm of the resonances, the Cβ and Cα nuclei can be found in the typical valine regions ∼30 and ∼60 ppm by tracing horizontal and vertical lines from the V24Cγ peak on the diagonal. The assignment of S26 is trivial, due to the characteristically high chemical shift of the Cβ nuclei. The S26Cα-Cβ and the Cβ-Cα pair can be seen either side of the high chemical shift end of the diagonal at ∼60 ppm. The remaining peaks in the short mixing time spectrum (Fig. 8.2 A)) belong to the resonances D23 and K28. Though initially this appears more troublesome to assign, and compared to the assignment of V24 and S26 it is, the distinctive pattern for K28 in DARR spectra can be seen due to the 5 carbons in the lysine sequence within the aliphatic region. These correspond to the peaks as identified in the spectrum, and though the peaks

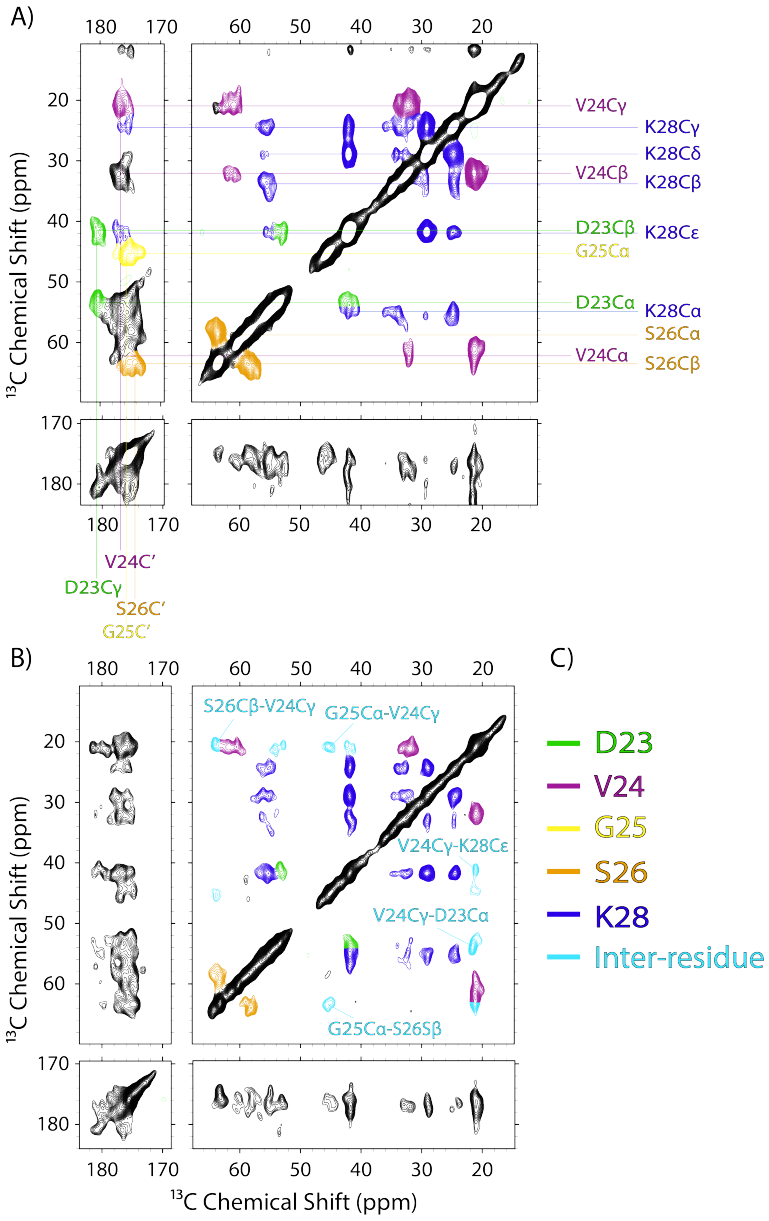

Figure 8.2: 2D ^{13}C-^{13}C DARR spectra obtained on A$\beta_{1\text{-}42}$CC 'Crys 1' with mixing times of A) 50 and B) 400 ms at a ^{1}H Larmor frequency of 850 MHz with 13 kHz MAS frequency. The full assignment pattern for the labelled K28 residue is particularly visible in the long mixing experiment (B) due to the large number of nuclei within the one residue. In § 7, assignment for carbonyl chemical shift values was particularly difficult, whereas here it can be seen that the partial labelling allows for C′ assignment. (C) displays the colour coding used for the residues. 64 (A) and 80 (B) transients were co-added for each 380 FIDs, the recycle delay was 3.0 s corresponding to an experimental time of ∼20 (A) and ∼25 (B) hours. 'Crys 1' contains labels at residues D23, V24, G25, S26 and K28. Base contour level: 2% (A) and 3% (B)

for K28Cα-Cϵ and D23Cα-Cβ are near to one another a distinction can be made and this is illustrated in the figure. The C$'$ nuclei of most of the labelled residues can also be assigned (including G25, which then provides a chemical shift value for G25Cα which can be verified with the longer mixing time spectrum, but excluding D23). To assign V24C$'$, identifying the C$'$-Cγ connectivity is the simplest option as the low chemical shift for V24Cγ locates the C$'$ resonance in a particularly clear region, as assigned in the figure. In a similar vein, identifying the S26C$'$-Cβ resonance is fairly easy as this is the highest chemical shift value in the aliphatic region. The D23Cγ resonance can be separated from the K28 resonance as there will be multiple peaks at the K28C$'$ resonance (with correlations to the various carbons in the chain, though, granted, not necessarily all carbons due to the short mixing time used). Two stand out D23Cγ resonances occur at the values previously unassigned as those belonging to D23Cα and D23Cβ, and this can therefore be assigned, and then checked in the longer mixing DARR spectrum. The K28C$'$ resonance will then be the other regularly occurring resonance in the carbonyl region, and this has been assigned in the figure. The C$'$ resonance which has yet to be assigned is therefore G25C$'$-Cα, revealing both assignments for the glycine residue, these can be checked in the longer mixing time spectrum, as they have been assigned based on a process of elimination as opposed to an active assignment process.

The long mixing time spectrum Fig. 8.2 B) allows the confirmation of the earlier G25 assignment, which is absent from the short mixing time spectrum in all but its connectivity to G25C$'$, with the G25Cα-V24Cγ resonance revealing the chemical shift assignment made previously was accurate. Further to this assignment, a few other longer range connectivities are also revealed: D23Cα-V24Cγ, V24Cγ-S26Cβ, V24Cγ-K28Cϵ, G25Cα-S26Cβ. All these long range connectivities are easily recognised on such a clear spectrum, and have been assigned in the figure to illustrate this. It is interesting that the V24 residue is well connected to the surrounding residues showing many inter-residue connectivities, but that the only other inter-residue assignment is from G25 and S26 whereby the resonance is likely to be a relayed transfer (where the magnetisation simply passes along the carbon backbone as opposed to transiting a distance through space). This certainly implies that the V24 side chain points into the hairpin, but reveals little about the organisation of the other sidechains in the area.

Fig. 8.3 shows a 2D ^{13}C-^{13}C DARR spectrum with a mixing time of 300 ms on a sample of 30% A$\beta_{1\text{-}42}$CC 'Crys 1' and 70% natural abundance (na) A$\beta_{1\text{-}42}$CC. This sample was designed to investigate whether the long-range bonds previously seen in

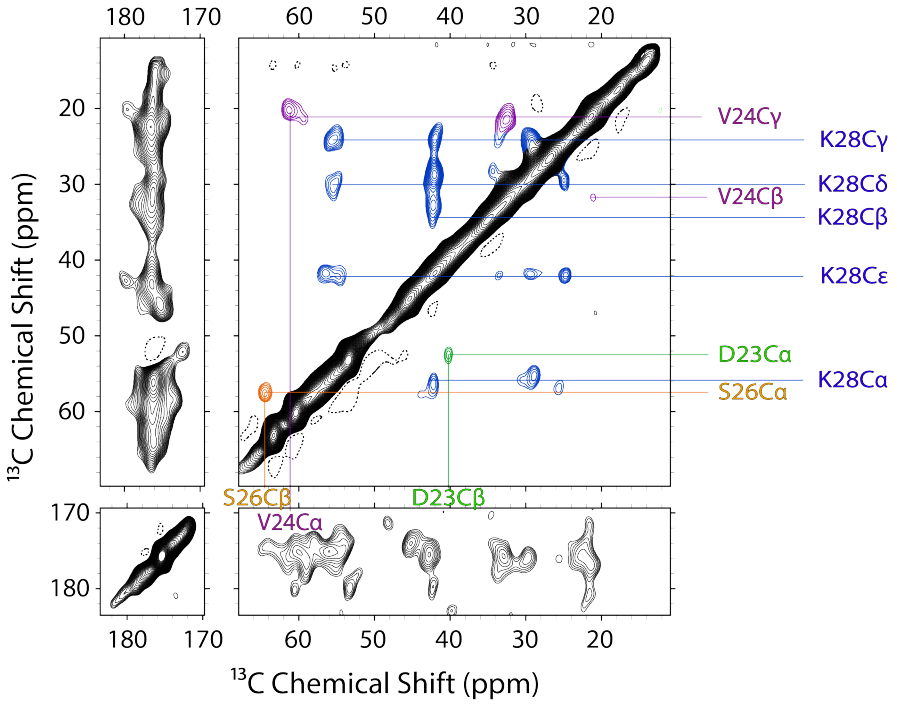

Figure 8.3: 2D ^{13}C-^{13}C DARR spectra obtained on 30% A$\beta_{1\text{-}42}$CC 'Crys 1' and 70% natural abundance A$\beta_{1\text{-}42}$CC with 300 ms mixing time at a ^{1}H Larmor frequency of 850 MHz with 13 kHz MAS. Many aliphatic assignments, made in Fig. 8.2, have been included. 160 transients were co-added for each 622 FIDs, the recycle delay was 2.0 s corresponding to an experimental time of ∼55 hours. 'Crys 1' contains labels at residues D23, V24, G25, S26 and K28. Base contour level: 6 %

Fig. 8.2 were intra-molecular or inter-molecular. As only 30% of the sample had labels at D23, V24, G25, S26 and K28 it was more likely that any labelled A$\beta_{1\text{-}42}$CC molecule had two natural abundance A$\beta_{1\text{-}42}$CC molecules as neighbouring molecules over another labelled molecule. Moreover, even if some labelled molecules did have labelled neighbouring molcules which some would have, over the entire sample the signal generated by these inter-molecular connectivities would not be as strong as intra-molecular signals. An experiment which was performed with the number of co-added transients adjusted to just see the first signals appearing, would ensure inter-molecular signals were absent. That the inter-residue cross peaks seen in Fig. 8.2 cannot be seen in Fig. 8.3 implies the correlations are inter-molecular, however although certain peaks are very strong in Fig. 8.3, such as K28Cϵ-Cδ, others are very weak, such as the absent S26Cα-Cβ peak. Had all the intra-residue correlations appeared and only the inter-residue correlations been absent it could be stated unambiguously that the inter-residue correlations were also inter-molecular, however,

that is not the case here.

Fig. 8.4 shows several 2D ^{13}C-^{13}C DARR spectra with various mixing times obtained for A$\beta_{1\text{-}42}$CC 'Crys 2' at two ^{1}H Larmor frequencies, 600 MHz and 850 MHz. A variety of mixing times were used to distinguish connectivities from short- to long-range and so a range of τ_m from 20 ms to 400 ms were used. As for the previous labelling scheme, a useful starting point for chemical shift assignment is the Cγ resonance of the valine residue, here V18Cγ which is located at $\sim$20 ppm. This occupies one of the lowest chemical shift values within this labelling scheme and so assignments for V18Cβ-Cγ, V18Cα-Cγ and V18C$'$-Cγ are all horizontally aligned at this value and can easily be assigned in both the 20 ms and 50 ms mixing time experiments, Fig. 8.4 A) and B). For clarity, V18 has been fully assigned in the 50 ms mixing time spectra (B). Methionine has two carbons with characteristically similar chemical shifts at $\sim$30 ppm, from resonances at the Cβ and Cγ nuclei, and these result in two peaks located next to one another at the M35Cα and M35Cϵ chemical shift values. The Cα chemical shift value for methione is typically around $\sim$55 ppm and the pair of resonances located at this value can be assigned, and are shown in Fig. 8.4 A). As methionine is a particularly large amino acid, with a sulphur separating Cγ and Cϵ, in the 20 and 50 ms mixing time spectra the Cϵ chemical shift value is more troublesome to assign than in the longer mixing time spectra. The low chemical shift M35Cϵ can easily be seen in Fig. 8.4 C), D), E) and F), though it has been assigned in A). The M35C$'$ chemical shift value can be assigned, by finding two resonances in the carbonyl region at the chemical shift values of the M35Cβ and M35Cγ resonances, as shown in Fig. 8.4 A). In this manner, the entire M35 residue can be assigned. Leucine has five aliphatic carbons, and so can be safely assumed to be responsible for all the peaks not already assigned to the valine and methionine residues; again the glycine resonance is unlikely to have appeared during a short mixing time experiment as explained previously. L17Cδ_1, Cδ_2 and also, but to a lesser extent, Cγ have similar chemical shifts and so are more difficult to discern between than other chemical shifts in this labelling scheme. As the typical region in which these resonances exist is clear ($\sim$25 ppm), it can be assumed that these resonances are responsible for all signals within this region and then horizontal and vertical paths can be taken so as to reveal assignments for L17Cα and Cβ, as shown in the figure. The Cδ/Cγ-Cβ region can be seen as containing two distinct peaks and so, in this way, separate assignments for the Cδ and Cγ resonances can be found, and have been made in Fig. 8.4 A). L17C$'$ can be assigned using the L17Cδ and Cγ resonances as, again, this region is relatively clear so the carbonyl resonance in this region can only refer to L17C$'$, this has also

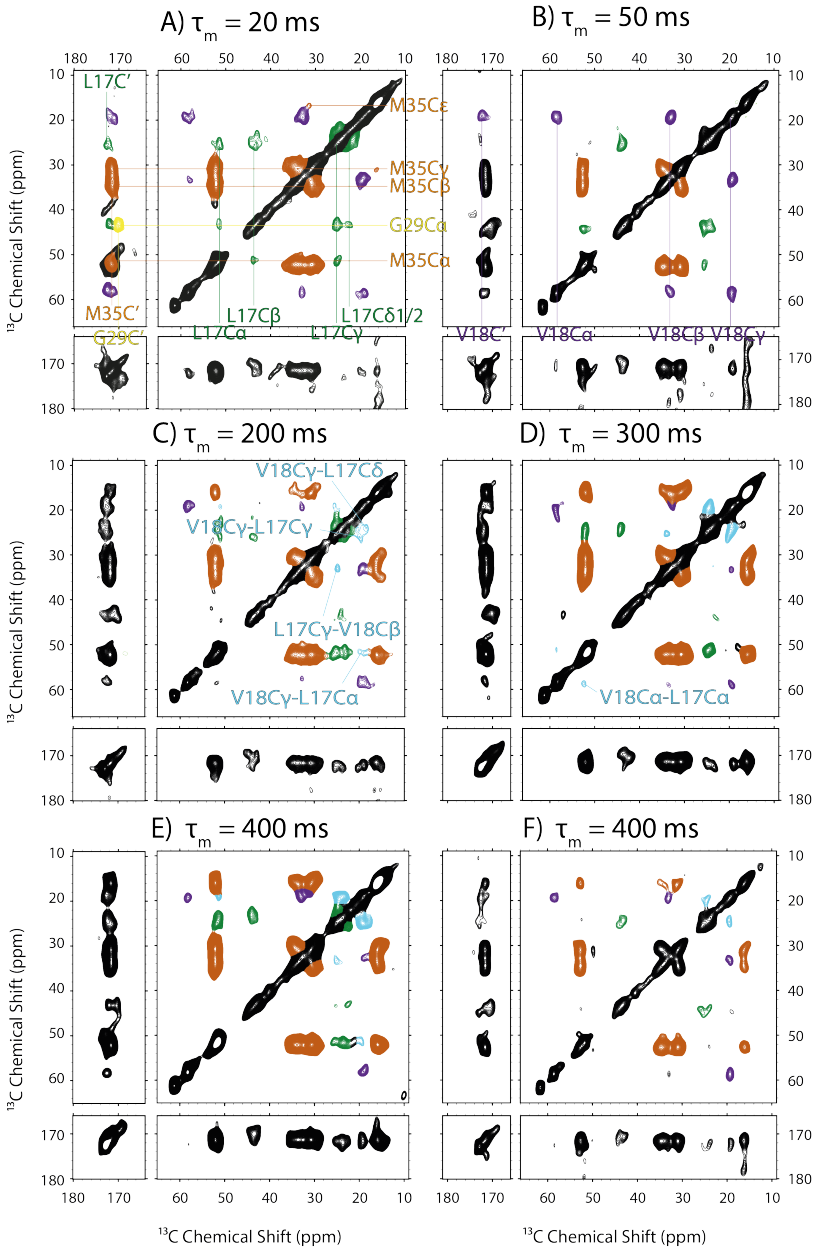

Figure 8.4: 2D ^{13}C-^{13}C DARR spectra obtained for A$\beta_{1\text{-}42}$CC 'Crys 2' with A) 20 ms, B) 50 ms, C) 200 ms, D) 300 ms, E) 400 ms, F) 400 ms mixing times, at a ^{1}H Larmor frequency of 600 MHz (A, C, D, E) and 10 kHz MAS frequency and 850 MHz (B, F) and 13 kHz MAS frequency. 128 (A, C and D), 48 (B), 164 (E) and 64 (F) transients were co-added for each 458 (A, C, D, E) and 650 (B, F) FIDs, the recycle delay was 2.0 (A, C, D, E) and 3.0 (B, F) s, corresponding to experimental times of ~33 (A, C and D), ~26 (B), ~41 (E) and ~35 (F) hours. 'Crys 2' contains labels at L17, V18, G29 and M35. Base contour levels: 3% (A, C, D, E, F) and 4% (B)

been shown in Fig. 8.4 A).

The longer mixing DARR spectra in Fig. 8.4 show some inter-residue connectivities such as V18Cγ-L17Cα, V18Cγ-L17Cγ, V18Cβ-L17Cγ and V18Cα-L17Cα, however as these residues are neighbours it is likely that relayed transfer can account for the cross peaks. The connectivities mentioned here are assigned in the longer mixing time DARR spectra. Unfortunately, no further long range connectivities can be found which implies that the side chains of L17 and V18 are not within a $\sim$5 Å proximity of the M35 side chain nor G29Cα. The G25C$'$-Cα resonance can be seen as a distinct peak in Fig. 8.4 E) in the same location as to that in A) where the resonance was assigned, which verifies this assignment.

Fig. 8.5 shows a combination of 2D ^{13}C-^{13}C short and long mixing time DARR spectra obtained for A$\beta_{1\text{-}42}$CC 'Crys 3' oligomers taken at two ^{1}H Larmor frequencies, 600 MHz and 850 MHz. The short mixing time DARR experiment (A) used a mixing time of 50 ms and experiments were also performed using 200 and 400 ms mixing time so as to investigate the longer distance connectivities within the sample. Once again, a sensible initial residue for assignment is the labelled valine of this labelling scheme, V36. V36Cγ has the lowest chemical shift value of the labelled nuclei, $\sim$20 ppm, and so the pairs of cross peaks that are aligned vertically from the low chemical shift end of the diagonal, which are located at $\sim$35 and $\sim$60 ppm, can be assigned as the V36Cγ-Cβ and V36Cγ-Cα cross peaks.[4] V36C$'$ can be assigned in the manner used previously; as the V36Cγ occupies the lowest chemical shift resonance on the 50 ms spectrum, therefore the peak in the carbonyl region that is aligned with this low chemical shift value peak must be V36C$'$-V36Cγ. K16 and N27 are both labelled in this scheme and though the Cα and Cβ for each residue will be in similar chemical shift regions, a distinction can be made based on the correlation of the K16Cα and Cβ to the intra-residue Cγ, Cδ and Cϵ nuclei. These correlations may not appear in the short mixing DARR spectrum, however they will exist in the longer mixing DARR spectra and so can serve as a check for the assignments made on the 50 ms mixing time spectrum. To begin assigning K16, it is sensible to start in the characteristic Cδ-Cγ region (as none of the other residues in this labelling scheme possess carbons with chemical shifts in this area), $\sim$25 ppm, whereby there should be two cross peaks just to either side of the diagonal, as shown in Fig. 8.5 A). From these assignments of K16Cδ and Cγ any cross peaks found to occur vertically or horizontally aligned at both these values of chemical shift can be confidently assigned as part of the K16 residue. The assignments that can be made using this technique have been included

[4] And vice versa, i.e. V36Cβ-Cγ, V36Cα-Cγ can be assigned as the horizontally aligned peaks

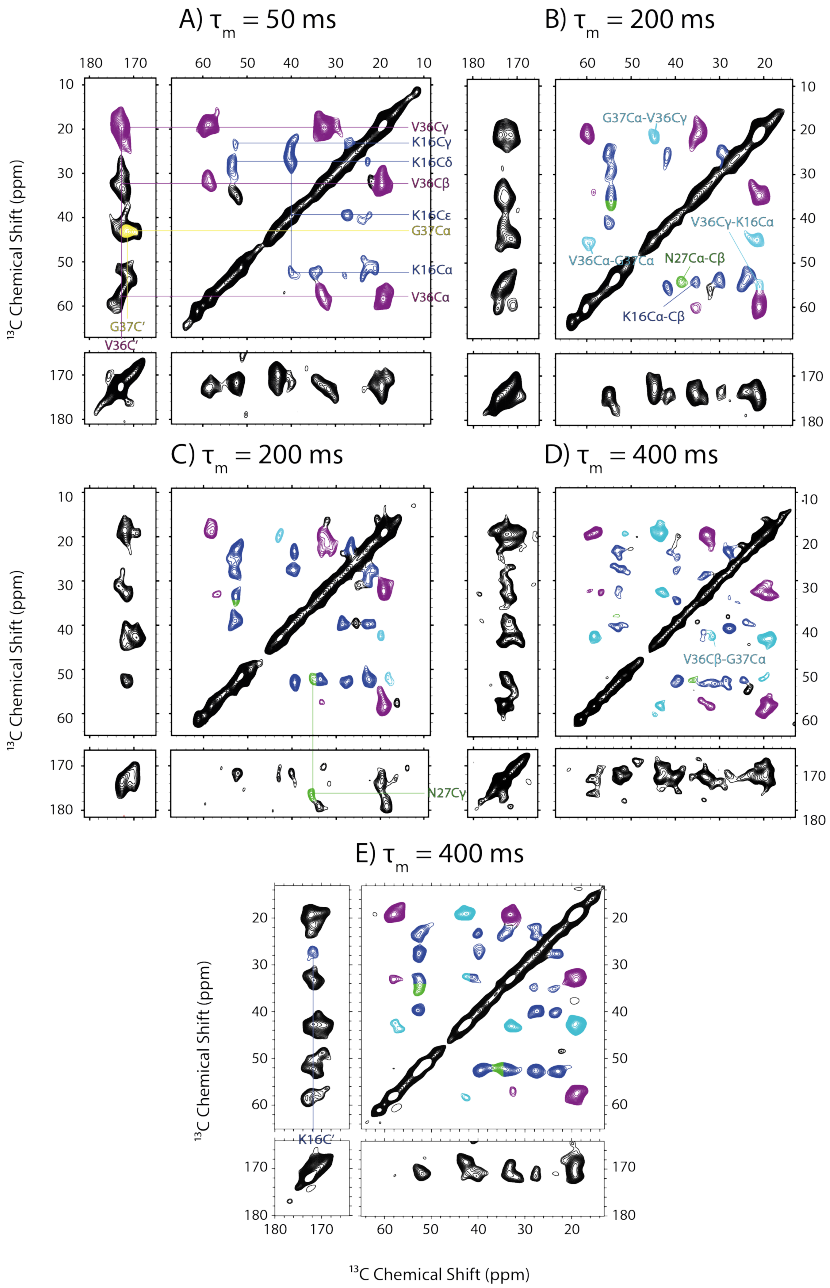

Figure 8.5: 2D ^{13}C-^{13}C DARR spectra obtained for A$\beta_{1\text{-}42}$CC 'Crys 3' with A) 50 ms, B) 200 ms, C) 200 ms, D) 400 ms and E) 400 ms mixing times, at a ^{1}H Larmor frequency of 600 MHz (A, B, D) and 850 MHz (C, E), all at 10 kHz MAS frequency. 112 (A), 58 (B), 160 (C), 120 (D) and 64 (E) transients were co-added for each 442 (A, B, D) and 620 (C, E) FIDs, the recycle delay was 2.8 (A, B, D) and 2.5 (C, E) s, corresponding to experimental times of ∼39 (A), ∼20 (B), ∼69 (C), ∼41 (D) and ∼28 (F) hours. 'Crys 3' contains labels at K16, N27, V36 and G37. Base contour levels: 3% (A, B, E), 2% (C) and 4% (D).

in Fig. 8.5 A), however only two more assignments have been made, whereas K16 has 5 aliphatic carbons. K16Cα can be confidently assigned as the second chemical shift value responsible for the cross peak found at $\sim$55 ppm, and there is another cross peak found at a chemical shift value of $\sim$40 ppm, which is likely to be Cϵ. A value for K16Cβ is not regularly found throughout the spectrum, and the cross peak found at ($\sim$35,$\sim$50) ppm is as likely to be N27Cβ-Cα as K16Cβ-Cα and so cannot be unambiguously assigned. In fact, the peak is more likely to eminate from the N27 residue, as no other cross peaks at the $\sim$35 ppm chemical shift value exist in the spectrum which would be expected if it was the Cβ from the K16 residue. This peak cannot be unambiguously assigned from the short mixing DARR spectrum and so it is necessary to use the longer mixing time spectra to reveal the chemical shift values for N27 and K16Cβ. Further chemical shift assignments that can be made using Fig. 8.5 A) are located within the carbonyl region and the cross peaks there. Though the G36Cα chemical shift cannot be assigned from the aliphatic region, the resonance located at a horizontal value of chemical shift at which there are no cross peaks in the aliphatic region must be the G36C$'$-Cα resonance, and one can be found at $\sim$45 ppm and has been assigned in the figure to illustrate this. There are no strong K16C$'$-Cγ, Cδ or Cϵ peaks which is most likely due to the significant distance between these nuclei and so, combining this with the ambiguity of the Cα and Cβ assignments for K16 and N27, no further C$'$ assignments can be made.

The use of the long mixing spectra shown in Fig. 8.5 B), C) and E) enables the remaining chemical shift values to be assigned. The cross peak at ($\sim$33,$\sim$52) ppm in the 50 ms mixing time DARR spectrum (A) becomes two distinct peaks in (B), the 200 ms mixing time DARR spectrum taken at 600 MHz ^{1}H Larmor frequency, and the same two peaks can be seen in (C), the 200 ms mixing time experiment taken at 850 MHz ^{1}H Larmor frequency. With the separation of this peak comes the ability to unambiguously assign the K16Cα-Cβ and the N27Cα-Cβ peak, and the assignments of these can be further validated in the 400 ms mixing experiments, in particular Fig. 8.5 D); these assignments have been made on the various spectra. K16C$'$ can also be unambiguously assigned using Fig. 8.5 E), the long mixing time used in this experiment enables magnetisation to pass between the distant C$'$ and Cδ, as can be seen in the figure. Specifically, the Cδ has been chosen because the chemical shift value for this nucleus is in a particularly clear section of the spectrum and, as such, the carbonyl region contains only one peak which is extremely likely to be K16C$'$-Cδ.[5]

[5]This peak could technically be a correlation between e.g. V36C$'$-K16Cδ if the K16 sidechain was directed into the sidechain and K16 was opposite the V36 residue, and that also the length of the mixing time was sufficient to allow magnetisation transfer over the distance, however the chemical

With K16C′ assigned, the only C′ assignment remaining is that of N27C′, however none of the figures display a suitably unambiguous resonance for this value, and, as such, this has remained unassigned. N27Cγ has been assigned however in Fig. 8.5 C), and this can be seen as having a suitably unambiguous correlation with N27Cα. The assignment in Fig. 8.5 B) and C) shows a V36Cγ - K16Cα cross peak on one side of the diagonal, which is long range and therefore of particular interest, although the K16 sidechain carbons show no connectivities to V36 which probably implies that the sidechain of V36 is directed into the hairpin and that of K16 is directed away from the hairpin. This leads to the possibility of a similarity in the sidechain organisation to the fibrillar structures suggested by the Tycko and Smith groups in [86, 93, 287]. However, this cross peak is not found in E) and might be found in D), see figure for assignment of these locations, and as such an unambiguous claim that the V36 sidechain is directed into the hairpin cannot be made.

Fig. 8.6 shows a 2D ^{13}C-^{13}C DARR spectrum obtained for A$\beta_{1\text{-}42}$CC 'F19I32' with 400 ms mixing time obtained at ^{1}H Larmor frequency of 850 MHz. The aliphatic carbon assignments for I32 are clear, and have been included in the spectrum to show this; the characteristic cross peak pattern of five horizontally aligned resonances at each of the five vertical chemical shift values clearly reveals the chemical shift values of the labelled isoleucine residue. The C′ chemical shift value is assigned easiest at the well resolved I31C′-Cγ_1 ($\sim$25 ppm), this has been shown in Fig. 8.6. Phenylalanine residues contain two aliphatic carbons, Cα and Cβ and these can be seen as the two cross peaks not within the typical isoleucine pattern of cross peaks ($\sim$55 for Cα and $\sim$40 for Cβ), and have been assigned in the figure. Phenylalanine also contains 6 aromatic carbons, with many of the carbons at a similar location. Cγ typically has the highest chemical shift value with Cδ_1 having the lowest, Cδ_2, Cϵ_1, Cϵ_2 and Cz have similar chemical shift values ($\sim$129 ppm) and so will be difficult to distinguish using this spectrum. Cγ can be assigned as it is set apart from the wide peak within the aromatic region, and has been assigned in the figure at $\sim$138 ppm. The broad peak within this region can be seen to contain at least two distinguishable peaks and possibly three using both the correlation to Cβ and to Cα. With the ambiguity inherent in assignment of such a broad peak, only 2 assignments have been made as shown in the figure.

This labelling scheme was used to investigate whether there was any cross correlations between the two residues, if the sidechains of both were pointing into the hairpin then

shift value is not similar enough to the previously assigned value of V36C′ for the cross peak to be considered as an inter-residue correlation

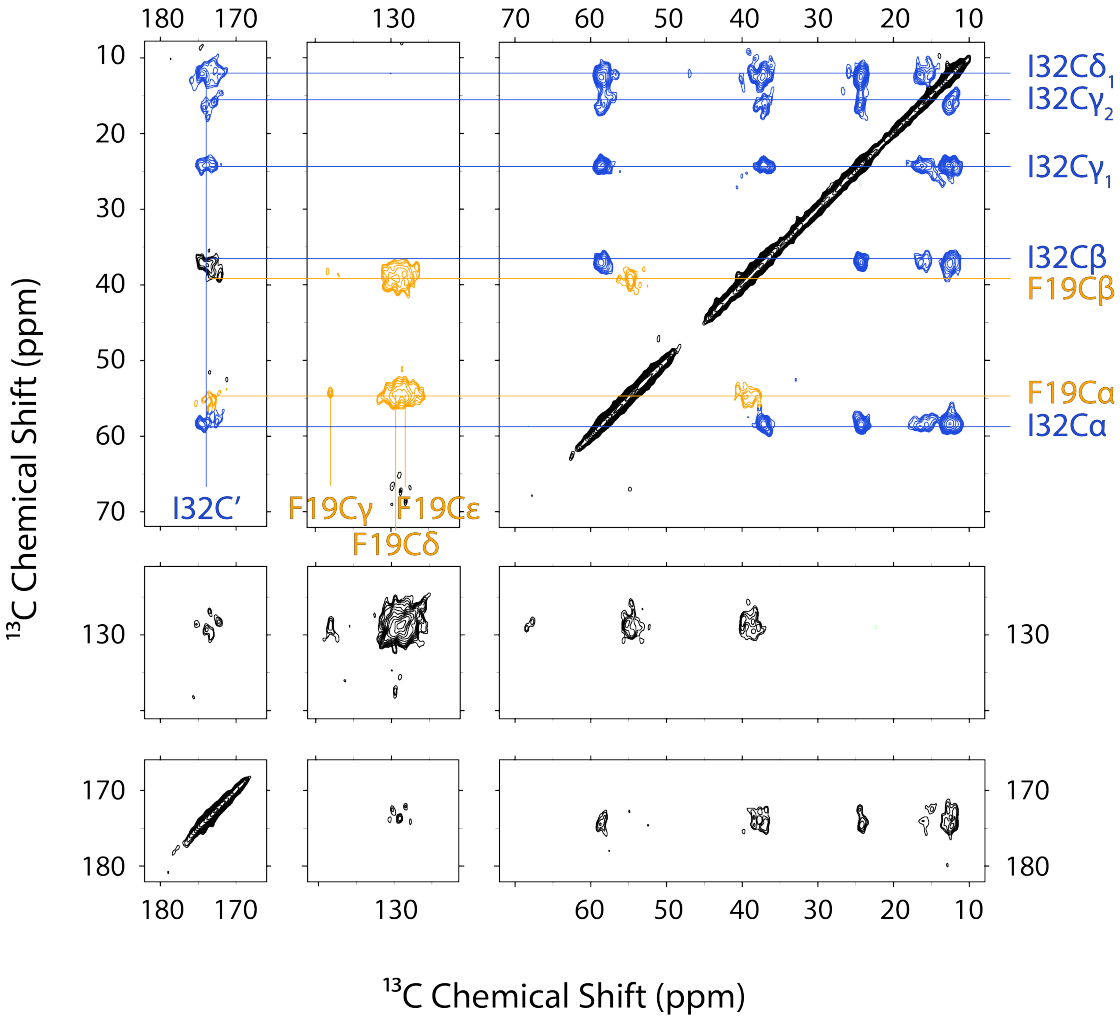

Figure 8.6: 2D ^{13}C-^{13}C DARR spectrum obtained for A$\beta_{1\text{-}42}$CC 'F19I32' with 400 ms mixing time, at a ^{1}H Larmor frequency of 850 MHz and 13 kHz MAS frequency. 36 transients were co-added for each 650 FIDs, the recycle delay was 4.0 s corresponding to an experimental time of ∼26 hours. Base contour level: 3%

a correlation might be seen between I32Cγ or δ and any of the aromatic carbons from F19. The aromatic region clearly does not show any cross peaks in areas other than those in correlation with F19Cα and Cβ which suggests that the two side chains are not directed towards one another. The earlier claim that the packing may be similar to that of previously published data would have been corroborated by a side chain connectivity between F19 and I32, which is not seen here.

Fig. 8.7 shows a 2D ^{13}C-^{13}C DARR spectrum obtained for A$\beta_{1\text{-}42}$CC 'F20I31' with 300 ms mixing time obtained at ^{1}H Larmor frequency of 850 MHz. The labelling scheme used here is complementary to the previous labelling scheme and so the spectrum can be assigned in a very similar manner. Though the linewidths here are significantly broader than those taken for the 'F19I32' sample, most assignments can be made for both residues. The isoleucine aliphatic carbons can be fully assigned as can the carbonyl chemical shift value ($\sim$174 ppm). The phenylalanine Cα and Cβ cross peak is well resolved on one side of the diagonal (Cα-Cβ) and so can be assigned using this. The carbonyl is not well resolved and the aromatic region contains only one broad peak, and so assignments within this region are limited. All assignments that have been made have been included in the figure.

Once again, the labelling scheme hoped to investigate the sidechain packing of the AβCC molecule, however with no visible correlation between the F20 and I31 residues in this spectrum, the implication is that both of the residues do not point into the hairpin. Using this and the previous labelling scheme it appears that the sidechain packing will be either F20-I32 or F19-I31, and further labelling schemes are required to investigate which two residues have their side chains directed into the hairpin.

Fig. 8.8 shows a 2D ^{13}C-^{13}C DARR spectrum with 50 ms mixing time obtained at ^{1}H Larmor frequency 600 MHz. The sample in Fig. 8.8 is uniformly U-[^{13}C, ^{15}N] labelled A$\beta_{1\text{-}42}$CC oligomers and the crowded aliphatic region looks similar to spectra shown in § 7 of a uniformly labelled sample of A$\beta_{1\text{-}40}$. The assignments obtained from the previous samples were sufficient for the modelling of the oligomer, and this spectrum was obtained so as to compare to the previous spectra and ensure that the various methods of creating the sample (uniformly labelled sample was created via bacterial expression, whereas the selectively labelled samples were made through the use of a peptide synthesizer) did not influence the overall structure of the oligomers. When overlain, the spectra correlate well, see Fig. 8.9, and thus the validity of using samples from either technique is proven. Fig. 8.9 shows 2D ^{13}C-^{13}C DARR spectra taken on four of the five labelling schemes used and compares these to the DARR spectrum obtained on the uniformly labelled sample. The labelling scheme not compared is

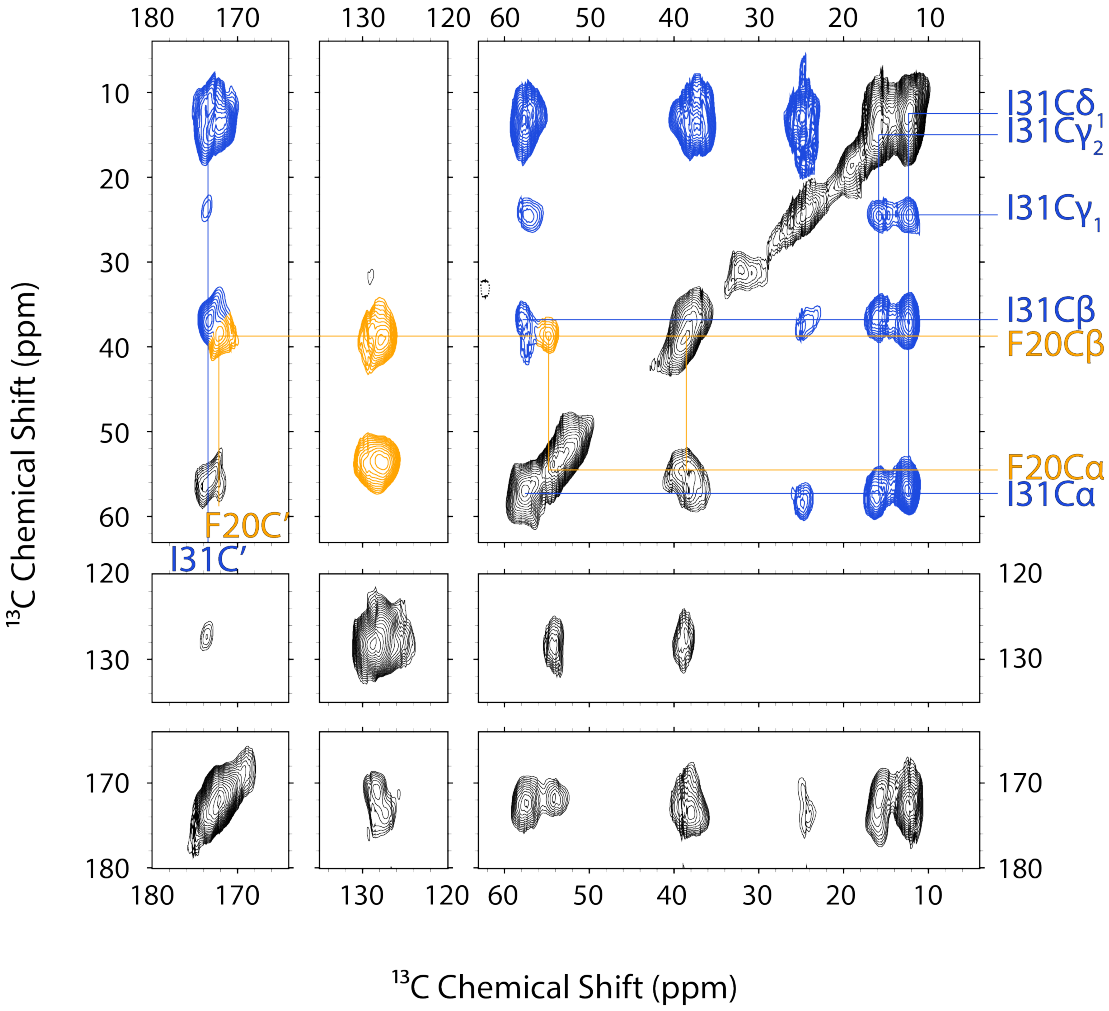

Figure 8.7: 2D ^{13}C-^{13}C DARR spectrum obtained for A$\beta_{1\text{-}42}$CC 'F20I31' with 300 ms mixing time, at a ^{1}H Larmor frequency of 850 MHz with 11.5 kHz MAS frequency. 64 transients were co-added for each 462 FIDs, the recycle delay was 2.5 s corresponding to an experimental time of ∼21 hours. Base contour level: 3%

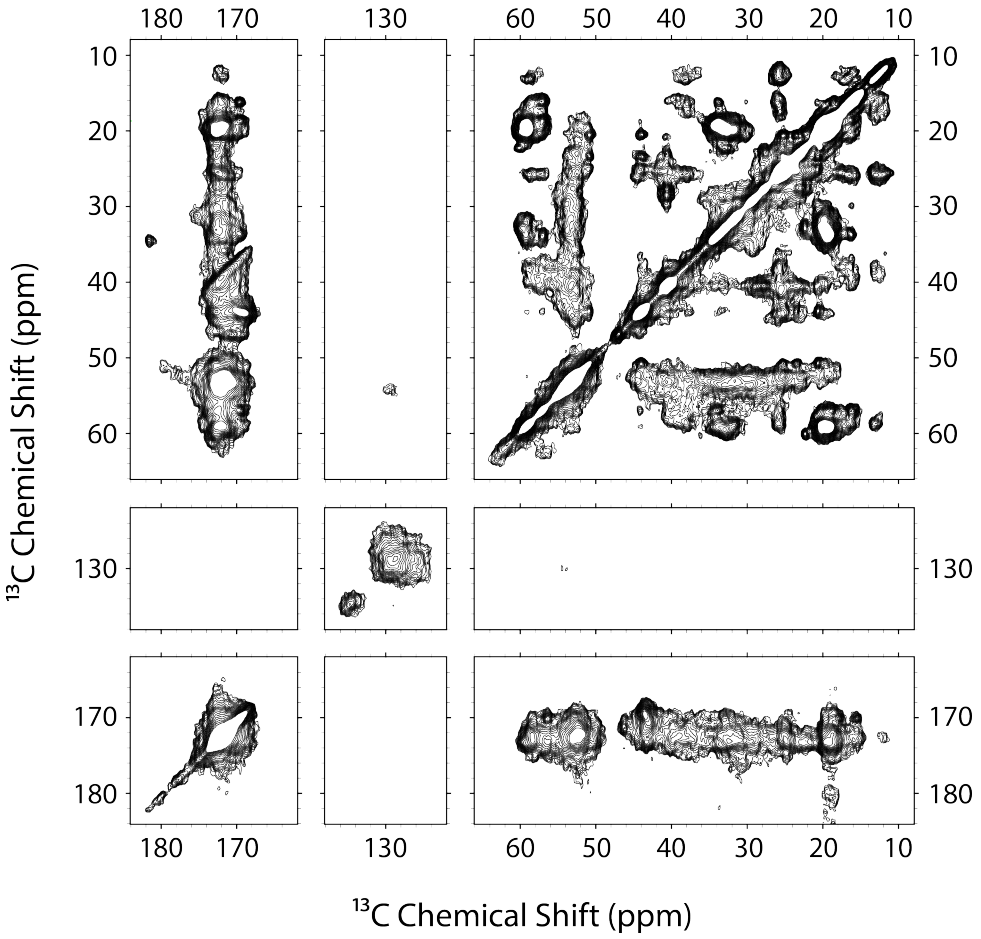

Figure 8.8: 2D ^{13}C-^{13}C DARR spectrum obtained for U-[^{13}C, ^{15}N] A$\beta_{1\text{-}42}$CC hydrated oligomers with 50 ms mixing time, at a ^{1}H Larmor frequency of 600 MHz and 10 kHz MAS frequency. 112 transients were co-added for each 458 FIDs, the recycle delay was 2.8 s corresponding to an experimental time of ∼41 hours. Base contour level: 3%

F20I31, and this is due to the significantly broad linewidths found in that spectrum, which, when overlain on the U-[^{13}C, ^{15}N] spectrum, therefore do not allow an informative comparison. Those that have been compared, for all four other labelling schemes, show that the peaks within the selectively labelled samples overlay peaks existent on the uniformly labelled sample. This implies that the chemical shifts of the samples are the same and, due to this, analysis of the samples made from either technique can be combined.

The chemical shifts obtained from all the selectively labelled, synthetically produced, samples are shown in Tables 8.1-8.3.

8.3.3 ^{13}C-^{1}H Inverse Detection Experiments

Fig. 8.10 shows a 2D inverse detection spectrum taken on U-[^{13}C, ^{15}N] A$\beta_{1\text{-}42}$CC hydrated oligomers at 850 MHz ^{1}H Larmor frequency and 78 kHz MAS frequency to observe ^{13}C-^{1}H correlations in the sample. Many carbon chemical shifts have been assigned and proton chemical shift values can be found for the protons bound to these previously assigned carbons. The experiment used a short back CP and proton-proton mixing time, and so the correlations in the figure are likely to be directly bonded carbon and proton pairs, this can be seen in the general diagonal trend of the location of the signals in the spectrum (as was the case in the short mixing ^{13}C-^{1}H experiments used in § 7); the sequences used can be seen in § 5.2. There are signals throughout the carbon dimension at ∼0 ppm and ∼4.8 ppm, which are due to almost complete suppression of the DSS and H_2O peak which would normally occur on the ^{13}C-^{1}H spectra. As the suppression is not complete, there have been no assignments made within these regions, as any potential assignment could not be made unambiguously. Assignments were made using previously assigned carbon chemical shifts and then assigning the proton chemical shifts correlated to these locations in the spectrum.[6] All proton assignments have been evaluated using the typical values for protons in the amino acid as listed by the BMRB. Where potential proton chemical shifts were significantly outside typical values, assignments were not made. 34 proton-carbon assignments have been made, and these are included in Tables 8.4 and 8.5.

Fig 8.11 displays four 2D ^{13}C-^{1}H inverse detection spectra obtained with various proton-proton mixing times, so as to investigate longer range contacts. Fig 8.11

[6]The chemical shifts used were either obtained by the author on the selectively labelled samples described earlier in the chapter or by Christofer Lendel on various other U-^{13}C, U-^{15}N and U-[^{13}C, ^{15}N] A$\beta_{1\text{-}42}$CC samples

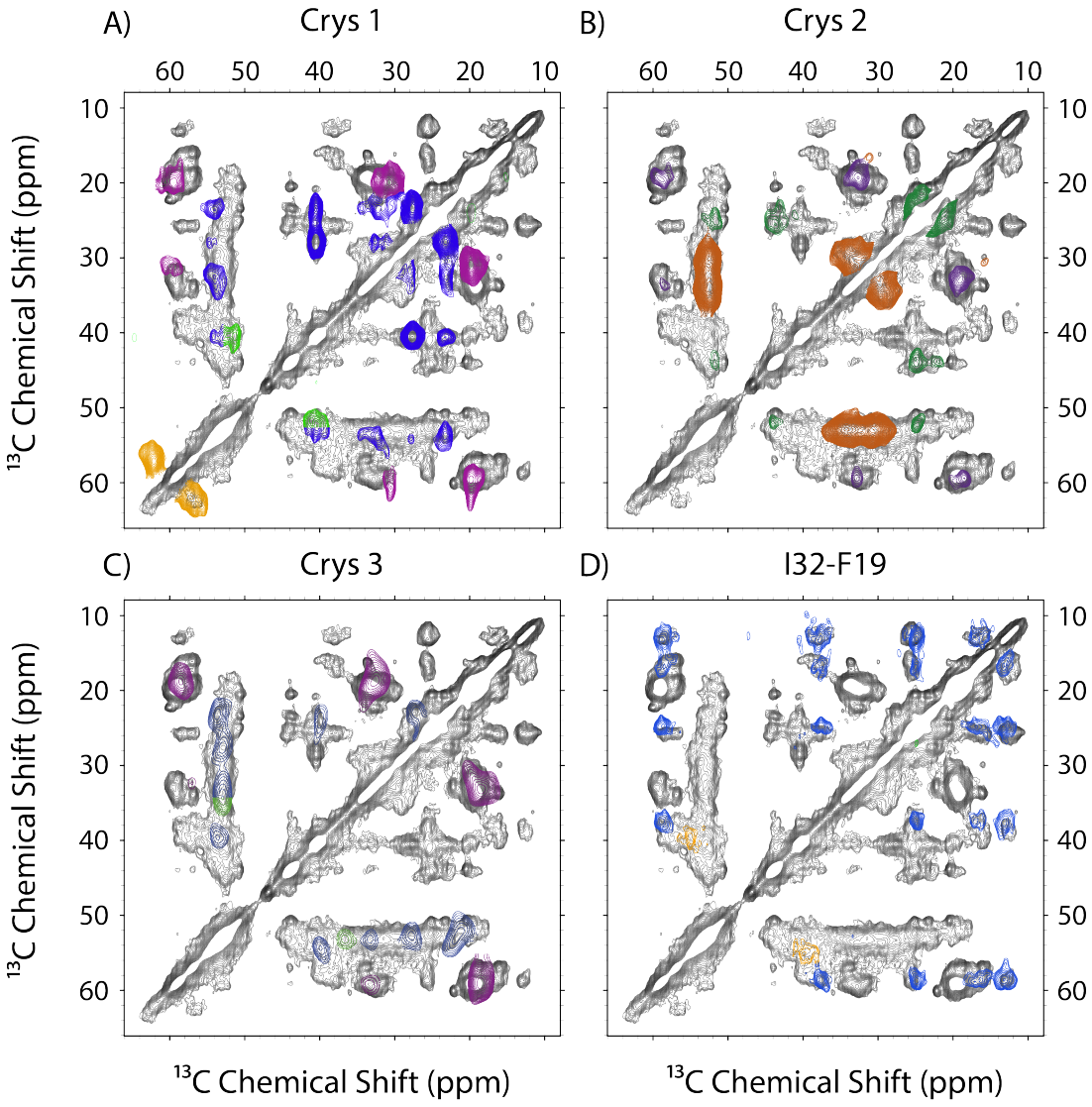

Figure 8.9: 2D ^{13}C-^{13}C 50 ms mixing time DARR spectrum obtained for uniformly labelled A$\beta_{1\text{-}42}$CC hydrated oligomers compared against spectra taken from selectively labelled samples. The labelling schemes used are A) Crys 1, B) Crys 2, C) Crys 3 and D) F19I32 (see § 8.2.1). The spectrum from F20I31 has not been used due to the poor resolution.

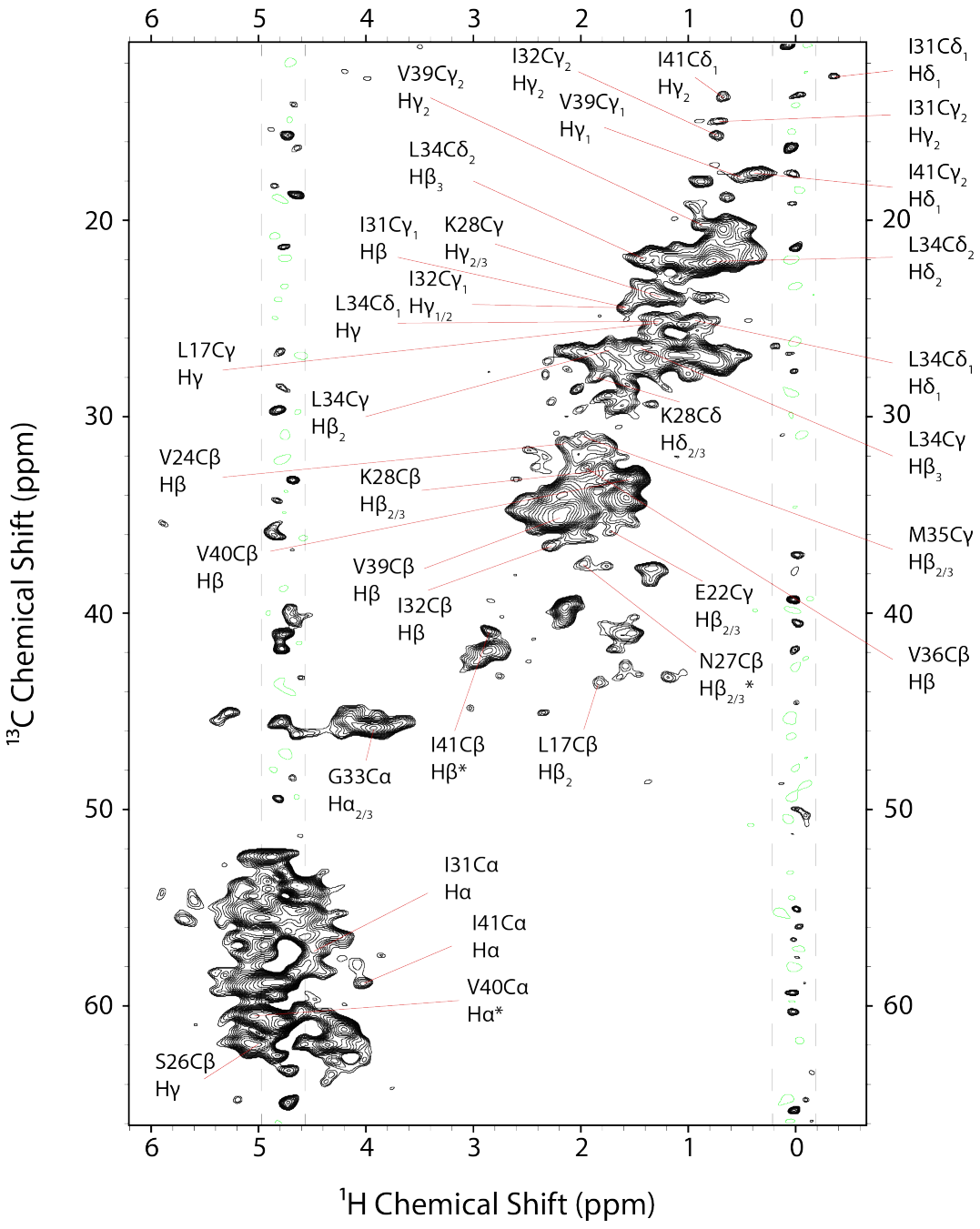

Figure 8.10: 2D ^{13}C-^{1}H inverse detection spectrum obtained for U-[^{13}C, ^{15}N] A$\beta_{1\text{-}42}$CC hydrated oligomers at a ^{1}H Larmor frequency 850 MHz and 78 kHz MAS frequency. Dashed regions indicate the DSS peak (∼0 ppm) and the water peak (∼4.9 ppm), assignments cannot be made unambiguously in these regions. No decoupling was applied on ^{13}C during ^{1}H acquisition. Asterisks indicate unusual proton chemical shifts, and so will be treated as tentative assignments. 80 transients were co-added for each 244 FIDs, the recycle delay was 1 s corresponding to an experimental time of ∼6 hours. Base contour level: 5%

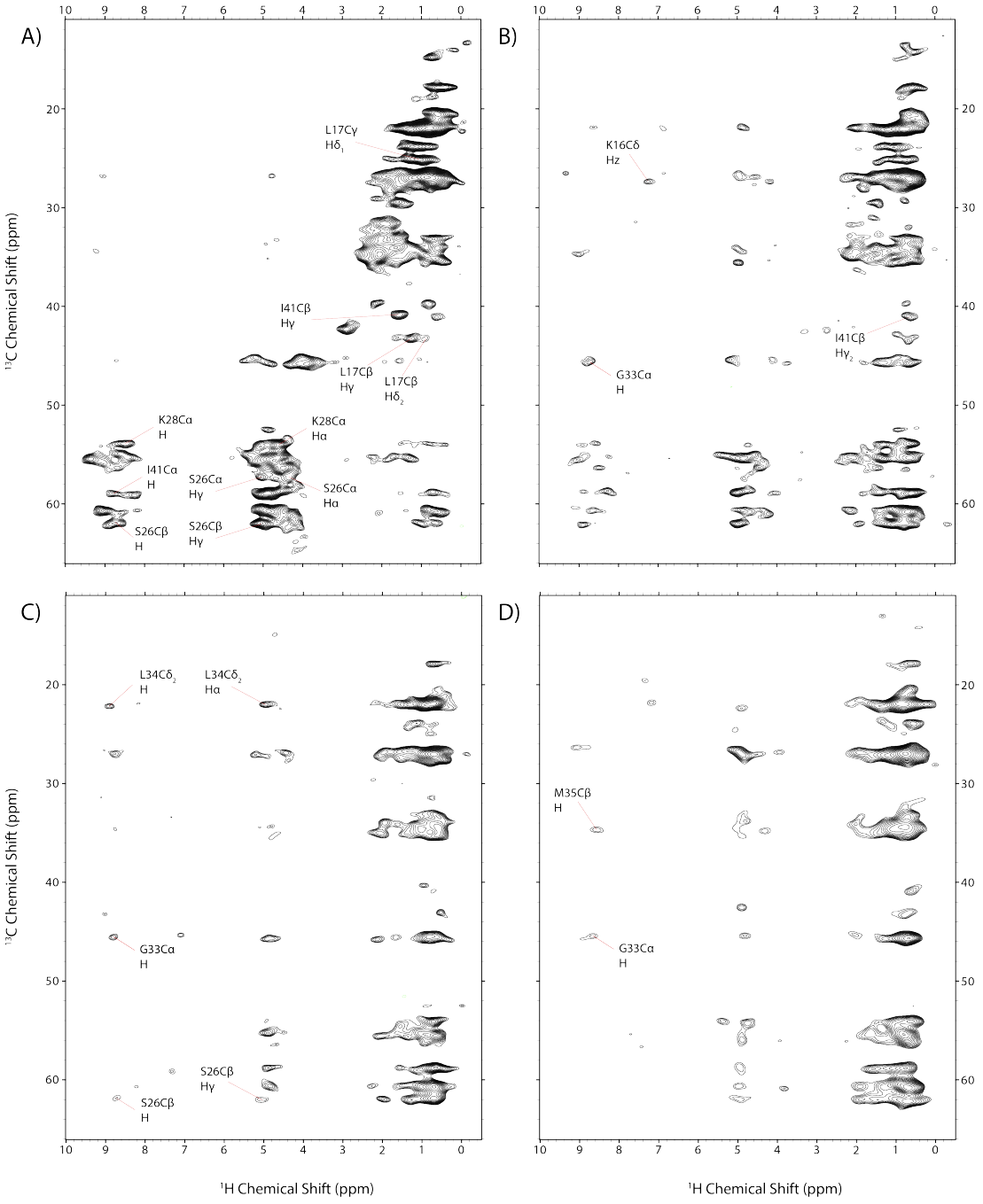

Figure 8.11: 2D ^{13}C-^{1}H inverse detection spectra obtained for U-[^{13}C, ^{15}N] A$\beta_{1\text{-}42}$CC hydrated oligomers at a ^{1}H Larmor frequency of 850 MHz and 78 kHz MAS frequency with various τ_{mix}; A) 620 µs, B) 2 ms, C) 4 ms and D) 6 ms. 10 kHz WALTZ decoupling with 100 µs pulses was applied on ^{13}C during ^{1}H acquisition. 80 transients were co-added for each 244 FIDs, the recycle delay was 0.5 s corresponding to an experimental time of ∼3 hours for all spectra. Base contour level: 5%

A) was obtained using the shortest mixing time (620 μs) and so only a few longer range contacts can be seen, such as the assignment I41Cα-H, which indicates that amide proton chemical shifts can be found and also that assignments are no longer necessarily due to a directly bonded carbon-proton pair. Some further assignments to those made from Fig 8.10 are also displayed in Fig 8.11 A). Fig 8.11 B), C) and D) also reveal further intra-residue cross peaks such as K16Cδ-Hz (B), G33Cα-H (C) and M35Cβ-H (D) with a total of 23 further proton-carbon assignments made. The spectrum in Fig 8.11 (D) is sparsely populated, with many of the correlations visible in the previous spectra having now faded, implying that the proton-proton mixing time of 6 ms was of a length sufficient to result in relaxation of various signals. Fig 8.11 (A), (B) and (C) however combine well to offer many assignments, and these have been included in Tables 8.4 and 8.5.

8.3.4 ^{15}N-^{1}H Inverse Detection Experiments

Fig. 8.12 shows a 2D ^{15}N-^{1}H inverse detection spectrum of U-[^{13}C, ^{15}N] A$\beta_{1\text{-}42}$CC hydrated oligomers taken at ∼78 kHz MAS frequency. The spectrum shows a similar proton-nitrogen correlation as the H-N inverse detection spectra shown in § 7, with a number of outliers existing in typical glycine nitrogen chemical shift regions. Limited nitrogen chemical shifts were supplied by collaborators on the project (based on ^{13}C-^{15}N PAIN-CP correlations) and the only unambiguous assignment was G33 at a chemical shift value of ∼106 ppm. Further carbon-nitrogen experiments will be performed to enable further nitrogen-proton assignments based on the data shown here.

8.3.5 Chemical Shift Analysis and Modelling

The chemical shift assignments for each Aβ_{42}CC sample have been summarised in Tables 8.1-8.5. These chemical shifts were used, alongside others taken by collaborators in Uppsala (Dr. C. Lendel) and Aarhus (Dr. M. Bjerring) for confirmation, to find the secondary structure of the Aβ_{42}CC protofibrils. Secondary chemical shift analysis suggests an extended β-strand between residues K16-V24, a β-strand within the C-terminus between residues 27-36 with a possible break at G33, a definite break through G37 and G38 before a final short β-sheet between residues V39-A42, see Fig. 8.13. These three or four separate β-sheets are crucial in the modelling of the structure of oligomers as determined by the Rosetta software (modelling was per-

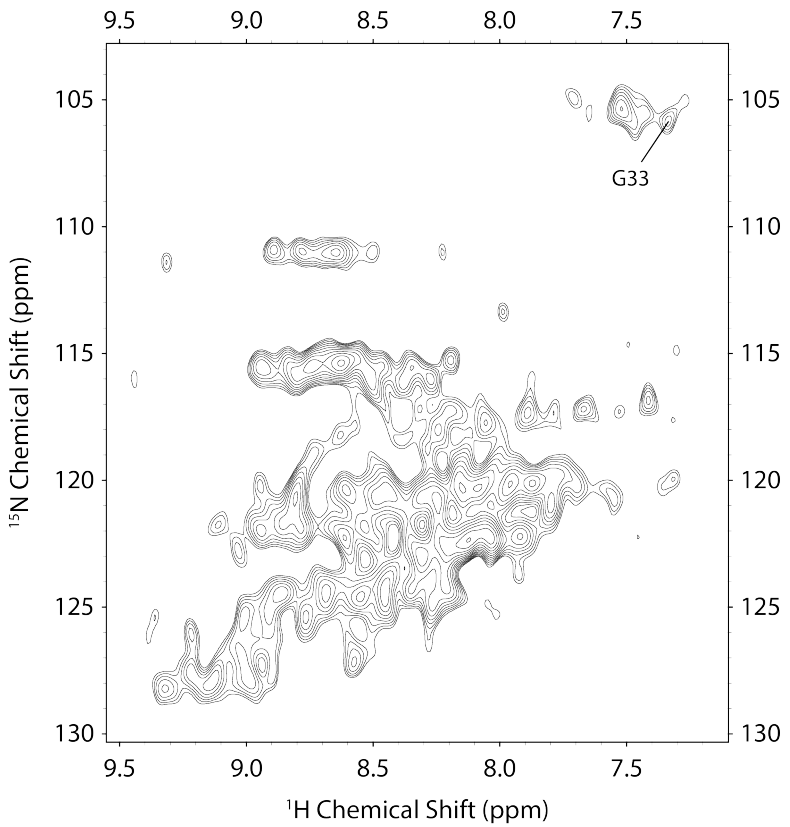

Figure 8.12: 2D ^{15}N-^{1}H inverse detection spectrum obtained for U-[^{13}C, ^{15}N] A$\beta_{1\text{-}42}$CC hydrated oligomers at a ^{1}H Larmor frequency of 850 MHz and 78 kHz MAS frequency, with 10 kHz WALTZ decoupling with 100 µs pulses on ^{15}N during ^{1}H acquisition. 80 transients were co-added for each 244 FIDs, the recycle delay was 0.5 s corresponding to an experimental time of ∼3 hours for all spectra. Base contour level: 4%

formed by Dr. C. Lendel). [288] The N-terminal residues 1-14 were not included in the modelling. For an in-depth discussion of the modelling procedure see [1]. In some detail, the chemical shift data for 63 chemical shifts from residues 15-42 were used to generate a peptide fragment library using the Rosetta web server. Single protomer models were calculated using the AbinitioRelax application in Rosetta using the chemical shift-based fragment library and 12 intramolecular distance restraints with an upper limit of 6.0 Å. The calculations converged to the model when calculating a total of 50,000 models. Oligomeric peptide building blocks were calculated using the 31 intermolecular distance restraints derived from a PAIN-CP spectrum (not shown, see [1]) with the same upper limit. Several symmetries were explored, however all dimeric, trimeric and fibrillar models significantly violated the experimen-

tal restraints. Symmetry was required in the model due to the existence of only one set of resonances for each residue, this can be seen in the spectra shown earlier. In the final round, 100,000 models were calculated with the ten models with lowest energy appearing in the same cluster. The lowest energy model (selected model) fulfills all intermolecular restraints with violations of <0.7 Å.

The model itself utilises four β-sheet sections, residues 16-24, 27-32, 34-36 and 39-42 with the first three in a typical β-hairpin structure before a turn section over residues 37 and 38, with the final short β-sheet interacting with residues 34-36 of the adjacent protomer, also shown in Fig 8.13. This fourth β-sheet adds a significant level of stability to the structure. The model can be seen in [1] and is a barrel with six-fold cylindrical symmetry whereby the packing forms a large hydrophobic core at one end of the barrel with the loops of each monomer collated at the opposite end. This model represents a possible building block of the protofibrils, and so the method by which the protofibril is built was also investigated. The shape complementarity score and hidden surface area was found for the three options of barrel binding: core-to-core; loop-to-loop; and core-to-loop. All three options were structurally reasonable, [1] although for protofibril formation core-to-core and loop-to-loop would have to occur together so as to produce a string of protomers. So, although loop-to-loop produces the highest shape complementarity conversely core-to-core possesses the worst and none of the ssNMR data taken within the study in the publication could determine which packing mechanism operates on these barrels. Previously obtained EM data of $A\beta_{42}$CC protofibrils, however, showed a periodicity of *ca.* 6 nm, [60] which agrees with a core-to-core/loop-to-loop formation (periodicity of ∼6 nm) as opposed to a core-to-loop formation (periodicity of ∼3 nm), revealing which packing mechanism applies in the formation of the protofibrils.

Various biological observations of Aβ aggregation can be explained using the above model: $A\beta_{42}$ is known to aggregate more rapidly than $A\beta_{40}$; [56] $A\beta_{42}$ has been shown to preferentially form hexamer units which assemble to form beaded structures that are similar to early protofibrils as opposed to the 1-40 version which forms protofibrils far less easily. [289] Residues 39-42 in this model form the final β-sheet which links to the adjacent protomer adding stability explaining both the rapid aggregation, and the preferential aggregation toward oligomer/protofibrils that is not found in the 1-40 variant. The hexamer-assembled beaded structures have already been shown to have 6 nm periodicity which, again, is in agreement with the model suggested in this work.

Table 8.1: (a) Aβ_{1-42}CC 'Crys 1' chemical shifts obtained from 50 and 400 ms mixing time DARR spectra displayed Fig. 8.2 and 8.3. (b) Chemical shifts obtained from a 300 ms mixing time DARR spectrum taken on a sample of 30% Aβ_{1-42}CC 'Crys 1' 70% na Aβ_{1-42}CC.

(a)

Residues	Assignment
D23	
Cα	51.5
Cβ	40.2
Cγ	180.1
V24	
C$'$	176.6
Cα	60.7
Cβ	31.1
Cγ	20.1
G25	
C$'$	175.7
Cα	44.0
S26	
C$'$	174.3
Cα	57.2
Cβ	62.0
K28	
Cα	53.7
Cβ	32.8
Cγ	23.7
Cδ	28.0
Cϵ	40.6

(b)

Residues	Assignment
D23	
Cα	51.6
Cβ	
Cγ	
V24	
C$'$	
Cα	
Cβ	31.2
Cγ	20.1
G25	
C$'$	
Cα	
S26	
C$'$	
Cα	56.8
Cβ	
K28	
Cα	55.1
Cβ	32.8
Cγ	23.3
Cδ	28.5
Cϵ	40.9

Table 8.2: (a) Aβ_{1-42}CC 'Crys 2' and (b) 'Crys 3' chemical shifts obtained from various mixing time DARR spectra displayed in Figs. 8.4 and 8.5.

(a)

Residues	Assignment
L17	
C′	172.3
Cα	51.5
Cβ	43.7
Cγ	25.2
$C\delta_1$	22.6
$C\delta_2$	22.6
V18	
C′	172.4
Cα	58.4
Cβ	33.3
Cγ	19.8
G29	
C′	170.1
Cα	43.5
M35	
C′	171.6
Cα	52.2
Cβ	34.6
Cγ	30.8
Cϵ	16.8

(b)

Residues	Assignment
K16	
C′	171.9
Cα	52.8
Cβ	27.8
Cγ	23.3
Cδ	27.5
Cϵ	39.7
N27	
C′	
Cα	53.0
Cβ	37.5
Cγ	176.2
V36	
C′	172.7
Cα	58.7
Cβ	32.6
Cγ	19.7
G37	
C′	171.5
Cα	43.0

Table 8.3: (a) Aβ_{1-42}CC 'F19I31' chemical shifts obtained from a 300 ms mixing time DARR spectrum shown in Fig. 8.7 and (b) Aβ_{1-42}CC 'F20I32' chemical shifts obtained from a 400 ms mixing time DARR spectrum shown in Fig. 8.6.

(a)

Residues	Assignment
F20	
C′	172.3
Cα	54.5
Cβ	38.7
Cδ	129.0
Cϵ	127.8
I31	
C′	173.6
Cα	57.4
Cβ	36.8
$C\gamma_1$	24.4
$C\gamma_2$	15.1
$C\delta_1$	12.5

(b)

Residues	Assignment
F19	
C′	171.4
Cα	54.7
Cβ	39.2
Cγ	138.0
Cδ	129.4
Cϵ	125.2
I32	
C′	173.9
Cα	58.8
Cβ	36.6
$C\gamma_1$	24.3
$C\gamma_2$	15.6
$C\delta_1$	12.0

Table 8.4: U-[^{13}C, ^{15}N] Aβ_{1-42}CC sedimented oligomer ^{13}C chemical shifts obtained from indirectly observed ^{13}C-^{1}H spectra, see Figs. 8.10 and 8.11, and various DARR spectra.

Residues	Cα	Cβ	Cγ1/Cγ#	Cγ2	Cδ1/Cδ#	Cδ2
K16					27.5	
L17		43.7	25.2			
E22			35.9			
V24		31.2				
S26	57.2	62.0				
N27		37.5				
K28	53.7	32.8	23.7		28.0	
I31	57.4		24.4	15.1	12.5	
I32		36.6	24.3	15.6		
G33	45.9					
L34			26.5		25.1	22.1
M35		34.6	30.8			
V36		32.6				
V39		35.1	17.8	20.2		
V40	60.5	33.2				
I41	58.8	40.9		17.6	13.8	

Table 8.5: U-[^{13}C, ^{15}N] Aβ_{1-42}CC sedimented oligomer ^{1}H chemical shifts taken from indirectly observed ^{13}C-^{1}H spectrum, see Figs. 8.10 and 8.11.

	H	Hα	Hβ/Hβ#	Hβ3/13	Hγ1/Hγ#	Hγ2	Hδ1/Hδ#	Hδ2/Hδ#	Hz
K16									7.2
L17			1.8		1.3		1.0	0.9	
E22			1.7	1.7	1.3				
V24			2.1						
S26	8.7	4.3			5.0				
N27			2.0	2.0					
K28	8.5	4.6	1.8	1.8	1.2	1.2	1.8	1.8	
I31	8.9	4.5	1.6		1.3	0.7	-0.4		
I32	8.8	5.2	2.2		1.6	0.7			
G33	8.8	3.9							
L34	8.9	5.0	1.7	1.4	1.3		0.9	0.8	
M35	8.6		2.0	2.0					
V36	8.9	4.9	1.9						
V39			2.2		0.5	0.9			
V40		5.0	1.5						
I41	8.8	4.0	2.9		1.6	0.7	0.4		

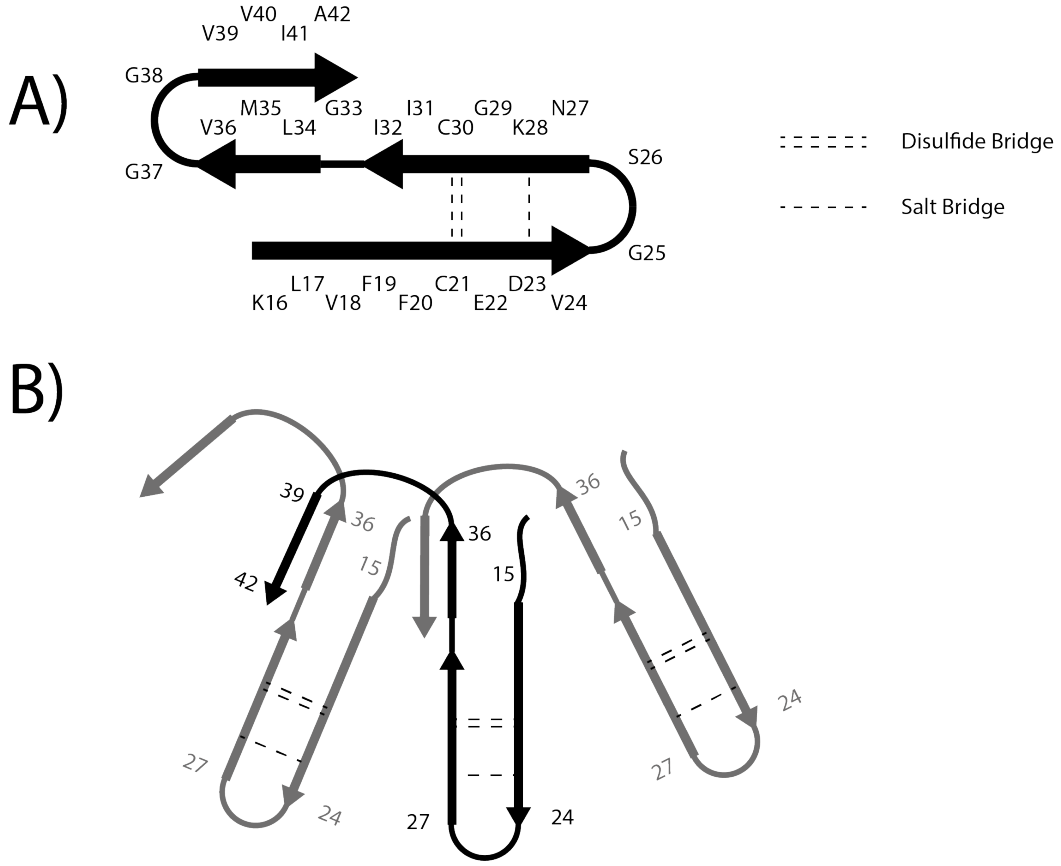

Figure 8.13: A) A structural model suggesting the secondary structure adopted by the $A\beta_{1\text{-}42}$CC peptide when in an oligomeric and protofibrillar conformation. B) A suggested organisation of the peptides within the oligomeric form. This illustrates why the additional short β-sheet section in the C-terminus in this conformation of $A\beta_{1\text{-}42}$ significantly increases the toxicity of the molecule, as the toxic form is stabilised and therefore can form faster and remain in this conformation for longer.

8.3.6 1D ^{31}P NMR Spectra

1D ^{31}P NMR experiments were performed on the phospholipid membrane samples I-X from § 8.2.1 and the resulting observed spectra are shown in Fig. 8.14. The intensity of the signals are compared and a decrease in signal is a sign of a destabilisation of the lipid membrane, as the repetitive structure generating the signal has been altered in some manner to a less homogeneous form, typically accompanied by a damaging effect on the membrane.

Fig. 8.14 (A) shows the 1D ^{31}P lineshape obtained from experiments performed on samples I, II and III. Sample I was pure phospholipid membrane (DMPC), whereas

samples II and III contained lipid and the addition of 5 mol % of cholesterol and curcumin, respectively. As can be seen, cholesterol has a destabilising effect on the membrane and causes a significant decrease in the intensity of the signal. Curcumin, the potentially therapeutic compound, has also been shown to disrupt the membrane but to a lesser extent. The incorporation of cholesterol into phospholipid bilayers clearly can induce changes in the structure and previously published work has shown the effect of cholesterol on the dynamics of the bilayer. [290] These alterations are the likely cause for the linebroadening in ^{31}P spectra, due to a variety in the structures present in the sample.

Fig. 8.14 (B) shows the lineshapes obtained from performing 1D ^{31}P NMR on samples of phospholipid and increasing amounts of curcumin, samples used were I, III, IV and V. (A) showed the effect of 5% curcumin on the phospholipid membrane and the effect of 15 and 30% molar weight of curcumin on DMPC is more drastic, as might be expected, and significant membrane disruption is caused by these high levels of the compound. The impact of increasing the amount of the curcumin from 15 to 30% does not further increase the disruption however, as the observed signal for 15% is less intense than that for 30%. A recent publication by Antzutkin et al has shown that curcumin has a solubility in phospholipid membranes of only up to ∼10 mol%, explaining the behaviour seen here. [291]

Fig. 8.14 (C) shows ^{31}P NMR spectra for the lipid when combined with monomeric (VI) and oligomeric (VIII) forms of the A$\beta_{1\text{-}42}$CC peptide. Both lineshapes show decreased intensity when compared to just DMPC, thereby showing that there is some level of membrane disruption due to both the monomeric and the oligomeric form of the peptide. There is a significant decrease in the intensity of the resonance due to the oligomeric form (which was to be expected) compared to the relatively limited membrane disruption caused by the monomeric form, confirming the significant disruption to the structure due to the particularly toxic species. Any further change in intensity between (C) and (D), where the sample also contains curcumin, must occur as a direct result of that inclusion.

Fig. 8.14 (D) shows the spectra obtained from performing 1D ^{31}P NMR on samples of DMPC with 5% curcumin and monomeric peptide (VII), and 5% curcumin and oligomeric peptide (IX). Also overlayed in the spectrum is the lineshape from sample (II) so as to compare the effect of curcumin alone and curcumin and peptide. As shown in (A), sample II showed a decreased intensity when compared to sample I, however sample VII results in a lower ^{31}P peak intensity than either the lipid or the lipid with 5% curcumin, which is to be expected if the peptide disrupts the membranes as is

thought to occur. Interestingly, the disruption for monomeric peptide and curcumin is greater than the disruption caused by either of the two substances alone, see samples II and VI. When the curcumin is combined with the oligomeric peptide however, which is thought to be the most cytotoxic form, the peak intensity is greater than for the previous 3 samples. This is as a result of the curcumin interacting with, and binding to, the oligomeric peptide thereby altering the disruptive effect of both the peptide and the molecule, and previously published results would lend support to this claim. [292] Within this publication, the authors state 'The molar ratios for successful Aβ fibril and aggregate inhibition by curcumin in the assays we used were clearly greater than 1:1, consistent with the idea that curcumin does not bind monomeric Aβ but rather to some secondary structure involved in later stages of assembly.' and this finding, that curcumin does not bind to Aβ monomers, is also reported in [293]. This could offer an explanation for the increased membrane disruption when curcumin and monomeric peptide are prepared together, however a significant decrease when the sample contains curcumin and oligomeric peptide.

Fig. 8.14 (E) shows 1D ^{31}P NMR spectra obtained from experiments on two different phospholipid membranes with 15 mol% curcumin, DMPC (IV) and DOPC (X). Although DMPC is the usual starting point for work on phospholipid membranes, as, among other reasons, it belongs to the family of glycerophopholipids representing the main lipid components of biological membranes, DOPC is one of the most typical cell membrane phospholipids and so offers an interesting and relevant comparison to the earlier work using DMPC membranes. [294] Sample IV displayed again, previously shown in (B), shows the significantly disruptive effect of high levels of curcumin on DMPC, however the effect is far greater on sample X, containing DOPC.

8.4 Discussion

8.4.1 Selectively Labelled Samples of A$\beta_{1\text{-}42}$CC

Selectively labelled samples of A$\beta_{1\text{-}42}$CC oligomers were synthesised and allowed an accurate assignment of the chemical shifts for many residues, including almost all residues in the β-turn found in the hairpin structure adopted by aggregating Aβ, through the use of 2D ^{13}C-^{13}C DARR experiments. A uniformly labelled sample of the oligomers provided confirmation that the peptide when formed through bacterial expression or using a peptide synthesiser adopted almost identical structures. Secondary chemical shift analysis, using further chemical shift assignments obtained by

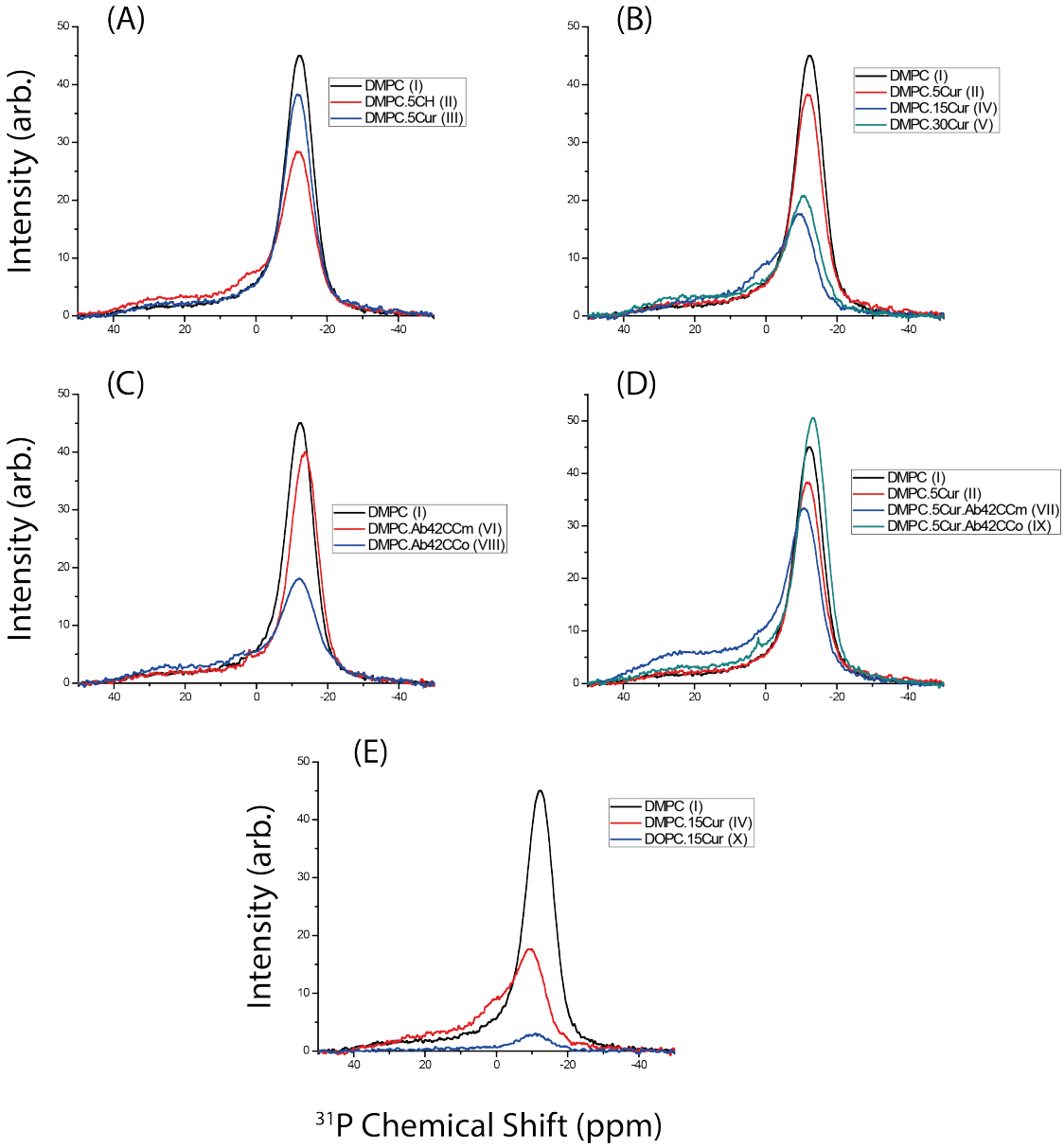

Figure 8.14: 1D ^{31}P CP MAS spectra taken on samples I-X. A) compares the spectra from partially labelled phospholipid membranes in association with 5 mol% cholesterol (CH) and 5 mol% curcumin (Cur) and only phospholipid membrane, B) compares the spectra from samples with increasing amounts of curcumin 5, 15 and 30 mol%, C) shows the effect of monomeric and oligomeric forms of A$\beta_{1\text{-}42}$CC on the phosphorus NMR spectra, D) shows the impact of curcumin on the monomeric and oligomeric peptide's effect and E) introduces a secondary phospholipid membrane.

collaborators, enabled the secondary structure adopted by the oligomer to be found. β-sheets were found between positions K16-V24, N27-I32, L34-V36 and V39-A42. The final β-sheet section, 39-42, has not been reported for the less toxic 1-40 variant of Aβ and the structural implications of this extra β-sheet could be the reason for the increased toxicity found for this sample.

The labelling schemes used were chosen so as to produce spectra without spectrally cluttered regions and, though some of the linewidths in the spectra are quite broad, nearly all the carbon chemical shifts for the labelled residues were found. The broad signals located within the aromatic regions of the spectra in Figs. 8.6 and 8.7 did not allow for full assignment of the resonances within this region, and so further experiments would be required to obtain unambiguous assignments for these nuclei. Many carbonyl assignments were made, in spite of the broad C′ resonances, which for a uniformly labelled sample is often particularly troublesome, see spectra from § 7 and Fig. 8.8.

Successful assignment of large proteins in the future of ssNMR may well depend on producing many samples with a limited number of residues labelled and altering the labelling scheme within each sample until the chemical shifts for the residues of the whole protein can be combined. With the use of 3D experiments, the labelling schemes need not be as restricted as those used in this work. However, by separating residues with chemical shifts that are likely to exist in similar spectral regions using the different labelling schemes, a detailed picture of large biomolecules may well be more easily obtained using ssNMR than through the use of uniformly labelled samples.

8.4.2 Amyloid-β_{42}CC Forms a Cytotoxic Hexamer Peptide Barrel

Collaborative work with Dr. Christofer Lendel, Dr. Anatoly Dubnovitsky and Prof. Torleif Härd from Uppsala University, Dr. Morten Bjerring and Prof. Niels Chr. Nielsen from Aarhus University and Dr. Andrei Filippov from Luleå University of Technology has led to a publication on some of the work in this chapter; chemical shifts, taken from uniformly and selectively labelled samples of Aβ_{42}CC, were combined with the Rosetta 3.2 modelling software [288] to produce a model of a potential building block of Aβ protofibrils. [1] This model also explains many phenomena associated with the aggregation of Aβ_{1-42} and is in agreement with many structural observations already published.

8.4.3 Interaction of Curcumin, Cholesterol and A$\beta_{1\text{-}42}$CC with Phospholipid Membranes

1D ^{31}P NMR experiments were used to investigate the effect on membrane stability of A$\beta_{1\text{-}42}$CC, cholesterol and a natural compound currently of significant scientific interest, curcumin. Aβ is known to damage cell membranes and the effect of cholesterol has significant biological implications for today's population, with the vast array of beneficial properties thought to be associated with curcumin making it a compound of interest for many research groups. [293, 295, 296] All three were shown to disrupt the membrane in some manner, however the oligomeric form of the peptide, which caused significant disruption to the membrane, was found to cause no destabilisation when combined, before incorporation with the membrane, with curcumin. The same was not seen of the monomeric peptide, agreeing with previous work, [292] and so the binding of curcumin and certain forms of Aβ could have significant therapeutic consequences. Previously curcumin was thought to not cross the blood brain barrier, which would eliminate it as an option for therapeutic treatment, however it is now believed that it does cross the barrier and work has begun on increasing its short systemic retention while in circulation and uptake. [297–299]

Regarding the impact of cholesterol on the formation of toxic Aβ species, a thorough review as to the questions surrounding amyloid-beta and its interactions with cholesterol and membranes was provided by the Müller group, [300] and it suggests that the interaction of cholesterol and amyloid beta is yet to be fully understood and that published results for the direct impact of the former on the cytotoxicity of the later are, at best, varied.

8.5 Outlook

The work in this chapter has shown that the particularly toxic, and previously elusive, conformation of A$\beta_{1\text{-}42}$ can be captured and, therefore, studied and that this work has enabled a model of this structure to be built. Therapeutic treatments which work on a structural level will require information of this type and may attempt to locate binding sites which can be manipulated so as to halt aggregation, or to reduce toxicity. Curcumin has been shown to be a candidate worthy of further study for its beneficial bioproperties, among which is included the binding to toxic Aβ species.

Detailed structural knowledge of the interaction sites and the structural consequences

of the binding of curcumin, amyloid-beta and also cholesterol to one another and to cell membranes will be discovered, and this will allow a more precise targeting of therapeutic candidates. Whether medical trials will already have found a suitable drug for disease treatment and prevention before this discovery, is to be seen. Without the structural information offered by techniques such as NMR, a proper understanding of the pathology of a disease, especially a complex, multifaceted disease such as Alzheimer's, is almost impossible and the design of therapeutic compounds is much less accurate. The importance of NMR in this field is only one of the many in which this technique can contribute, and as it continues to develop it will be able to solve problems of greater complexity, with the consequence for this field being greater structural knowledge as a basis for developing accurate and well-targeted therapeutics.

9

Summary and Outlook

The work contained in this thesis has utilised solid-state NMR as a tool to investigate the atomic-level structure of $A\beta_{1\text{-}40}$ aggregates formed in the presence of copper and $A\beta_{1\text{-}42}$ oligomers stabilised by a sulphur bridge due to the mutations A21C and A30C. The combined use of 2D ^{13}C-^{13}C homonuclear and ^{15}N-^{13}C heteronuclear spectra alongside 2D and 3D X-^{1}H, X-^{1}H-^{1}H and X-X-^{1}H Inverse Detection spectra have enabled chemical shift values to be found for the samples.

For the $A\beta_{1\text{-}40}$/Cu aggregates, torsion angle restraints were calculated using TALOS-N and secondary chemical shift analysis identified regions of β-sheet and the hairpin-turn regularly found in Aβ fibrils. The structure of the $A\beta_{1\text{-}40}$ aggregates was found to be similar to a brain derived sample of $A\beta_{1\text{-}40}$ fibrils, and so underlines the importance of copper in re-creating physiologically accurate conditions when forming fibrils, the structural information from which will be used in developing therapeutic treatments. An exciting experimental setup was required for the Inverse Detection experiments, namely ultra-fast MAS (∼100 kHz) and rapid acquisition of data with a recycle delay of 0.2 s due to the paramagnetic copper in the sample, enabling well-resolved 3D experiments to be obtained in a few hours.

The turn region of $A\beta_{1\text{-}42}$CC oligomers was well characterised using selectively labelled samples. The oligomers have previously been shown to be toxic, and, here, were found to disrupt lipid membranes. 1D ^{31}P NMR allowed an investigation of the de-stabilising effect of $A\beta_{1\text{-}42}$CC oligomers on lipid membranes. The effect of cholesterol and curcumin on this de-stabilisation was also investigated. Curcumin was found to disrupt membranes, however when combined with oligomers and membranes the membrane was found to remain undisrupted, suggesting the curcumin and

oligomers bind in a way that reduces the membrane disruption and, therefore, the toxic behaviour. These results suggest that curcumin may have a role in reducing neurodegeneration during Alzheimer's disease and further work should be performed investigating the therapeutic properties of the molecule.

A

Reduced Wigner Rotation Matrices

$$d^0_{00}(\beta) = 1 \tag{A.1a}$$

$$d^1_{00}(\beta) = \cos(\beta) \tag{A.1b}$$

$$d^1_{01}(\beta) = d^1_{-10}(\beta) = -d^1_{0-1}(\beta) = -d^1_{10}(\beta) = \frac{1}{\sqrt{2}}\sin(\beta) \tag{A.1c}$$

$$d^1_{1-1}(\beta) = d^1_{-11}(\beta) = \sin^2\left(\frac{\beta}{2}\right) = \frac{1}{2}(1-\cos\beta) \tag{A.1d}$$

$$d^1_{11}(\beta) = d^1_{-1-1}(\beta) = \cos^2\left(\frac{\beta}{2}\right) = \frac{1}{2}(1+\cos\beta) \tag{A.1e}$$

$$d^2_{00}(\beta) = \frac{1}{2}(3\cos^2\beta - 1) \tag{A.1f}$$

$$d^2_{10}(\beta) = d^2_{0-1}(\beta) = -d^2_{01}(\beta) = -d^2_{-10}(\beta) = -\sqrt{\frac{3}{2}}\sin(\beta)\cos(\beta) \tag{A.1g}$$

$$d^2_{1-1}(\beta) = d^2_{-11}(\beta) = \frac{1}{2}(2\cos\beta + 1)(1-\cos\beta) \tag{A.1h}$$

$$d^2_{11}(\beta) = d^2_{-1-1}(\beta) = \frac{1}{2}(2\cos\beta - 1)(1+\cos\beta) \tag{A.1i}$$

$$d^2_{20}(\beta) = d^2_{02}(\beta) = -d^2_{-20}(\beta) = -d^2_{0-2}(\beta) = -\sqrt{\frac{3}{8}}\sin^2(\beta) \tag{A.1j}$$

$$d^2_{21}(\beta) = -d^2_{12}(\beta) = -d^2_{-2-1}(\beta) = -d^2_{-1-2}(\beta) = -\frac{1}{2}\sin(\beta)(\cos(\beta)+1) \tag{A.1k}$$

$$d^2_{2-1}(\beta) = d^2_{1-2}(\beta) = -d^2_{-21}(\beta) = -d^2_{-12}(\beta) = \frac{1}{2}\sin(\beta)(\cos(\beta)-1) \tag{A.1l}$$

$$d^2_{22}(\beta) = d^2_{-2-2}(\beta) = \cos^4\left(\frac{\beta}{2}\right) \tag{A.1m}$$

$$d^2_{2-2}(\beta) = d^2_{-22}(\beta) = \sin^4\left(\frac{\beta}{2}\right) \tag{A.1n}$$

B

Amino Acids

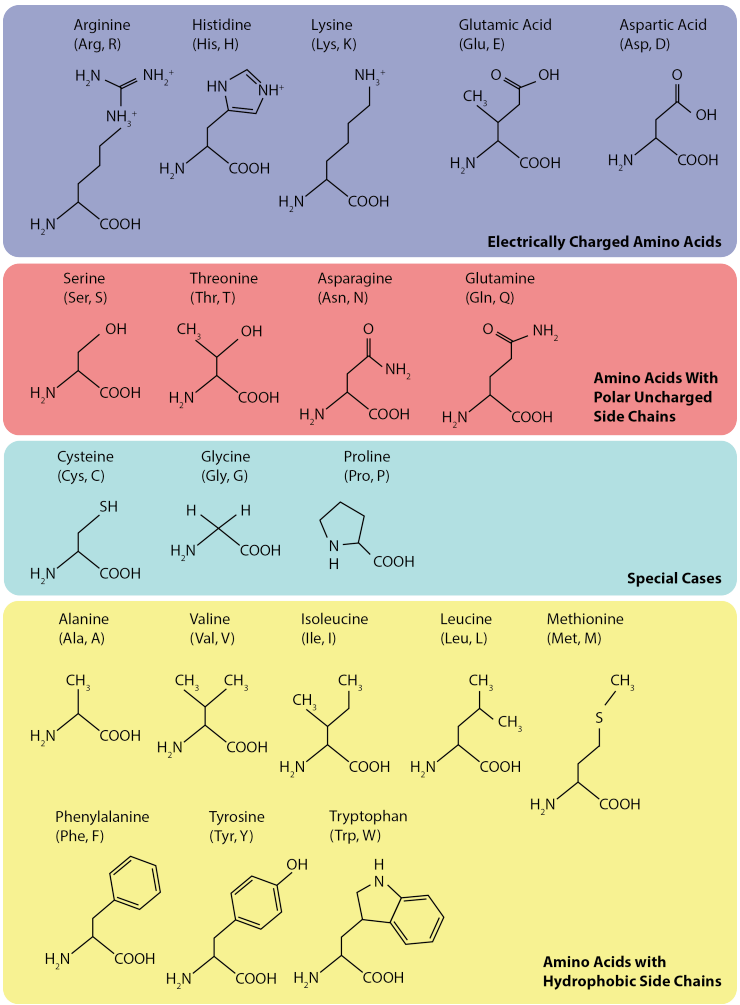

Figure B.1: The structures of 20 amino acids

C

Curcumin & Cholesterol

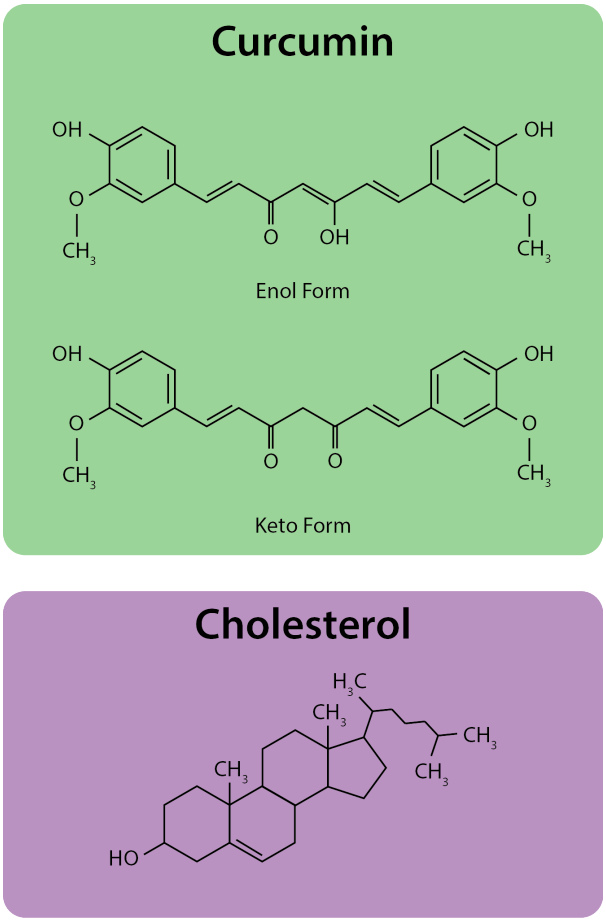

Figure C.1: The structures of curcumin and cholesterol

Bibliography

[1] Lendel C, et al. (2014) A Hexameric Peptide Barrel as a Building Block of Amyloid-β Protofibrils. *Angew. Chem. Int. Ed.* 53:12756–12760.

[2] Antzutkin ON, et al. (2012) Hydrogen Bonding in Alzheimers Amyloid-β Fibrils Probed by ^{15}N $\{^{17}$O$\}$ REAPDOR Solid-State NMR Spectroscopy. *Angew. Chem. Int. Ed.* 124:10435–10438.

[3] Purcell EM, Torrey H, Pound RV (1946) Resonance Absorption by Nuclear Magnetic Moments in a Solid. *Phys. Rev.* 69:37–38.

[4] Bloch F, Hansen WW, Packard M (1946) The Nuclear Induction Experiment. *Phys. Rev.* 70:474–485.

[5] Gerlach W, Stern O (1922) Der Experimentelle Nachweis der Richtungsquantelung im Magnetfeld. *EPJ A* 9:349–352.

[6] Uhlenbeck GE, Goudsmit S (1926) Spinning Electrons and the Structure of Spectra. *Nature* 117:264–265.

[7] Schrödinger E (1926) An Undulatory Theory of the Mechanics of Atoms and Molecules. *Phys. Rev.* 28:1049.

[8] Heisenberg W (1927) Über Den Anschaulichen Inhalt der Quantentheoretischen Kinematik und Mechanik. *EPJ* 43:172–198.

[9] Pauli W (1927) On the Quantum Mechanics of Magnetic Electrons. *Nature* 119:282.

[10] Phipps T, Taylor J (1927) The Magnetic Moment of the Hydrogen Atom. *Phys. Rev.* 29:309.

[11] Dirac PA (1928) The Quantum Theory of the Electron. *Proc. R. Soc. A* pp 610–624.

[12] Gorter C (1936) Negative Result of an Attempt to Detect Nuclear Magnetic Spins. *Physica* 3:995–998.

[13] Gorter C, Broer L (1942) Negative Result of an Attempt to Observe Nuclear Magnetic Resonance in Solids. *Physica* 9:591–596.

[14] Bloembergen N, Purcell EM, Pound RV (1948) Relaxation Effects in Nuclear Magnetic Resonance Absorption. *Phys. Rev.* 73:679.

[15] Pake G (1948) Nuclear Resonance Absorption in Hydrated Crystals: Fine Structure of the Proton Line. *J. Chem. Phys.* 16:327–336.

[16] Hahn EL (1950) Spin Echoes. *Phys. Rev.* 80:580.

[17] Lowe I, Norberg R (1957) Free-Induction Decays in Solids. *Phys. Rev.* 107:46.

[18] Andrew E, Bradbury A, Eades R (1958) Nuclear Magnetic Resonance Spectra from a Crystal Rotated at High Speed. *Nature* 182:1659.

[19] Lowe I (1959) Free Induction Decays of Rotating Solids. *Phys. Rev. Lett.* 2:285.

[20] Hartmann S, Hahn E (1962) Nuclear Double Resonance in the Rotating Frame. *Phys. Rev.* 128:2042–2053.

[21] Mehring M, Pines A, Rhim WK, Waugh J (1971) Spin-Decoupling in the Resolution of Chemical Shifts in Solids by Pulsed NMR. *J. Chem. Phys.* 54:3239–3240.

[22] Pines A, Gibby M, Waugh J (1972) Proton-Enhanced Nuclear Induction Spectroscopy. A Method for High Resolution NMR of Dilute Spins in Solids. *J. Chem. Phys.* 56:1776–1777.

[23] Schaefer J, Stejskal E (1976) Carbon-13 Nuclear Magnetic Resonance of Polymers Spinning at the Magic Angle. *J. Am. Chem. Soc.* 98:1031–1032.

[24] Gullion T, Schaefer J (1989) Rotational-Echo Double-Resonance NMR. *J. Magn. Reson.* 81:196–200.

[25] Shore SE, Ansermet JP, Slichter CP, Sinfelt JH (1987) Nuclear Magnetic Resonance Study of the Bonding and Diffusion of CO Chemisorbed on Pd. *Phys. Rev. Lett.* 58:953.

[26] Tycko R, Dabbagh G (1990) Measurement of Nuclear Magnetic DipoleDipole Couplings in Magic Angle Spinning NMR. *Chem. Phys. Lett.* 173:461–465.

[27] Wüthrich K, Wagner G (1978) Internal Motion in Globular Proteins. *Trends Biochem. Sci.* 3:227–230.

[28] Aue W, Bartholdi E, Ernst RR (1976) Two-Dimensional Spectroscopy. Application to Nuclear Magnetic Resonance. *J. Chem. Phys.* 64:2229–2246.

[29] Jeener J, Meier B, Bachmann P, Ernst R (1979) Investigation of Exchange Processes by Two-Dimensional NMR Spectroscopy. *J. Chem. Phys.* 71:4546–4553.

[30] Kumar A, Ernst R, Wüthrich K (1980) A Two-Dimensional Nuclear Overhauser Enhancement (2D NOE) Experiment for the Elucidation of Complete Proton-Proton Cross-Relaxation Networks in Biological Macromolecules. *Biochem. Biophys. Res. Commun.* 95:1–6.

[31] Williamson MP, Havel TF, Wüthrich K (1985) Solution Conformation of Proteinase Inhibitor IIA from Bull Seminal Plasma by ^{1}H Nuclear Magnetic Resonance and Distance Geometry. *J. Mol. Biol.* 182:295–315.

[32] Opella S, et al. (1999) Structures of the M2 Channel-Lining Segments from Nicotinic Acetylcholine and NMDA Receptors by NMR Spectroscopy. *Nat. Struc. Mol. Biol.* 6:374–379.

[33] Wu C, Ramamoorthy A, Opella S (1994) High-Resolution Heteronuclear Dipolar Solid-State NMR Spectroscopy. *J. Magn. Reson.* 109:270–272.

[34] Ramamoorthy A, Wei Y, Lee DK (2004) PISEMA Solid-State NMR Spectroscopy. *Annu. Rep. NMR Spectrosc.* 52:1–52.

[35] Castellani F, et al. (2002) Structure of a Protein Determined by Solid-State Magic-Angle-Spinning NMR Spectroscopy. *Nature* 420:98–102.

[36] Szeverenyi NM, Sullivan MJ, Maciel GE (1982) Observation of Spin Exchange by Two-Dimensional Fourier Transform ^{13}C Cross Polarization-Magic-Angle Spinning. *J. Magn. Reson.* 47:462–475.

[37] Comellas G, Rienstra CM (2013) Protein Structure Determination by Magic-Angle Spinning Solid-State NMR, and Insights into the Formation, Structure, and Stability of Amyloid Fibrils. *Annu. Rev. of Biophys.* 42:515–536.

[38] Zhou DH, et al. (2007) Solid-State Protein-Structure Determination with Proton-Detected Triple-Resonance 3D Magic-Angle-Spinning NMR Spectroscopy. *Angew. Chem. Int. Ed.* 46:8380–8383.

[39] Huber M, et al. (2011) A Proton-Detected 4D Solid-State NMR Experiment for Protein Structure Determination. *ChemPhysChem* 12:915–918.

[40] Robustelli P, Cavalli A, Vendruscolo M (2008) Determination of Protein Structures in the Solid State from NMR Chemical Shifts. *Structure* 16:1764–1769.

[41] Loquet A, et al. (2012) Atomic Model of the Type III Secretion System Needle. *Nature* 486:276–279.

[42] Daviso E, Eddy MT, Andreas LB, Griffin RG, Herzfeld J (2013) Efficient Resonance Assignment of Proteins in MAS NMR by Simultaneous Intra-and Inter-Residue 3D Correlation Spectroscopy. *J. Biomol. NMR* 55:257–265.

[43] Creuzet F, et al. (1991) Determination of Membrane Protein Structure by Rotational Resonance NMR: Bacteriorhodopsin. *Science* 251:783–786.

[44] Andronesi OC, et al. (2005) Determination of Membrane Protein Structure and Dynamics by Magic-Angle-Spinning Solid-State NMR Spectroscopy. *J. Am. Chem. Soc.* 127:12965–12974.

[45] Etzkorn M, et al. (2007) Secondary Structure, Dynamics, and Topology of a Seven-Helix Receptor in Native Membranes, Studied by Solid-State NMR Spectroscopy. *Angew. Chem. Int. Ed.* 46:459–462.

[46] De Angelis AA, Howell SC, Nevzorov AA, Opella SJ (2006) Structure Determination of a Membrane Protein with Two Trans-Membrane Helices in Aligned Phospholipid Bicelles by Solid-State NMR Spectroscopy. *J. Am. Chem. Soc.* 128:12256–12267.

[47] McDermott A (2009) Structure and Dynamics of Membrane Proteins by Magic Angle Spinning Solid-State NMR. *Annu. Rev. of Biophys.* 38:385–403.

[48] Chiti F, Dobson CM (2006) Protein Misfolding, Functional Amyloid, and Human Disease. *Annu. Rev. Biochem.* 75:333–366.

[49] Tycko R (2011) Solid State NMR Studies of Amyloid Fibril Structure. *Annu. Rev. Phys. Chem.* 62:279–299.

[50] Holtzman DM, John CM, Goate A (2011) Alzheimer's Disease: The Challenge of The Second Century. *Sci. Transl. Med.* 3:1–12.

[51] Schenkman M, et al. (2011) Profile of Functional Limitations and Task Performance Among People With Early-and Middle-Stage Parkinson Disease. *Phys Ther.* 91:1339–1354.

[52] Linser R, et al. (2011) Proton-Detected Solid-State NMR Spectroscopy of Fibrillar and Membrane Proteins. *Angew. Chem. Int. Ed.* 50:4508–4512.

[53] Comellas G, et al. (2011) Structured Regions of α-Synuclein Fibrils Include the Early-Onset Parkinson's Disease Mutation Sites. *J. Mol. Biol.* 411:881–895.

[54] Karpinar DP, et al. (2009) Pre-fibrillar α-Synuclein Variants with Impaired β-Structure Increase Neurotoxicity in Parkinson's Disease Models. *EMBO J.* 28:3256–3268.

[55] Mithu VS, et al. (2011) Zn^{++} Binding Disrupts the Asp^{23}-Lys^{28} Salt Bridge without Altering the Hairpin-Shaped Cross-β Structure of Aβ_{42} Amyloid Aggregates. *Biophys. J.* 101:2825.

[56] Antzutkin ON (2004) Amyloidosis of Alzheimer's Aβ Peptides: Solid-State Nuclear Magnetic Resonance, Electron Paramagnetic Resonance, Transmission Electron Microscopy, Scanning Transmission Electron Microscopy and Atomic Force Microscopy Studies. *Magn. Reson. Chem.* 42:231–246.

[57] Murrell J, Farlow M, Ghetti B, Benson MD (1991) A Mutation in the Amyloid Precursor Protein Associated with Hereditary Alzheimer's Disease. *Science* 254:97–99.

[58] Kosik KS (1992) Alzheimer's Disease: A Cell Biological Perspective. *Science* 256:780–783.

[59] Seeman P, Seeman N (2011) Alzheimer's Disease: β-Amyloid Plaque Formation in Human Brain. *Synapse* 65:1289–1297.

[60] Sandberg A, et al. (2010) Stabilization of Neurotoxic Alzheimer Amyloid-β Oligomers by Protein Engineering. *Proc. Natl. Acad. Sci. U.S.A.* 107:15595–15600.

[61] Petkova AT, et al. (2002) A Structural Model for Alzheimer's β-Amyloid Fibrils based on Experimental Constraints from Solid State NMR. *Proc. Natl. Acad. Sci. U.S.A.* 99:16742–16747.

[62] Petkova AT, et al. (2005) Self-Propagating, Molecular-Level Polymorphism in Alzheimer's ß-Amyloid Fibrils. *Science* 307:262–265.

[63] Bertini I, Gonnelli L, Luchinat C, Mao J, Nesi A (2011) A New Structural Model of Aβ_{40} fibrils. *J. Am. Chem. Soc.* 133:16013–16022.

[64] Paravastu AK, Qahwash I, Leapman RD, Meredith SC, Tycko R (2009) Seeded Growth of β-Amyloid Fibrils from Alzheimer's Brain-Derived Fibrils produces a Distinct Fibril Structure. *Proc. Natl. Acad. Sci. U.S.A.* 106:7443–7448.

[65] Dahlgren KN, et al. (2002) Oligomeric and Fibrillar Species of Amyloid-β Peptides Differentially Affect Neuronal Viability. *J. Biol. Chem.* 277:32046–32053.

[66] Streltsov VA, Varghese JN, Masters CL, Nuttall SD (2011) Crystal Structure of the Amyloid-β p3 Fragment Provides a Model for Oligomer Formation in Alzheimer's Disease. *J. Neurosci.* 31:1419–1426.

[67] Spencer RG, et al. (1991) An Unusual Peptide Conformation may Precipitate Amyloid Formation in Alzheimer's Disease: Application of Solid-State NMR to the Determination of Protein Secondary Structure. *Biochemistry* 30:10382–10387.

[68] Lansbury PT, et al. (1995) Structural Model for the β-Amyloid Fibril based on Interstrand Alignment of an Antiparallel-Sheet Comprising a C-Terminal Peptide. *Nat. Struc. Mol. Biol.* 2:990–998.

[69] Costa P, Kocisko D, Sun B, Lansbury P, Griffin R (1997) Determination of Peptide Amide Configuration in a Model Amyloid Fibril by Solid-State NMR. *J. Am. Chem. Soc.* 119:10487–10493.

[70] Benzinger TL, et al. (1998) Propagating Structure of Alzheimer's β-Amyloid (10–35) is Parallel β-Sheet with Residues in Exact Register. *Proc. Natl. Acad. Sci. U.S.A.* 95:13407–13412.

[71] Gregory D, Wolfe G, Jarvie T, Shiels J, Drobny G (1996) Double-Quantum Filtering in Magic-Angle-Spinning NMR Spectroscopy Applied to DNA Oligomers. *Mol. Phys.* 89:1835–1849.

[72] Gregory DM, et al. (1998) Dipolar Recoupling NMR of Biomolecular Self-Assemblies: Determining Inter-and Intrastrand Distances in Fibrilized Alzheimer's β-Amyloid Peptide. *Solid State NMR* 13:149–166.

[73] Benzinger TL, et al. (2000) Two-Dimensional Structure of β-Amyloid (10-35) Fibrils. *Biochemistry* 39:3491–3499.

[74] Burkoth TS, et al. (2000) Structure of the β-Amyloid$_{(10\text{-}35)}$ Fibril. *J. Am. Chem. Soc.* 122:7883–7889.

[75] Balbach JJ, et al. (2000) Amyloid Fibril Formation by A$\beta_{16\text{-}22}$, a Seven-Residue Fragment of the Alzheimer's β-Amyloid Peptide, and Structural Characterization by Solid State NMR. *Biochemistry* 39:13748–13759.

[76] Antzutkin ON, et al. (2000) Multiple Quantum Solid-State NMR indicates a Parallel, not Antiparallel, Organization of β-Sheets in Alzheimer's β-Amyloid Fibrils. *Proc. Natl. Acad. Sci. U.S.A.* 97:13045–13050.

[77] Balbach JJ, et al. (2002) Supramolecular Structure in Full-Length Alzheimer's β-Amyloid Fibrils: Evidence for a Parallel β-Sheet Organization from Solid-State Nuclear Magnetic Resonance. *Biophys. J.* 83:1205–1216.

[78] Antzutkin ON, Leapman RD, Balbach JJ, Tycko R (2002) Supramolecular Structural Constraints on Alzheimer's β-Amyloid Fibrils from Electron Microscopy and Solid-State Nuclear Magnetic Resonance. *Biochemistry* 41:15436–15450.

[79] Török M, et al. (2002) Structural and Dynamic Features of Alzheimer's Aβ Peptide in Amyloid Fibrils Studied by Site-Directed Spin Labeling. *J. Biol. Chem.* 277:40810–40815.

[80] Tycko R, Ishii Y (2003) Constraints on Supramolecular Structure in Amyloid Fibrils from Two-Dimensional Solid-State NMR Spectroscopy with Uniform Isotopic Labeling. *J. Am. Chem. Soc.* 125:6606–6607.

[81] Antzutkin ON, Balbach JJ, Tycko R (2003) Site-Specific Identification of Non β-Strand Conformations in Alzheimer's β-Amyloid Fibrils by Solid-State NMR. *Biophys. J.* 84:3326–3335.

[82] Petkova A, et al. (2004) Solid State NMR Reveals a pH-Dependent Antiparallel β-Sheet Registry in Fibrils Formed by a β-Amyloid Peptide. *J. Mol. Biol.* 335:247–260.

[83] Gordon DJ, Balbach JJ, Tycko R, Meredith SC (2004) Increasing the Amphiphilicity of an Amyloidogenic Peptide Changes the β-Sheet Structure in the Fibrils from Antiparallel to Parallel. *Biophys. J.* 86:428–434.

[84] Sciarretta KL, Gordon DJ, Petkova AT, Tycko R, Meredith SC (2005) Aβ40-Lactam (D23/K28) Models a Conformation Highly Favorable for Nucleation of Amyloid. *Biochemistry* 44:6003–6014.

[85] Chimon S, Ishii Y (2005) Capturing Intermediate Structures of Alzheimer's β-Amyloid, Aβ (1-40), by Solid-State NMR Spectroscopy. *J. Am. Chem. Soc.* 127:13472–13473.

[86] Petkova AT, Yau WM, Tycko R (2006) Experimental Constraints on Quaternary Structure in Alzheimer's β-Amyloid Fibrils. *Biochemistry* 45:498–512.

[87] Paravastu AK, Petkova AT, Tycko R (2006) Polymorphic Fibril Formation by Residues 10–40 of the Alzheimer's β-Amyloid Peptide. *Biophys. J.* 90:4618–4629.

[88] Sato T, et al. (2006) Inhibitors of Amyloid Toxicity Based on β-Sheet Packing of Aβ40 and Aβ42. *Biochemistry* 45:5503–5516.

[89] Olofsson A, Sauer-Eriksson AE, Öhman A (2006) The Solvent Protection of Alzheimer Amyloid-β-(1–42) Fibrils as Determined by Solution NMR Spectroscopy. *J. Biol. Chem.* 281:477–483.

[90] Chimon S, et al. (2007) Evidence of Fibril-Like β-Sheet Structures in a Neurotoxic Amyloid Intermediate of Alzheimer's β-Amyloid. *Nat. Struc. Mol. Biol.* 14:1157–1164.

[91] Bu Z, Shi Y, Callaway DJ, Tycko R (2007) Molecular Alignment within β-Sheets in A$\beta_{14\text{-}23}$ Fibrils: Solid-State NMR Experiments and Theoretical Predictions. *Biophys. J.* 92:594–602.

[92] Thurber KR, Tycko R (2008) Biomolecular Solid State NMR with Magic-Angle Spinning at 25 K. *J. Magn. Reson.* 195:179–186.

[93] Paravastu AK, Leapman RD, Yau WM, Tycko R (2008) Molecular Structural Basis for Polymorphism in Alzheimer's β-Amyloid Fibrils. *Proc. Natl. Acad. Sci. U.S.A.* 105:18349–18354.

[94] Tycko R, Sciarretta KL, Orgel JP, Meredith SC (2009) Evidence for Novel β-Sheet Structures in Iowa Mutant β-Amyloid Fibrils. *Biochemistry* 48:6072–6084.

[95] Smith DP, et al. (2006) Copper-Mediated Amyloid-β Toxicity is Associated with an Intermolecular Histidine Bridge. *J. Biol. Chem.* 281:15145–15154.

[96] Lau TL, et al. (2006) Amyloid-β Peptide Disruption of Lipid Membranes and the Effect of Metal Ions. *J. Mol. Biol.* 356:759–770.

[97] Ishii Y (2010) A Solid-State NMR Study Reveals Structure and Dynamics in Copper (II)-Binding to Alzheimer's Beta-Amyloid Fibrils. *Biophys. J.* 98:457a–458a.

[98] Scheidt HA, Morgado I, Rothemund S, Huster D, Fändrich M (2011) Solid-State NMR Spectroscopic Investigation of Aβ Protofibrils: Implication of a β-Sheet Remodeling upon Maturation into Terminal Amyloid Fibrils. *Angew. Chem. Int. Ed.* 50:2837–2840.

[99] Cloe AL, Orgel JP, Sachleben JR, Tycko R, Meredith SC (2011) The Japanese Mutant Aβ (ΔE22-A$\beta_{1\text{-}39}$) Forms Fibrils Instantaneously, with Low-Thioflavin T Fluorescence: Seeding of Wild-Type A$\beta_{1\text{-}40}$ into Atypical Fibrils by ΔE22-A$\beta_{1\text{-}39}$. *Biochemistry* 50:2026–2039.

[100] Qiang W, Yau WM, Tycko R (2011) Structural Evolution of Iowa Mutant β-Amyloid Fibrils from Polymorphic to Homogeneous States under Repeated Seeded Growth. *J. Am. Chem. Soc.* 133:4018–4029.

[101] Qiang W, Yau WM, Luo Y, Mattson MP, Tycko R (2012) Antiparallel β-Sheet Architecture in Iowa-Mutant β-Amyloid Fibrils. *Proc. Natl. Acad. Sci. U.S.A.* 109:4443–4448.

[102] Parthasarathy S, et al. (2011) Molecular-Level Examination of Cu^{2+} Binding Structure for Amyloid Fibrils of 40-Residue Alzheimer's β by Solid-State NMR Spectroscopy. *J. Am. Chem. Soc.* 133:3390–3400.

[103] Scheidt HA, Morgado I, Huster D (2012) Solid-State NMR Reveals a Close Structural Relationship between Amyloid-β Protofibrils and Oligomers. *J. Biol. Chem.* 287:22822–22826.

[104] Scheidt HA, Morgado I, Rothemund S, Huster D (2012) Dynamics of Amyloid β Fibrils Revealed by Solid-State NMR. *J. Biol. Chem.* 287:2017–2021.

[105] Wang S, Ishii Y (2012) Revealing Protein Structures in Solid-Phase Peptide Synthesis by ^{13}C Solid-State NMR: Evidence of Excessive Misfolding for Alzheimer's β. *J. Am. Chem. Soc.* 134:2848–2851.

[106] Sciacca MF, et al. (2012) Two-Step Mechanism of Membrane Disruption by Aβ through Membrane Fragmentation and Pore Formation. *Biophys. J.* 103:702–710.

[107] Chandrakesan M, et al. (2013) The Basic Structural Motif and Major Biophysical Properties of Amyloid-β are Encoded in the Fragment 18–35. *Chem. Phys.* 422:80–87.

[108] Parthasarathy S, Nishiyama Y, Ishii Y (2013) Sensitivity and Resolution Enhanced Solid-State NMR for Paramagnetic Systems and Biomolecules under Very Fast Magic Angle Spinning. *Acc. Chem. Res.* 46:2127–2135.

[109] Parthasarathy S, Inoue M, Xiao Y, Hoshi M, Ishii Y (2013) Solid-State NMR Study of Pathologically Relevant Amyloid Intermediate of 42-Residue Alzheimer's Beta. *Biophys. J.* 104:359.

[110] Lu JX, et al. (2013) Molecular Structure of β-Amyloid Fibrils in Alzheimer's Disease Brain Tissue. *Cell* 154:1257–1268.

[111] Rienstra CM (2013) Amyloid Structures from Alzheimer's Disease Patients. *Struct.* 21:1722–1723.

[112] Adler J, Scheidt HA, Krüger M, Thomas L, Huster D (2014) Local Interactions Influence the Fibrillation Kinetics, Structure and Dynamics of Aβ (1–40) but Leave the General Fibril Structure Unchanged. *Phys. Chem. Chem. Phys.* 16:7461–7471.

[113] Tang TC, et al. (2014) Conformational Changes Induced by the A21G Flemish Mutation in the Amyloid Precursor Protein Lead to Increased Aβ Production. *Struct.* 22:387–396.

[114] Parthasarathy S, Yoo B, McElheny D, Tay W, Ishii Y (2014) Capturing a Reactive State of Amyloid Aggregates NMR-BASED CHARACTERIZATION OF COPPER-BOUND ALZHEIMER DISEASE AMYLOID β-FIBRILS IN A REDOX CYCLE. *J. Biol. Chem.* 289:9998–10010.

[115] Lim GP, et al. (2001) The Curry Spice Curcumin Reduces Oxidative Damage and Amyloid Pathology in an Alzheimer Transgenic Mouse. *J. Neurosci.* 21:8370–8377.

[116] Ono K, Hasegawa K, Naiki H, Yamada M (2004) Curcumin has Potent Anti-Amyloidogenic Effects for Alzheimer's β-Amyloid Fibrils in vitro. *J. Neurosci. Res.* 75:742–750.

[117] Mithu VS, et al. (2014) Curcumin Alters the Salt Bridge-containing Turn Region in Amyloid β (1–42) Aggregates. *J. Biol. Chem.* 289:11122–11131.

[118] Chen Z, Krause G, Reif B (2005) Structure and Orientation of Peptide Inhibitors Bound to Beta-Amyloid Fibrils. *J. Mol. Biol.* 354:760–776.

[119] Baldus M (2006) Molecular Interactions Investigated by Multi-Dimensional Solid-State NMR. *Curr. Opin. Struct. Biol.* 16:618–623.

[120] Terzi E, Hölzemann G, Seelig J (1997) Interaction of Alzheimer β-Amyloid Peptide (1-40) with Lipid Membranes. *Biochemistry* 36:14845–14852.

[121] Buffy JJ, Waring AJ, Hong M (2005) Determination of Peptide Oligomerization in Lipid Bilayers using ^{19}F Spin Diffusion NMR. *J. Am. Chem. Soc.* 127:4477–4483.

[122] Lindström F, Bokvist M, Sparrman T, Gröbner G (2002) Association of Amyloid-β Peptide with Membrane Surfaces monitored by Solid State NMR. *Phys. Chem. Chem. Phys.* 4:5524–5530.

[123] Yoshiike Y, et al. (2001) New Insights on how Metals Disrupt Amyloid β-Aggregation and their Effects on Amyloid-β Cytotoxicity. *J. Biol. Chem.* 276:32293–32299.

[124] Karr JW, Szalai VA (2008) Cu (II) Binding to Monomeric, Oligomeric, and Fibrillar Forms of the Alzheimer's Disease Amyloid-β Peptide. *Biochemistry* 47:5006–5016.

[125] Zong XH, et al. (2004) Effect of pH and Copper (II) on the Conformation Transitions of Silk Fibroin based on EPR, NMR, and Raman Spectroscopy. *Biochemistry* 43:11932–11941.

[126] Buchete NV, Tycko R, Hummer G (2005) Molecular Dynamics Simulations of Alzheimer's β-Amyloid Protofilaments. *J. Mol. Biol.* 353:804–821.

[127] Khandogin J, Brooks CL (2007) Linking Folding with Aggregation in Alzheimer's β-Amyloid Peptides. *Proc. Natl. Acad. Sci. U.S.A.* 104:16880–16885.

[128] Klimov D, Straub JE, Thirumalai D (2004) Aqueous Urea Solution Destabilizes A$\beta_{16\text{-}22}$ Oligomers. *Proc. Natl. Acad. Sci. U.S.A.* 101:14760–14765.

[129] Baumketner A, Shea JE (2007) The Structure of the Alzheimer Amyloid β 10-35 Peptide Probed Through Replica-Exchange Molecular Dynamics Simulations in Explicit Solvent. *J. Mol. Biol.* 366:275–285.

[130] Miller Y, Ma B, Nussinov R (2010) Polymorphism in Alzheimer Aβ Amyloid Organization Reflects Conformational Selection in a Rugged Energy Landscape. *Chem. Rev.* 110:4820–4838.

[131] Griffiths JM, et al. (1995) Rotational Resonance Solid-State NMR Elucidates a Structural Model of Pancreatic Amyloid. *J. Am. Chem. Soc.* 117:3539–3546.

[132] Jack E, Newsome M, Stockley PG, Radford SE, Middleton DA (2006) The Organization of Aromatic Side Groups in an Amyloid Fibril Probed by Solid-State ^{2}H and ^{19}F NMR Spectroscopy. *J. Am. Chem. Soc.* 128:8098–8099.

[133] Luca S, Yau WM, Leapman R, Tycko R (2007) Peptide Conformation and Supramolecular Organization in Amylin Fibrils: Constraints from Solid-State NMR. *Biochemistry* 46:13505–13522.

[134] Madine J, et al. (2008) Structural Insights into the Polymorphism of Amyloid-Like Fibrils Formed by Region 20-29 of Amylin Revealed by Solid-State NMR and X-Ray Fiber Diffraction. *J. Am. Chem. Soc.* 130:14990–15001.

[135] Ritter C, et al. (2005) Correlation of Structural Elements and Infectivity of the HET-s Prion. *Nature* 435:844–848.

[136] Siemer AB, et al. (2006) Observation of Highly Flexible Residues in Amyloid Fibrils of the HET-s Prion. *J. Am. Chem. Soc.* 128:13224–13228.

[137] Siemer AB, et al. (2006) ^{13}C, ^{15}N Resonance Assignment of Parts of the HET-s Prion Protein in its Amyloid Form. *J. Biomol. NMR* 34:75–87.

[138] Madine J, Doig AJ, Middleton DA (2008) Design of an N-Methylated Peptide Inhibitor of α-Synuclein Aggregation Guided by Solid-State NMR. *J. Am. Chem. Soc.* 130:7873–7881.

[139] Jaroniec CP, MacPhee CE, Astrof NS, Dobson CM, Griffin RG (2002) Molecular Conformation of a Peptide Fragment of Transthyretin in an Amyloid Fibril. *Proc. Natl. Acad. Sci. U.S.A.* 99:16748–16753.

[140] van der Wel PC, Lewandowski JR, Griffin RG (2007) Solid-State NMR Study of Amyloid Nanocrystals and Fibrils Formed by the Peptide GNNQQNY from Yeast Prion Protein Sup35p. *J. Am. Chem. Soc.* 129:5117–5130.

[141] Andronesi OC, et al. (2008) Characterization of Alzheimer's-Like Paired Helical Filaments from the Core Domain of Tau Protein using Solid-State NMR Spectroscopy. *J. Am. Chem. Soc.* 130:5922–5928.

[142] Tycko R (2000) Solid-State NMR as a Probe of Amyloid Fibril Structure. *Curr. Opin. Chem. Biol.* 4:500–506.

[143] Lynn DG, Meredith SC (2000) Review: Model Peptides and the Physicochemical Approach to β-Amyloids. *J. Struct. Biol.* 130:153–173.

[144] Tycko R (2003) Insights into the Amyloid Folding Problem from Solid-State NMR. *Biochemistry* 42:3151–3159.

[145] Makin OS, Serpell LC (2005) Structures for Amyloid Fibrils. *FEBS J.* 272:5950–5961.

[146] Heise H (2008) Solid-State NMR Spectroscopy of Amyloid Proteins. *ChemBioChem* 9:179–189.

[147] Tycko R, Wickner RB (2013) Molecular Structures of Amyloid and Prion Fibrils: Consensus Versus Controversy. *Acc. Chem. Res.* 46:1487–1496.

[148] Morgan C, Colombres M, Nuñez MT, Inestrosa NC (2004) Structure and Function of Amyloid in Alzheimer's Disease. *Prog. Neurobiol.* 74:323–349.

[149] Glabe CG (2004) Conformation-Dependent Antibodies Target Diseases of Protein Misfolding. *Trends Biochem. Sci.* 29:542–547.

[150] Gazit E (2005) Mechanisms of Amyloid Fibril Self-Assembly and Inhibition. *FEBS J.* 272:5971–5978.

[151] Teplow DB (2006) Preparation of Amyloid β-Protein for Structural and Functional Studies. *Methods Enzymol.* 413:20–33.

[152] Estrada L, Soto C (2007) Disrupting β-Amyloid Aggregation for Alzheimer Disease Treatment. *Curr. Top. Med. Chem.* 7:115–126.

[153] Faller P, Hureau C (2009) Bioinorganic Chemistry of Copper and Zinc Ions Coordinated to Amyloid-β Peptide. *Dalton Trans.* pp 1080–1094.

[154] Hureau C, Faller P (2009) Aβ-Mediated ROS Production by Cu Ions: Structural Insights, Mechanisms and Relevance to Alzheimer's Disease. *Biochimie* 91:1212–1217.

[155] Härd T, Lendel C (2012) Inhibition of Amyloid Formation. *J. Mol. Biol.* 421:441–465.

[156] Levitt MH (2008) *Spin Dynamics: Basics of Nuclear Magnetic Resonance* (Wiley, Hoboken, NJ).

[157] Duer MJ (2004) *Introduction to Solid-State NMR Spectroscopy* (Blackwell publishing, Hoboken, NJ).

[158] Mehring M (1983) *High Resolution NMR in Solids* (Springer, Berlin).

[159] Veshtort M, Griffin RG (2006) SPINEVOLUTION: A Powerful Tool for the Simulation of Solid and Liquid State NMR Experiments. *J. Magn. Reson.* 178:248–282.

[160] Bak M, Rasmussen JT, Nielsen NC (2000) SIMPSON: A General Simulation Program for Solid-State NMR Spectroscopy. *J. Magn. Reson.* 147:296–330.

[161] Bloch F (1946) Nuclear Induction. *Phys. Rev.* 70:460–474.

[162] Spiess HW (1978) *NMR Basic Principles and Progress* (Springer, Berlin) Vol. 15.

[163] Brink DM, Satchler GR (1968) *Angular Momentum* (Clarendon Press Oxford).

[164] Edén M (2003) Computer Simulations in Solid-State NMR. I. Spin Dynamics Theory. *Concepts in Magn. Reson. A* 17:117–154.

[165] Abragam A (1961) *The Principles of Nuclear Magnetism* (Oxford University Press).

[166] De Paëpe G (2012) Dipolar Recoupling in Magic Angle Spinning Solid-State Nuclear Magnetic Resonance. *Annu. Rev. Phys. Chem.* 63:661–684.

[167] Maricq MM, Waugh J (1979) NMR in Rotating Solids. *J. Chem. Phys.* 70:3300–3316.

[168] Griffin R (1998) Dipolar Recoupling in MAS Spectra of Biological Solids. *Nat. Struc. Mol. Biol.* 5:508–512.

[169] Ramamoorthy A (2010) *NMR Spectroscopy of Biological Solids* (CRC Press, Boca Raton, FL) Vol. 34.

[170] Shen Y, Bax A (2013) Protein Backbone and Sidechain Torsion Angles Predicted from NMR Chemical Shifts using Artificial Neural Networks. *J. Biomol. NMR* 56:227–241.

[171] Keeler J, Neuhaus D (1985) Comparison and Evaluation of Methods for Two-Dimensional NMR Spectra with Absorption-Mode Lineshapes. *J. Magn. Reson.* 63:454–472.

[172] States D, Haberkorn R, Ruben D (1982) A Two-Dimensional Nuclear Overhauser Experiment with Pure Absorption Phase in Four Quadrants. *J. Magn. Reson.* 48:286–292.

[173] Marion D, Wüthrich K (1983) Application of Phase Sensitive Two-Dimensional Correlated Spectroscopy (COSY) for Measurements of ^{1}H-^{1}H Spin-Spin Coupling Constants in Proteins. *Biochem. Biophys. Res. Commun.* 113:967–974.

[174] Redfield A, Kunz SD (1975) Quadrature Fourier NMR Detection: Simple Multiplex for Dual Detection and Discussion. *J. Magn. Reson.* 19:250–254.

[175] Bodenhausen G, Kogler H, Ernst R (1984) Selection of Coherence-Transfer Pathways in NMR Pulse Experiments. *J. Magn. Reson.* 58:370–388.

[176] Keeler J (2013) *Understanding NMR spectroscopy* (John Wiley & Sons, Chichester).

[177] Shi C, et al. (2014) BSH-CP Based 3D Solid-State NMR Experiments for Protein Resonance Assignment. *J. Biomol. NMR* 59:15–22.

[178] Habenstein B, et al. (2011) Extensive de novo Solid-State NMR Assignments of the 33 kDa C-terminal Domain of the Ure2 Prion. *J. Biomol. NMR* 51:235–243.

[179] Linser R, Bardiaux B, Higman V, Fink U, Reif B (2011) Structure Calculation from Unambiguous Long-Range Amide and Methyl ^{1}H-^{1}H Distance Restraints for a Microcrystalline Protein with MAS Solid-State NMR Spectroscopy. *J. Am. Chem. Soc.* 133:5905–5912.

[180] Paulson EK, et al. (2003) High-Sensitivity Observation of Dipolar Exchange and NOEs between Exchangeable Protons in Proteins by 3D Solid-State NMR Spectroscopy. *J. Am. Chem. Soc.* 125:14222–14223.

[181] Higman VA, et al. (2011) The Conformation of Bacteriorhodopsin Loops in Purple Membranes Resolved by Solid-State MAS NMR Spectroscopy. *Angew. Chem. Int. Ed.* 50:8432–8435.

[182] Takegoshi K, Nakamura S, Terao T (2001) ^{13}C–^{1}H Dipolar-Assisted Rotational Resonance in Magic-Angle Spinning NMR. *Chem. Phys. Lett.* 344:631–637.

[183] Schaefer J, McKay R, Stejskal E (1979) Double-Cross-Polarization NMR of Solids. *J. Magn. Reson.* 34:443–447.

[184] Ishii Y, Tycko R (2000) Sensitivity Enhancement in Solid State ^{15}N NMR by Indirect Detection with High-Speed Magic Angle Spinning. *J. Magn. Reson.* 142:199–204.

[185] Slichter CP (1990) *Principles of Magnetic Resonance* (Springer, Berlin) Vol. 1.

[186] Redfield AG (1955) Nuclear Magnetic Resonance Saturation and Rotary Saturation in Solids. *Phys. Rev.* 98:1787.

[187] Pines A, Gibby M, Waugh J (1973) Proton-Enhanced NMR of Dilute Spins in Solids. *J. Chem. Phys.* 59:569–590.

[188] Metz G, Wu X, Smith S (1994) Ramped-Amplitude Cross Polarization in Magic-Angle-Spinning NMR. *J. Magn. Reson.* 110:219–227.

[189] Peersen OB, Wu X, Kustanovich I, Smith SO (1993) Variable-Amplitude Cross-Polarization MAS NMR. *J. Magn. Reson.* 104:334–339.

[190] Bax A, Kontaxis G, Tjandra N (2001) Dipolar Couplings in Macromolecular Structure Determination. *Methods Enzymol.* 339:127.

[191] Baldus M, Geurts D, Hediger S, Meier B (1996) Efficient ^{15}N–^{13}C Polarization Transfer by Adiabatic-Passage Hartmann–Hahn Cross Polarization. *J. Magn. Reson.* 118:140–144.

[192] Pauli J, Baldus M, van Rossum B, de Groot H, Oschkinat H (2001) Backbone and Side-Chain ^{13}C and ^{15}N Signal Assignments of the α-Spectrin SH3 Domain by Magic Angle Spinning Solid-State NMR at 17.6 Tesla. *ChemBioChem* 2:272–281.

[193] Ishii Y, Yesinowski JP, Tycko R (2001) Sensitivity Enhancement in Solid-State ^{13}C NMR of Synthetic Polymers and Biopolymers by ^{1}H NMR Detection with High-Speed Magic Angle Spinning. *J. Am. Chem. Soc.* 123:2921–2922.

[194] Chevelkov V, et al. (2003) ^{1}H Detection in MAS Solid-State NMR Spectroscopy of Biomacromolecules Employing Pulsed Field Gradients for Residual Solvent Suppression. *J. Am. Chem. Soc.* 125:7788–7789.

[195] Paulson EK, et al. (2003) Sensitive High Resolution Inverse Detection NMR Spectroscopy of Proteins in the Solid State. *J. Am. Chem. Soc.* 125:15831–15836.

[196] Zhou DH, et al. (2007) Proton-Detected Solid-State NMR Spectroscopy of Fully Protonated Proteins at 40 kHz Magic-Angle Spinning. *J. Am. Chem. Soc.* 129:11791–11801.

[197] Brown SP (2012) Applications of High-Resolution ^{1}H Solid-State NMR. *Solid State NMR* 41:1–27.

[198] Samoson A, et al. (2010) in *Encyclopedia of Magnetic Resonance*, eds Harris RK, Wasylishen RE (John Wiley, Chichester) DOI 10.1002/9780470034590.emrstm1017.

[199] Reif B, Griffin R (2003) ^{1}H Detected ^{1}H,^{15}N Correlation Spectroscopy in Rotating Solids. *J. Magn. Reson.* 160:78–83.

[200] Akbey Ü, et al. (2010) Optimum Levels of Exchangeable Protons in Perdeuterated Proteins for Proton Detection in MAS Solid-State NMR Spectroscopy. *J. Biomol. NMR* 46:67–73.

[201] Berjanskii MV, Neal S, Wishart DS (2006) PREDITOR: A Web Server for Predicting Protein Torsion Angle Restraints. *Nucleic Acids Res.* 34:W63–W69.

[202] Cheung MS, Maguire ML, Stevens TJ, Broadhurst RW (2010) DANGLE: a Bayesian Inferential Method for Predicting Protein Backbone Dihedral Angles and Secondary Structure. *J. Magn. Reson.* 202:223–233.

[203] Lewandowski JR, et al. (2010) Measurement of Site-Specific ^{13}C Spin-Lattice Relaxation in a Crystalline Protein. *J. Am. Chem. Soc.* 132:8252–8254.

[204] Nielsen N, Bildsøe H, Jakobsen H, Levitt M (1994) Double-Quantum Homonuclear Rotary Resonance: Efficient Dipolar Recovery in Magic-Angle Spinning Nuclear Magnetic Resonance. *J. Chem. Phys.* 101:1805.

[205] Bloom AL, Shoolery JN (1955) Effects of Perturbing Radiofrequency Fields on Nuclear Spin Coupling. *Phys. Rev.* 97:1261.

[206] Hodgkinson P (2005) Heteronuclear Decoupling in the NMR of Solids. *Prog. Nucl. Magn. Reson. Spectrosc.* 46:197–222.

[207] Ernst M, Zimmermann H, Meier BH (2000) A Simple Model for Heteronuclear Spin Decoupling in Solid-State NMR. *Chem. Phys. Lett.* 317:581–588.

[208] Tekely P, Palmas P, Canet D (1994) Effect of Proton Spin Exchange on the Residual ^{13}C MAS NMR Linewidths. Phase-Modulated Irradiation for Efficient Heteronuclear Decoupling in Rapidly Rotating Solids. *J. Magn. Reson.* 107:129–133.

[209] Mehring M, Sinning G, Pines A (1976) NMR Line Broadening in Solids by Slowing Down of Spin Fluctuations. *EPJ B* 24:73–76.

[210] Laage S, et al. (2009) Fast Acquisition of Multi-Dimensional Spectra in Solid-State NMR Enabled by Ultra-Fast MAS. *J. Magn. Reson.* 196:133–141.

[211] Samoson A, et al. (2005) in *New Techniques in Solid-State NMR* (Springer, Berlin), pp 15–31.

[212] Kobayashi T, et al. (2013) Study of Intermolecular Interactions in the Corrole Matrix by Solid-State NMR under 100 kHz MAS and Theoretical Calculations. *Angew. Chem.* 125:14358–14361.

[213] Kentgens A, et al. (2008) High-Resolution Liquid-and Solid-State Nuclear Magnetic Resonance of Nanoliter Sample Volumes using Microcoil Detectors. *J. Chem. Phys.* 128:052202.

[214] Shaka A, Keeler J, Frenkiel T, Freeman R (1983) An Improved Sequence for Broadband Decoupling: WALTZ-16. *J. Magn. Reson.* 52:335–338.

[215] Bennett AE, Rienstra CM, Auger M, Lakshmi K, Griffin RG (1995) Heteronuclear Decoupling in Rotating Solids. *J. Chem. Phys.* 103:6951–6958.

[216] Fung B, Khitrin A, Ermolaev K (2000) An Improved Broadband Decoupling Sequence for Liquid Crystals and Solids. *J. Magn. Reson.* 142:97–101.

[217] Anderson W, Nelson F (1963) Removal of Residual Splitting in Nuclear Magnetic Double Resonance. *J. Chem. Phys.* 39:183–189.

[218] Levitt MH (1982) Symmetrical Composite Pulse Sequences for NMR Population Inversion. I. Compensation of Radiofrequency Field Inhomogeneity. *J. Magn. Reson.* 48:234–264.

[219] Raleigh DP, Grey CP, Soffe N, Dobson CM (1992) Multiple-Frequency Decoupling in Magic-Angle-Spinning NMR of Paramagnetic Solids. *J. Magn. Reson.* 97:162–170.

[220] Gan Z, Ernst R (1997) Frequency-and Phase-Modulated Heteronuclear Decoupling in Rotating Solids. *Solid State NMR* 8:153–159.

[221] Takegoshi K, Mizokami J, Terao T (2001) ^{1}H Decoupling with Third Averaging in Solid NMR. *Chem. Phys. Lett.* 341:540–544.

[222] Khitrin A, Fung B (2000) Design of Heteronuclear Decoupling Sequences for Solids. *J. Chem. Phys.* 112:2392–2398.

[223] De Paëpe G, Eléna B, Emsley L (2004) Characterization of Heteronuclear Decoupling Through Proton Spin Dynamics in Solid-State Nuclear Magnetic Resonance Spectroscopy. *J. Chem. Phys.* 121:3165–3180.

[224] Thakur RS, Kurur ND, Madhu P (2006) Swept-Frequency Two-Pulse Phase Modulation for Heteronuclear Dipolar Decoupling in Solid-State NMR. *Chem. Phys. Lett.* 426:459–463.

[225] Thakur RS, Kurur ND, Madhu P (2007) Improved Heteronuclear Dipolar Decoupling Sequences for Liquid-Crystal NMR. *J. Magn. Reson.* 185:264–269.

[226] Vinod Chandran C, Madhu P, Kurur ND, Bräuniger T (2008) Swept-Frequency Two-Pulse Phase Modulation (SWf-TPPM) Sequences with Linear Sweep Profile for Heteronuclear Decoupling in Solid-State NMR. *Magn. Reson. Chem.* 46:943–947.

[227] Yu Y, Fung B (1998) An Efficient Broadband Decoupling Sequence for Liquid Crystals. *J. Magn. Reson.* 130:317–320.

[228] Müller N, Madhu PK (2003) *Current Developments in Solid State NMR Spectroscopy* (Springer, New York, NY).

[229] Ladizhansky V (2009) Homonuclear Dipolar Recoupling Techniques for Structure Determination in Uniformly ^{13}C-Labeled Proteins. *Solid State NMR* 36:119–128.

[230] Bayro MJ, et al. (2009) Dipolar Truncation in Magic-Angle Spinning NMR Recoupling Experiments. *J. Chem. Phys.* 130:114506.

[231] LeMaster DM, Kushlan DM (1996) Dynamical Mapping of E. Coli Thioredoxin via 13C NMR Relaxation Analysis. *J. Am. Chem. Soc.* 118:9255–9264.

[232] Hong M, Jakes K (1999) Selective and Extensive ^{13}C Labeling of a Membrane Protein for Solid-State NMR Investigations. *J. Biomol. NMR* 14:71–74.

[233] Zech SG, Wand AJ, McDermott AE (2005) Protein Structure Determination by High-Resolution Solid-State NMR Spectroscopy: Application to Microcrystalline Ubiquitin. *J. Am. Chem. Soc.* 127:8618–8626.

[234] Brown SP (2007) Probing Proton–Proton Proximities in the Solid State. *Prog. Nucl. Magn. Reson. Spectrosc.* 50:199–251.

[235] De Paëpe G, Lewandowski JR, Loquet A, Böckmann A, Griffin RG (2008) Proton Assisted Recoupling and Protein Structure Determination. *J. Chem. Phys.* 129:245101.

[236] Lewandowski JR, De Paëpe G, Griffin RG (2007) Proton Assisted Insensitive Nuclei Cross Polarization. *J. Am. Chem. Soc.* 129:728–729.

[237] Grommek A, Meier BH, Ernst M (2006) Distance Information from Proton-Driven Spin Diffusion under MAS. *Chem. Phys. Lett.* 427:404–409.

[238] Oas T, Griffin R, Levitt M (1988) Rotary Resonance Recoupling of Dipolar Interactions in Solid-State Nuclear Magnetic Resonance Spectroscopy. *J. Chem. Phys.* 89:692–695.

[239] Takegoshi K, Nakamura S, Terao T (1999) ^{13}C–^{13}C Polarization Transfer by Resonant Interference Recoupling under Magic-Angle Spinning in Solid-State NMR. *Chem. Phys. Lett.* 307:295–302.

[240] Colombo M, Meier B, Ernst R (1988) Rotor-Driven Spin Diffusion in Natural-Abundance ^{13}C Spin Systems. *Chem. Phys. Lett.* 146:189–196.

[241] Maas W, Veeman W (1988) Natural Abundance ^{13}C Spin Diffusion Enhanced by Magic-Angle Spinning. *Chem. Phys. Lett.* 149:170–174.

[242] Suter D, Ernst R (1985) Spin Diffusion in Resolved Solid-State NMR Spectra. *Phys. Rev. B* 32:5608.

[243] Fritzsching K, Yang Y, Schmidt-Rohr K, Hong M (2013) Practical Use of Chemical Shift Databases for Protein Solid-State NMR: 2D Chemical Shift Maps and Amino-Acid Assignment with Secondary-Structure Information. *J. Biomol. NMR* 56:155–167.

[244] Andrew E, Clough S, Farnell L, Gledhill T, Roberts I (1966) Resonant Rotational Broadening of Nuclear Magnetic Resonance Spectra. *Phys. Lett.* 21:505–506.

[245] Raleigh D, Levitt M, Griffin R (1988) Rotational Resonance in Solid State NMR. *Chem. Phys. Lett.* 146:71–76.

[246] Levitt M, Raleigh D, Creuzet F, Griffin R (1990) Theory and Simulations of Homonuclear Spin Pair Systems in Rotating Solids. *J. Chem. Phys.* 92:6347–6364.

[247] Karlsson T, Helmle M, Kurur N, Levitt MH (1995) Rotational Resonance Echoes in the Nuclear Magnetic Resonance of Spinning Solids. *Chem. Phys. Lett.* 247:534–540.

[248] Helmle M, et al. (1999) Anomalous Rotational Resonance Spectra in Magic-Angle Spinning NMR. *J. Magn. Reson.* 140:379–403.

[249] Bennett A, Griffin R, Ok J, Vega S (1992) Chemical Shift Correlation Spectroscopy in Rotating Solids: Radio Frequency-Driven Dipolar Recoupling and Longitudinal Exchange. *J. Chem. Phys.* 96:8624–8627.

[250] Lee M, Goldburg WI (1965) Nuclear-Magnetic-Resonance Line Narrowing by a Rotating RF Field. *Phys. Rev.* 140:A1261–A1271.

[251] Wishart DS, Bigam CG, Holm A, Hodges RS, Sykes BD (1995) ^{1}H, ^{13}C and ^{15}N Random Coil NMR Chemical Shifts of the Common Amino Acids. I. Investigations of Nearest-Neighbor Effects. *J. Biomol. NMR* 5:67–81.

[252] Harris RK, et al. (2008) Further Conventions for NMR Shielding and Chemical Shifts IUPAC Recommendations 2008. *Solid State NMR* 33:41–56.

[253] Wishart DS, Sykes BD (1994) The ^{13}C Chemical-Shift Index: a Simple Method for the Identification of Protein Secondary Structure using ^{13}C Chemical-Shift Data. *J. Biomol. NMR* 4:171–180.

[254] Wishart DS, Sykes BD (1994) Chemical Shifts as a Tool for Structure Determination. *Methods Enzymol.* 239:363.

[255] Pastore A, Saudek V (1990) The Relationship between Chemical Shift and Secondary Structure in Proteins. *J. Magn. Reson.* 90:165–176.

[256] Wishart DS, Sykes BD, Richards FM (1991) Relationship between Nuclear Magnetic Resonance Chemical Shift and Protein Secondary Structure. *J. Mol. Biol.* 222:311–333.

[257] Wishart D, Sykes B, Richards F (1992) The Chemical Shift Index: a Fast and Simple Method for the Assignment of Protein Secondary Structure through NMR Spectroscopy. *Biochemistry* 31:1647–1651.

[258] Vranken WF, et al. (2005) The CCPN Data Model for NMR Spectroscopy: Development of a Software Pipeline. *Proteins: Struct., Funct., Bioinf.* 59:687–696.

[259] Goddard TD, Kneller DG (2008) SPARKY 3. (http://www.cgl.ucsf.edu/home/sparky/).

[260] Ando I, Saito H, Tabeta R, Shoji A, Ozaki T (1984) Conformation-Dependent Carbon-13 NMR Chemical Shifts of Poly (L-Alanine) in the Solid State: FPT INDO Calculation of N-Acetyl-N'-Methyl-L-Alanine Amide as a Model Compound of Poly (L-Alanine). *Macromolecules* 17:457–461.

[261] Saitô H (1986) Conformation-Dependent ^{13}C Chemical Shifts: A New Means of Conformational Characterization as Obtained by High-Resolution Solid-State ^{13}C NMR. *Magn. Reson. Chem.* 24:835–852.

[262] Spera S, Bax A (1991) Empirical Correlation Between Protein Backbone Conformation and C. Alpha. and C. Beta. ^{13}C Nuclear Magnetic Resonance Chemical Shifts. *J. Am. Chem. Soc.* 113:5490–5492.

[263] Cornilescu G, Delaglio F, Bax A (1999) Protein Backbone Angle Restraints from Searching a Database for Chemical Shift and Sequence Homology. *J. Biomol. NMR* 13:289–302.

[264] Shen Y, Delaglio F, Cornilescu G, Bax A (2009) TALOS+: A Hybrid Method for Predicting Protein Backbone Torsion Angles from NMR Chemical Shifts. *J. Biomol. NMR* 44:213–223.

[265] Delaglio F, et al. (1995) NMRPipe: A Multidimensional Spectral Processing System Based on UNIX Pipes. *J. Biomol. NMR* 6:277–293.

[266] Brännström K, Öhman A, Olofsson A (2011) Aβ Peptide Fibrillar Architectures Controlled by Conformational Constraints of the Monomer. *PLOS ONE* 6:e25157.

[267] Harper JD, Lansbury Jr PT (1997) Models of Amyloid Seeding in Alzheimer's Disease and Scrapie: Mechanistic Truths and Physiological Consequences of the Time-Dependent Solubility of Amyloid Proteins. *Annu. Rev. Biochem.* 66:385–407.

[268] Jehle S, et al. (2011) N-Terminal Domain of αB-Crystallin Provides a Conformational Switch for Multimerization and Structural Heterogeneity. *Proc. Natl. Acad. Sci. U.S.A.* 108:6409–6414.

[269] Shahid SA, et al. (2012) Membrane-Protein Structure Determination by Solid-State NMR Spectroscopy of Microcrystals. *Nat. Methods* 9:1212–1217.

[270] Amir A, et al. (2012) Nucleoside-5'-Phosphorothioate Analogues are Biocompatible Antioxidants Dissolving Efficiently Amyloid Beta–Metal Ion Aggregates. *Dalton Trans.* 41:8539–8549.

[271] Nadaud PS, Helmus JJ, Sengupta I, Jaroniec CP (2010) Rapid Acquisition of Multidimensional Solid-State NMR Spectra of Proteins Facilitated by Covalently Bound Paramagnetic Tags. *J. Am. Chem. Soc.* 132:9561–9563.

[272] Park SH, Yang C, Opella SJ, Mueller LJ (2013) Resolution and Measurement of Heteronuclear Dipolar Couplings of a Noncrystalline Protein Immobilized in a Biological Supramolecular Assembly by Proton-Detected MAS Solid-State NMR Spectroscopy. *J. Magn. Reson.* 237:164–168.

[273] Dawson DM, et al. (2013) High-Resolution Solid-State ^{13}C NMR Spectroscopy of the Paramagnetic Metal–Organic Frameworks, STAM-1 and HKUST-1. *Phys. Chem. Chem. Phys.* 15:919–929.

[274] Cherny RA, et al. (2001) Treatment with a Copper-Zinc Chelator Markedly and Rapidly Inhibits β-Amyloid Accumulation in Alzheimer's Disease Transgenic Mice. *Neuron* 30:665–676.

[275] Singh I, et al. (2013) Low Levels of Copper Disrupt Brain Amyloid-β Homeostasis by Altering its Production and Clearance. *Proc. Natl. Acad. Sci. U.S.A.* 110:14771–14776.

[276] Faux NG, et al. (2010) PBT2 Rapidly Improves Cognition in Alzheimer's Disease: Additional Phase II Analyses. *J. Alzheimers Dis.* 20:509–516.

[277] Nguyen M, Robert A, Sournia-Saquet A, Vendier L, Meunier B (2014) Characterization of New Specific Copper Chelators as Potential Drugs for the Treatment of Alzheimers Disease. *Chem. Eur. J.* 20:6771–6785.

[278] Franz KJ (2013) Clawing Back: Broadening the Notion of Metal Chelators in Medicine. *Curr. Opin. Chem. Biol.* 17:143–149.

[279] Cleary JP, et al. (2004) Natural Oligomers of the Amyloid-β Protein Specifically Disrupt Cognitive Function. *Nat. Neurosci.* 8:79–84.

[280] Walsh DM, et al. (2002) Naturally Secreted Oligomers of Amyloid β Protein Potently Inhibit Hippocampal Long-Term Potentiation In Vivo. *Nature* 416:535–539.

[281] Haass C, Selkoe DJ (2007) Soluble Protein Oligomers in Neurodegeneration: Lessons from the Alzheimer's Amyloid β-Peptide. *Nat. Rev. Mol. Cell Biol.* 8:101–112.

[282] Shankar GM, et al. (2008) Amyloid-β Protein Dimers Isolated Directly from Alzheimer's Brains Impair Synaptic Plasticity and Memory. *Nat. Med.* 14:837–842.

[283] Klyubin I, et al. (2005) Amyloid β Protein Immunotherapy Neutralizes Aβ Oligomers that Disrupt Synaptic Plasticity In Vivo. *Nat. Med.* 11:556–561.

[284] Dubnovitsky A, et al. (2013) Amyloid-β Protofibrils: Size, Morphology and Synaptotoxicity of an Engineered Mimic. *PLOS ONE* 8:e66101.

[285] Joe B, Vijaykumar M, Lokesh B (2004) Biological Properties of Curcumin-Cellular and Molecular Mechanisms of Action. *Crit. Rev. Food Sci. Nutr.* 44:97–111.

[286] Barry J, et al. (2009) Determining the Effects of Lipophilic Drugs on Membrane Structure by Solid-State NMR Spectroscopy: the Case of the Antioxidant Curcumin. *J. Am. Chem. Soc.* 131:4490–4498.

[287] Ahmed M, et al. (2010) Structural Conversion of Neurotoxic Amyloid-[beta] 1-42 Oligomers to Fibrils. *Nat. Struc. Mol. Biol.* 17:561–567.

[288] Leaver-Fay A, et al. (2011) ROSETTA3: An Object-Oriented Software Suite for the Simulation and Design of Macromolecules. *Methods Enzymol.* 487:545–574.

[289] Bitan G, et al. (2003) Amyloid β-Protein (Aβ) Assembly: Aβ40 and Aβ42 Oligomerize Through Distinct Pathways. *Proc. Natl. Acad. Sci. U.S.A.* 100:330–335.

[290] Yu X, Zheng J (2012) Cholesterol Promotes the Interaction of Alzheimer β-Amyloid Monomer with Lipid Bilayer. *J. Mol. Biol.* 421:561–571.

[291] Filippov AV, Kotenkov SA, Munavirov B, Antzutkin ON (2014) Effect of Curcumin on Lateral Diffusion of Phosphatidylcholines in Saturated and Unsaturated Bilayers. *Langmuir* 30:10686–10690.

[292] Yang F, et al. (2005) Curcumin Inhibits Formation of Amyloid β Oligomers and Fibrils, Binds Plaques, and Reduces Amyloid in vivo. *J. Biol. Chem.* 280:5892–5901.

[293] Masuda Y, et al. (2011) Solid-State NMR Analysis of Interaction Sites of Curcumin and 42-Residue Amyloid β-Protein Fibrils. *Bioorg. Med. Chem.* 19:5967–5974.

[294] Orsi M, Michel J, Essex JW (2010) Coarse-Grain Modelling of DMPC and DOPC Lipid Bilayers. *J. Phys.: Condens. Matter* 22:155106.

[295] Zhang X, et al. (2013) Design and Synthesis of Curcumin Analogues for in Vivo Fluorescence Imaging and Inhibiting Copper-Induced Cross-Linking of Amyloid Beta Species in Alzheimers Disease. *J. Am. Chem. Soc.* 135:16397–16409.

[296] Yanagisawa D, et al. (2011) *In vivo* Detection of Amyloid β Deposition using ^{19}F Magnetic Resonance Imaging with a ^{19}F-Containing Curcumin Derivative in a Mouse Model of Alzheimer's Disease. *Neuroscience* 184:120–127.

[297] Tsai YM, Chien CF, Lin LC, Tsai TH (2011) Curcumin and its Nano-Formulation: the Kinetics of Tissue Distribution and Blood–Brain Barrier Penetration. *Int. J. Pharm.* 416:331–338.

[298] Meng J, et al. (2014) The Anti-Tumor Histone Deacetylase Inhibitor SAHA and the Natural Flavonoid Curcumin Exhibit Synergistic Neuroprotection against Amyloid-Beta Toxicity. *PLOS ONE* 9:e85570.

[299] Konno H, et al. (2014) Synthesis and Evaluation of Curcumin Derivatives Toward an Inhibitor of Beta-Site Amyloid Precursor Protein Cleaving Enzyme 1. *Bioorg. Med. Chem. Lett.* 24:685–690.

[300] Gibson Wood W, Eckert GP, Igbavboa U, Müller WE (2003) Amyloid Beta-Protein Interactions with Membranes and Cholesterol: Causes or Casualties of Alzheimer's Disease. *Biochim. Biophys. Acta* 1610:281–290.